Non-conventional synthesis and characterization of selected MAX phases and antiperovskite materials

Unkonventionelle Synthese und Charakterisierung ausgewählter MAX-Phasen und Antiperovskitmaterialien

TECHNISCHE UNIVERSITÄT DARMSTADT

Vom Fachbereich Chemie

der Technischen Universität Darmstadt

zur Erlangung des akademischen Grades

Doctor rerum naturalium

(Dr. rer. nat.)

Dissertation

von

M.Sc. Niels Kubitza

Erstgutachterin: Prof. Dr. Christina S. Birkel

Zweitgutachter: Prof. Dr. Ulf Wiedwald

Darmstadt 2023

Tag der Einreichung: 24.10.2023

Tag der mündlichen Prüfung: 11.12.2023

Diese Arbeit wurde im Zeitraum von Oktober 2020 bis Dezember 2023 am Eduard-Zintl-Institut der Technischen Universität Darmstadt durchgeführt. In dieser Zeit erfolgten drei Forschungsaufenthalte an der Arizona State University (USA) in der dortigen Arbeitsgruppe von Frau Prof. Dr. Christina S. Birkel mit einer Dauer von insgesamt zweieinhalb Monaten. Die Betreuung der Arbeit wurde durch Frau Prof. Birkel geleitet und durch Herrn Prof. Dr. Ulf Wiedwald (Universität Duisburg-Essen) unterstützt.

Finanzielle Unterstützung dieser Arbeit erfolgte im Rahmen des Sonderforschungsbereichs/Transregio 270 HoMMage der Technischen Universität Darmstadt sowie der Universität Duisburg-Essen.

Teile dieser wurden veröffentlicht oder sind auf Fachkonferenzen vorgestellt worden:

Publikationen

1) **Niels Kubitza,** Andreas Reitz, Anne-Marie Zieschang, Hanna Pazniak, Barbara Albert, Curran Kalha, Christoph Schlueter, Anna Regoutz, Ulf Wiedwald and Christina S. Birkel; From MAX Phase Carbides to Nitrides: Synthesis of V_2GaC, V_2GaN, and the Carbonitride $V_2GaC_{1-x}N_x$, *Inorganic Chemistry,* **2022**, *61, 28*, 10634-10641. https://doi.org/10.1021/acs.inorgchem.2c00200
N.K. conducted material syntheses with the support of A.Reitz. N.K. conducted the SEM and XRD study. A.Z. and B.A. assisted with the design of the ammonia plant. H.P. and U.W. conducted the TEM/EELS study. C.K., C.S., A.Regoutz conducted the XPS study.

2) Andreas Reitz, Hanna Pazniak, Chen Shen, Harish K. Singh, K. Jayanthi, **Niels Kubitza**, Alexandra Navrotsky, Hongbin Zhang, Ulf Wiedwald, and Christina S. Birkel; Cr_3GeN: A Nitride with Orthorombic Antiperovskite Structure, *Chemistry of Materials,* **2022**, *34*, 10304-10310.
N.K. supported the material syntheses and the evaluation of the XRD data.

3) **Niels Kubitza**, Ruiwen Xie, Ivan Tarasov, Chen Shen, Hongbin Zhang, Ulf Wiedwald, and Christina S. Birkel; Microwave-Assisted Synthesis of the New Solid-Solution $(V_{1-x}Cr_x)_2GaC$ ($0 \leq x \leq 1$), a Pauli Paramagnet Almost Matching the Stoner Criterion for $x = 0.80$, *Chemistry of Materials,* **2023**, *35, 11,* 4427–4434. https://doi.org/10.1021/acs.chemmater.3c00591
N.K. conducted the material syntheses, the SEM and XRD study. R.X. and C.S. conducted the DFT study. I.T. and U.W. conducted the magnetic study.

4) **Niels Kubitza,** Carina Büchner, Jordan Sinclair, Rose Snyder, and Christina S. Birkel; Extending the Chemistry of Layered Solids and Nanosheets: Chemistry and Structure of MAX Phases, MAB Phases and MXenes, *ChemPlusChem,* **2023**, *88*, e202300214. https://doi.org/10.1002/cplu.202300214

5) **Niels Kubitza**, Pedram Babaei, Ulf Wiedwald, and Christina S. Birkel; Rapid sol-gel synthesis approach for the preparation of the magnetocaloric antiperovskite Mn_3GaC, *Chemistry of Materials,* **2023***,* accepted.
N.K. conducted the material syntheses, the SEM and XRD study. P.B. conducted the DSC/TGA measurements. U.W. conducted the magnetic study.

6) **Niels Kubitza**, Benedikt Beckmann, Sanja Jankovic, Konstantin Skokov, Aysha A. Riaz, Christoph Schlueter, Anna Regoutz, Oliver Gutfleisch, and Christina S. Birkel; Exploring the potential of nitride and carbonitride MAX phases: Synthesis and characterization of V_2GeC, $V_2GeC_{0.5}N_{0.5}$, and V_2GeN, *Chemistry of Materials*, **2023**, submitted.
N.K. conducted material syntheses with the support of S.J. N.K. conducted the SEM and XRD study. B.B. conducted the magnetic study. K.K. conducted the electronic study. A.A.R., C.S., and A.R. conducted the XPS study.

7) **Niels Kubitza**, Isabel Huck, David Koch, Curran Kalha, Hanna Pazniak, Bo Zhao, Pardeep K. Thakur, Tien-Lin Lee, Aysha A. Riaz, Wolfgang Donner, Hongbin Zhang, Benjamin Moss, Ulf Wiedwald, Anna Regoutz, and Christina S. Birkel; Between carbide and nitride MAX phases: Sol-gel assisted synthesis and characterization of the carbonitride phase $Cr_2GaC_{1-x}N_x$, in preparation.
N.K. conducted material syntheses with the support of I.H. N.K. conducted the SEM and XRD study. D.K. conducted the *T*-dependent XRD study. B.Z. conducted the DFT study. P.T., T.L., A.A.R., and A.R. conducted the XPS study. H.P. and U.W. conducted the magnetic study.

Konferenzbeiträge

Poster:

Niels Kubitza, and Christina S. Birkel; Sol-gel assisted synthesis of new carbonitride MAX phases $V_2GaC_{1-x}N_x$ and $Cr_2GaC_{1-x}N_x$, CIMTEC 2022, 15th International Ceramics Congress, 20.06-24.06.2022, Perugia, Italien.

Niels Kubitza, Ulf Wiedwald, Hanna Pazniak, Anna Regoutz, and Christina S. Birkel; Hybrid solid-state methods to access nitride and carbonitride MAX phases; 21st Conference on Inorganic Chemistry, 26.09-28.09.2022, Marburg, Deutschland.

Vorträge:

Niels Kubitza, Ulf Wiedwald, Hanna Pazniak, Anna Regoutz, and Christina S. Birkel; Wet-chemical assisted synthesis of nitride and carbonitride MAX phases; ECerS 2023, Conference and Exhibition of the Ceramic Society, 02.07.-06.07.2023, Lyon, Frankreich.

Niels Kubitza, Ulf Wiedwald, Anna Regoutz, and Christina S. Birkel; Wet-chemical assisted synthesis of nitride and carbonitride MAX phases as potential MXene precursors, ECOSS 36, 36th European Conference on Surface Science, 28.08.-01.09.2023, Lodz, Polen.

Danksagung

Mein erster großer Dank gilt Prof. Dr. Christina S. Birkel, für die Möglichkeit meine Dissertation unter Ihrer Leitung anfertigen zu dürfen, für die stetige unvergleichliche Unterstützung in dieser prägenden Zeit sowie für die uneingeschränkte Ermöglichung diverser Reisen und Auslandsaufenthalte, welche unbezahlbare Erfahrungswerte beschert haben.

Ein weiterer besonderer Dank gilt Prof. Dr. Ulf Wiedwald, welcher durch seine stetige persönliche Unterstützung sowie seiner großen Expertise im Bereich des Magnetismus und der Materialcharakterisierung, ein unverzichtbarer Kooperationspartner und Zweitbetreuer dieser Arbeit wurde.

Des Weiteren möchte ich Dr. Anna Regoutz danken, für die vielen XPS/HAXPES Messungen und die fruchtbare Zusammenarbeit bei allen zusammen durchgeführten Projekten.

Danke an Dr. Hanna Pazniak und Benedikt Beckmann, für die wertvolle Unterstützung in gemeinsamen Projekten und den Messungen zur magnetischen Charakterisierung sowie Prof. Hongbin Zhang für die Unterstützung bei den theoretischen Berechnungen. Ein weiterer Dank an alle weiteren Kooperationspartner und Mitglieder des CRC/TRR 270 für die projektorientierte und wertvolle gemeinsame Arbeit.

Danke an Prof. Dr. Barbara Albert, Dr. Kathrin Hofmann und Dr. Felix Reinauer für die uneingeschränkte Nutzung der Labore und Messgeräte sowie allen restlichen Mitgliedern des AK Alberts für die tolle gemeinsame Zeit. Ein ebenfalls wichtiger Dank gilt allen Praktikant*innen und Studierenden, welche ich auf Ihrem Weg begleiten durfte und welche mich bei meinen Arbeiten unterstützt haben. Ganz besonders möchte ich mich hierbei bei Isabel Huck und Sanja Jankovic für Ihr großartiges Engagement, Ihre Unterstützung und Ihre Freude an der gemeinsamen Arbeit bedanken.

Seit nunmehr 5 Jahren darf ich ein Teil der wunderbaren Birkel-Lab Group sein. Allen Mitgliedern, die mich auf diesem Weg begleitet haben, gilt ein unbeschreiblicher Dank. Insbesondere Danke an Dr. Minh Hai Tran, Dr. Andreas Reitz, Dr. Jan-Paul Siebert, Dr. Christin Hamm, Dr. Carina Büchner und Rita Klemens. Ebenfalls ein riesiges Dankeschön an Ellen Pfeifer, für die dauerhafte Unterstützung bei allen bürokratischen Herausforderungen. Natürlich möchte ich auch nicht den amerikanischen Teil unserer Gruppe vergessen: Thank you guys, for an unforgettable time in the valley of the sun!

Abschließend gilt es den Menschen Danke zu sagen, die mir diesen Weg überhaupt erst ermöglicht haben und mich in allen erdenklichen Situationen unterstützen. Danke an meine Familie, insbesondere Mama und Papa sowie allen Freunden-Ihr seid die Besten!

Zusammenfassung

MAX-Phasen und Antiperovskitmaterialien sind anorganische Verbindungsklassen, die insbesondere aufgrund ihres vielfältigen Eigenschaftsprofils faszinieren. Während MAX-Phasen als ternäre Übergangsmetallcarbide und -(carbo)nitride definiert werden, mit *M* als Übergangsmetall, *A* als A-Gruppenelement und *X* als Kohlenstoff und/oder Stickstoff, zeichnen sich Antiperovskite insbesondere durch die allgemeine Summenformel X_3BA aus. In dieser werden *A* und *B* klassischerweise als Anionen definiert, wohingegen *X* die Position als Kation besetzt. Die Synthese beider Verbindungsklassen basiert überwiegend auf konventionellen festkörperchemischen Methoden, in welchen lange Reaktionszeiten von teilweise mehreren Tagen und hohen Temperaturen von häufig über 1000 °C benötigt werden. Dies führt zu einer schlechten Energieeffizienz sowie zu einer teilweise eingeschränkten Phasenvielfalt. Um diesen Nachteilen entgegenzuwirken, beschäftigt sich diese Arbeit mit unkonventionellen Synthesen der angeführten Materialklassen, in Verbindung mit neuen Elementkombinationen und deren Eigenschaften. In der Klasse der MAX-Phasen erfolgte die Synthese neuer Mischkristallphasen auf der *M*- und *X*-Seite. Auf der *M*-Seite bestand die Motivation überwiegend auf der Synthese neuer magnetisch interessanter Phasen, ein Feld, welches aufgrund seiner Komplexität weiterhin großes Potential besitzt. Hierbei wurden drei neue Mischkristallsysteme synthetisiert, wobei ausschließlich die Methode des Mikrowellenofenheizens verwendet wurde. Dies verkürzt die die Reaktionszeit der Verbindungen auf eine Stunde bis hin zu lediglich mehreren Minuten, im Vergleich zu Stunden bzw. Tagen mit konventionellen Methoden. Das erste Mischkristallsystem war $(V_{1-x}Cr_x)_2GaC$, welches keine Mischungslücke aufwies und ein lineares Verhalten der Gitterparameter aufzeigte. Die magnetische Charakterisierung in Verbindung mit theoretischen Berechnungen zeigte, dass es sich bei diesem System um einen itineranten Pauli-Paramagneten handelt, dessen Suszeptibilität um 400 % in nicht linearer Form variiert. Bei einer Zusammensetzung von $x = 0.80$ erreicht das System ein Maximum und ist auf Grundlage der Stoner-Theorie nahezu magnetisch geordnet. Das zweite Mischkristallsystem basiert auf der Dotierung von V_2GaC mit Mangan $(V_{1-x}Mn_x)_2GaC$, in welchem es möglich war, einen nominellen Dotierungsgrad von $x = 0.11$ nahezu phasenrein zu realisieren. In Verbindung mit der Cr/V-Mischkristallphase bildet dies eine Grundlage für zukünftige Studien, um eine magnetische Fernordnung in den betrachteten Systemen zu induzieren. Im dritten Projekt erfolgte die Synthese von $(Cr_{1-x}Mo_x)_2GaC$ mit $x = 0.50$. Bis zum angeführten Mischkristallgrad folgten die Gitterparameter linearem Verhalten, wohingegen ab höheren Anteilen von Molybdän das binäre Carbid Mo_2C die Hauptphase bildet. Aufgrund der erhöhten Elektronendichte des Molybdäns wären auch hier zukünftige magnetische Studien interessant.

Auf der *X*-Seite hingegen bestand die Motivation darin, die Phasenvielfalt im Bereich der Nitride/Carbonitride zu erhöhen, welche im Bereich der MAX-Phasen signifikant unterrepräsentiert sind. Als Grund hierfür ist insbesondere die herausfordernde Synthese von nitridischen Verbindungen zu

nennen, die stark durch die hohe Bindungsenergie des Stickstoffs und dessen gasförmigen physikalischen Zustand unter Normalbedingungen beeinflusst wird. Ein vielversprechender Ansatz diese Nachteile zu umgehen ist die Verwendung von nasschemischen Methoden, die gleichzeitig kürzere Reaktionszeiten, niedrigere Temperaturen und eine bessere Reaktionskontrolle erlauben. Analog zur *M*-Seite erfolgte die Synthese von drei neuen Mischkristallphasen. Hierbei wurden zunächst die sogenannte „Harnstoff-Glas“ Sol-Gel-Methode und die Methode flüssigen Ammoniak als Lösungsmittel und Stickstoffquelle zu nutzen, verwendet, um ternäre carbonitridische bzw. binäre nitridische Präkursorenverbindungen zu erhalten. Diese Verbindungen wurden daraufhin mit elementaren Reaktanden versetzt, um die Phasen $V_2GaC_{1-x}N_x$, sowie V_2GaN zu synthetisieren. Dieser zweistufige Prozess stellt eine neue Methode dar, um nitridische bzw. carbonitridische MAX-Phasen zu synthetisieren. Insbesondere die Sol-Gel basierte Methode wurde im nächsten Projekt für die Synthese von $Cr_2GaC_{1-x}N_x$ verwendet. Die Phase wurde umfassend charakterisiert, um eine Spindichtewelle als magnetischen Zustand zu identifizieren, welcher ebenfalls bei der rein nitridischen Cr_2GaN Phase auftritt. Jedoch erfolgte die Unterdrückung des SDW-Zustandes durch den Einbau von Kohlenstoff in die Struktur der MAX-Phase. Das dritte Projekt beschäftigte sich mit der Synthese und Charakterisierung des Systems $V_2GeC_{1-x}N_x$. Hierbei wurde ein alternativer Hybridansatz verfolgt, in welchem zunächst ein binärer VN-Präkursor mittels Mikrowellenheizen hergestellt wurde, bevor die Umsetzung zur MAX-Phasen mit den fehlenden Elementen finalisiert wurde. Abschließendes Verdichten der Proben zur umfassenden Charakterisierung erfolgte mittels Spark-Plasma-Sintering. Magnetische Analysen sowie Widerstandsmessungen zeigten auf, dass die Materialeigenschaften basierend auf dem Stickstoffgehalt eingestellt werden können, was das große Potential der unterrepräsentierten carbonitridischen Verbindungen verstärkt.

Im Bereich der Antiperovskite erfolgte die Entwicklung einer neuen Syntheseroute der magnetokalorisch interessanten Phase Mn_3GaC. Hierbei gelang es das erste Mal die Verbindung rein auf einer nasschemischen Methode mittels einer zitronensäuregestützten Sol-Gel-Methode zu synthetisieren. DSC/TG Messungen konnten genutzt werden, um den carbothermischen Reduktionsmechanismus aufzuklären, wohingegen magnetische Messungen literaturbekannte magnetische Eigenschaften bestätigen konnten. Durch die Synthese der Mischkristallphase $Mn_{2.8}Cr_{0.2}GaC$ und der Phase Mn_3SnC konnte gezeigt werden, dass sich die eingeführte Methode ebenfalls auf andere Stoffsysteme übertragen lässt, wodurch die Methode eine vielversprechende, zeitsparende Alternative zur Synthese von carbidischen Antiperovskitmaterialien darstellt.

Zusammenfassend konnte im Rahmen dieser Arbeit gezeigt werden, dass unkonventionelle Synthesemethoden erhebliches Potential besitzen, um sowohl neue als auch bestehende Materialsysteme mit faszinierenden Eigenschaften energie- und zeiteffizient, sowie mit einer verbesserten Kontrolle des Syntheseprozesses, herzustellen.

I Table of contents

1. Introduction

The continuing technical progress in demanding engineering and functional applications requires the development and exploration of high-performing materials combined with energy-efficient processing methods.[1] Particularly, the latter has become one crucial factor in the ongoing age of global warming. However, in the field of conventional solid-state chemistry, this aspect can often be not satisfied. Techniques, such as hot isostatic pressing, arc melting or annealing, or pressureless sintering are dominated by long reaction times (several hours up to days) and high temperatures (often >1000 °C) resulting in poor energy efficiency, as well as drawbacks regarding the control of particle sizes, the chemical versatility, or morphology of the target materials.[1,2] Nonetheless, these types of methods have also enabled the synthesis of a hardly tangible variety of different fascinating material classes such as the so-called MAX phases or antiperovskite materials.

The former are classically defined as ternary transition metal-based carbides or (carbo)nitrides, where *M* is a transition metal, *A* a main group element (mostly groups 13-15), and *X* is carbon and/or nitrogen. They crystallize in a hexagonally layered crystal structure, which lends these materials a unique property profile to combine both, metallic and ceramic characteristics within one substance class.[3] However, this set of properties is constantly growing, with the synthesis of new materials, such as high-entropy MAX phases,[4,5] magnetically complex alloys,[6,7] or the ability to act as precursors for a rising class of 2D materials, the so-called MXenes, which can be defined as nanosheets synthesized by selective etching.[8,9]

On the other hand, antiperovskite phases have their origin in one of the most important materials classes in the field of solid-state materials, the perovskites, a class whose history dates back to the first half of the 19th century.[10] While traditional perovskites follow the general sum formula ABX_3, with *A* and *B* as cations while *X* is the anion, antiperovskites are electronically inverted, resulting in a sum formula X_3AB, with *X* as the cation site.[11] In the cubic crystal structure, this leads to corner-shared BX_6 octahedra, a structural segment that is mainly responsible for a manifold range of functionalities, such as ionic conductivity,[12,13] superconductivity,[14,15] or magnetism.[16,17]

Despite the wide range of interesting and modern functionalities of both material classes in the focus of this thesis, their main preparation routes are still based on traditional time-consuming solid-state methods. As a result, this work aims to broaden the field of preparation techniques by applying wet-chemical methods, as well as non-conventional heating mechanisms in combination with the exploration of new possible element variations in the field of MAX phases and antiperovskite materials.

In terms of MAX phases, the synthesis of hitherto not reported solid-solution systems on two elemental sites (*M and X-site*) was performed. For the transition metal-based *M*-site, three solid-solution phases were synthesized, with the focus on potential new magnetic MAX phases. Particularly, due to its complexity and the preparative challenges, this field still offers big potential to work on.

Here, the first project dealt with the synthesis and characterization of the system $(V_{1-x}Cr_x)_2GaC$ $(0 \leq x \leq 1)$, which turned out to be an itinerant Pauli paramagnet that is nearly magnetically ordered. In the remaining two solid-solution phases, the incorporation of elements, exhibiting a higher electron density (e.g., Mn, Mo) was investigated. Starting with the parent phase V_2GaC, it was possible to incorporate manganese up to a nominal doping amount of 11 at-% leading to $(V_{1-x}Mn_x)_2GaC$ $(0 \leq x \leq 0.11)$, while molybdenum was incorporated up to 50 at-% in Cr_2GaC, resulting in $(Cr_{1-x}Mo_x)_2GaC$ $(0 \leq x \leq 0.50)$. All new solid-solution phases were synthesized using microwave heating, a method that enables exceptional high heating rates (~600 °C/min) and short reaction times (≤ 1 hour) due to the direct interaction of microwave radiation with the reactants.

On the *X*-site, three solid-solution phases were synthesized as well. The motivation for focusing on nitride and carbonitride MAX phases is based on the significant underrepresentation of the latter in comparison to the predominant carbide materials (~90 % of all reported phases).[18] Furthermore, the incorporation of nitrogen increases the density of states in the system which can be beneficially influence functional properties (e.g., magnetism, conductivity). Reasons for the low numbers of nitrogen-containing MAX phases can be found in the demanding synthesis of nitrides which is highly influenced by the high bonding energy of nitrogen or its gaseous state under normal conditions. An elegant way to circumvent these challenges is to use wet-chemical-based methods, such as sol-gel synthesis,[19] or to use liquid ammonia as a solvent and nitrogen source.[20]

By applying the so-called "urea glass"[19] sol-gel method, as well as the liquid ammonia method,[20,21] it was possible to synthesize and characterize the materials V_2GaN, and $V_2GaC_{1-x}N_x$ in a new precursor-based two-step process, resulting in lower reaction temperatures and a unique morphology. The sol-gel-based approach was then expanded to $Cr_2GaC_{1-x}N_x$, which was comprehensively characterized to investigate potential similarities to the spin density wave system Cr_2GaN. In the third *X*-site based project a different hybrid solid-state approach was used to produce $V_2GeC_{1-x}N_x$. Here, a binary nitride precursor was synthesized using microwave heating, which was subsequently further processed in a conventional heat treatment with the remaining reactants, while Spark Plasma Sintering was applied to obtain dense samples for a further magnetic and electronic characterization.

In terms of antiperovskites, the projects focused on Mn-based carbide phases, where primarily the Mn_3GaC system was comprehensively investigated. The latter exhibits interesting magnetic properties with the big potential to be used in magnetocaloric applications,[22] a technique utilizing a changing magnetic field for cooling or heating materials.[23]

For the synthesis of Mn_3GaC which was hitherto only synthesized via conventional time-consuming methods a one-step citric acid-based sol-gel approach[24] was applied.

The reaction time was reduced to only 5 hours while maintaining the literature-known magnetic characteristics. In order to prove the suitability of this method, the solid solution phase $Mn_{2.8}Cr_{0.2}GaC$, as well as Mn_3SnC were successfully synthesized following the same procedure. A schematic summary of all investigated material systems is shown in **Figure 1**.

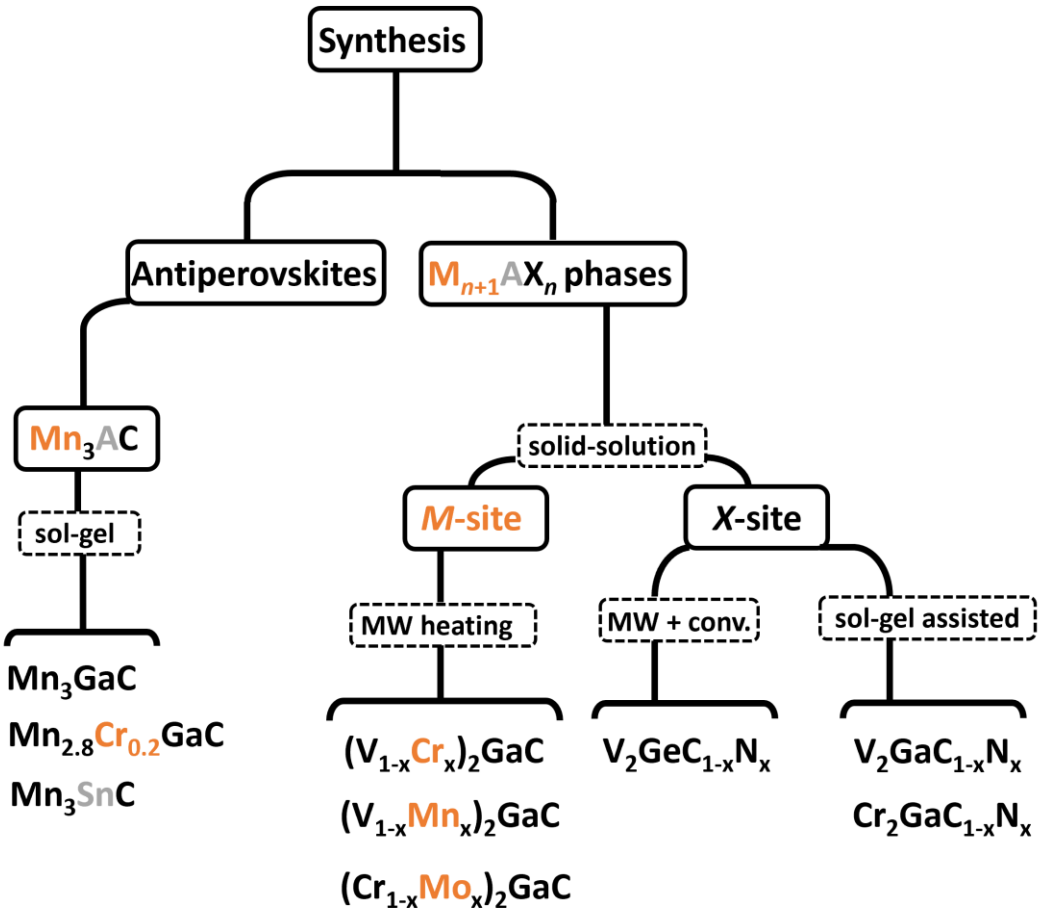

Figure 1: Schematic summary of all investigated target materials discussed and synthesized in the frame of this work.

2. Fundamentals

2.1. Material classes

2.1.1. MAX phases

MAX phases are described as layered ternary transition metal carbides and nitrides, where *M* is an (early) transition metal, *A* an A-group element (mostly of groups 13-15), and *X* carbon and/or nitrogen.[18] Their general sum formula is $M_{n+1}AX_n$ with n values of mainly n = 1,2,3,4 leading to so-called 211-(M_2AX), 312-(M_3AX_2), 413- (M_4AX_3), and 514 phases (M_5AX_4), respectively. They crystallize in a hexagonally anisotropic structure with the space group $P6_3/mmc$, where layers of *A*-elements interleave edge-shared M_6X octahedra (**Figure 2**). The value of n defines the number of *M*-element layers separating the respective *A*-element layers. Consequently, the unit cell increases towards the *c*-direction (up to ~ 28 Å (514 phase)), whereas the *a*-lattice parameter remains at ~ 3 Å.[18,25]

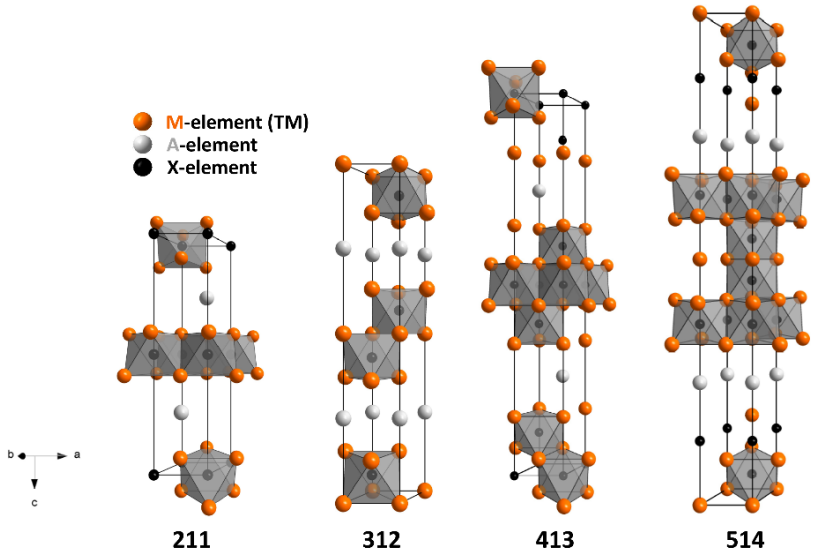

Figure 2: Crystal structures of the hexagonally layered MAX phases (up to 514 phases) that crystallize in space group $P6_3/mmc$. These and all following structures in this work are created using the software *Diamond 4*.

First reports relating to MAX phases date back to the 1960s when KUDIELKA *et al.* synthesized titanium and zirconium-based carbosulfides.[26] Further substantial work was conducted by JEITSCHKO and NOWOTNY *et al.* in the same decade, with the synthesis of the so-called *H*-phases.[27–32] Amongst them were ~ 29 phases that can be nowadays categorized into the group of MAX phases. However, in the following 30 years, no further studies with this class of materials were reported until BARSOUM *et al.* synthesized and characterized the carbide phase Ti_3SiC_2 in 1996.[33] The latter exhibited a unique combination of metallic and ceramic properties, which is today one of the main characteristics of what MAX phases are known for. The term "MAX phases" itself was introduced by BARSOUM *et al.* in the early 2000s and now includes more than 150 phases (>150 carbides,<15 nitrides, <5 carbonitrides), also

going beyond the initial definition of early transition metals carbides and nitrides (**Figure 3**).[18,34] Also, boron has been introduced as an *X*-element.[35]

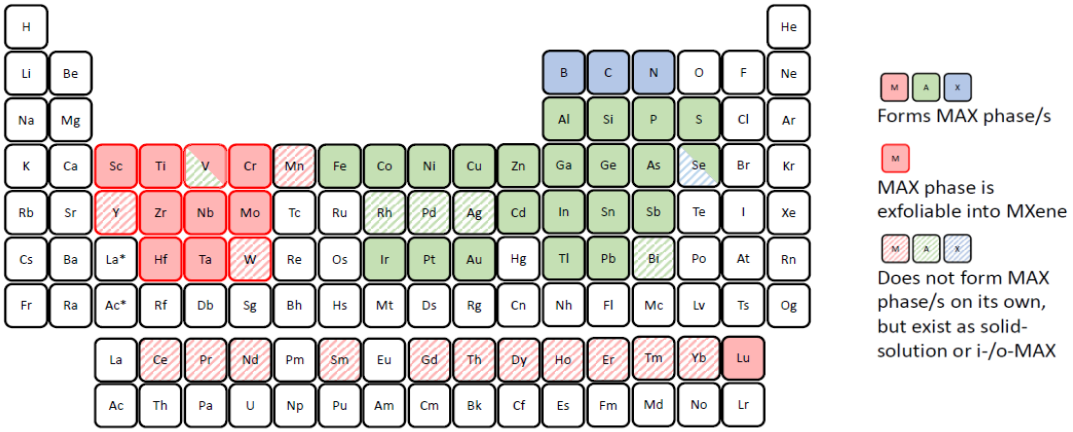

Figure 3: Periodic table showing the elements that form MAX phases and can be exfoliated into MXenes, the two-dimensional siblings of MAX phases. The figure is published in the open-source Review article mentioned above.[36]

The origin for the combination of metallic (e.g., thermal and electrical conductivity, good machinability) and ceramic properties (e.g., oxidation and corrosion resistance, high elastic moduli) can be explained by the layered crystal structure including strong covalent *M-X* bonds, weak ionic *M-A* bonds, as well as metallic contributions by the overlapping *d*-orbitals of the *M*-elements.[18,34] By serving as precursors for the synthesis of highly promising 2D materials (MXenes (**Figure 3**))[8] or by incorporating magnetically interesting elements such as Mn,[37–39] Fe,[40] as well as rare earth elements,[41,42] the property profile of MAX phases has been even more broadened over recent years. The incorporation of *RE* elements additionally influences the structure of the materials, leading to *in-plane (i)* and *out-of-plane (o)* ordered MAX phases (**Figure 4**). While the *in-plane* ordering causes symmetry reduction towards monoclinic (*C*2/*c*, *C*2/*m*[42](less common)) and orthorhombic structures (*Cmcm*), the *out-of-plane* ordering (only for n>2) still follows the hexagonal structure with space group $P6_3/mmc$, however, with different Wyckoff positions of the *M*-elements.[41,42]

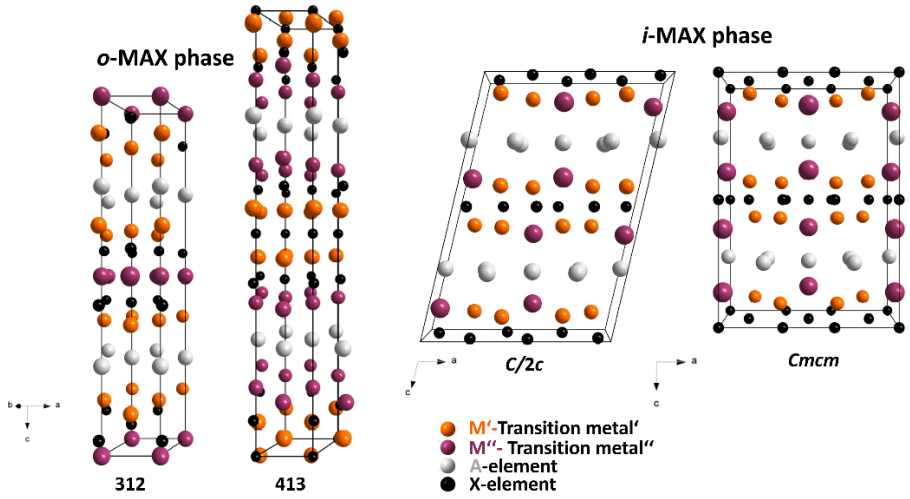

Figure 4: Crystal structures of *out-of-plane* (*o*) ordered ($P6_3/mmc$) and *in-plane (i)* ordered (*C*/2*c*; *Cmcm*) MAX phases.

2.1.2. Antiperovskite phases

One of the most important substance classes in solid-state chemistry is represented by the so-called perovskite materials. First reports reach back to GUSTAV ROSE in 1840,[10] who reported the discovery of the mineral $CaTiO_3$ (*"perovskite"*), which he named after the Russian mineralogist PEROVSKI. Based on $CaTiO_3$, the general sum formula of perovskites can be defined as ABX_3, where *A* and *B* are cations, while *X* is an anion.[11,43]

In the case of an antiperovskite, the formula is electronically inverted, leading to *A* and *B* being anions, while *X* is taking the place of the cation (X_3BA). Antiperovskites usually crystallize in the cubic space group *Pm*-3*m* with corner-shared BX_6 octahedra (**Figure 5**). Depending on the difference in the atomic radii (*r*) of the constituents, the cubic structure can deviate towards structures with lower crystallographic symmetry such as tetragonal or orthorhombic structures. For perovskites, the so-called tolerance factor (*t*) was defined (see below) to predict which symmetry will likely exist.[11]

$$t = \frac{(r_A + r_X)}{[\sqrt{2}(r_B + r_X)]}$$

If *t* is in the range of $t = 0.85\text{-}1.00$ the ideal cubic structure is likely formed, while with lower *t* values the structures with lower symmetry will be predominant. However, most of the antiperovskites contain *p*-elements (e.g., Al, Ga, Ge) that form covalent bonds or *d*-elements (e.g., V, Cr, Mn) with metallic bonds. In such cases, the tolerance factor is only hard to use as a prediction tool.[11] Either way, particularly, the presence of *p* and *d*-elements mainly dictate the interesting properties of antiperovskite phases reaching from ionic conductivity[12,13], over superconductivity[14,15], to magnetism[16,17]. The origin of this set of properties can be structurally explained by the uncommon sixfold coordination of the cation *X* (often *d*-elements) combined with the abundant cationic *X*-sites, strongly influencing the band structure of the materials.[11]

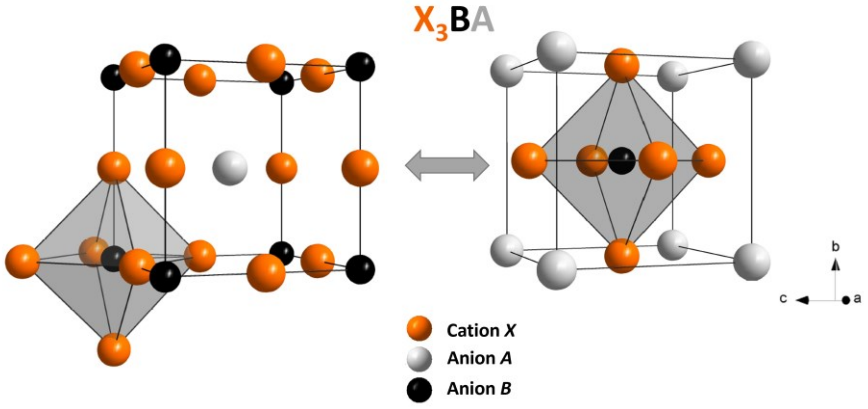

Figure 5: Cubic crystal structure (space group *Pm*-3*m*) in which antiperovskite phases usually crystallize. The structure can be visualized in two different ways, either with cation *X* located at the origin of the unit cell (0 0 0) or anion *A*.

2.2. Synthesis methods

2.2.1. Microwave-assisted solid-state synthesis

Microwave-assisted solid-state synthesis is an alternative heating method where a direct interaction of the sample and microwave radiation causes a heating of the material. Microwave radiation itself can be categorized in the spectrum of electromagnetic radiation with a wavelength of 0.01 to 1 m (**Figure 6**), which corresponds to frequencies between 0.3 and 300 GHz.[44]

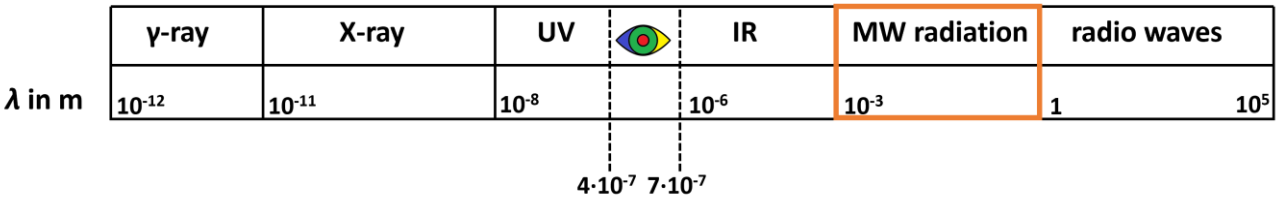

Figure 6: Electromagnetic spectrum based on the wavelength λ in m. MW radiation can be classified between IR and radio waves.

Due to the widespread use of microwave radiation within the communication sector, laboratory instruments for heating purposes are regulated to frequencies of 2.45 GHz. For generating microwaves, magnetrons are used that consist of an anode-cathode combination that is surrounded by a permanent magnet. In between, cylindrical cavities are installed in which high-frequency radio fields are produced that form the basis for the resulting microwaves. However, microwaves do not interact with every material in the same way, which allows a further classification into three types of materials. First, the microwave reflecting materials (e.g., metals as bulk materials), second, the microwave transmitting materials (e.g., quartz, Teflon), and the last group includes the microwave absorbing materials which heat up rapidly in a microwave field.[1,45]

The heating mechanism within microwave ovens is mainly based on the interaction of the electric component of the MW field and the charged particles or electrons of the materials. Typically, in the liquid phase, charges are bound as dipoles, which are then rotated by the external electromagnetic field. If a fast oscillation of the electromagnetic field is present, the dipoles lag behind the external oscillation, leading to dielectric loss and resistive heating. An evaluation of how well a material interacts with microwave radiation is given by the so-called loss tangent tan δ which is defined as the ratio of the dielectric loss factor (ε'') and the real part of the dielectric constant (ε'). On the other hand, if the charge carriers are mobile, such as in electron conductors (e.g., metals), the alternating MW field induces a current in the direction of the field, resulting in resistive heating. This mechanism is predominant in solid-state materials and can be defined as conduction heating. Consequently, the direct interaction between microwave radiation and the sample leads to exceptionally high heating rates and therefore fast reaction times with a minimal need for energy. As soon as the microwave power stops, the heating of the material immediately stops, which can lead to metastable reaction products.[1,44]

Contrary to conventional furnaces, the resulting temperature profile is inverse, and volumetrical heating can be realized. However, this is only possible if every reactant is homogeneously mixed and interacts equally with microwave radiation. If not, this can be used for selective heating where specific regions exhibit much higher temperatures than others. In order to bypass higher temperature gradients or to allow non-interacting reactants to be heat treated, microwave susceptors, such as graphite, can be added around the sample.[44] In this work, a *MARS 6 (CEM)* microwave oven was used. All reactions were carried out in an insulation house of alumina fibers to protect the microwave chamber. To maintain reproducible reaction conditions, graphite was used as a susceptor material. The temperature profiles were acquired by using the IR pyrometer *CTlaser 3MH* (*Optris GmbH*) aligned to the susceptor material. The fundamental reaction setup is shown in **Figure 7**.

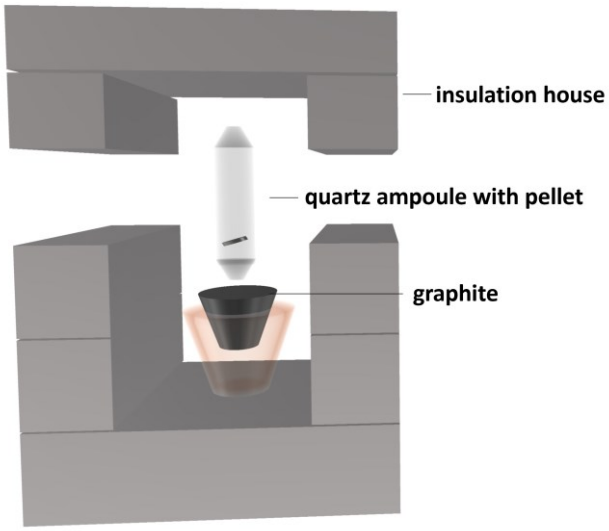

Figure 7: Synthesis setup within the microwave chamber consisting of an insulation house (alumina fibers), the sample, and graphite as a susceptor material.

2.2.2. Spark-Plasma-Sintering (SPS)

Spark-Plasma-Sintering (SPS) is a method that allows to densify and/or synthesize solid-state materials in one step. The term SPS itself is highly discussed in the literature because no spark or plasma has been detected in the synthesis process, yet. This, in turn, gave rise to around 60 different names related to this method, such as “field-assisted sintering technique”, or “pulsed electric current synthesis”. Nonetheless, SPS forms the most stated denomination.[46]

The method is similar to the hot pressing (HP) technique however, the heating mechanisms of both methods are significantly different. While in the HP method, conventional heating mechanisms occur, the SPS method utilizes pulsed high DC current to heat the sample based on the mechanism of joule heating.[1] In general, a mechanical loading system is used, which also acts as an electrical circuit (**Figure 8**). The reactant powder is loaded inside a die (normally graphite) equipped with an upper and

lower punch. Inside the SPS chamber, a uniaxial adjustable pressure is applied to the powder. Simultaneously, a current is passed through the die, and if the sample is conductive, also through the latter, resulting in resistive heating. Consequently, direct heating of the sample with high heating rates of up to 1000 °C/min, as well as high quenching rates of up to 400 °C/min, can be realized. Thus, faster reaction times with better energy efficiency as in conventional methods (e.g., HP) are achieved.[1,46,47]
In this work, the SPS system *SPS-211Lx* (*Fuji Electronic Industrial CO. LTD*) is used. The pellet dies, such as the suitable punches (10 mm x 20 mm), are made of graphite with an inner diameter of d_i = 10.5 mm and an outer diameter of d_{ii} = 10 mm. Before loading the die with powder, the inner wall is covered with graphite foil (0.2 mm thickness) to prevent further damage to the pellet die. Additionally, the outer wall of the pellet die is covered with graphite felt to minimize heat loss during the sintering process. The temperature is controlled using a pyrometer focused on the pellet die. Further information is given in the respective experimental parts.

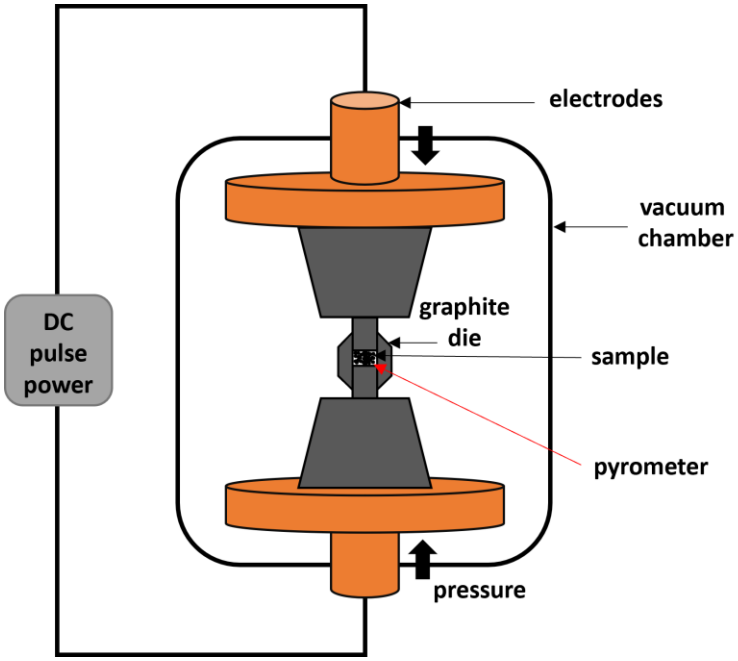

Figure 8: Schematic setup in a Spark-Plasma-Sintering (SPS) experiment, including the power and press section.

2.2.3. Sol-gel synthesis

Sol-gel synthesis is a solution-based synthesis method, in which homogeneous gel-like precursors are transformed into solid-state materials, such as ceramics[48,49] or inorganic polymers.[50,51] The synthesis process can be divided into three main steps. The first step is the formation of a colloidal dispersion, the so-called sol, which is afterwards converted into a two-phase network-like structure, the so-called gel. Often, the gel formation is enabled by polycondensation reactions to form metal-oxo-metal or metal-hydroxy-metal bonds. The last main step includes product formation by drying and calcinating the gel.[51] Thus, the sol-gel synthesis can be described as a hybrid model between low-temperature and high-temperature synthesis methods, where fast reaction times, lower temperatures, and homogeneous products can be realized. Since the first reports on silica gels in the 1800s,[49] the sol-gel method has become highly versatile allowing it to specifically influence the synthesis procedure (e.g., pH value, templates, or gelling agents) and to access many different material systems, such as inorganic borides,[52] nitrides,[53] or carbides[54] with alternating properties.[51] Two important sol-gel methods for synthesizing carbides are the so-called cictric acid[51] and "urea-glass"[53] approach, whereas the latter is also used for the synthesis of (carbo)nitrides. In a typical citric acid-based sol-gel synthesis, an aqueous solution of metal salts, mainly nitrate precursors, and citric acid is formed. By heating the solution, a gel is formed, where citric acid acts as a chelating agent (**Figure 9**). The calcination step can be influenced by choosing the right atmosphere to obtain either oxide or carbide products. During the heat treatment, the nitrates act as oxidants, whereas the citric acid forms the "organic fuel".[51] The reaction mechanism for the carbide synthesis can be described as a carbothermal reduction.[24,55] On the other hand, the so-called "urea-glass" method is typically a non-aqueous-based sol-gel method developed by GIORDANO and ANTONIETTI *et al.*[53] Here, mostly metal chloride precursors are mixed with ethanol, where metal orthoesters are formed under the release of HCl. This step is crucial for further procedure since undissolved or unreacted salts cannot be further processed. For gel formation, urea in a specific metal precursor/urea ratio (*R*) is added as a chelating agent (**Figure 9**). By changing *R*, it is possible to influence the product formation towards nitrides or carbides during the calcination step under flowing nitrogen. Similar to the citric acid sol-gel approach, the reaction mechanism can be described as a carbothermal reduction nitridation process (CRN).[19,53]

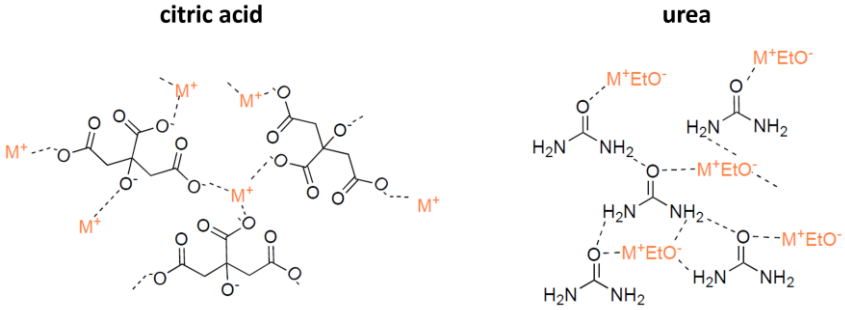

Figure 9: Exemplary illustration of the network gel structure caused by the gelling agents citric acid (left) and urea (right).

2.2.4. Synthesis in liquid ammonia

Ammonia under normal conditions is a colorless toxic gas that has a boiling point of -33 °C. In its liquid form, ammonia exhibits various similarities to water, such as the auto-ioniziation, a low specific conductivity, or a good solubility behavior for ionic liquids, as well as many inorganic salts (e.g., ammonium salts or halides).[56,57]

Nonetheless, it also exhibits significant differences. It is highly hygroscopic and reacts strongly with carbon dioxide, which requires handling under inert conditions. Importantly, this enables oxygen-free reaction conditions. Additionally, the increased N-H bonding strength stabilizes reactions, that are unstable in aqueous solutions. [56,57] However, one of the biggest differences is that liquid ammonia can dissolve alkaline and some earth-alkaline metals, as well as ytterbium and europium without any further chemical reaction.[57–59] During the dissolving process, the metals dissociate into metal cations and solvated electrons. The latter causing a concentration-dependent discoloration of the liquid ammonia, from blue (low solvated electron concentration) towards copper-colored (high solvated-electron concentration).[60] Another property of the solvated electron solutions is to provide a high reduction potential for reduction reactions for both organic and inorganic reactions. Combined with the low temperature and the ability to stabilize free radicals, these solutions are also suitable for the synthesis of nanoparticles.[60] Furthermore, the ammonia-based solutions can act as precursors for the preparation of nitrides.[20,61] Due to its sensitivity to atmospheric conditions, the ammonia was handled in an all-glass synthesis plant, connected to vacuum and argon (**Figure 10**). The plant can be divided into three segments, where the first segment is represented by the ammonia cylinder. The synthesis gas is condensed in segment two, which consists of a cooling trap, filled with sodium to remove oxygen and water impurities. The reactions occur in segment three. Further information is provided in chapter 4.2.

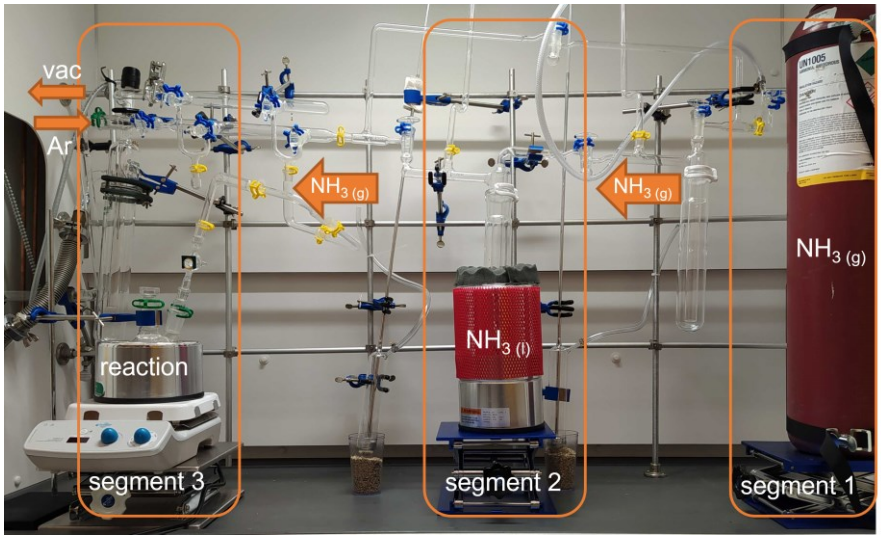

Figure 10: Glass-plant for syntheses in liquid ammonia, consisting of an NH_3 cylinder (1), a Na-filled cooling trap (2), and a reaction segment (3).

2.3. X-ray-based characterization methods

2.3.1. Powder X-ray diffraction (XRD)

X-ray diffraction experiments are one of the most powerful and important techniques in solid-state chemistry to identify and characterize (poly)crystalline solids. Based on its wavelength of λ = 0.5-2.5 Å, which corresponds to the atomic distances in crystal lattices, X-ray radiation can interact with the latter. Here, the crystal lattice with its three-dimensional periodic structure can act as a grating for incoming X-rays which are then diffracted at the electron shell of the atoms located in the lattice. During the diffraction process, interference phenomena occur where constructive interference between diffracted X-ray waves generates a signal at the detector at given 2θ angle. On the other hand, destructively interfering X-ray waves erase themselves. The conditions for constructive interference are given by the so-called Bragg's law (see below), which states that the path difference of adjacent lattice planes must be a multiple of the wavelength λ under the glancing angle θ. This leads to an overall reflection angle of the incoming X-rays of 2θ (**Figure 11**).[62,63]

$$n \cdot \lambda = 2d \cdot \sin(\theta)$$

n = diffraction order
λ = wavelength of incident X-rays
d = interplanar distance
θ = glancing angle

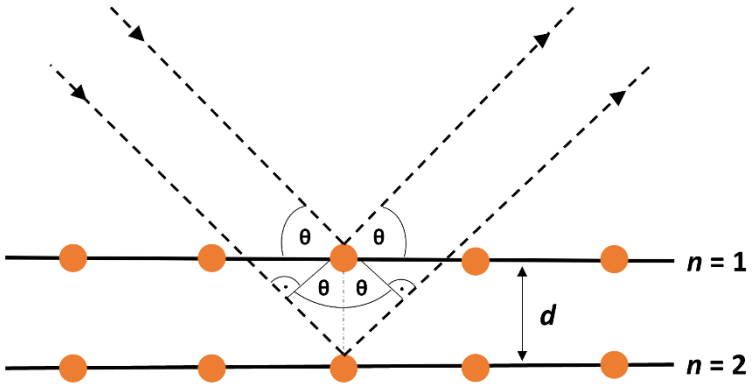

Figure 11: Illustration of the Braggs's law, which defines the constructive interference conditions for X-ray diffraction experiments.

For powder diffraction experiments, diffractometers are used that mainly consist of three components, the X-ray source, a movable detector, and the powder sample. Depending on the measurement geometry, which can be either in reflection mode (Bragg-Brentano-geometry) or transmission mode (Debye-Scherrer-geometry), the sample is rotated horizontally or orthogonally to the X-ray source. The latter can be defined as an X-ray tube, where a focused electron beam is accelerated towards an anode of a high-purity metal (usually copper or molybdenum). This leads to an ionization of the metal, resulting in diverse relaxation processes causing the simultaneous emission of X-rays with various defined wavelengths. Therefore, monochromators can be used to filter one defined wavelength, which is commonly based on the $K_{\alpha,1}$ transition. With both geometries, the collected X-ray diffraction pattern provides information about the lattice parameters and space group based on the 2θ values of the diffraction peaks, as well as the arrangement and types of atoms in the lattice, based on the intensity of the peaks. Another important parameter is the peak profile which can provide information about the instrument or crystallite sizes.[62,64] Depending on the respective project of this work, powder X-ray

diffraction data were obtained using both measurement geometries, as well as both, copper and molybdenum, radiation. Further instrument specifications are given in the respective experimental parts.

2.3.2. Rietveld refinement

Rietveld refinement, developed by HUGO RIETVELD in the late 60s,[65] is a method to elucidate and determine the structural parameters of crystalline materials using neutron or X-ray diffraction data. In a refinement process, a calculated profile, based on a reported crystal structure (e.g., *ICSD* database[66]), is fitted to the experimental diffraction data by optimizing various structural and instrumental parameters. Here, the weighted sum of squared differences between the experimental data points and the calculated profile is attempted to be minimized. Further mathematical parameters, such as the profile *R*-factor (R_P), the weighted profile *R*-factor *(*R_{wp}), the expected *R*-factor (R_{exp}), and the goodness of fit (GOF*)* are used to evaluate the quality of the refinement. Under ideal conditions, the value for the goodness(GOF) is 1.[67,68]

$$R_p = \frac{\sum_i |y_{io} - y_{ic}|}{\sum_i y_{io}} \qquad R_{wp} = \sqrt{\frac{\sum_i w_i (y_{io} - y_{ic})^2}{\sum_i w_i \cdot y_{io}^2}} \qquad R_{exp} = \sqrt{\frac{(N-P)}{\sum_i w_i \cdot y_{io}^2}} \qquad GOF = \frac{R_{wp}}{R_{exp}}$$

y_{io} = observed intensity at position i
y_{ic} = calculated intensity at position i
w_i = weight value for y_{io} (related to its standard uncertainty $w_i = \sigma^{-2}(y_{io})$
N = number of data points
P = number of independent parameters

In a typical refinement procedure, long-time powder X-ray diffraction data were conducted (at least 6 ranges of 0.5 hours) and were then further processed with the software *TOPAS (Bruker)*. Here, based on the instrumental parameters, the background of the experimental data was fitted first, before the lattice parameters and the profile function (pV-TCHZ[69]) were refined. In the last step, the crystallite sizes of selected samples were refined based on the Scherrer equation[70] (see below), which can normally applied to crystallite sizes up to 200 nm, even up to 1 μm in rare cases.[71]

$$L = \frac{K \cdot \lambda}{\beta \cdot \cos(\theta)}$$

L = crystallite size
K = Scherrer constant
β = integral breadth
λ = wavelength of incident X-rays
θ = glancing angle

In specific cases, the Le Bail method[72] was used, in which the intensities of the XRD data are extracted during the refinement. This enables to find peak intensities that facilitate the determination and refinement of atomical structural parameters.

2.3.3. X-ray photoelectron spectroscopy (XPS)

X-ray photoelectron spectroscopy (XPS) is an analytical method based on the photoelectric effect, mainly used for an element specific comprehensive characterization of materials surfaces. In a typical procedure, a sample is irradiated with soft X-rays (~2 kEV) produced by irradiating an anode material (e.g., Al or Mg) with accelerated electrons. Based on the photoelectric effect, irradiation with electromagnetic radiation causes the emission of so-called photoelectrons. Due to a complete transfer of the X-ray energy to a core-level electron, the latter can be excited into the vacuum level and its kinetic energy can be detected. This enables determining the binding energy of electrons, a material's property which also provides information about the chemical state and environment of the elements contained in the sample. Mathematically, the binding energy (*BE*) can be expressed by subtracting the kinetical energy of the photoelectrons (*KE*) and a spectrometer constant (Φs) from the energy of the X-rays ($h\nu$):[73]

$$BE = h\nu - KE - \Phi s$$

BE	=	binding energy
$h\nu$	=	energy of incident X-rays
KE	=	kinetical energy of photoelectrons
Φs	=	spectrometer constant

Since the binding energy is a material's constant, it is independent of the used X-ray source, solely the kinetic energy of the photoelectrons can vary. Simultaneously, with the emission of a photoelectron, a core hole is produced which is subsequently filled with an electron of higher-lying shells. During the relaxation process, energy is released which can also cause the excitation of other electrons into the vacuum level, the so-called Auger electrons. The detection of the latter is often used for the qualitative analysis of the sample, whereas photoelectron peaks can be frequently used for the quantitative analysis. The notation of the former is based on the element and the orbital where the excitation took place, such as "C 1s". On the other hand, the notation for Auger electron peaks is based on the K, L, M nomenclature for atomic orbitals. Here, it is included in which orbital the photoelectron was produced, from which orbital the whole is filled, and which orbital is involved in the excitation of the Auger electrons.[73]
Although X-rays can probe the samples a few micrometers, inelastic scattering of excited electrons within the sample material restricts the probing depth to ~ 10 nm with conventional soft X-ray sources such as aluminum or magnesium. In order to increase the probing depth, alternative X-ray sources with higher energies, such as silver (Ag K_α = 2.984 keV) or chromium (Cr K_α = 5.417 keV) can be used. This is then defined as hard X-ray photoelectron spectroscopy (HAXPES). Another advantage of higher X-ray energies is an increase in the resolution of the spectra, as well as the prevention of eventual spectral overlaps.[73,74] In this work both, the SXPS and HAXPES techniques were used, also by applying synchrotron radiation, exploiting the advantage of tunable X-ray energies combined with high

intensities. Further information on the X-ray sources and instruments is given in the respective experimental parts.

2.4. Imaging methods

2.4.1. Scanning electron microscopy (SEM)

Scanning electron microscopy (SEM) can be categorized into the field of imaging methods that uses accelerated electrons (1-30 kV accelerating voltage) for generating sample images with an enlargement factor of up to 500,000. In the imaging process, a focused electron beam is scanned sequentially across a specimen, where various inelastic and elastic interactions occur at the surface of the sample. For SEM imaging, the so-called secondary electrons (SE) and backscattered electrons (BSE) are essential. Secondary electrons are generated by an inelastic excitation of electrons of the valence or conduction band into the vacuum level by the highly energetic incoming electron beam. The number of emitted secondary electrons depends on the shape of the sample surface, as well as the incidence angle of the electron beam. This in turn allows the collection of topographical information of the sample surface. On the other hand, backscattered electrons (BSE) stem from elastic interactions of the electron beam with the surface atoms and can be used to visualize the material contrast of the investigated material.[75]

In a fundamental SEM setup (**Figure 12**), tungsten cathodes, LaB_6 rods, as well as field emission cathodes (highly energetic) can be used as an electron source. The electron beam is then focused and controlled by various electromagnetic lenses before it hits the sample that must be vacuum stable and electrically conductive. For signal detection, suitable detectors (e.g., Everhart-Thornley detector[76] for SE electrons) have to be installed.[75] Further information on the used instrumentation is given in the respective experimental parts.

.

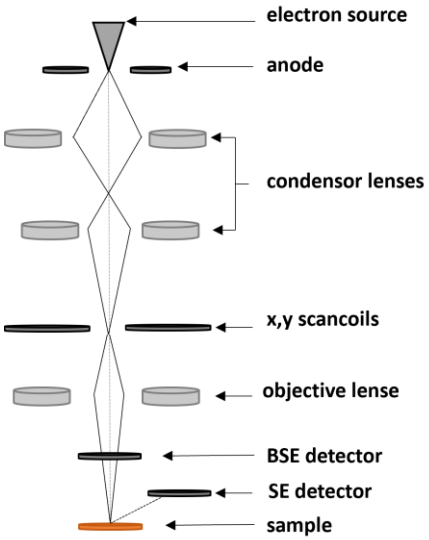

Figure 12: Fundamental SEM setup, including electron source, electromagnetic lenses, the sample and suitable electron detectors.

2.4.2. Transmission electron microscopy (TEM)

While in the SEM, information about the topography of materials is generated, transmission electron microscopy (TEM) is designed to examine the internal microstructure of an investigated sample. This can be realized by transmitting accelerated electrons (80-300 kV accelerating voltage) through a vacuum stable sample with a maximum thickness of 200 μm. Due to the high energy of the accelerated electrons, enlargement factors up to 1 million times can be reached. The standard imaging mode in the TEM is the so-called bright-field (BF) imaging, where it is utilized that the accelerated electrons are either elastically or inelastically scattered by passing through the sample. The scattered electrons can be then separated by apertures which enables a contrast-rich image. The brightness distribution can also be inverted by detecting the scattered electrons, leading to so-called dark-field (DF) imaging. Other common imaging modes are electron diffraction and high-resolution (HRTEM) imaging. The former allows to collect information of the crystallographic structure of the material, while the latter can produce images in atomic resolution.[75]

Analogous to the SEM microscope, some TEM instruments (**Figure 13**) are also equipped with a scanning mode (STEM), which facilitates an accurate elemental analysis of small areas. On the other hand, the possibility of many different imaging methods results in a much more complex setup and electromagnetic lens system than in the SEM (**Figure 12**).[75] Further information on the used instrumentation is given in the respective experimental parts.

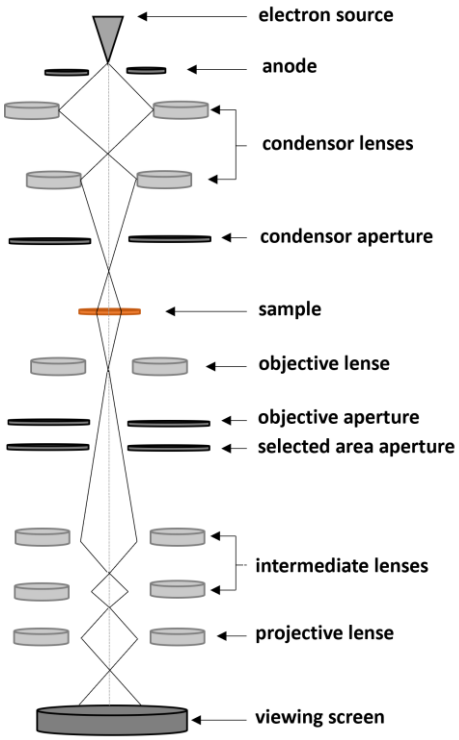

Figure 13: Fundamental TEM setup, including electron source, a complex electromagnetic lens system and suitable detectors.

2.4.3. Energy-dispersive X-ray spectroscopy (EDX)

Energy-dispersive X-ray spectroscopy (EDX) is a standard analytical technique used in SEM or TEM microscopes to determine the atomic composition of the investigated material. It is based on the direct interaction of the atoms with the highly energetic electron beam. When the latter hits the sample, electrons out of near-nucleus shells can be excited into the vacuum level. The resulting vacancies are subsequently refilled by electrons located in higher-lying shells. This is accompanied by a release of characteristic and element-specific X-ray radiation, which is detected and plotted against the energy. Here, the peak position indicates the respective element, and the signal intensity allows to quantify the concentration in the sample. Additionally, it is also possible to visualize the distribution of the elements in a sample as an elemental map. Thus, EDX can be used as both, a qualitative and quantitative method.[75,77]

2.4.4. Electron-energy loss spectroscopy (EELS)

Electron-energy loss spectroscopy (EELS) is used in TEM microscopes, analogous to EDX, for chemically analyzing the investigated material. Besides the chemical composition, it also provides information about the electronic structure and optical properties of the system. The technique is based on detecting the primary electrons that are inelastically scattered after passing through the sample. The scattered electrons can be then separated by energy filters according to their energy loss and counted to form an EELS spectrum with an energy resolution of ~0.5-1 eV. Alternatively, in the so-called energy-filtered TEM (EFTEM) it is possible to create pictures of the sample at selected electron energy loss. A typical EELS spectrum can be divided into three regions, the zero-loss peak (ZLP), the valence EELS or low-loss region, and the ionization edges or core-loss region. While the ZLP is mainly used to examine the energy resolution, the stability of the system and to set the zero-point for energy losses, the valence EELS region provides information about the optical properties, whereas the intensity of the ionization edges is proportional to the elements contained in the sample. Here, in particular, the EELS technique is very suitable to detect light elements such as B, C, N, or O and can be therefore complementarily used with standard EDX analysis.[75,78]

2.5. Characterization of material properties

2.5.1. Vibrating sample magnetometry (VSM)

Vibrating sample magnetometry (VSM) is a standard analytical technique established by Foner *et al.* in the 1950s[79] to determine the magnetic moment of a sample that is perpendicularly vibrated to a uniform magnetic field. For measurements in the conventional way, the sample is mounted on a sample holder that is placed between two electromagnet poles that are equipped with pick-up coils. The optimum position of the sample, the so-called "saddle point", is adjusted by a calibration procedure prior to the measurement. Afterwards, the sample is forced to a constant vertical vibration at a fixed frequency. Based on Faraday's law of induction,[80,81] an AC voltage is induced due to the change in magnetic flux, caused by the steady vibration of the sample. To gain information about the magnetic moment of the sample, the induced voltage is detected by the pickup coils. With this technique changes of 10^{-5} to 10^{-6} emu = 10^{-8} to 10^{-9} Am^2 are detectable.[82] In this work, VSM measurements were performed using a physical property measurement system (PPMS) by *Quantum Design* which allows to measure various material properties by only one device. In contrast to the conventional VSM setup, the *H*-field is produced by a superconducting magnet and applied parallel to the linear movement of the sample (**Figure 14**) and the induced voltage is detected using the lock-in technique.

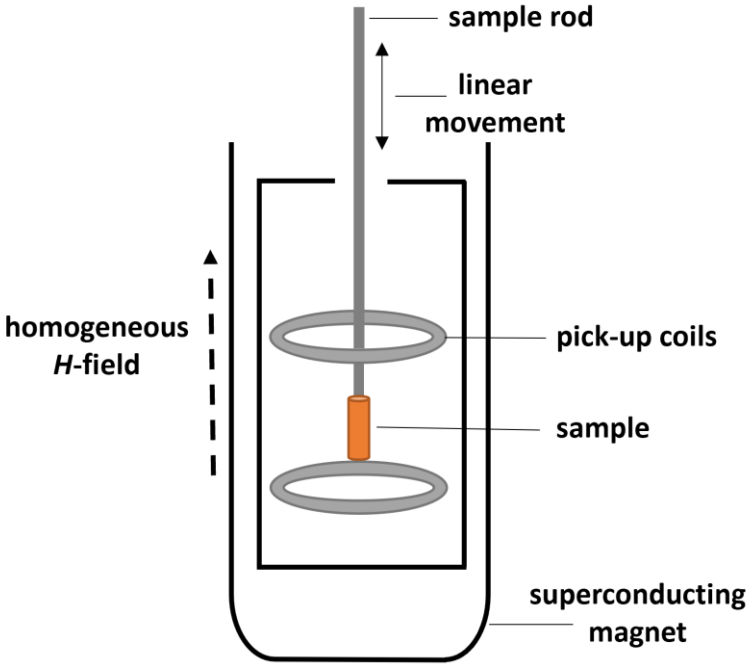

Figure 14: Fundamental VSM setup in the PPMS system, including a vibrating sample, a superconducting magnet for producing a homogeneous *H*-field, and pickup coils.

2.5.2. Resistivity measurements

Electrical resistivity is a material property, highly dependent on the chemical binding in the investigated system and can be defined as a parameter inversely proportional to the carrier density, as well as the carrier mobility.[83] Analogous to the VSM measurements, resistivity measurements were performed in a PPMS by *Quantum Design*. Both, a two-electrode and four-electrode in-line setup was used, measuring the voltage drop across a densified sample. Further information is given in the respective experimental section.

2.5.3. Differential Scanning Calorimetry (DSC)

Differential scanning calorimetry (DSC) is a thermal analysis method for investigating the thermal behavior of materials or chemical reactions. In principle, a sample and a reference material are simultaneously treated with a controlled temperature program in the form of either, heating, cooling, or an isothermic program. During the measurement, the sample and the reference material are kept at nearly the same temperature. However, as soon as thermally detectable transitions occur in the sample material, the relative heat flow changes to maintain the same temperature as the reference material. By detecting the change in heat flow, exothermic as well as endothermic transitions and reactions can be evaluated, including for instance crystallization processes, melting points, or decomposition reactions. Oftentimes, DSC measurements are combined with the so-called thermogravimetric analysis (TGA), where the change in sample mass is detected depending on the temperature. This combination enables further insights into monitoring and evaluating reactions where gaseous substances leave the sample material.[84,85] In this work, a heat flux DSC calorimeter was used, following the general setup illustrated in **Figure 15**. Further information is given in the respective experimental parts.

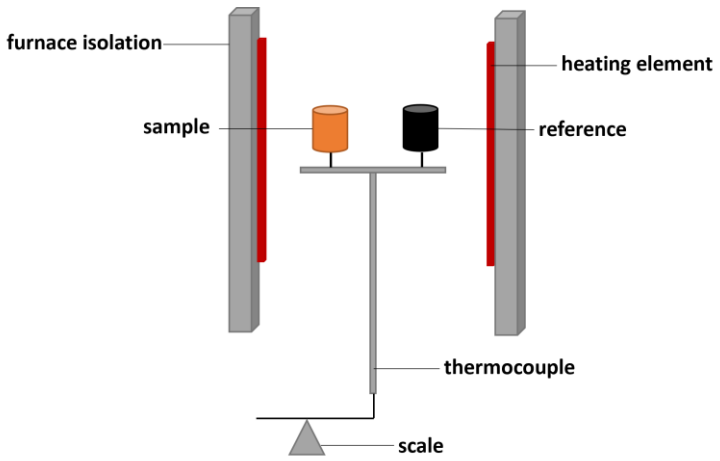

Figure 15: Fundamental DSC/TGA setup, including the heating section and a scale for performing simultaneous TGA measurements.

3. *M*-site solid-solution MAX phases

3.1. State of the Art

The following parts in chapters 3.1.1 and 3.1.2 are published and partially adapted as parts of an open source review article (CC BY-NC-ND 4.0 licensing) published as "Niels Kubitza, Carina Büchner, Jordan Sinclair, Rose Snyder, Christina S. Birkel; Extending the Chemistry of Layered Solids and Nanosheets: Chemistry and Structure of MAX Phases, MAB Phases and MXenes, *ChemPlusChem,* **2023**, *88*, e202300214.

3.1.1. Early transition metals

First investigations of *M*-site solid-solution phases reach back to 1980s, when SCHUSTER and NOWOTNY *et al.*[86–88] already reported H-phases that exhibit solubility on the M-site. Here, the choice of *M*-elements was restricted to groups 4,5, and 6, and combinations of Ti-Nb, V-Nb, V-Cr, V-Ti, Cr-Ti, and Ti-Ta were tested. All phases, except for the $(Cr_{1-x}Ti_x)_2AlC$[87] solid-solution exhibit complete miscibility on the *M*-site by maintaining the $P6_3/mmc$ structure. Roughly 20 years later, first property measurements of solid-solution phases were conducted in the $(Ti,Nb)_2AlC$ system and the at that time newly added solid-solution phase $(Ti,Hf)_2InC$ by SALAMA[89] and BARSOUM *et al.*[90] For instance, the formation of the Ti-Nb solid-solution improved the oxidation resistance in comparison to the parent phases.[89] In the following years, the reports of new solid-solution MAX phases increased significantly and the initial *M*-site compositions of SCHUSTER *et al.* with the addition of zirconium-based[91] phases were also applied to 312 and 413 or even higher aluminum-carbide-based systems. Interestingly, two Cr-Ti solid-solution phases $(Cr_{2/3}Ti_{1/3})_3AlC_2$ and $(Cr_{5/8}Ti_{3/8})_4AlC_3$ were reported,[92] even though the parent phases Cr_3AlC_2, Cr_4AlC_3, and Ti_4AlC_3, were not been predicted to be stable.[93] Recent studies on phases with three or more elements (e.g., $(Ti,Nb,Ta,V)_4AlC_3$[94]) push towards "high entropy"[4,5] MAX phases using the common transition metals of group 4-5 leading to compounds with enhanced mechanical properties. On the other hand, the above-stated examples show that the research of early transition metal solid-solution MAX phases is predominantly concentrated on aluminum-based MAX phases, whereas gallium-based phases have not been reported, yet. Nonetheless, the synthesis and characterization of *M*-site solid-solution phases consisting of the early transition metals, that MAX phases were initially known for, have enabled tailoring specific materials properties such as oxidation resistance,[95,96] mechanical characteristics,[94,97] or thermal properties.[98]

3.1.2. Later transition metals

The property profile of solid-solution MAX phases was even more broadened with the introduction of mid-/later transition metals, such as manganese or iron, on the *M*-site. In 2013, INGASON *et al.*[99]

reported the successful incorporation of 25 at-% manganese on the *M*-site of Cr_2GeC thin films, resulting in the first magnetic MAX phase. Since then, and particularly after the synthesis of Mn_2GaC thin films exhibiting ferromagnetic characteristics up to $T = 230$ K in the same year,[6] many doping studies with manganese on the *M*-site have been conducted. As parent phases, mostly chromium-based 211 MAX phases Cr_2AC with A = Al,[100–102] Ga,[101,103,104] and Ge[101,102,105] as *A*-elements were studied in detail. For example, the group around ROSEN synthesized $(Cr_{0.8}Mn_{0.2})_2AlC$ thin films that revealed a magnetic response significantly above room temperature.[106] This was followed by the synthesis of magnetically ordered $(Cr_{0.5}Mn_{0.5})_2GaC$ films in 2015.[103] Nonetheless, the research was not only restricted to MAX phase thin films but also bulk systems, such as conventionally synthesized $(Cr_{0.94}Mn_{0.06})_2AlC$,[107] $(Cr_{0.85}Mn_{0.15})_2GaC$,[107] or $(Cr_{1-x}Mn_x)_2GeC$ $0 \leq x \leq 0.25$.[108] While the Al-based MAX phases revealed no magnetic response, the Ga-containing ones may be magnetic, whereas the Ge-based phase exhibited weak ferromagnetism with a T_C close to room temperature for a doping level of $x = 0.20$. However, as the above-cited examples have shown, the magnetic behavior of MAX phases is very complex as a consequence of their inherently nanolaminated character. Furthermore, the magnetic properties are highly dependent on the sample quality. Particularly, the latter has turned out to be very challenging due to the formation of thermodynamically more stable side phases, such as antiperovskite phases, binary phases, or other MAX phases that also influence the observed magnetic properties.[7] In order to circumvent several disadvantages that are accompanied by conventional solid-state synthesis procedures (e.g., long reaction times, questionable energy efficiency, equilibrium towards thermodynamical stable phases)[2] HAMM *et al.* applied microwave heating to increase the doping level of manganese towards 10 % and reached a doping level of 2 % iron on the M-site of Cr_2AlC.[40] This synthesis technique was also applied by the synthesis of manganese-doped V_2AlC, which is hitherto the only vanadium-based bulk system where the magnetic properties are studied.[39] In 2021, SOBOLEV *et al.* were able to increase the Mn-amount up to 16 at-% in the $(Cr_{1-x}Mn_x)_2AlC$ phase using the arc melting technique, however, the magnetic ordering is restricted to paramagnetism.[37] Other non-conventional bulk synthesis approaches were made by SIEBERT *et al.* applying a sol-gel approach to synthesize manganese-doped Cr_2GaC with a doping level up to 16 %. While not in the bulk, the authors found Mn-rich areas of the MAX phase that may be magnetically ordered.[38] Going beyond 211 systems, only the magnetically ordered 312 phase $(V,Mn)_3GaC_2$ as a thin film was reported by TAO *et al.*,[109] whereas no examples for 413 phases can be found. This further affirms the complexity of incorporating later transition metals into the MAX phase structure. On the other hand, this also shows that this field of research is still in its infancy and provides a tremendous space for further investigations which is also confirmed by theoretical calculations where new MAX phases containing later transition metals (e.g., Mn as a sole element) have been predicted to be stable.[110,111] In terms of magnetism, TAO *et al.*[42] synthesized chemically and magnetically ordered

rare earth-doped MAX phases that form a suitable complementation of the previously introduced late transition metal doped MAX phases.

3.2. Microwave-assisted synthesis of $(V_{1-x}Cr_x)_2GaC$ ($0 \leq x \leq 1$) MAX phase

The parts (including text, figures, and tables) of the following chapter were published and reproduced (adapted) with permission from "Niels Kubitza, Ruiwen Xie, Ivan Tarasov, Chen Shen, Hongbin Zhang, Ulf Wiedwald and Christina S. Birkel; Microwave-Assisted Synthesis of the New Solid-Solution $(V_{1-x}Cr_x)_2GaC$ ($0 \leq x \leq 1$), a Pauli Paramagnet Almost Matching the Stoner Criterion for x = 0.80, *Chemistry of Materials,* **2023**, *35, 11,* 4427–4434. Copyright (2023) American Chemical Society."

3.2.1. Motivation

As introduced in chapter 3.1.2, the magnetic studies of bulk MAX phases are mainly restricted to chromium-based MAX phases with aluminum as an *A*-element that are doped with small amounts of later transition metals (e.g., Mn, Fe). However, despite the small amounts of dopants, these approaches are accompanied by preparative challenges and the occurrence of side phases. This significantly complicates the interpretation of the data which in turn requires investigating different strategies to approach long-range magnetic ordering in bulk MAX phases. Due to the dominance of MAX phases with aluminum as an *A*-element, this study aims to investigate the magnetic behavior of gallium-based systems over the complete range of a solid-solution phase. V_2GaC was chosen as a starting material to increase the electron density in the system in a controlled manner by stepwise adding chromium without facing the likely problem of ferromagnetic side phases as in the case of using iron or manganese. Additionally, the literature known miscibility of V- and Cr-based[87] phases generally reduces the probability of strongly interfering side phases. Besides, for V_2GaC, no *M*-site solid-solution phases have been reported in the literature, yet.

3.2.2. Experimental section

For the syntheses of the parent phases V_2GaC and Cr_2GaC, as well as solid-solution phases $(V_{1-x}Cr_x)_2GaC$ (x = 0.20, 0.40, 0.50, 0.60, 0.80), the elemental precursor amounts were based on 0.5 g of the desired product. A detailed summary of the used precursor amounts can be found in the (**Table 1**). Initially, gallium flakes (Alfa Aesar, > 99 %) were cut under atmospheric conditions and subsequently transferred into an argon-filled glovebox. Chromium (Sigma-Aldrich, 99 %, ~325 mesh), vanadium (Alfa Aesar, 99.5 %, ~325 mesh), and carbon (Alfa Aesar, >99.9%, APS 2-15 micron) powders were thoroughly mixed using an agate mortar. The mixture was then loosely mixed with the cut gallium flakes and pressed into a dense pellet (⌀ = 10 mm, 3 t, 10 s). All pellets were subsequently sealed into an evacuated fused silica ampoule which was placed into 7 g of activated charcoal (Grüssing, 2.5 mm) acting as a susceptor

material, and annealed inside a microwave oven (*CEM, MARS6*) following a defined temperature program (**Table 2**). The respective heating profiles of the syntheses are illustrated in **Figure 16**. Prior to further characterization steps, the pellets were finely ground (< 100 μm using an agate mortar and stored under atmospheric conditions.

Table 1: Weighing amounts of the prepared MAX phase samples based on 0.5 g of the target material.

Nominal composition	*m*(V) in g	*m*(Cr) in g	*m*(Ga) in g	*m*(C) in g
V_2GaC	0.2774 (2.0 eq.)	-	0.2088 (1.1 eq.)	0.0294 (0.9 eq)
$(V_{0.80}Cr_{0.20})_2GaC$	0.2214 (1.6 eq.)	0.0565 (0.4 eq.)	0.2084 (1.1 eq.)	0.0294 (0.9 eq.)
$(V_{0.60}Cr_{0.40})_2GaC$	0.1657 (1.2 eq.)	0.1128 (0.8 eq.)	0.2079 (1.1 eq.)	0.0293 (0.9 eq.)
$(V_{0.50}Cr_{0.50})_2GaC$	0.1379 (1.0 eq.)	0.1408 (1.0 eq.)	0.2077 (1.1 eq.)	0.0293 (0.9 eq.)
$(V_{0.40}Cr_{0.60})_2GaC$	0.1102 (0.8 eq.)	0.1687 (1.2 eq.)	0.2074 (1.1 eq.)	0.0292 (0.9 eq.)
$(V_{0.20}Cr_{0.80})_2GaC$	0.0550 (0.4 eq.)	0.2245 (1.6 eq.)	0.2084 (1.1 eq.)	0.0294 (0.9 eq.)
Cr_2GaC	-	0.2800 (2.0 eq.)	0.1877 (1.0 eq.)	0.0291 (0.9 eq.)

Table 2: Summary of the temperature programs applied in the microwave-assisted syntheses.

Nominal composition	Temperature programs
V_2GaC	1000 W, 30 mins
$(V_{0.80}Cr_{0.20})_2GaC$	1000 W, 30 mins
$(V_{0.60}Cr_{0.40})_2GaC$	1000 W, 30 mins
$(V_{0.50}Cr_{0.50})_2GaC$	1000 W, 30 mins
$(V_{0.40}Cr_{0.60})_2GaC$	1200 W, 30 mins
$(V_{0.20}Cr_{0.80})_2GaC$	1200 W, 30 mins
Cr_2GaC	1300 W, 20 mins

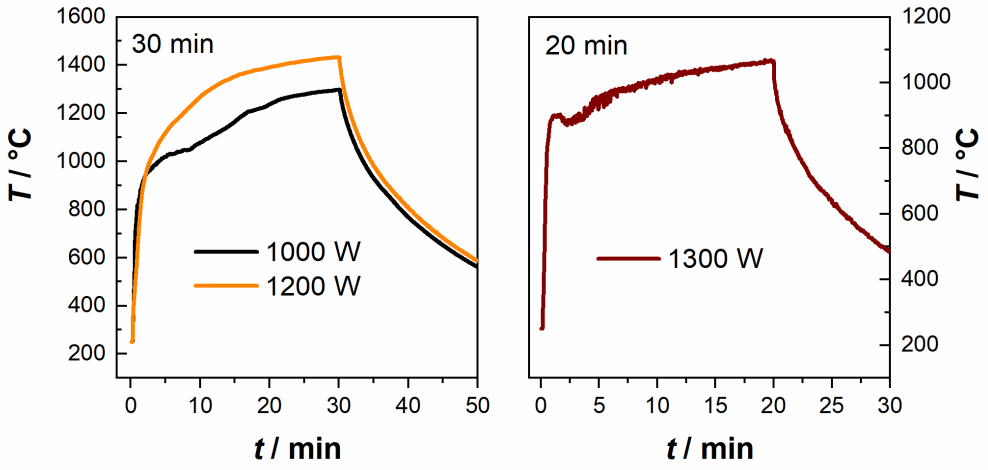

Figure 16: Representative temperature profiles for the applied microwave synthesis parameters summarized in **Table 1**.

3.2.3. Characterization

X-ray powder diffraction data were obtained using a *Stadi P* (*Stoe & Cie GmbH*) with monochromatized Cu-$K_{\alpha,1}$ radiation (λ = 1.540596 Å) and the *Mythen 1K* (*Dectris*) detector in transmission geometry at room temperature. For measurements, small sample amounts were deposited between X-ray amorphous adhesive film (*Scotch*) on a flat sample holder and rotated orthogonally to the X-ray source. Rietveld refinements were performed using the program *TOPAS* (*Bruker*). First, based on the respective structural models, the side phase amounts in wt-% were determined before a detailed refinement of the lattice parameters was conducted based on the Le Bail method.

SEM images were taken at the *XL30 FEG* (*Philips*) using an acceleration voltage of 25 kV adapted with an *APOLLO X-SDD* detector (*EDAX*) for collecting EDX data. The EDX data was evaluated using the software *EDAX GENESIS*.

Magnetic properties were studied by vibrating sample magnetometry (VSM) in a *PPMS DynaCool* system (*Quantum Design*). Dried powder (20-50 mg) was weighed and put into polymer capsules. Measurements were taken within the field range of ±9 T at variable temperatures ranging from 3 K-400 K.

The *ab initio* calculations of the magnetic susceptibility were performed in the fully relativistic regime using the SPR-KKR package,[112,113] which utilizes the linear response theory based on the Green's function technique. The *k*-mesh convergence for both self-consistent and magnetic susceptibility calculations were carefully tested and a *k*-mesh of 17×17×3 was adopted. The cut-off l_{max} = 3 was selected for the angular momentum expansion of the Green's function and the generalized gradient approximation (GGA (PBE)) was adopted for the exchange-correlation functional. $(V_{1-x}Cr_x)_2GaC$ alloys were simulated with the experimentally measured lattice parameters using the coherent potential approximation (CPA),[114] in which V and Cr were assumed to be chemically disordered on the *M*-sites.

3.2.4. Structural analysis

Starting from the parent phase V_2GaC, the amount of chromium was nominally increased in steps of 20 at-% (except for the additional sample with 50 at-%) until the second parent phase Cr_2GaC was obtained. As shown in the refined X-ray powder diffraction data (**Figure 17**), V_2GaC was obtained single-phase, whereas Cr_2GaC revealed small amounts of Cr_3Ga (0.3 wt-%) and $CrGa_4$ (1.8 wt-%) side phases. All solid-solution samples were obtained nearly single phase with $CrGa_3$ (1.3 wt-% for x = 0.20) and $CrGa_4$ (2.8 wt-% for x = 0.40; 1.7 wt-% for x = 0.50) as assignable side phases. By increasing the amount of chromium, a monotonous peak-shift towards higher 2θ angles is observed, which is in accordance with the smaller atomic radius of chromium (2.33 Å) compared to vanadium (2.52 Å),[115] following Vegard's law.[116]

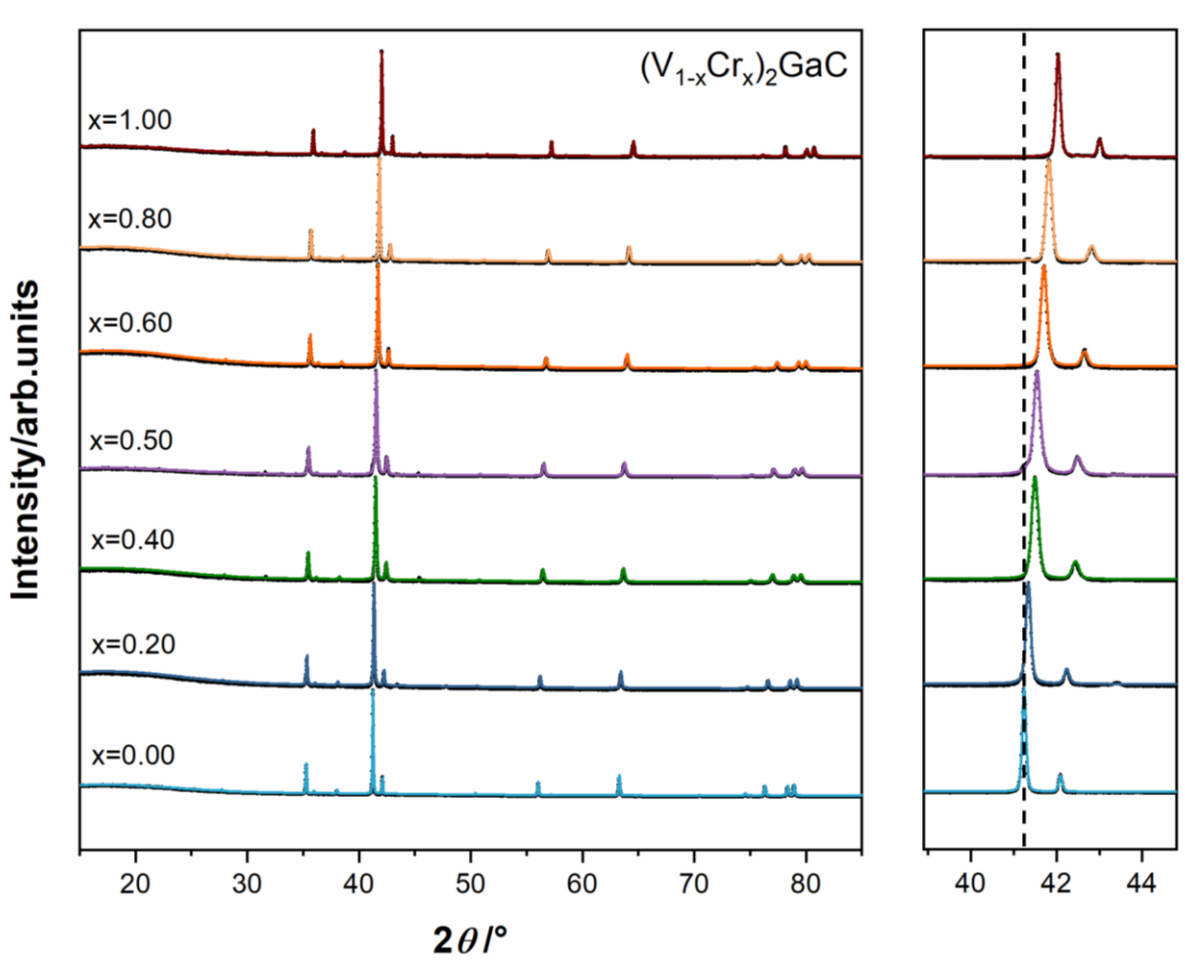

Figure 17: Le Bail refinements (colored lines) of the X-Ray powder diffraction data of the solid-solution phase $(V_{1-x}Cr_x)_2GaC$ (black dots) based on the structural model of V_2GaC[117] providing the space group $P6_3/mmc$. X was nominally increased in steps of 20 at-% (except for 50 at-%).

In order to extract the lattice parameters of all studied MAX phases (**Table 3**), Le Bail refinements were performed based on the structural model of V_2GaC[117] with space group $P6_3/mmc$. A detailed summary of the refinements can be found in **Table 4**-**10**. The lattice parameters of the parent phases V_2GaC and Cr_2GaC are in good agreement with those reported in the literature.[117,118] Following the 2θ peak shift towards higher diffraction angles, the lattice parameters and cell volumes of the solid-solution phases (**Table 3**) exhibit an almost linear decrease towards Cr_2GaC. A graphical illustration of this trend is visualized in **Figure 18**, where a- and c-lattice parameters, as well as cell volumes, are plotted against the actual averaged amount of vanadium (at-%) determined via EDX analysis (**Figure 20**; **Table 11**-**15**). The latter are in good agreement with the nominal compositions. In addition, a simple linear regression of the data validates the approximate linear behavior with R^2 values close to 1 (R^2(a-lattice) = 0.98; R^2(c-lattice) = 0.99; R^2(cell volumes) = 0.99). This in turn also confirms Vegard's law, which describes the linear dependency of the lattice parameters and the percentual composition of the solid-solution phase.[116]

Table 3: Summary of the extracted lattice parameters of the solid-solution $(V_{1-x}Cr_x)_2GaC$ based on Le Bail refinements with the respective errors shown in parentheses.

Nominal composition	Actual composition	*a*-lattice parameter/Å	*c*-lattice parameter/Å	cell volume/Å^3
V_2GaC	V_2GaC	2.9371(3)	12.8752(2)	96.19(2)
$(V_{0.80}Cr_{0.20})_2GaC$	$(V_{0.80}Cr_{0.20})_2GaC$	2.9302(5)	12.8268(3)	95.38(4)
$(V_{0.60}Cr_{0.40})_2GaC$	$(V_{0.59}Cr_{0.41})_2GaC$	2.9205(7)	12.7676(3)	94.31(5)
$(V_{0.50}Cr_{0.50})_2GaC$	$(V_{0.52}Cr_{0.48})_2GaC$	2.9160(7)	12.7442(4)	93.85(5)
$(V_{0.40}Cr_{0.60})_2GaC$	$(V_{0.37}Cr_{0.63})_2GaC$	2.9088(6)	12.7173(3)	93.19(5)
$(V_{0.20}Cr_{0.80})_2GaC$	$(V_{0.19}Cr_{0.81})_2GaC$	2.8999(5)	12.6589(3)	92.19(4)
Cr_2GaC	Cr_2GaC	2.8845(5)	12.6062(3)	90.84(4)

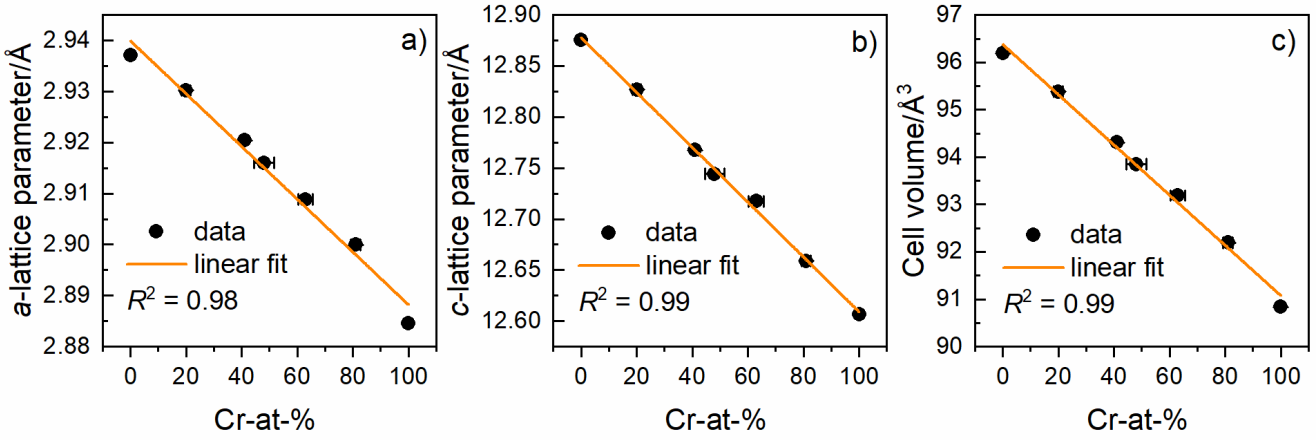

Figure 18: Graphical illustration of the dependency between both, the a-lattice parameters (a), c-lattice parameters (b), the cell volumes (c), and the actual atomic weight-% of chromium including error bars, including simple linear fit (orange lines).

SEM micrographs (**Figure 19**) reveal the typical morphology of the samples, which can be described as a mixture of the characteristic anisotropic MAX phase layered structures combined with surfaces, partially covered with drop-like particles and finer substructures. In general, no meaningful dependency of the morphology on the Cr/V ratio was observed and the morphologies are very similar.

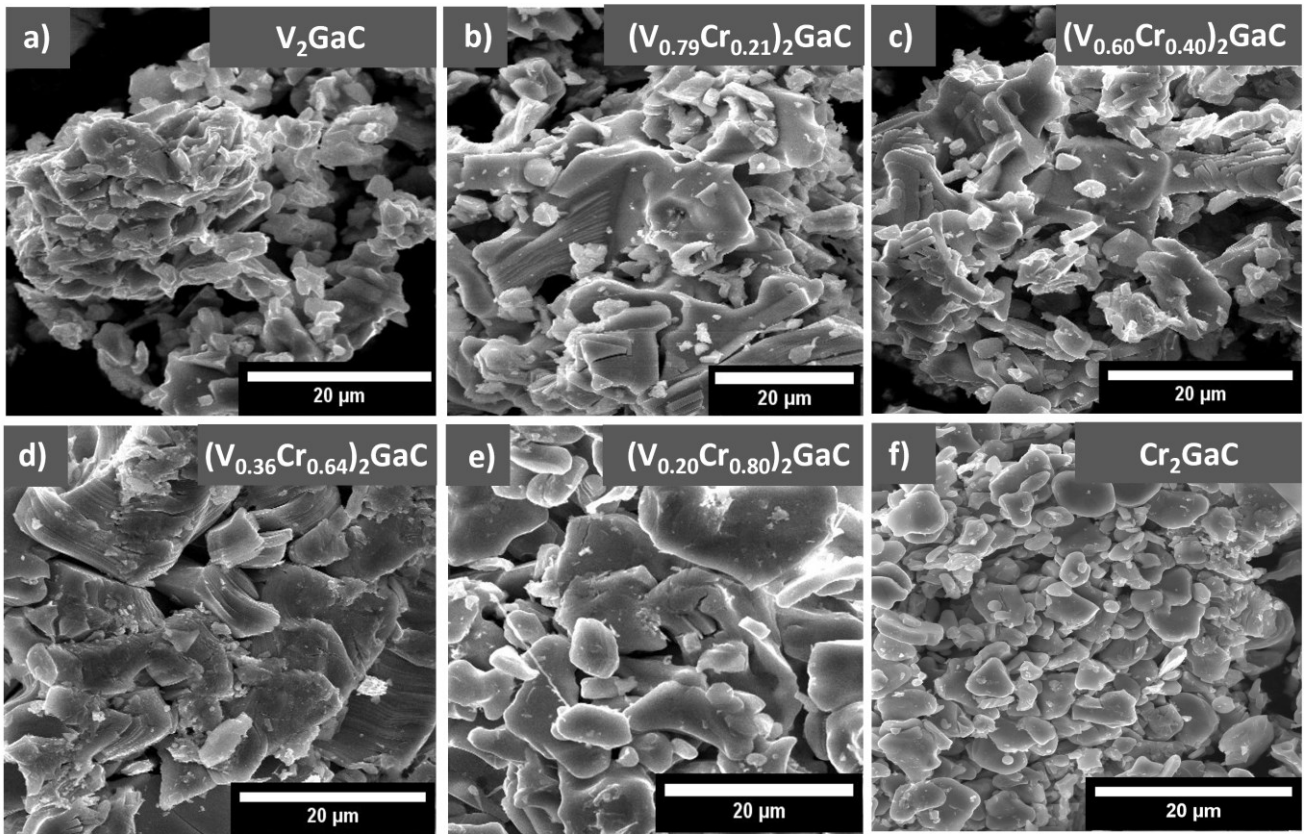

Figure 19: SEM-micrographs showing the typical morphology of V_2GaC (a), $(V_{0.79}Cr_{0.21})_2GaC$ (b), $(V_{0.60}Cr_{0.40})_2GaC$ (c), $(V_{0.36}Cr_{0.64})_2GaC$ (d), $(V_{0.20}Cr_{0.80})_2GaC$ and Cr_2GaC (d), respectively, representing the non-conventionally synthesized solid-solution system $(V_{1-x}Cr_x)_2GaC$ ($0 \leq x \leq 1$).

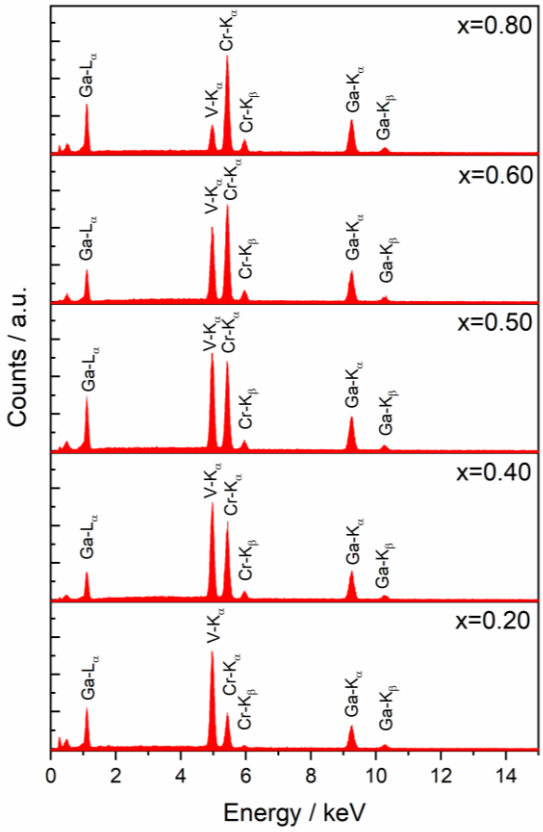

Figure 20: Representative EDX spectra for every investigated nominal composition in the $(V_{1-x}Cr_x)_2GaC$ system.

3.2.5. Magnetic Analysis

The magnetic response of the $(V_{1-x}Cr_x)_2GaC$ $(0 \leq x \leq 1)$ system is presented in **Figure 21**. As a representative for the full series, the field-dependent magnetization of the $(V_{0.37}Cr_{0.63})_2GaC$ powder sample is strictly linear at $T = 300$ K indicating paramagnetism. At lower temperatures, a slight non-linearity sets in as shown in **Figure 21 (a)**. The small absolute magnetization at 9 T is below 0.2 $Am^2\ kg^{-1}$ at $T = 3$ K and only about 50 % larger than the magnetization at 300 K. Such small variations point to temperature-independent Pauli paramagnetism of the conduction electrons as observed before for the Cr_2GaC MAX phase.[119] The non-linear response, however, can be ascribed to tiny amounts of impurity phases not visible in the X-ray diffraction data which is an often-observed complication in the characterization of paramagnetic MAX phases.[40,119] The remanent magnetization of the $(V_{0.37}Cr_{0.63})_2GaC$ sample is $4 \cdot 10^{-3}$ $Am^2\ kg^{-1}$ at $T = 3$ K, decreasing with increasing temperature and a factor of 50 lower than the paramagnetic response of the MAX phase at large fields. Assuming a typical saturation magnetization of 10 $Am^2\ kg^{-1}$ or more of a ferromagnetic impurity phase means that the sample is essentially phase pure and the phase content of the ferromagnetic impurity is maximally 0.04%. Such amounts are not detectable by structural methods but significant as add-ons in magnetometry.

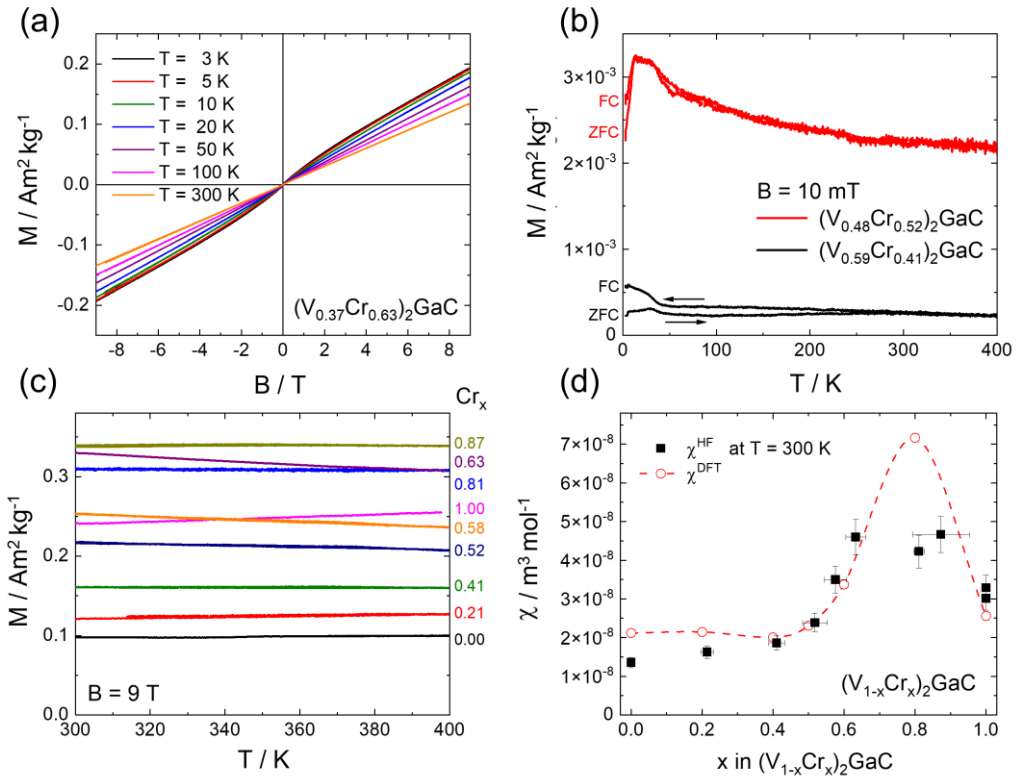

Figure 21: Magnetic properties of the $(V_{1-x}Cr_x)_2GaC$ solid-solution system. (a) Field-dependent magnetization of the $(V_{0.37}Cr_{0.63})_2GaC$ sample at various temperatures between 3 K and 300 K. (b) Zero-field cooling and field cooling curves in B = 10 mT for the $(V_{0.48}Cr_{0.52})_2GaC$ and $(V_{0.59}Cr_{0.41})_2GaC$ samples. (c) Temperature-dependent magnetization of all solid-solution samples. Numbers on the right indicate the x in $(V_{1-x}Cr_x)_2GaC$. (d) Magnetic susceptibility from the field-dependent magnetization in $(V_{1-x}Cr_x)_2GaC$ samples at 300 K. The susceptibility is extracted from a linear fitting of the signal in the interval $|B|$ = 6-9 T. Circles indicate the DFT-calculated magnetic susceptibility. The line is a guide to the eye.

Both, the small temperature dependence of the MAX phase magnetic response and an add-on component at smallest amounts also show up in the zero-field cooling (ZFC) and field cooling (FC) curves in B = 10 mT as presented in **Figure 21 (b)** for the $(V_{0.48}Cr_{0.52})_2GaC$ and $(V_{0.59}Cr_{0.41})_2GaC$ samples, respectively. Both samples show almost constant magnetization values at T = 300 K and above. The $(V_{0.48}Cr_{0.52})_2GaC$ sample magnetization gradually increases with decreasing temperature while below T = 15 K a steep reduction is observed. ZFC/FC of the $(V_{0.59}Cr_{0.41})_2GaC$ sample splits at 230 K indicating a ferromagnetic side phase. However, the differences remain small as compared to the constant paramagnetic offset. The data shown in **Figure 21 (a)** and **(b)** is representative of all the sample series. At low temperatures, deviations from a constant positive value as expected for Pauli paramagnetism are observed due to tiny amounts of side phases. Thus, in the following, the data analysis is restricted to higher temperatures at which the traces of paramagnetic or ferromagnetic impurities have the lowest contribution to the signals.

Figure 21 (c) shows the magnetization as a function of temperature in the largest available field of B = 9 T in the interval 300-400 K. The numbers Cr_x on the right reflect the composition of the $(V_{1-x}Cr_x)_2GaC$ samples. First, it is striking that the magnetization is almost temperature-independent further indicating Pauli paramagnetism. Following the different stoichiometries, the values rise from V_2GaC to x = 0.63 saturating to a plateau up to x = 0.87, and decrease again for Cr_2GaC. Since Pauli paramagnetism is dominant at 300-400 K in these samples the signals point towards an enhanced density of states at the Fermi level E_F. This becomes clearer in **Figure 21 (d)** showing the magnetic susceptibility as extracted from linear fits of the field-dependent magnetization in the interval $|B|$ = 6-9 T at T = 300 K. This high-field susceptibility χ is strictly constant as also shown in **Figure 21 (a)** by the linear response for $(V_{0.37}Cr_{0.63})_2GaC$. The error bars reflect the stoichiometry scattering as determined by SEM-EDX and the uncertainty of the susceptibilities for the ordinate and the abscissa, respectively. Between x = 0.60 and 0.90 an enhanced susceptibility is obtained that is 4 times larger than for V_2GaC and 50% increased as compared to Cr_2GaC.

Summarizing the magnetic data, all samples of the $(V_{1-x}Cr_x)_2GaC$ MAX phases system for $0 \leq x \leq 1$ are Pauli paramagnets. At low temperatures, trace amounts appear as add-on signals. From 300-400 K almost constant magnetic susceptibilities are obtained which, however, vary up to 400 % as a function of stoichiometry. It must be noted that the magnetic energy splitting of spin-up and spin-down states of the conduction electrons at the Fermi level is much smaller at B = 9 T (meV) than the Fermi energy (several eV). At this point, one is tempted to use the Pauli relation $\chi = \chi_P = \mu_0 \mu B^2 D(E_F)$ to determine the density of states at the Fermi level. While for V_2AlC[39] and Cr_2GaC[24] this works reasonably, in the present case the increased susceptibility for $0.63 < x < 0.87$ leads to extremely large numbers $D(E_F)$ appearing unrealistic on first glance. Thus, it was decided to extract the susceptibility directly from DFT

calculations and compare with experiments. The results are shown in **Figure 21 (d)** and will be discussed in the following.

3.2.6. *Ab initio* Calculations

Overall, the magnetic susceptibilities derived from magnetometry and DFT calculations (**Figure 21 (d)**) agree well with respect to the Cr concentration. In both cases, the same trend with a non-linear behavior and a maximum susceptibility at around x = 0.80 is observed. Except for the nominal composition of x = 0.80, the experimentally derived magnetic susceptibilities exhibit only small deviations in comparison to the calculated ones. In order to exclude systematic mistakes, the preparation and magnetic characterization $(V_{0.20}Cr_{0.80})_2GaC$ has been conducted twice following the same method, however, with no further convergence to the calculated values. Sample information of the latter can be found in **Figure 22** and **Table 16-17**.

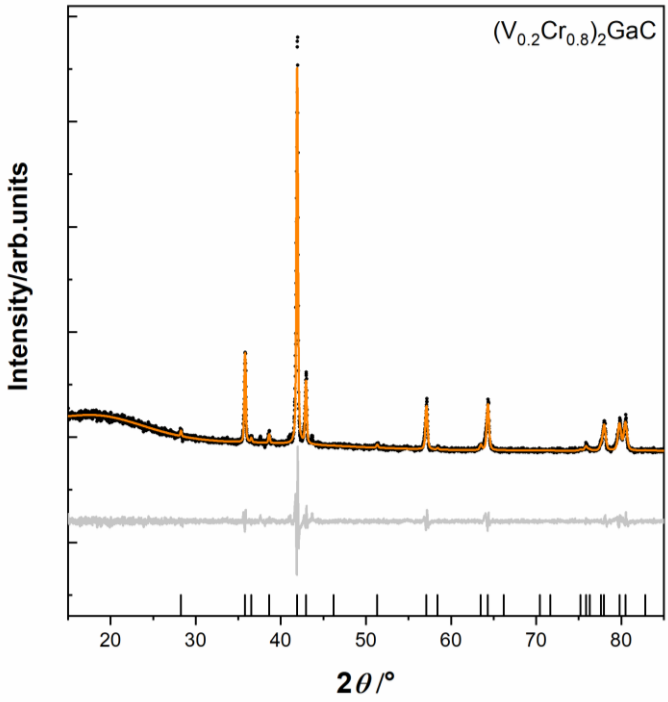

Figure 22: Le Bail refinement (orange line) of the X-ray powder diffraction data of the solid-solution phase $(V_{0.20}Cr_{0.80})_2GaC$ (black) based on the structural model of V_2GaC[117] providing the space group $P6_3/mmc$. This sample was synthesized and characterized to exclude systematic mistakes in the magnetic characterization of the samples.

The element-resolved V and Cr contributions to the magnetic susceptibilities are shown in **Figure 23**. The total magnetic susceptibility χ_{tot} is composed of the total spin susceptibility, which is a sum of the spin susceptibility χ_s including the spin-orbit coupling (SOC) induced spin susceptibility, the total Van Vleck orbital susceptibility χ_o, which includes the enhanced orbital susceptibility and the SOC-induced orbital susceptibility, and finally the diamagnetic susceptibility χ_{dia} consisting of core and band contributions.

As shown in **Figure 23**, the total spin susceptibility of Cr is responsible for the peak at x = 0.80 in the $(V_{1-x}Cr_x)_2GaC$ MAX phase system, while χ_o and χ_{dia} are insensitive to the change of Cr content.

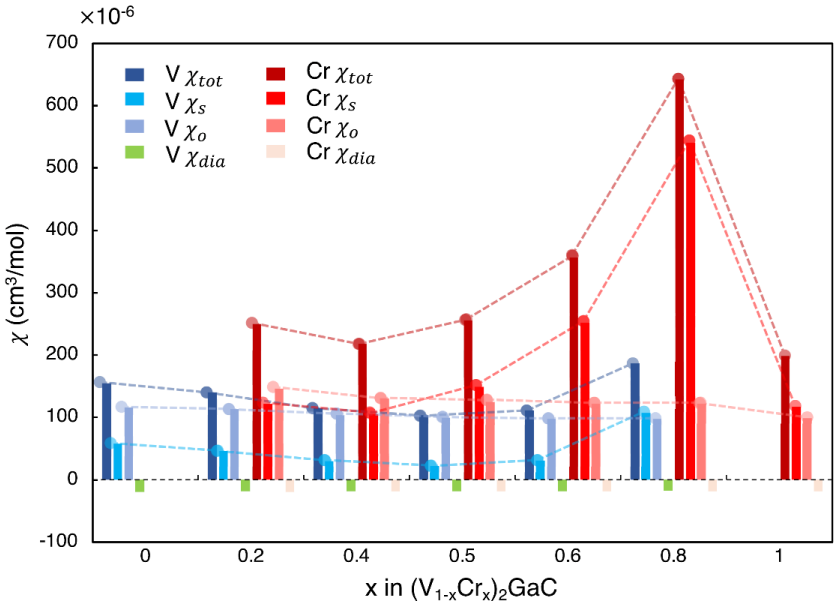

Figure 23: Element-resolved total magnetic susceptibility (χ_{tot}), total spin susceptibility (χ_s), total Van Vleck orbital susceptibility (χ_o) and diamagnetic susceptibility (χ_{dia}) as a function of Cr doping x in $(V_{1-x}Cr_x)_2GaC$.

Such a non-linear dependence of the spin susceptibility on the Cr concentration can be understood based on the Stoner theory.[120] The obtained Stoner parameter I, the nonmagnetic density of states (DOS) at the Fermi level per atom $n(E_F)$, the product of I and $n(E_F)$, and the Stoner enhancement parameter $(1\text{-}I{\cdot}n(E_F))\text{-}1$ are plotted in **Figure 24** as a function of the Cr content x. As is well known, the Stoner parameter I is a quasi-atomic property, which can be slightly tuned by the chemical effects.[120] For *bcc* V and Cr, the Stoner parameters[120] are around 0.71 and 0.76 eV, respectively, which are close to the calculated values in the current work, being approximately 0.78 eV for V_2GaC and 0.86 eV for Cr_2GaC. As demonstrated in **Figure 24 (b)** and **(c)**, $n(E_F)$ and $I{\cdot}n(E_F)$ display apparently analogous trends for the variation of magnetic susceptibility with the Cr content, indicating that the magnetic response of the $(V_{1-x}Cr_x)_2GaC$ MAX phase system is in the itinerant regime. The maximum $I{\cdot}n(E_F)$ is about 0.82 for x = 0.80, which is smaller than 1, resulting in no magnetic long-range order in these systems. Correspondingly, the susceptibility can be formulated as $\chi = \chi_0 \cdot (1 - I{\cdot}n(E_F))\text{-}1$, where χ_0 is the Pauli susceptibility, and the Stoner enhancement parameter $(1 - I{\cdot}n(E_F))\text{-}1$ can reproduce the dependence of the susceptibility on the chemical composition. Therefore, both the experimentally derived magnetic susceptibilities and the theoretical calculations have proven that the $(V_{1-x}Cr_x)_2GaC$ MAX phase system is a prototypical itinerant paramagnet, which is nearly magnetically ordered. Increasing the density of states $n(E_F)$ further around x = 0.80, e.g., by Mn doping can lead to overcoming the Stoner criterion of

long-range magnetic order. Alternatively, two-dimensional MXene materials can shape the density of states further.

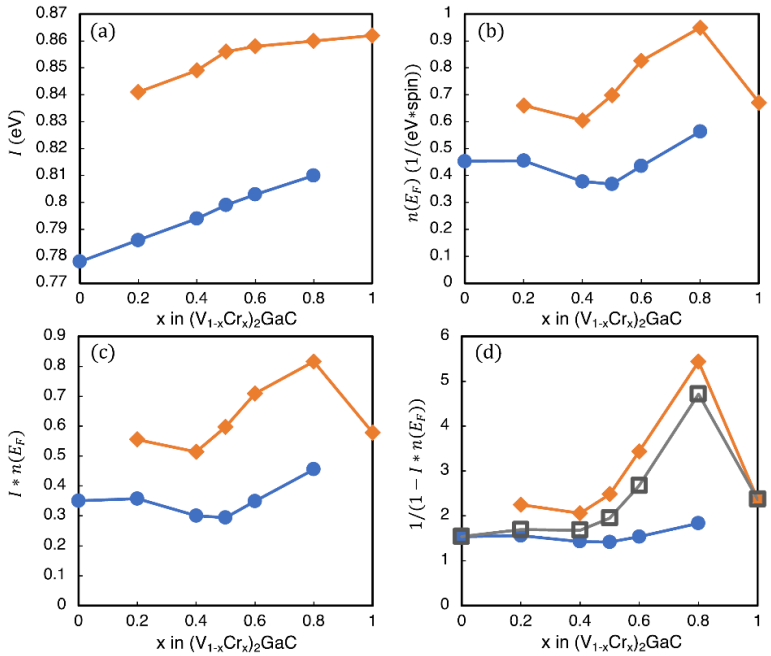

Figure 24: (a) Stoner parameter I, (b) density of states at Fermi level n(E_F) per atomic site, (c) product of I and n(E_F) and (d) Stoner enhancement parameter $(1\text{-}I{\cdot}n(E_F))^{-1}$ as a function of Cr doping x in $(V_{1-x}Cr_x)_2GaC$ MAX phases. Blue lines with circles and orange lines with diamonds denote the corresponding parameters for V and Cr, respectively. In (d), the grey line with squares represents the Stoner enhancement parameter averaged with respect to the V and Cr contents.

3.2.7. Conclusions

In this chapter, the synthesis of a new gallium-containing MAX phase solid-solution $(V_{1-x}Cr_x)_2GaC$ $(0 \leq x \leq 1)$ was demonstrated using the microwave-assisted heating technique. The solid-solution exhibits no miscibility gap and the refined lattice parameters almost perfectly follow Vegard's law. SEM micrographs show that the composition of the phases does not influence the typical MAX phase-like morphology of the bulk compounds. On the other hand, the magnetic behavior of the phases is highly dependent on the composition. VSM measurements revealed that all samples are Pauli paramagnets, however, the obtained susceptibilities vary non-linear by up to 400% with a maximum at $x = 0.80$. By considering the Stoner theory, ab initio calculations confirm the experimental magnetic data and identify the $(V_{1-x}Cr_x)_2GaC$ system as a prototypical itinerant paramagnet which is nearly magnetically ordered ($I{\cdot}n(E_F) = 0.82$). Overall, these findings provide a necessary starting point for the challenging synthesis of new magnetically ordered MAX phases.

3.2.8. Supplementary Information

Table 4: Results of the Rietveld refinement of V_2GaC.

Phase name	V_2GaC
Percentage/weight-%	(100)
Spacegroup	*P*6$_3$/*mmc*
Lattice parameters *a, c*/ Å	2.9371(3) 12.8752(2)
Cell volume/ Å^3	96.19(2)
Background order	15
R_p	2.65
R_{wp}	3.70
R_{exp}	2.12
GOF	1.75

Table 5: Results of the Rietveld refinement of $(V_{0.80}Cr_{0.20})_2GaC$.

Phase name	$(V_{0.80}Cr_{0.20})_2GaC$	Cr_3Ga
Percentage/weight-%	98.7(6)	1.3(6)
Spacegroup	*P*6$_3$/*mmc*	*Pm*-3*n*
Lattice parameters *a, c*/ Å	2.9302(5) 12.8268(3)	4.6588(5)
Cell volume/ Å^3	95.38(4)	101.12(3)
Background order	15	
R_p	2.81	
R_{wp}	4.19	
R_{exp}	2.14	
GOF	1.96	

Table 6: Results of the Rietveld refinement of $(V_{0.60}Cr_{0.40})_2GaC$.

Phase name	$(V_{0.60}Cr_{0.40})_2GaC$	$CrGa_4$
Percentage/weight-%	97.2(9)	2.8(9)
Spacegroup	*P*6$_3$/*mmc*	*Im*-3m
Lattice parameters *a, c*/ Å	2.9205(7) 12.7676(3)	5.6454(3)
Cell volume/ Å^3	94.31(6)	179.92(3)
Background order	15	
R_p	3.18	
R_{wp}	4.86	
R_{exp}	2.23	
GOF	2.18	

Table 7: Results of the Rietveld refinement of $(V_{0.50}Cr_{0.50})_2GaC$.

Phase name	$(V_{0.50}Cr_{0.50})_2GaC$	$CrGa_4$
Percentage/weight-%	98.3(8)	1.7(8)
Spacegroup	*P*6$_3$/*mmc*	*Im*-3m
Lattice parameters *a, c*/ Å	2.9160(7) 12.7442(4)	5.6431(5)
Cell volume/ Å^3	93.85(5)	180.65(5)
Background order	15	
R_p	4.20	
R_{wp}	6.27	
R_{exp}	3.46	
GOF	1.81	

Table 8: Results of the Rietveld refinement of $(V_{0.40}Cr_{0.60})_2GaC$.

Phase name	$(V_{0.40}Cr_{0.60})_2GaC$
Percentage/weight-%	(100)
Spacegroup	*P*6$_3$/*mmc*
Lattice parameters *a, c*/ Å	2.9088(6) 12.7173(3)
Cell volume/ Å^3	93.19(6)
Background order	15
R_p	2.94
R_{wp}	4.04
R_{exp}	2.40
GOF	1.68

Table 9: Results of the Rietveld refinement of $(V_{0.20}Cr_{0.80})_2GaC$.

Phase name	$(V_{0.20}Cr_{0.80})_2GaC$
Percentage/weight-%	(100)
Spacegroup	*P*6$_3$/*mmc*
Lattice parameters *a, c*/ Å	2.8999(5) 12.6589(3)
Cell volume/ Å^3	92.19(4)
Background order	15
R_p	2.74
R_{wp}	3.83
R_{exp}	2.07
GOF	1.85

Table 10: Results of the Rietveld refinement of Cr_2GaC.

Phase name	Cr_2GaC	Cr_3Ga	$CrGa_4$
Percentage/weight-%	97.9(2)	0.3(6)	1.8(2)
Spacegroup	*P6₃/mmc*	*Pm-3n*	*Im-3m*
Lattice parameters *a, c* /Å	2.8845(5) 12.6062(3)	4.6403(2)	5.6365(5)
Cell volume/ Å ^{3}	90.84(4)	99.92(7)	179.08(5)
Background order	15		
R_p	3.74		
R_{wp}	5.72		
R_{exp}	2.10		
GOF	2.73		

Table 11: Summary of the EDX measurements determining the vanadium and chromium ratio of $(V_{0.80}Cr_{0.20})_2GaC$.

Spot	V-At-%	Cr-At-%
1	79.27	20.73
2	76.22	23.78
3	79.60	20.40
4	78.62	21.38
5	80.57	19.43
6	78.62	21.38
7	80.25	19.75
8	83.24	16.76
9	80.56	19.45
10	79.30	20.70
Average:	79.63	20.28
Deviation:	± 1.79	± 1.79

Table 12: Summary of the EDX measurements determining the vanadium and chromium ratio of $(V_{0.60}Cr_{0.40})_2GaC$.

Spot	V-At-%	Cr-At-%
1	59.43	40.57
2	59.11	40.89
3	60.40	39.60
4	61.57	38.43
5	60.73	39.27
6	55.34	44.66
7	61.45	38.55
8	58.18	41.82
9	55.60	44.40
10	58.38	41.62
Average:	59.02	40.98
Deviation:	± 2.21	± 2.21

Table 13: Summary of the EDX measurements determining the vanadium and chromium ratio of $(V_{0.50}Cr_{0.50})_2GaC$.

Spot	V-At-%	Cr-At-%
1	56.80	43.20
2	52.72	47.28
3	50.59	49.41
4	49.68	50.20
5	54.08	45.92
6	53.98	46.02
7	53.00	47.00
8	54.46	45.54
9	48.68	51.32
10	44.40	55.60
Average:	51.84	48.16
Deviation:	± 3.57	± 3.57

Table 14: Summary of the EDX measurements determining the vanadium and chromium ratio of $(V_{0.40}Cr_{0.60})_2GaC$.

Spot	V-At-%	Cr-At-%
1	32.12	67.88
2	38.38	61.62
3	34.33	65.67
4	37.89	62.11
5	37.15	62.85
6	37.89	62.11
7	35.88	64.12
8	42.57	57.43
9	35.77	64.23
10	35.41	64.59
Average:	36.74	63.26
Deviation:	± 2.79	± 2.79

Table 15: Summary of the EDX measurements determining the vanadium and chromium ratio of $(V_{0.20}Cr_{0.80})_2GaC$.

Spot	V-At-%	Cr-At-%
1	21.53	78.47
2	19.63	80.37
3	17.84	82.16
4	21.17	78.83
5	17.92	82.08
6	17.81	82.19
7	18.03	81.97
8	17.07	82.93
9	18.87	81.13
10	19.00	81.00
Average:	19.00	81.11
Deviation:	± 1.49	± 1.49

Table 16: Results of the Rietveld refinement of $(V_{0.2}Cr_{0.8})_2GaC$.

Phase name		**$(V_{0.20}Cr_{0.80})_2GaC$**
Percentage/weight-%		(100)
Spacegroup		*P*6$_3$/*mmc*
Lattice parameters *a, c*/ Å		2.8946(2) 12.6276(7)
Cell volume/ Å^3		91.63(9)
Background order		15
R_p		7.05
R_{wp}		9.54
R_{exp}		7.44
GOF		1.28

Table 17: Summary of the EDX measurements determining the vanadium and chromium ratio of $(V_{0.20}Cr_{0.80})_2GaC$.

Spot	V-At-%	Cr-At-%
1	24.17	75.83
2	13.21	86.79
3	13.60	86.40
4	3.75	96.25
5	27.61	72.39
6	14.79	85.21
7	6.63	93.37
8	6.60	93.40
9	11.73	88.27
10	4.44	95.56
Average:	12.65	87.35
Deviation:	± 8.05	± 8.05

3.3. Microwave-assisted synthesis of $(V_{1-x}Mn_x)_2GaC$ ($0 \leq x \leq 0.20$) MAX phase

3.3.1. Motivation

The synthesis of the solid-solution phase $(V_{1-x}Cr_x)_2GaC$ in chapter 3.2 provides a new starting point for the preparation of magnetically ordered MAX phases. However, a further increase of the electron density in the system is required to overcome the Stoner criterion which leads to the investigation of the doping behavior with manganese. Since doping experiment of manganese in the Cr_2GaC system are literature known,[38] the V_2GaC system is studied in the following.

3.3.2. Experimental Section

For the syntheses of V_2GaC and the solid-solution phases $(V_{1-x}Mn_x)_2GaC$ the elemental precursor amounts were based on 0.5 g of the desired product. A detailed summary of the used precursor amounts can be found in **Table 18**. Initially, gallium flakes (Alfa Aesar, > 99 %) were cut under atmospheric conditions and subsequently transferred into an argon-filled glovebox. Vanadium (Alfa Aesar, 99.5 %, ~325 mesh), manganese (Sigma-Aldrich, ≥ 99 %), and carbon (Alfa Aesar, >99.9%, APS 2-15 micron) powders were thoroughly mixed using an agate mortar. The mixture was then loosely mixed with the cut gallium flakes and pressed into a dense pellet (⌀ = 10 mm, 3 t, 10 s). All pellets were subsequently sealed into an evacuated fused silica ampoule which was placed into 7 g of activated charcoal (Grüssing, 2.5 mm) acting as a susceptor material, and annealed inside a microwave oven (*CEM, MARS6*) at 1000 W for 30 minutes. Prior to further characterization steps, the pellets were finely ground using an agate mortar and stored under atmospheric conditions.

Table 18: Weighing amounts of the prepared MAX phase samples. All amounts are calculated based on the nominal compositions of 0.5 g of the target material.

Nominal composition	*m*(V) in g	*m*(Mn) in g	*m*(Ga) in g	*m*(C) in g
V_2GaC	0.2774 (2.00 eq.)	-	0.2088 (1.1 eq.)	0.0294 (0.9 eq)
$(V_{0.95}Mn_{0.05})_2GaC$	0.2630 (1.90 eq.)	0.0149 (0.10 eq.)	0.2084 (1.1 eq.)	0.0294 (0.9 eq.)
$(V_{0.90}Mn_{0.10})_2GaC$	0.2486 (1.80 eq.)	0.0298 (0.20 eq.)	0.2079 (1.1 eq.)	0.0293 (0.9 eq.)
$(V_{0.89}Mn_{0.11})_2GaC$	0.2457 (1.78 eq.)	0.0328 (0.22 eq.)	0.2079 (1.1 eq.)	0.0293 (0.9 eq.)
$(V_{0.88}Mn_{0.12})_2GaC$	0.2429 (1.76 eq.)	0.0357 (0.24 eq.)	0.2078 (1.1 eq.)	0.0293 (0.9 eq.)
$(V_{0.85}Mn_{0.15})_2GaC$	0.2343 (1.70 eq.)	0.0446 (0.30 eq.)	0.2075 (1.1 eq.)	0.0292 (0.9 eq.)
$(V_{0.85}Mn_{0.20})_2GaC$	0.2200 (1.60 eq.)	0.0593 (0.40 eq.)	0.2070 (1.1 eq.)	0.0292 (0.9 eq.)

3.3.3. Characterization

X-ray powder diffraction data were obtained using a *Stadi P* (*Stoe & Cie GmbH*) with monochromatized Cu-$K_{\alpha,1}$ radiation (λ = 1.540596 Å), and the *Mythen 1K* (*Dectris*) detector in transmission geometry at room temperature. For measurements, small sample amounts were deposited between X-ray amorphous adhesive film (*Scotch*) on a flat sample holder and rotated orthogonally to the X-ray source. Rietveld refinements (Le Bail method) were performed using the program *TOPAS* (*Bruker*). SEM images were taken at the *XL30 FEG* (*Philips*) using an acceleration voltage of 25 kV adapted with an *APOLLO X-SDD* detector (*EDAX*) for collecting EDX data. The EDX data was evaluated using the software *EDAX GENESIS*.

3.3.4. Structural analysis

Starting from the parent phase V_2GaC, manganese was doped in steps of 5 at-% (except for 11- and 12 at-%) up to 20 at-%. As shown in (**Figure 25**) the solid-solution phases were obtained nearly single phase up to 11 at-%, whereas at a doping level of 12 at-%, the amount of side phases starts to increase heavily towards elemental manganese, the antiperovskite phase Mn_3GaC, and yet not assignable side phases. As already shown in various reports,[40,107] such as in the very similar material system $(V_{1-x}Mn_x)_2AlC$,[39] almost no peak shift with increasing amount of doped manganese is observed. To further analyze the X-ray powder diffraction data and to investigate the evolution of the lattice parameters by increasing the manganese amount, Le Bail refinements (**Figure 26**; **Table 19**) were performed based on the structural model of V_2GaC up to a doping amount of 11 at-%.[117]

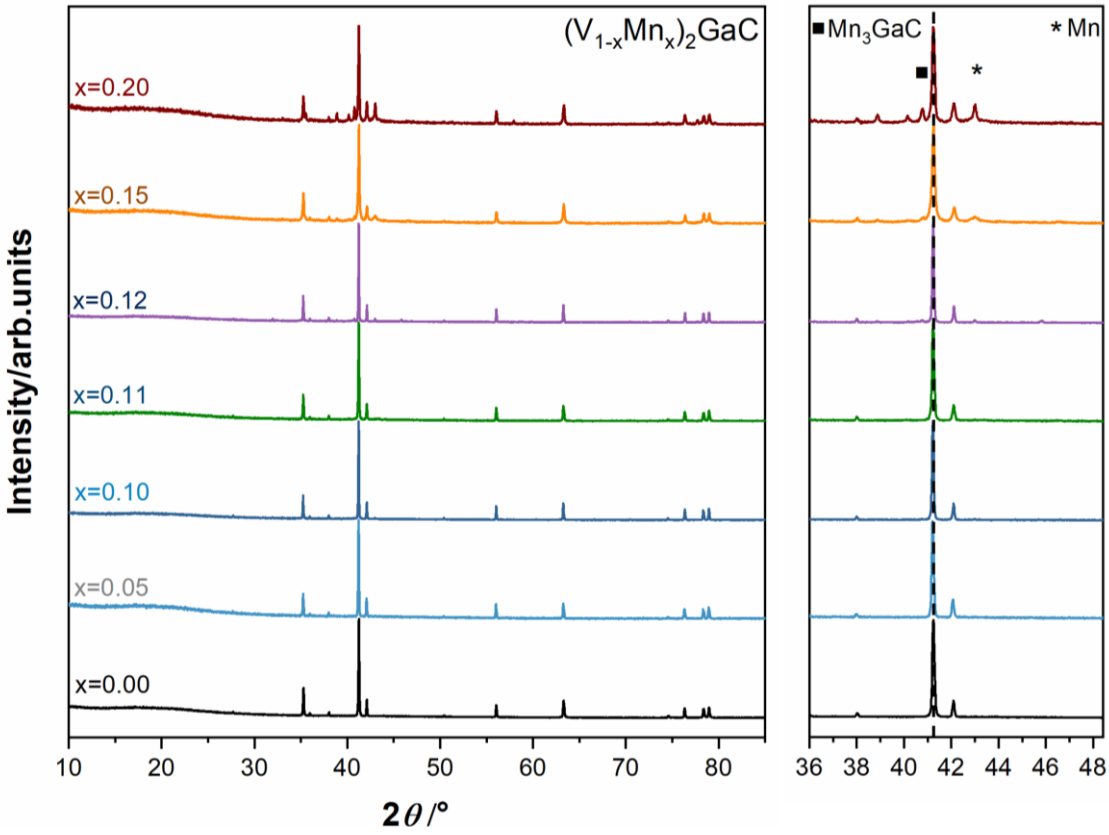

Figure 25: X-ray powder diffraction data of the solid solution phase $(V_{1-x}Mn_x)_2GaC$ with $x = 0 \leq x \leq 0.20$, including the enlarged region of ~36-48° 2θ.

A graphical illustration of the lattice parameters is shown in **Figure 27**. In accordance with chapter 3.2.3, the lattice parameters of V_2GaC are in good agreement with the ones reported in literature.[117] On the other hand, all Mn-doped phases show a slight decrease in both, the *a*- and *c*-lattice parameters, however, with no clear trend. While the *c*-lattice parameter decreases almost linearly up to 10 at-% of manganese and increases again at 11 at-%, the *a*-lattice parameter exhibits anomalies at already 5 at-% of manganese. The overall decrease in the lattice parameters/cell volume of this system follows the reported 211 $(V_{1-x}Mn_x)_2AlC$ system.[39]

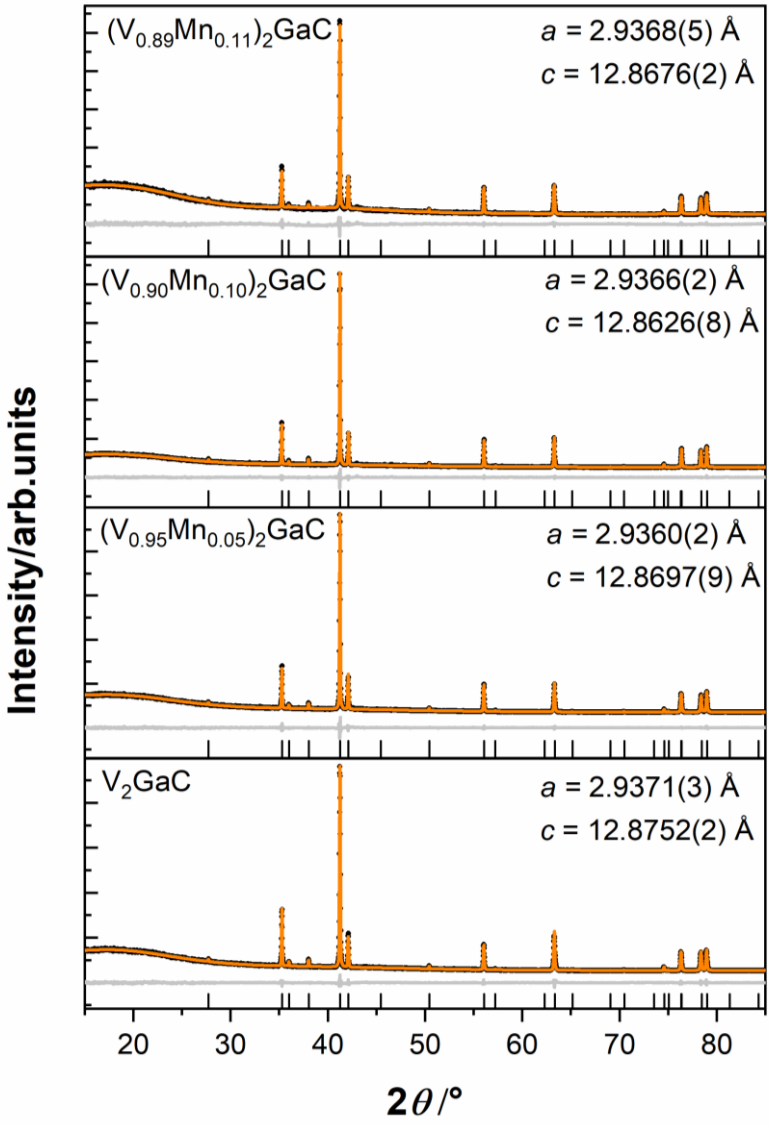

Figure 26: Results of the Le Bail refinements (orange lines) and residuum curves (grey) of the X-ray powder diffraction data (black dots) of the solid-solution phase $(V_{1-x}Mn_x)_2GaC$ up to a nominal doping amount of x = 0.11 at-%. The refinements were conducted based on the structural model of V_2GaC.[117]

Table 19: Results of the Rietveld refinements of the solid-solution phases $(V_{1-x}Mn_x)_2GaC$ with x = 0.00, 0.05, 0.10, 0.11.

Phase name	V_2GaC	$(V_{0.95}Mn_{0.05})_2GaC$	$(V_{0.90}Mn_{0.10})_2GaC$	$(V_{0.89}Mn_{0.11})_2GaC$
Spacegroup	*P*6$_3$/*mmc*	*P*6$_3$/*mmc*	*P*6$_3$/*mmc*	*P*6$_3$/*mmc*
Lattice parameters/Å	a = 2.9371(3) c = 12.8752(2)	a = 2.9360(2) c =12.8697(9)	a =2.9366(2) c =12.8626(8)	a = 2.9368(5) c =12.8676(2)
Cell volume/Å^3	96.19(2)	96.08(2)	96.06(2)	96.11(3)
Background order	15	15	15	15
R_p	2.65	2.82	2.90	3.56
R_{wp}	3.70	3.73	3.99	5.11
R_{exp}	2.12	2.49	2.25	2.17
GOF	1.75	1.50	1.77	2.36

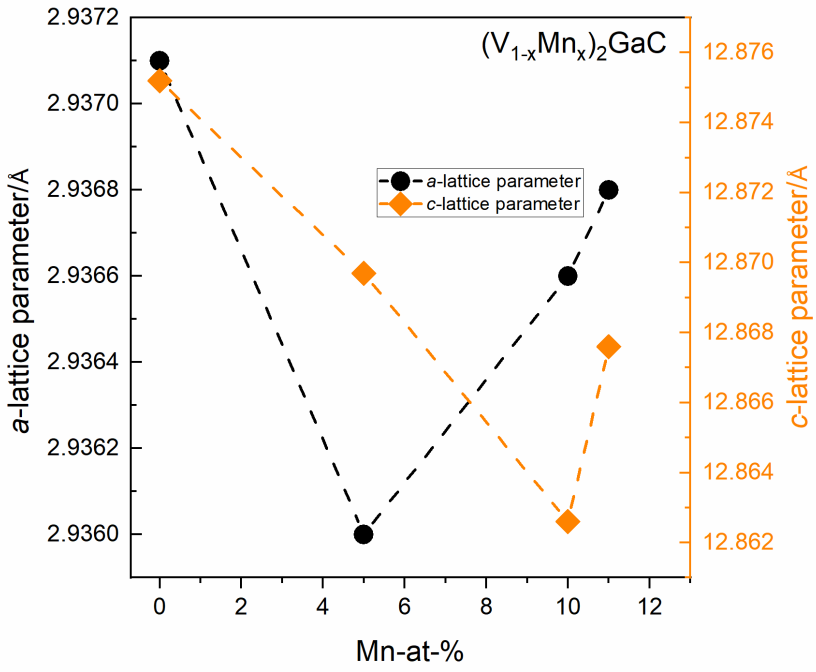

Figure 27: Graphical illustration of the *a*- and *c*-lattice parameters of the $(V_{1-x}Mn_x)_2GaC$ up to a nominal doping amount of x = 0.11 at %.

Even though the change in lattice parameters indicates successful incorporation of the manganese into the MAX phase structure, the change in lattice parameters is very small and requires further analysis methods to comprehensively evaluate the results of the doping experiments.[38,39] Therefore, SEM mappings were performed in order to visualize the distribution of the manganese in the MAX phase samples. As shown in **Figure 28**, already small doping amounts of 5 at-% manganese lead to a partly inhomogeneous distribution of the manganese which also applies to the higher doping amounts of x = 0.10 and x = 0.11, whereas the gallium and vanadium signals do not show any anomalies.

Nonetheless, it must be emphasized that most of the manganese in the investigated particles is homogeneously distributed, which further supports the XRD data that amounts of the doped manganese have been incorporated into the MAX phase structure. However, due to the partly pronounced inhomogeneities, no further standard EDX spot measurements were performed to quantify the actual amount of manganese. Here, methods such as the EPMA analysis would be more accurate to adequately quantify the incorporated amount of manganese.[40] By looking at the morphology of the particles, typical anisotropic MAX phase-like structures, as well as bulky particles can be observed.

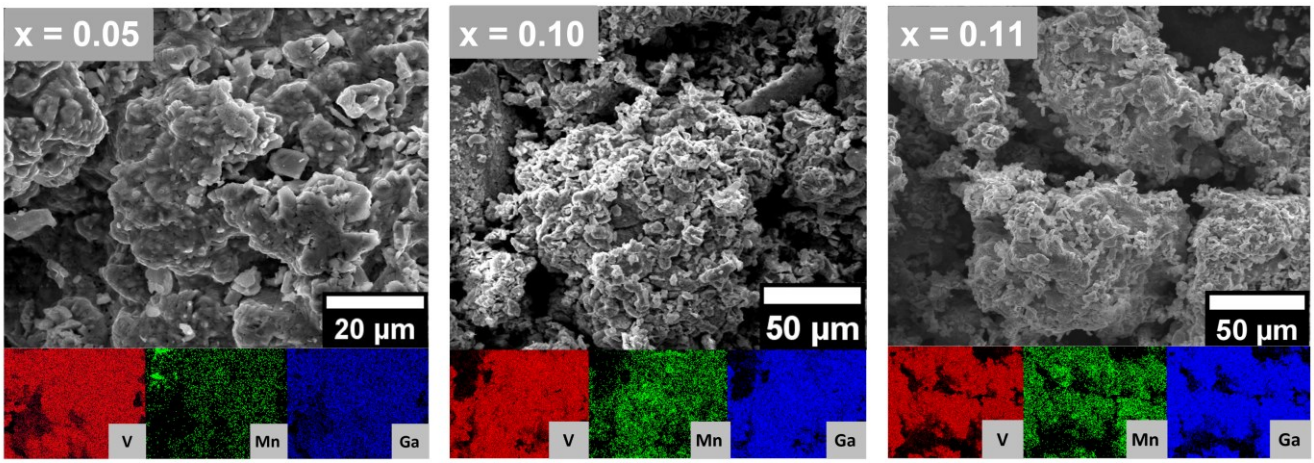

Figure 28: SEM micrographs showing the morphology of the obtained MAX phase solid-solutions $(V_{1-x}Mn_x)_2GaC$ (x = 0.05, 0.10, 0.11) and EDX mappings showing the elemental distribution of vanadium, manganese and gallium.

3.3.5. Conclusion

In this project, the synthesis of the hitherto unknown MAX phase solid-solution $(V_{1-x}Mn_x)_2GaC$ was performed up to a nominal doping level of x = 0.20 using the microwave-assisted heating technique. X-ray diffraction data exhibit no detectable side phase amounts up to a doping level of 11 at-%, however, Le Bail refinements show no clear trend of the evolution of the lattice parameters. Still, an overall decrease in the cell volume is observed, which is in accordance with literature reports of the similar system $(V_{1-x}Mn_x)_2AlC$.[39] While the XRD data show no side phase peaks at lower doping levels, EDX measurements reveal at a doping level of already 5 at-% slightly inhomogeneous distributions of manganese, indicating the presence of side phases. This complicates further analyses such as magnetic measurements (see chapter 3.2) which were not conducted for this reason. Nonetheless, the results of the XRD data and EDX measurements clearly indicate that small amounts of manganese have been incorporated into the MAX phase structure, leading to the synthesis of a new solid-solution with the potential to be connected to the previously discussed $(V_{1-x}Cr_x)_2GaC$ system in chapter 3.2.

3.4. Microwave-assisted synthesis of $(Cr_{1-x}Mo_x)_2GaC$ ($0 \leq x \leq 1$) MAX phase

3.4.1. Motviation

Going beyond the V_2GaC system and manganese doping, studies about molybdenum are only hardly represented in the MAX phase literature of conventional 211 phases.[18,121] In order to investigate the doping behavior with a literature-known system, Cr_2GaC was chosen as a parent phase, as both chromium and molybdenum belong to group 6 in the periodic table. Additionally, due to the high electron density of the solid-solution phase, magnetic studies could be interesting.

3.4.2. Experimental section

For the syntheses of Cr_2GaC and the solid-solution phases $(Cr_{1-x}Mo_x)_2GaC$ the elemental precursor amounts were based on 0.5 g of the desired product. A detailed summary of the used precursor amounts can be found in **Table 20**. Initially, gallium flakes (Alfa Aesar, > 99 %) were cut under atmospheric conditions and subsequently transferred into an argon-filled glovebox. Chromium (Sigma-Aldrich, 99 %, ~325 mesh), molybdenum (Alfa Aesar, 99,95 %, 100 mesh), and carbon (Alfa Aesar, >99.9%, APS 2-15 micron) powders were thoroughly mixed using an agate mortar. The mixture was then loosely mixed with the cut gallium flakes and pressed into a dense pellet (⌀ = 10 mm, 3 t, 10 s). All pellets were subsequently sealed into an evacuated fused silica ampoule which was placed into 7 g of activated charcoal (Grüssing, 2.5 mm) acting as a susceptor material, and annealed inside a microwave oven (*CEM, MARS6*) following a defined temperature program (**Table 21**). Prior to further characterization steps, the pellets were finely ground using an agate mortar and stored under atmospheric conditions.

Table 20: Weighing amounts of the prepared MAX phase samples. All amounts are calculated based on the nominal compositions of 0.5 g of the target material.

Nominal composition	*m*(Cr) in g	*m*(Mo) in g	*m*(Ga) in g	*m*(C) in g
Cr_2GaC	0.2800 (2.0 eq.)	-	0.2065 (1.1 eq.)	0.0323 (1.0 eq)
$(Cr_{0.95}Mo_{0.05})_2GaC$	0.2598 (1.9 eq.)	0.0252 (0.1 eq.)	0.2017 (1.1 eq.)	0.0316 (1.0 eq.)
$(Cr_{0.90}Mo_{0.10})_2GaC$	0.2406 (1.8 eq.)	0.0493 (0.2 eq.)	0.1971 (1.1 eq.)	0.0309 (1.0 eq.)
$(Cr_{0.85}Mo_{0.15})_2GaC$	0.2222 (1.7 eq.)	0.0723 (0.3 eq.)	0.1928 (1.1 eq.)	0.0302 (1.0 eq.)
$(Cr_{0.80}Mo_{0.20})_2GaC$	0.2046 (1.6 eq.)	0.0944 (0.4 eq.)	0.1886 (1.1 eq.)	0.0295 (1.0 eq.)
$(Cr_{0.60}Mo_{0.40})_2GaC$	0.1412 (1.2 eq.)	0.1737 (0.8 eq.)	0.1736 (1.1 eq.)	0.0272 (1.0 eq.)
$(Cr_{0.50}Mo_{0.50})_2GaC$	0.1132 (1.0 eq.)	0.2089 (1.0 eq.)	0.1670 (1.1 eq.)	0.0261 (1.0 eq.)
$(Cr_{0.40}Mo_{0.60})_2GaC$	0.0872 (0.8 eq.)	0.2414 (1.2 eq.)	0.1608 (1.1 eq.)	0.0252 (1.0 eq.)
$(Cr_{0.30}Mo_{0.70})_2GaC$	0.0631 (0.6 eq.)	0.2716 (1.4 eq.)	0.1551 (1.1 eq.)	0.0243 (1.0 eq.)
$(Cr_{0.10}Mo_{0.90})_2GaC$	0.0196 (0.2 eq.)	0.3260 (1.8 eq.)	0.1448 (1.1 eq.)	0.0227 (1.0 eq.)

Mo_2GaC	-	0.3506 (2 eq.)	0.1402 (1.4 eq.)	0.0219 (1.0 eq.)

Table 21: Summary of the applied temperature programs in the microwave-assisted synthesis of $(Cr_{1-x}Mo_x)_2GaC$.

Nominal composition	Temperature programs
Cr_2GaC	1300 W, 20 mins
$(Cr_{0.95}Mo_{0.05})_2GaC$	1000 W, 30 mins
$(Cr_{0.90}Mo_{0.10})_2GaC$	1000 W, 30 mins
$(Cr_{0.85}Mo_{0.15})_2GaC$	1000 W, 60 mins
$(Cr_{0.80}Mo_{0.20})_2GaC$	1000 W, 60 mins
$(Cr_{0.60}Mo_{0.40})_2GaC$	1000 W, 60 mins
$(Cr_{0.50}Mo_{0.50})_2GaC$	1000 W, 60 mins
$(Cr_{0.40}Mo_{0.60})_2GaC$	1000 W, 60 mins
$(Cr_{0.30}Mo_{0.70})_2GaC$	1000 W, 60 mins
$(Cr_{0.10}Mo_{0.90})_2GaC$	1000 W, 60 mins
Mo_2GaC	1000 W, 60 mins

3.4.3. Characterization

X-ray powder diffraction data were obtained using a *Stadi P* (*Stoe & Cie GmbH*) with monochromatized Cu-$K_{\alpha,1}$ radiation (λ = 1.540596 Å), and the Mythen 1K (*Dectris*) detector in transmission geometry at room temperature. For measurements, small sample amounts were deposited between X-ray amorphous adhesive film (*Scotch*) on a flat sample holder and rotated orthogonally to the X-ray source. Rietveld refinements (Le Bail method) were performed using the program *TOPAS* (*Bruker*).
SEM images were taken at the *XL30 FEG* (*Philips*) using an acceleration voltage of 25 kV adapted with an *APOLLO X-SDD* detector (*EDAX*) for collecting EDX data. The EDX data was evaluated using the software *EDAX GENESIS*.

3.4.4. Structural analysis

Starting from the parent phase Cr_2GaC, molybdenum was doped in different step sizes (5 at-%, 10 at-%, 20 at-%) towards the nominal target phase Mo_2GaC. As shown in the enlarged region of the characteristic (103) and (006) peaks in **Figure 29**, up to a doping amount of 50 at-%, a constant shift towards lower 2θ angles is observed. This is in accordance with the higher atomic radius of molybdenum (2.44 Å) compared to chromium (2.33 Å).[115] The peak shift is accompanied by a significant broadening of the XRD peaks, which could be an indication for imperfections in the crystal lattice[122] emerged due to the solid-solution formation. Nonetheless, up to 50 at-%, the samples exhibit a good sample quality with side phase peaks of small intensity that can be assigned to Mo_2C. However, at 60 at-%, the amount of

Mo_2C increases significantly, while at a molybdenum doping level of 70 at-%, the MAX phase formation seems to be almost fully suppressed, and Mo_2C forms the main phase.

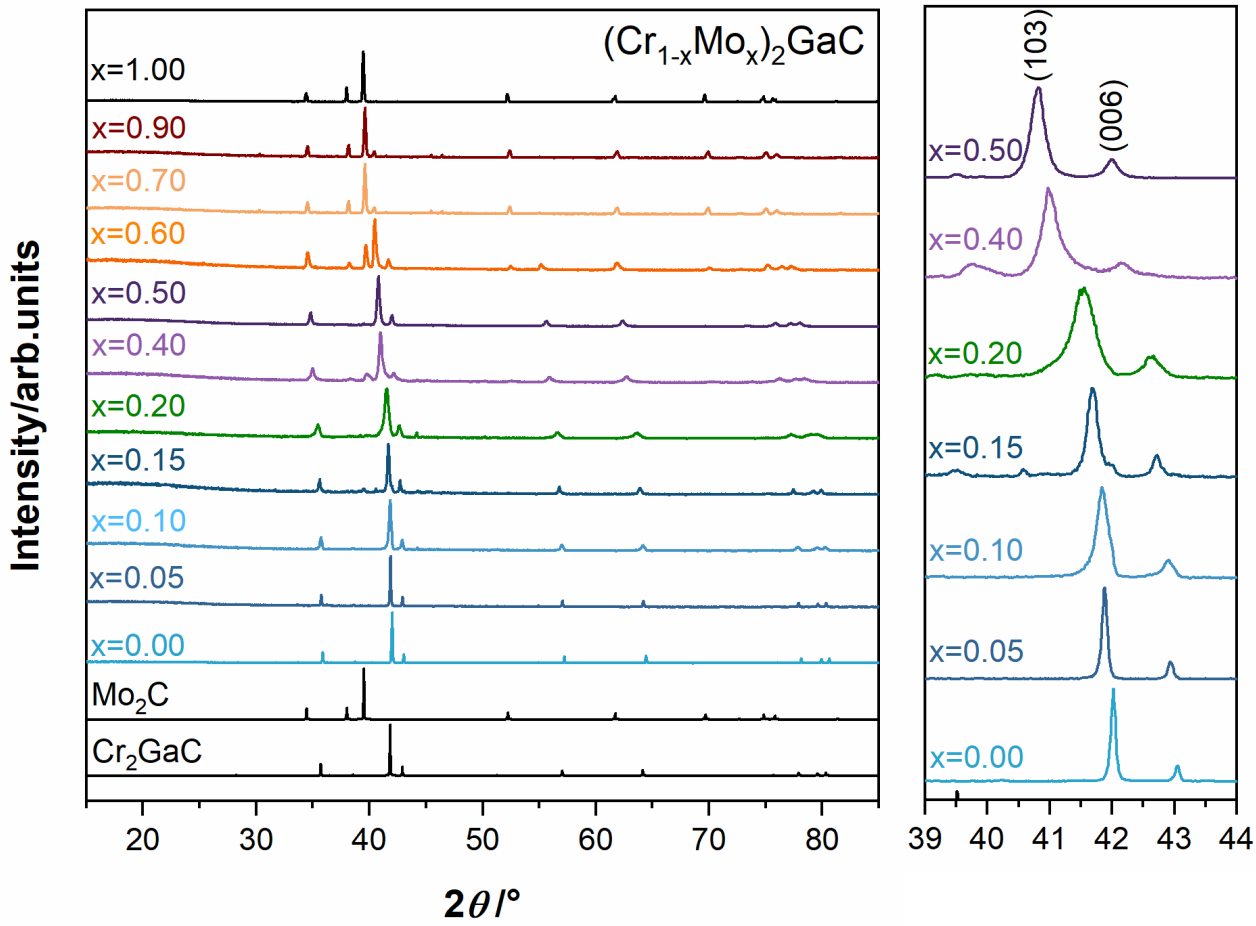

Figure 29: X-ray powder diffraction data of the solid-solution phase $(Cr_{1-x}Mo_x)_2GaC$ with $0 \leq x \leq 1$, including the literature references of Cr_2GaC[123] and Mo_2C[124]. The amount of molybdenum was nominally increased.

Reasons for the suppression of the MAX phase could be explained due to the restricted temperature stability (~900 °C) of the Mo_2GaC parent phase, as reported by BARSOUM *et al.*[121] While the reported temperature behavior was only related to conventional heating methods, further experiments with lower microwave powers were conducted to investigate the behavior within the Mo-Ga-C system further. Here, it was started with Mo_2C and gallium as reactants according to reported synthesis protocols.[121] However, as shown in the Supplementary Information (**Figure 33**), no formation of the MAX phase was realized using microwave heating over a wide range of applied microwave power. To further investigate the successful solid-solution row up to a doping level of 50 at-% molybdenum, Le Bail refinements (**Figure 30**) were performed using the structural model of Cr_2GaC[123] providing the space group $P6_3/mmc$. Following the constant peak shift, the extracted lattice parameters, as well as cell volumes exhibit an almost linear increase (**Figure 31**). This is validated by a simple linear regression with R^2 values close to 1 and thus confirms Vegard's law, analogous to the reported $(V_{1-x}Cr_x)_2GaC$ system in chapter 3.2. The lattice parameters of the parent Cr_2GaC phase are in good agreement with the reported

values in the literature. A detailed summary of the Le Bail refinements can be found in the Supplementary Information (**Table 22-28**).

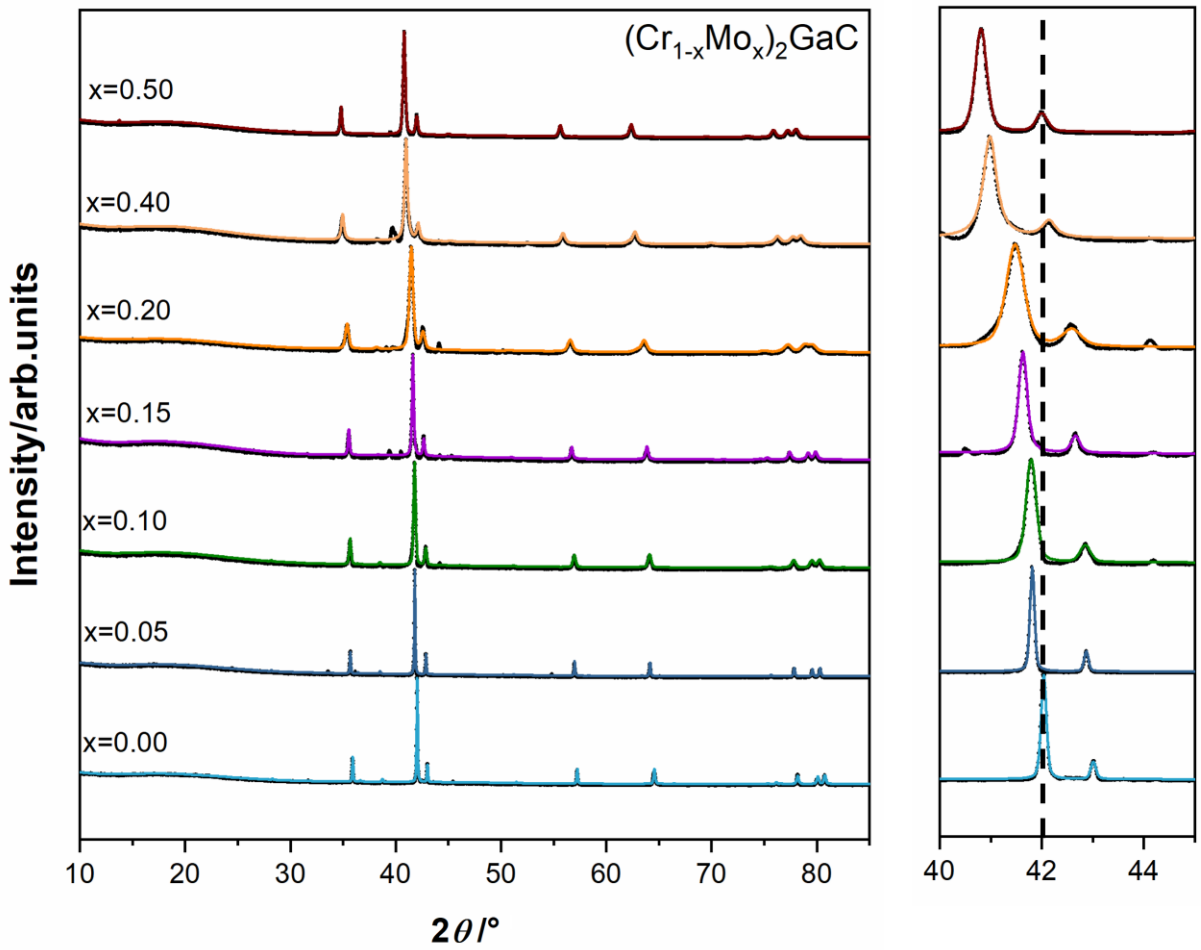

Figure 30: Le Bail refinements (colored lines) of the X-Ray powder diffraction data of the solid-solution phase $(Cr_{1-x}Mo_x)_2GaC$ (black dots) based on the structural model of Cr_2GaC[123] providing the space group $P6_3/mmc$. X was nominally increased in different step sizes.

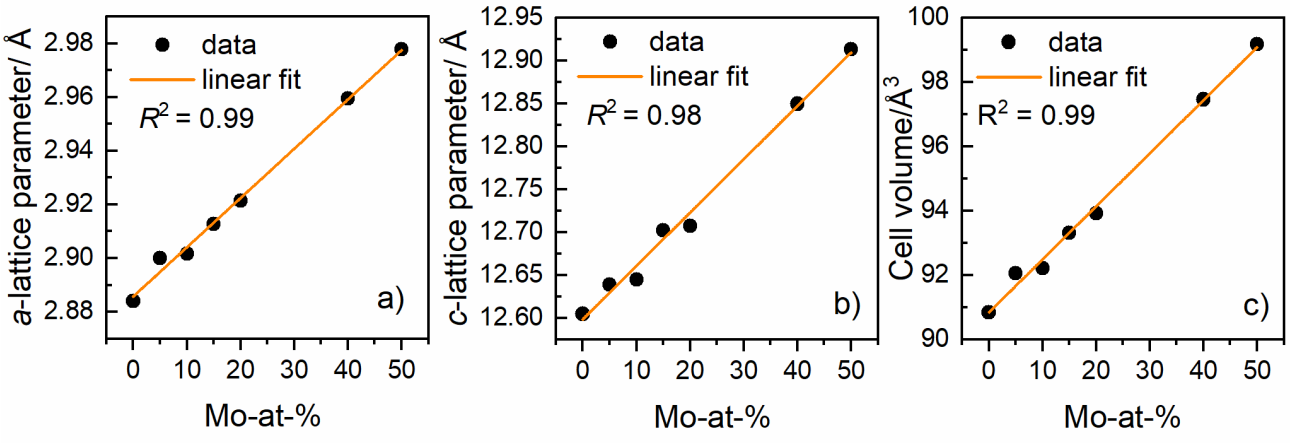

Figure 31: Graphical illustration of the dependency between both, the a-lattice parameters (a), c-lattice parameters (b), the cell volumes (c), and the actual atomic weight-% of molybdenum, including simple linear fit (orange lines).

EDX mappings support the results obtained by X-ray diffraction data characterization and show a predominantly homogeneous distribution of molybdenum in the particles, while the corresponding

micrographs reveal MAX phase typical anisotropic and partly bulkier structures analogous to the previous chapters 3.2 and 3.3. As representative examples, nominal doping levels of 10 at-%, 20 at-%, and 50 at-% are shown in **Figure 32**.

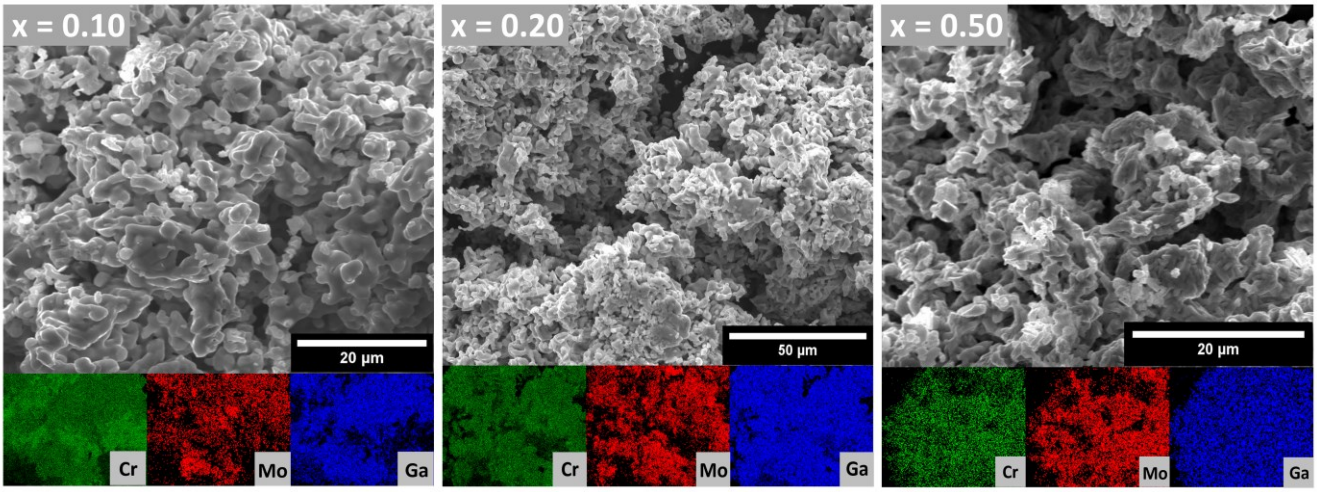

Figure 32: SEM micrographs showing the morphology of the obtained MAX phase solid-solutions $(Cr_{1-x}Mn_x)_2GaC$ (x = 0.05, 0.10, 0.11) and EDX mappings showing the elemental distribution of vanadium, manganese, and gallium.

3.4.5. Conclusion

In this project, the synthesis of the hitherto unknown solid-solution phase $(Cr_{1-x}Mo_x)_2GaC$ with $0 \leq x \leq 1$ was conducted, using the microwave-assisted heating technique. X-ray diffraction data reveal the successful formation of a solid-solution phase up to a doping level of $x = 0.50$ by satisfying Vegard's behavior. These findings were supported by EDX mapping, showing a predominantly homogeneous distribution of molybdenum in the samples. Due to the increased electronic density in this system, further studies on magnetism would interesting in future projects. However, at a doping level of 60 at-%, the amount of MAX phase shrinks heavily, while Mo_2C forms the new main phase in the system. Already, at a doping level of 70 at-% of molybdenum, Mo_2C was obtained almost single phase. The exact reasons for the suppression/decomposition still must be elaborated with further experiments and parameter variations.

3.4.6. Supplementary Information

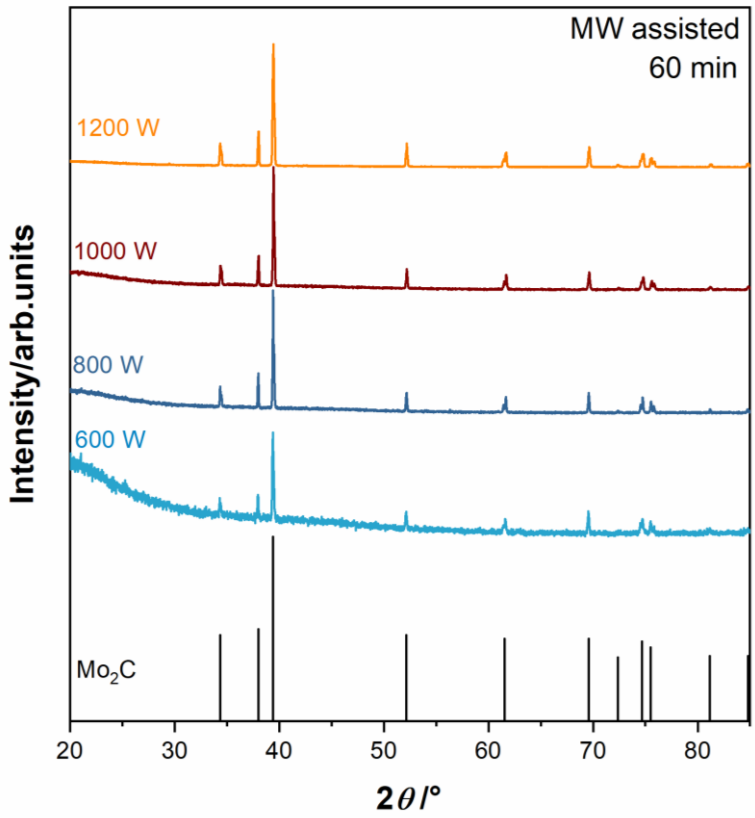

Figure 33: Experiments to investigate the behavior of the Mo-Ga-C system over a wide microwave power range. The used reactants have been molybdenum carbide (1 eq.) and gallium (1.4 eq.) according to synthesis protocols reported in literature.[121]

Table 22: Results of the Le Bail refinement of Cr_2GaC.

Phase name	Cr_2GaC
Spacegroup	$P6_3/mmc$
Lattice parameters *a, c*/ Å	2.8845(5) 12.6062(3)
Cell volume/ $Å^3$	90.84(4)
Background order	15
R_p	3.74
R_{wp}	5.72
R_{exp}	2.10
GOF	2.73

Table 23: Results of the Le Bail refinement of $(Cr_{0.95}Mo_{0.05})_2GaC$.

Phase name	$(Cr_{0.95}Mo_{0.05})_2GaC$
Spacegroup	$P6_3/mmc$
Lattice parameters *a, c*/ Å	2.9001(4) 12.6388(2)
Cell volume/ Å^3	92.06(3)
Background order	15
R_p	3.33
R_{wp}	4.94
R_{exp}	3.27
GOF	1.51

Table 24: Results of the Le Bail refinement of $(Cr_{0.90}Mo_{0.10})_2GaC$.

Phase name	$(Cr_{0.90}Mo_{0.10})_2GaC$
Spacegroup	$P6_3/mmc$
Lattice parameters *a, c*/ Å	2.9017(2) 12.6452(5)
Cell volume/ Å^3	92.21(8)
Background order	15
R_p	3.95
R_{wp}	6.07
R_{exp}	3.01
GOF	2.02

Table 25: Results of the Le Bail refinement of $(Cr_{0.85}Mo_{0.15})_2GaC$.

Phase name	$(Cr_{0.85}Mo_{0.15})_2GaC$
Spacegroup	$P6_3/mmc$
Lattice parameters *a, c*/ Å	2.9127(2) 12.7023(6)
Cell volume/ Å^3	93.33(1)
Background order	15
R_p	4.41
R_{wp}	6.91
R_{exp}	2.08
GOF	3.32

Table 26: Results of the Le Bail refinements $(Cr_{0.80}Mo_{0.20})_2GaC$.

Phase name	$(Cr_{0.80}Mo_{0.20})_2GaC$
Spacegroup	$P6_3/mmc$
Lattice parameters *a, c*/ Å	2.9215(3) 12.7074(2)
Cell volume/ Å^3	93.93(2)
Background order	15
R_p	5.24
R_{wp}	8.26
R_{exp}	3.60
GOF	2.30

Table 27: Results of the Le Bail refinements $(Cr_{0.60}Mo_{0.40})_2GaC$.

Phase name	$(Cr_{0.80}Mo_{0.20})_2GaC$
Spacegroup	$P6_3/mmc$
Lattice parameters *a, c*/ Å	2.9594(3) 12.8497(2)
Cell volume/ Å^3	97.46(3)
Background order	15
R_p	4.91
R_{wp}	9.03
R_{exp}	3.11
GOF	2.90

Table 28: Results of the Le Bail refinements $(Cr_{0.50}Mo_{0.50})_2GaC$.

Phase name	$(Cr_{0.50}Mo_{0.50})_2GaC$
Spacegroup	$P6_3/mmc$
Lattice parameters *a, c*/ Å	2.9779(1) 12.9130(5)
Cell volume/ Å^3	99.17(7)
Background order	15
R_p	3.12
R_{wp}	4.52
R_{exp}	3.04
GOF	1.49

4. *X*-site solid-solution MAX phases

4.1. State of the Art

The following parts in chapter 4.1.1 and 4.1.2 are published and partly adapted as parts of an open source review article (CC BY-NC-ND 4.0 licensing) published as "Niels Kubitza, Carina Büchner, Jordan Sinclair, Rose Snyder, Christina S. Birkel; Extending the Chemistry of Layered Solids and Nanosheets: Chemistry and Structure of MAX Phases, MAB Phases and MXenes, *ChemPlusChem,* **2023***88*, e202300214.

4.1.1. MAX phase nitrides

When looking at the overall numbers of known MAX phases, MAX phase nitrides represent only a small part of them (n<15) and are outnumbered by carbides by a factor of ten (>150). The significant difference in these numbers can be related to challenges during the synthesis of nitrides. Besides the gaseous state under normal conditions, the nitrogen molecule exhibits partially low diffusion rates, as well as a high bonding energy that heavily inhibits direct nitridation reactions.[125] Hence, in contrary to carbides, where carbon is frequently used as an elemental precursor, binary nitride precursors are required to maintain MAX phase stoichiometry. Apart from these challenges, nitrides in general are recognized as demonstrating advantages over their carbide counterparts, such as an enhanced magnetic exchange correlation[126] or higher electronic conductivities. For instance, the latter can be observed for the Ti_2AlN phase where the nitride phase beats the carbide one.[127–131] On the other hand, similar to the carbide phases, the Ti-Al system also represents the most studied system in the field of nitride MAX phases. Many synthesis protocols including property measurements have been published for the 211 system.[110, 105–109] New studies also address the ability of Ti_2AlN to act as a coating material[133] or as a nanocomposite material in a MAX phase/cellulose acetate membrane.[134] Going beyond 211 phases, the Ti-based 413 phase Ti_4AlN_3 served as the precursor for the first nitride MXene in 2016,[135] which further substantiates the interest in the Ti-Al-N system. Nonetheless, the interest in nitride phases is not only restricted to the Ti-based phases. The 211 Cr_2GaN phase also represents an important nitride candidate. While most of the magnetic properties of the MAX phases arise from doping experiments (see chapter 3.1.2), this phase exhibits, without any doping, a magnetic phase transition in form of a spin density wave (SDW) at T_N = 170 K.[118,119] No comparable behavior is known for any reported carbide MAX phase. Further efforts were made to suppress the SDW state by Ge-doping experiments to induce a superconducting state in the system, however, without success.[136] Thus, Ti_2InN stays the only superconducting nitride MAX phase with a transition temperature of T_C = 7.3 K.[137] The remaining of the reported nitride MAX phases are mostly known since the early reports on H-phases by NOWOTNY *et al.* in the 1960s[28,132,138,139] but without any further comprehensive characterization steps such as

crystallographic data or materials properties (**Table 29**). Overall, the interesting properties of already characterized MAX phase nitrides, the challenging synthesis procedures, as well as the unknown potential of hitherto unknown phase systems makes research in the field of MAX phase nitrides at least as important as work in the predominant field of MAX phase carbides.

Table 29: A list of the currently reported MAX phase nitrides.

4d *M*-metal		5d *M*-metal
Ti_2AlN[132]	Ti_2FeN[140]	V_2GaN[28]
Ti_4AlN_3[135]	$Ti_2(Al_{0.1}Cu_{0.9})N$[141]	V_2GeN[28]
Ti_2GaN[138]	Zr_2InN[138]	**6d *M*-metal**
Ti_2InN [138]	Zr_2TlN[28]	Cr_2GaN[139]
Ti_2ZnN[142]	Hf_2SnN[34]	
	Hf_2InN[28]	

4.1.2. MAX phase carbonitrides

Even more scarcely represented than nitrides are carbonitride MAX phases with less than 5 reported compounds (**Table 30**). However, analogous to the parent carbides and nitrides, Ti-Al-based phases are the most studied ones. First reports of carbonitrides reach back to the work of PIETZKA *et al.* in the 90s with the synthesis of $Ti_2AlC_{1-x}N_x$ ($0 \leq x \leq 1$).[143] In 2008, SCABAROZI *et al.* synthesized the 211 and 312 phase with $x = 0.50$ and studied the thermal and electrical properties in comparison to the parent phases.[128] Here, the resistivity of the carbonitride members is significantly higher than those of the pure *X*-site phases due to scattering factors such as vacancies or other defects whereas the thermal conductivity is similar to the parent phases.[3,128] On the other hand, the 211 $Ti_2AlC_{0.5}N_{0.5}$ phase exhibits enhanced mechanical properties, such as higher hardness and stiffness than Ti_2AlC and Ti_2AlN.[130] Furthermore, it has been shown that it is possible to synthesize stable carbonitrides with at least 20 % vacancies on the C or N site, which is not achievable for carbide phases.[144] More complex carbonitrides have been synthesized by DU *et al.*, who combined a high entropy approach on the *M*-site with an *X*-site solid solution.[5] The carbonitride was then used as a precursor for MXenes, resulting in a product with high mechanical strains and good catalytic activities. As shown by the latter examples and the small number of reported carbonitrides, the field has immense potential to be expanded in future studies, in order to further increase the phase variety of MAX phases with the potential to obtain products possessing improved properties compared to the parent phases.

Table 30: A list of the currently reported MAX phase carbonitrides.

Carbonitride phases
$Ti_2AlC_{1-x}N_x$ [143]
$Ti_3Al(C_{1-x}N_x)_2$ [128]
$(Ti_{1/3}V_{1/6}Zr_{1/6}Nb_{1/6}Ta_{1/6})_2AlC_{1-x}N_x$ [5]

4.2. Sol-gel assisted synthesis of the carbonitride MAX phase $V_2GaC_{1-x}N_x$

The parts (including text, figures, and tables) of the following chapter were published and reproduced (adapted) with permission from "Niels Kubitza, Andreas Reitz, Anne-Marie Zieschang, Hanna Pazniak, Barbara Albert, Curran Kalha, Christoph Schlueter, Anna Regoutz, Ulf Wiedwald and Christina S. Birkel; From MAX Phase Carbides to Nitrides: Synthesis of V_2GaC, V_2GaN, and the Carbonitride $V_2GaC_{1-x}N_x$, *Inorganic Chemistry,* **2022**, *61, 28*, 10634-10641. Copyright (2022) American Chemical Society."

4.2.1. Motivation

Following the previous studied *M*-site solid-solution phases, the V_2GaC phase forms the starting point to investigate the *X*-site solid-solution behavior as a role model system to synthesize a hitherto unknown carbonitride phase $V_2GaC_{1-x}N_x$. In order to circumvent the several challenges of conventional nitride syntheses (see chapter 4.1.1) which are additionally accompanied with drawbacks concerning potential variations in the chemical compositions, as well as control of morphology, wet-chemical-based precursor synthesis approaches are applied (e.g., sol-gel and liq. ammonia synthesis). The interplay of both, wet-chemical methods and conventional techniques shall demonstrate an alternative preparation route to further access the hardly investigated field of MAX phase nitrides and carbonitrides.

4.2.2. Experimental section

Due to the extensive combination of different preparation techniques, a schematic summary of the synthesis of the samples discussed in chapter 4.2 is illustrated in **Figure 34**. The respective experimental conditions and preparation steps are described below.

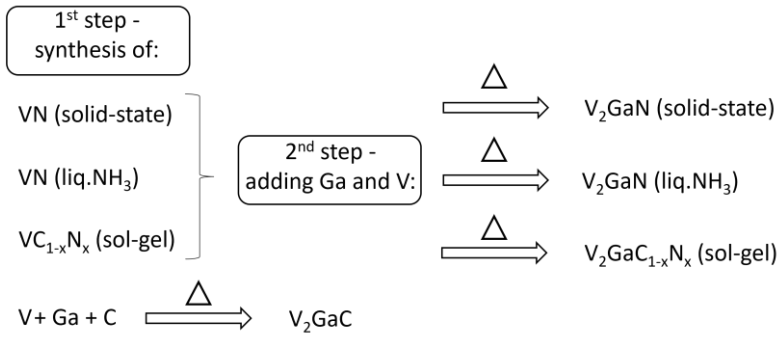

Figure 34: Schematic summary of the discussed V-based MAX phases samples, including the used precursors and synthesis methods.

Step 1: VN and $VC_{1-x}N_x$ precursor synthesis

$VC_{1-x}N_x$ (sol-gel): Following the method by GIORDANO and ANTONIETTI *et al.*[19], 0.6 ml (1.10 g, 6.32 mmol) of $VOCl_3$ (Sigma Aldrich, 99 %) were dissolved in ~3 ml ethanol under the release of HCl gas (inside a fume hood). The solution was stirred for 15 min and heated to 50 °C where 1.14 g (18.96 mmol) urea (Sigma Aldrich, >99 %) as gelation agent was added. The resulting homogeneous and highly viscous brownish gel was then transferred into an alumina crucible and annealed inside a horizontal tube furnace (Carbolite) at 850 °C (heating rate 2 °C/min) for eight hours under a continuous flow of nitrogen.

VN (liquid ammonia): Due to the high sensitivity of oxygen and water impurities in this synthesis technique, all glassware was heated under vacuum and purged with argon prior to synthesis. According to ZIESCHANG *et al.*,[21] 2.97 g (18.90 mmol) of VCl_3 (Sigma Aldrich, >99 %) were weighed into a two-neck Schlenk flask equipped with a glass-coated magnetic stirrer in an argon-filled glovebox. Subsequently, ~60 ml of predried liquid ammonia (Praxair, UHP) were distilled into the two-neck Schlenk flask before 3.5 eq. sodium (1.51 g, 65.40 mmol) (Alfa Aesar, >99 %) were added under flowing argon. The suspension immediately turned black and was stirred for one hour at – 77 °C using an isopropanol-dry ice cooling bath. To remove remaining ammonia residues after completion of the reaction, the suspension was allowed to warm up to room temperature overnight. The obtained greyish powder was then annealed inside a vertical tube furnace (*Carbolite*) under vacuum following a defined temperature program (**Table 32**). To remove the side phase NaCl, the product was washed multiple times with 20 ml of predried methanol (molecular sieves 3 Å). The resulting finely dispersed black powder was stored inside an argon-filled glovebox.

VN (solid-state): 0.5 g (9.82 mmol) vanadium powder (Alfa Aesar, ~325 mesh, 99.5 %) were weighed into an alumina crucible in an argon-filled glovebox. Afterwards, the crucible was transferred into a horizontal tube furnace (*Carbolite*) and annealed for eight hours at 1250 °C (heating rate 5 °C/min) under a continuous flow of nitrogen.

Step 2: MAX phase synthesis

As illustrated in the scheme in **Figure 34**, V_2GaC is prepared by exclusively using elemental precursors, such as vanadium, gallium, and carbon in a solid-state reaction according to the following reaction equation:

$$2\,V + Ga + C \rightarrow V_2GaC$$

All syntheses of the (carbo)nitride MAX phases encompass two steps: In the first step, vanadium carbonitride and nitride precursors were prepared by different techniques, namely solid-state and liquid

ammonia leading to nitrides, and “urea-glass” sol-gel leading to a carbonitride (details below). In the second step, the precursors (VN and $VC_{1-x}N_x$) were reacted with additional vanadium and gallium to ensure the target 2:1:1 stoichiometry according to the following two reaction equations:

$$VC_{1-x}N_x + V + Ga \rightarrow V_2GaC_{1-x}N_x$$

$$VN + V + Ga \rightarrow V_2GaN$$

A typical synthesis involves mixing of the precursors based on 0.5 g (2.25 mmol) of the desired MAX phase. A detailed summary of the used amounts can be found in **Table 31**. Briefly, gallium flakes (Alfa Aesar, >99 %) were cut under atmospheric conditions and subsequently transferred into an argon-filled glovebox. A small excess of gallium was used to account for the slight gallium loss during the reaction. Inside the glovebox, vanadium powder (Alfa Aesar, ~325 mesh, 99.5 %), the vanadium (carbo)nitride prepared in step 1 (see above), or carbon (Alfa Aesar, APS 2-15 micron, 99.999 %) were weighed and thoroughly homogenized using an agate mortar. Afterwards, the powder mixture was loosely mixed with the gallium flakes and pressed into a dense pellet (⌀ = 10 mm, 3t, 5 s). All pellets were then annealed inside a horizontal tube furnace (*Carbolite*) following a defined temperature program (**Table 32**) under the exclusion of oxygen.

Table 31: Weighing amounts of the prepared MAX phase samples.

Sample	*m*(VN)/$VC_{1-x}N_x$ in g	*m*(V) in g	*m*(Ga) in g	*m*(C) in g
V_2GaN solid-state	0.1461 (1.0 eq.)	0.1146 (1.0 eq.)	0.2039 (1.3 eq.)	-
V_2GaN liq. NH_3	0.1461 (1.0 eq.)	0.1146 (1.0 eq.)	0.2039 (1.3 eq.)	-
$V_2GaN_{1-x}C_x$ (3 eq. Urea)	0.1461 (1.0 eq.)	0.0802 (0.7 eq.)	0.2039 (1.3 eq.)	-
$V_2GaN_{1-x}C_x$ (8 eq. Urea)	0.1461 (1.0 eq.)	0.0802 (0.7 eq.)	0.2039 (1.3 eq.)	-
V_2GaC	-	0.2292 (2.0 eq.)	0.1726 (1.1 eq.)	0.0243 (0.9 eq.)

Table 32: Summary of the conducted temperature programs for sample preparation.

Sample	1st ramp	1st holding time	2nd ramp	2nd holding time
VN liq. NH_3	2 °C/min to 200 °C	1.5 h	2 °C/min to 600 °C	1.0 h
V_2GaN solid-state	5 °C/min to 850 °C	10.0 h	5 °C/min to 1700 °C	20 min
V_2GaN liq. NH_3	5 °C/min to 850 °C	10.0 h	5 °C/min to 1050 °C	1.0 h
$V_2GaN_{1-x}C_x$ (3 eq. Urea)	2 °C/min to 900 °C	10.0 h	-	-

$V_2GaN_{1-x}C_x$ (8 eq. Urea)	4 °C/min to 900 °C	10.0 h	-	-
V_2GaC	5 °C /min to 1050 °C	20.0 h	-	-

4.2.3. Characterization

X-ray powder diffraction data were obtained using a *D2 Phaser diffractometer* (*Bruker*) with Cu-$K_{\alpha,1}$ (λ = 1.540596 Å) and Cu-$K_{\alpha,2}$ (λ = 1.544493 Å) in Bragg-Brentano geometry at room temperature. Prior to measurements, all samples were finely ground using an agate mortar and deposited on a low-background silicon specimen holder (*Bruker*). Rietveld refinements of the XRD data were conducted using *DIFFRAC.TOPAS* (*Bruker*). To maximize the accuracy of the lattice parameters, LaB_6 was used as an internal standard for all MAX phase samples (**Figure 47**).

SEM images were taken at the *FEG XL30* (*FEI*) choosing acceleration voltages of 10-30 kV. The EDX data was collected with the *XL-30* (*EDAX*) detector.

TEM samples were prepared by ultrasound-assisted dispersing the MAX phase powder in ethanol for 2 h and drop casting 3 μL on a Cu grid covered with a lacey carbon film. HRTEM images were acquired with a *JEOL JEM-2200FS* C_s-corrected transmission electron microscope at an acceleration voltage of 200 kV using a 2k x 2k *GATAN UltraScan®1000XP* CCD camera.

The electron energy loss spectroscopy (EELS) spectra were recorded in imaging mode. The core edges were extracted from the background signal using a power law. Both soft and hard X-ray photoelectron spectroscopy (SXPS and HAXPES) were used to characterize the chemical environments and oxidation states within the samples. SXPS data were recorded on a *Thermo Scientific K-Alpha+ X-ray Photoelectron Spectrometer* (XPS) system using monochromated, micro-focused Al-K_α X-ray radiation ($h\nu$ = 1.4867 keV, further referred to as 1.5 keV for simplicity) and a 180° double-focusing hemispherical analyzer with a two-dimensional detector. The X-ray source was operated at 6 mA emission current and 12 kV anode bias. Data was collected using a 400 μm X-ray spot and a pass energy of 200 eV for survey and 20 eV for core level spectra. A flooding electron gun was used to minimize sample charging. HAXPES data were collected at beamline *P22* at *PETRA III*, German Electron Synchrotron *DESY* in Hamburg, Germany.[145] A photon energy of 6.0054 keV (further referred to as 6 keV for simplicity) were used for all experiments, with the energy selected using a Si (111) double crystal monochromator and a Si (333) post-monochromator. All measurements were conducted in grazing incidence geometry (5°). A *Phoibos 225HV analyzer* (*SPECS*, Berlin, Germany) was used with the small area lens mode and a slit size of 3 mm. Spectra were collected using a pass energy of 30 eV. The total energy resolution in this setup was determined to be 242 meV 16/84% Fermi edge (E_F) width of a polycrystalline gold foil.

4.2.4. Structural analysis

All nitride and carbonitride precursors are single-phase (**Figure 35**). For VN, the particles obtained from liquid ammonia show broader peaks in their XRD data, which indicates reduced crystallite sizes in comparison to the solid-state prepared ones with sharper peaks. The sol-gel derived carbonitride precursor also delivers broad peaks which is expected as a result of the wet chemical preparation. Indeed, crystallite sizes obtained from Scherrer broadening during Rietveld refinement range from an average of 30 nm (NH_3) to an average of 140 nm (sol-gel) (**Table 33**).

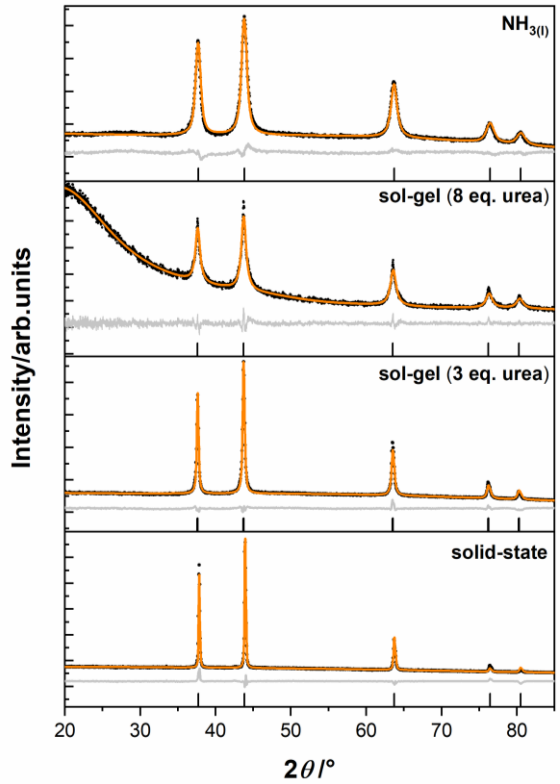

Figure 35: Powder XRD patterns (black) and Rietveld refinements (orange), residuum (grey) of the various vanadium nitride precursors synthesized prior MAX phase synthesis. The refinements were conducted based on the structure model of VN.[146]

Table 33: Results of the Rietveld refinements of the various VN precursors, including the estimated crystallite sizes for the sol-gel and liq. NH_3 precursors.

Preparation	solid-state	sol-gel (3 eq.)	sol-gel (8 eq.)	liq. NH_3
Spacegroup	*Fm-3m*	*Fm-3m*	*Fm-3m*	*Fm-3m*
Lattice parameter /Å	a = 4.137(3)	a = 4.139(2)	a = 4.134(4)	a = 4.129(5)
Cell volume/ Å^3	70.82(2)	70.93(2)	70.64(2)	70.40(3)
Crystallite size (Lorentz)/nm	--	140(30)	16(2)	30(3)
Background order	5	5	18	5
R_p	4.50	3.52	2.75	3.28
R_{wp}	7.21	4.60	3.60	4.20
R_{exp}	3.07	54.33	2.54	48.59
GOF	2.35	0.08	1.42	0.09

The Rietveld refinements of the X-ray powder diffraction data of all target MAX phase samples are shown in **Figure 36**, which also includes the refined lattice parameters. Here, the structural models of V_2GaC[117] and side phases (VN[146]/($VC_{1-x}N_x$,) V_2O_3[147]) were fitted (orange line) to the diffraction data (black dots). To increase the accuracy of the calculated lattice parameters, LaB_6 was used as an internal standard (**Figure 47**).

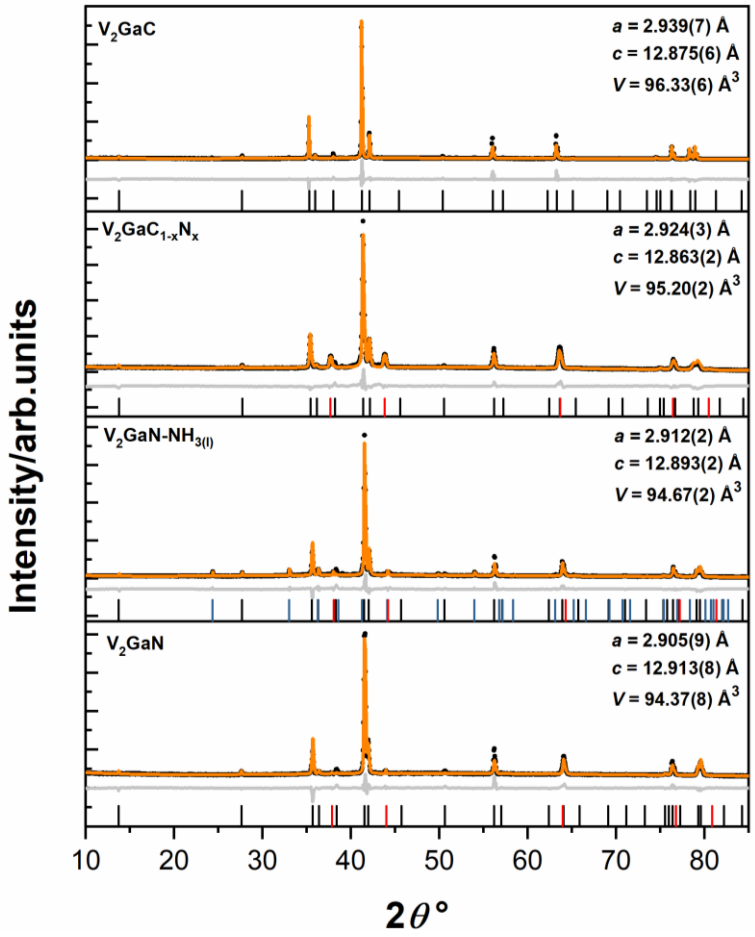

Figure 36: Results of the Rietveld refinements (orange lines) and residuum curves (grey) of the X-ray powder diffraction data (black dots) of the nitride, carbonitride, and carbide phases in the 211 V-Ga-C-N system. The refinements were conducted based on structural models of V_2GaC,[117] (black) VN[146] (red), and V_2O_3[147] (blue). The products are ordered according to increasing cell volumes. A full summary of the Rietveld data can be found in the SI.

The full sets of results from the Rietveld refinements, including the phase fractions, are summarized in **Table 34-39**. In all samples, the MAX phase forms the main phase with weight percentages up to 95 wt-% (V_2GaN). The observed oxide impurities in the liquid ammonia derived sample can be explained by oxygen impurities occurring during the very sensitive precursor synthesis. The powder XRD data of all samples show an absence of the (002) peak. This has also been observed in previous works focused on Ga-based phases.[24,148] However, its origin still has to be elucidated. The lattice parameters of the nearly phase pure carbide phase V_2GaC are in good agreement with those reported in the literature.[117] In comparison, the *a*-lattice parameter of the conventionally synthesized nitride phase V_2GaN is noticeably smaller, while the *c*-parameter exhibits a larger value. Despite the increase of the latter, the overall cell

volume shrinks by roughly 1 Å^3 to V = 94.37(8) Å^3 going from the carbide to the nitride. Considering the reported experimental lattice parameters[34] (a = 3.00 Å, c = 13.3 Å) for V_2GaN that lead to a cell volume of ~V = 103.7 Å^3, this shows a discrepancy between our experimental values for V_2GaN compared to the literature. Nonetheless, the calculated values of BOUHEMADOU *et al.*[149], as well as the smaller atomic radius of nitrogen compared to carbon, support our finding with a lower value in volume of the nitride. Furthermore, the cell volume (V = 94.67(2) Å^3) of our second V_2GaN sample (the one prepared from the liquid ammonia derived VN) confirms the smaller volume in comparison to the literature report. The carbonitride MAX phase prepared from the "urea-glass" precursors shows lattice parameters that fall in between those of the carbide and the nitride (closer to those of the carbide phase). This is an indication of C and N mixing on the *X*-site of the MAX phase structure in $V_2GaC_{1-x}N_x$. This needs to be validated by further techniques (see below). In order to confirm the feasibility of the sol-gel based synthesis approach, another exemplary $V_2GaC_{1-x}N_x$ phase was synthesized using a $VC_{1-x}N_x$ precursor prepared with a higher urea amount (8 eq. urea, **Figure 48**). Beside the lattice parameter determination, *ex-situ* X-ray powder data (**Figure 37**) were used to elucidate the formation mechanism of the hitherto unknown carbonitride MAX phase, which can be described as follows. First, the elemental precursors vanadium and gallium form an intermetallic vanadium-gallium species (Ga_5V_2) at moderate temperatures, which further reacts either with VN or carbon at higher temperatures towards the desired MAX phase.

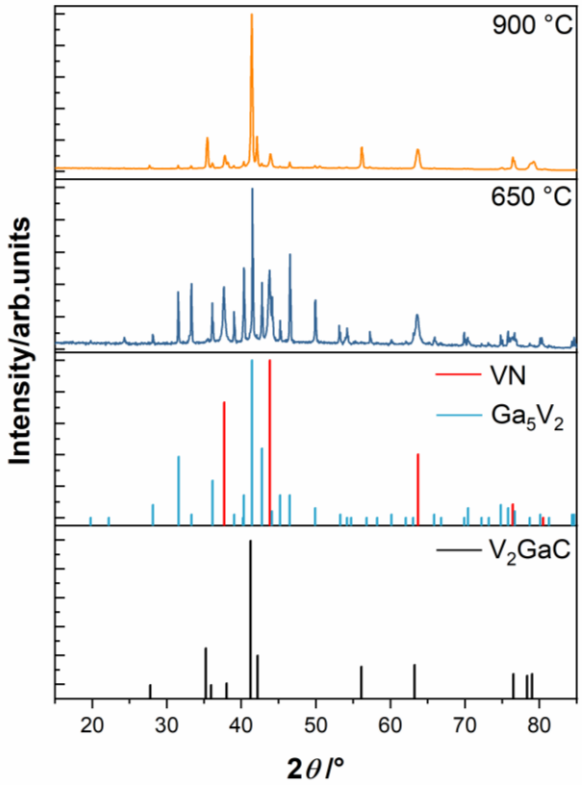

Figure 37: Powder X-ray diffraction data of a $V_2GaN_{1-x}C_x$ sample which was firstly heat-treated at 650 °C (dark blue) before a second heat treatment was conducted at 900 °C (orange). Comparison with literature data (peak positions and intensities) of V_2GaC[117], Ga_5V_2[150], and VN[146] prove the transition of the initially formed intermetallic phase Ga_5V_2 that further reacts with VN towards the MAX phase at elevated temperatures.

Electron micrographs (**Figure 38**) show the morphology of the different MAX phase samples. They reveal the opportunity to influence the size, shape, and microstructure of the target phases by applying the above-described hybrid synthesis methods.

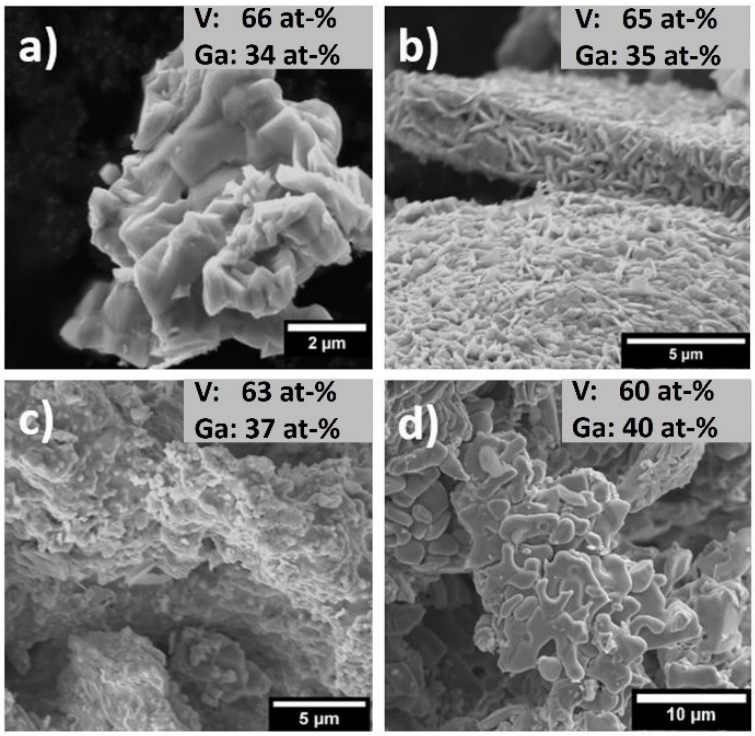

Figure 38: SEM micrographs of V_2GaC (a), $V_2GaC_{1-x}N_x$ (b), $V_2GaN\text{-}NH_{3(l)}$ (c), and V_2GaN (d), showing the various morphologies of the samples. The elemental compositions included in the micrographs were determined using EDX measurements (**Table 41-45**).

While the morphology of the conventionally synthesized pure carbide V_2GaC is mainly dominated by the characteristic anisotropic MAX phase layered structure (**Figure 38(a)**), the sol-gel derived samples (**Figure 38**(**b**)) additionally exhibit a covered surface with needle-like structures (see also **Figure 48** for the carbonitride sample prepared with 8 eq. urea).

On the other hand, the conventionally synthesized pure nitride V_2GaN (**Figure 38(d)**) shows coarse and flake-like structures, whereas the liq. ammonia derived V_2GaN (**Figure 38(c)**) reveals finer substructures and drop-like particles partially covering the surface. This is most likely due to the nanoparticular character of the VN-precursor, which simultaneously influences the thermal behavior of the resulting MAX phase. While the conventional solid-state approach showed best results at 1700 °C, the ammonia derived MAX phase already decomposed at 1400 °C (**Figure 39**). Especially the latter example impressively demonstrates that the choice of the precursor and the resulting morphology can have a tremendous effect on the materials properties. Despite small deviations in the 2:1 V/Ga ratio, the compositions of the MAX phases were confirmed using EDX measurements (**Figure 38**, **Table 41-45**).

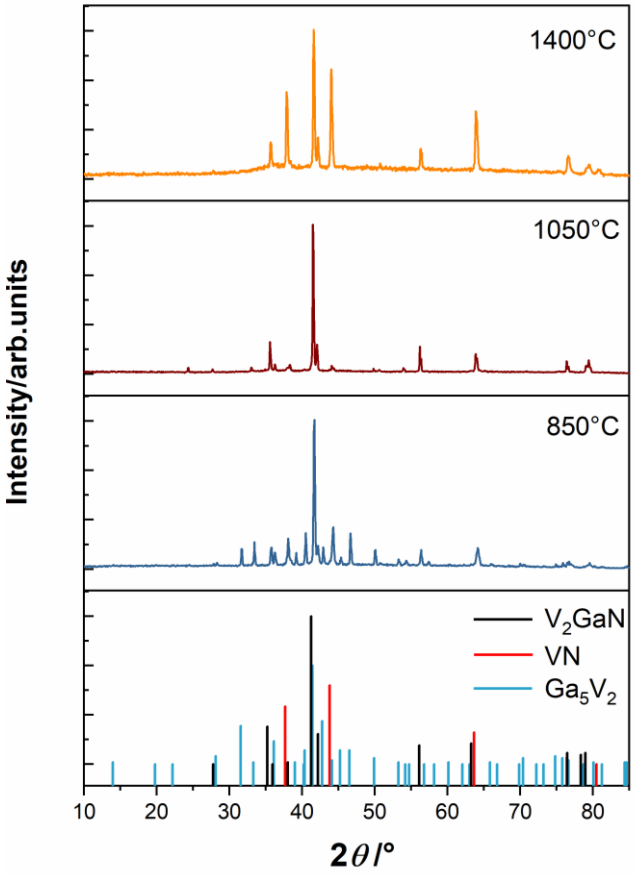

Figure 39: Powder X-Ray diffraction data of a V_2GaN ($NH_{3(l)}$) sample which was heat treated at three different temperatures (850 °C (dark blue), 1050 °C (wine red), and 1400 °C (orange) to evaluate the thermal stability of the phase. It is shown that 850 °C is too low to induce a full formation of the MAX phase, whereas 1050 °C provide a good sample quality. At 1400 °C a decomposition towards the binary nitride VN can be observed. The data were evaluated based on literature data (peak positions and intensities) of V_2GaN (based on[117]) , Ga_5V_2,[150] and VN.[146]

The microstructure of $V_2GaC_{1-x}N_x$ was further studied by high-resolution transmission electron microscopy. **Figure 40 (a)** shows anisotropic flake-like morphology of the synthesized particles, while the corresponding HRTEM image reveals a well-ordered layered structure typical for nanolaminated MAX phases (further TEM data is shown in **Figure 48**).

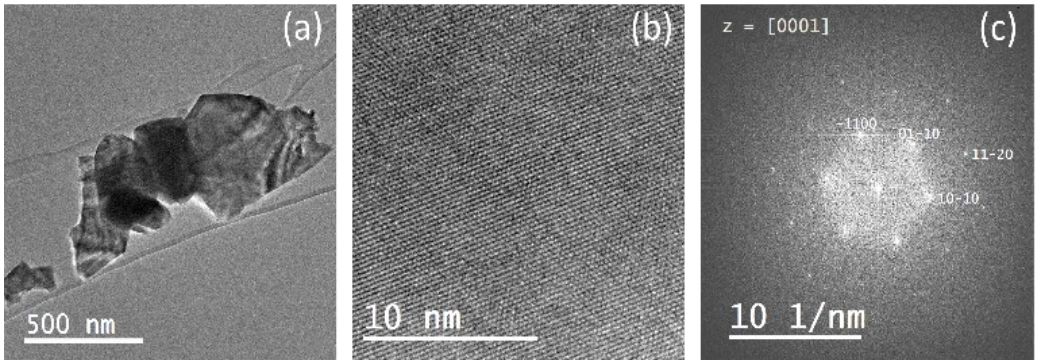

Figure 40: The microstructure of $V_2GaC_{1-x}N_x$ was further studied by high-resolution transmission electron microscopy. **Figure 41a** shows anisotropic flake-like morphology of the synthesized particles, while the corresponding HRTEM image reveals a well-ordered layered structure typical for nanolaminated MAX phases.

Core-loss EELS spectra recorded in the region from 250 to 600 eV clearly indicate the presence of the C, N, and V edges at about 290 eV, 400 eV, and 510 eV, respectively (**Figure 42**). It must be noted that the C-K edge signal is slightly different from the typical MAX phase C-K edge describing a slight broadening of the second peak (≈295 eV), while the N-K edge shows all the features earlier observed for N-based MAX phases (**Figure 42**, inset).[151,152] These findings evidence that for the $V_2GaC_{1-x}N_x$ MAX phase N-atoms are less sensitive to the perturbation induced by solid-solution effects as compared to C atoms. Focusing further on the C-K and N-K edges, the C and N content is quantified, which is on average 45 at-% and 55 at-%, respectively. In this way, a sum formula can be formulated that approximately corresponds to a 0.5/0.5 ratio of carbon and nitrogen.

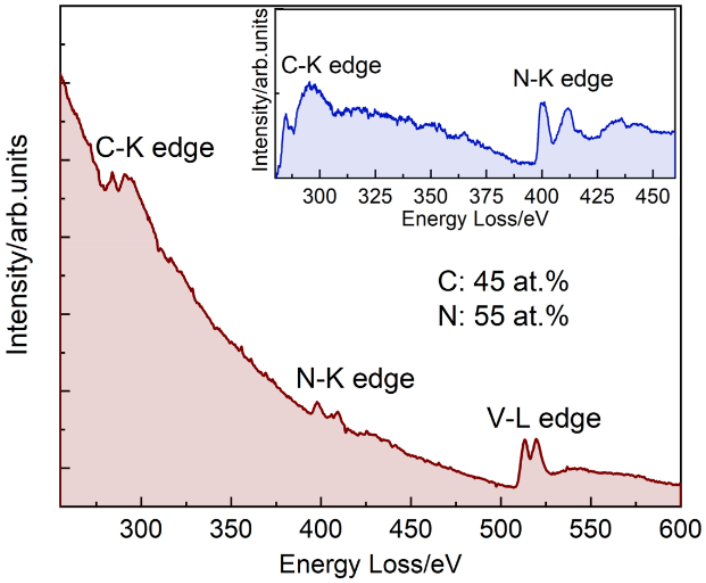

Figure 42: EELS spectra of C-K,N-K, and V-$L_{2,3}$ edges of a representative region of a $V_2GaC_{1-x}N_x$ particle and C and N composition as derived from elemental quantification of C-K and N-K edges EELS spectra (b, inset).

Based on the determined C/N ratio by core-loss EELS spectra, a conventional solid-state approach using VN (solid-state), carbon, vanadium, and gallium was conducted. When applying the same reaction conditions as in the sol-gel based approach, the X-ray powder diffraction data of the resulting product show the simultaneous presence of both, the parent phases V_2GaN and V_2GaC, and no clear evidence for a formation of the desired carbonitride phase (**Figure 43**). Only at 1100 °C a formation of $V_2GaC_{1-x}N_x$ can be realized, however, with a higher amount of side phase impurities (**Figure 43**, **Table 40**). These findings further support that the sol-gel-based synthesis approach is a valuable option to extend the compositional space of MAX phases in terms of carbonitrides in combination with lower synthesis temperatures.

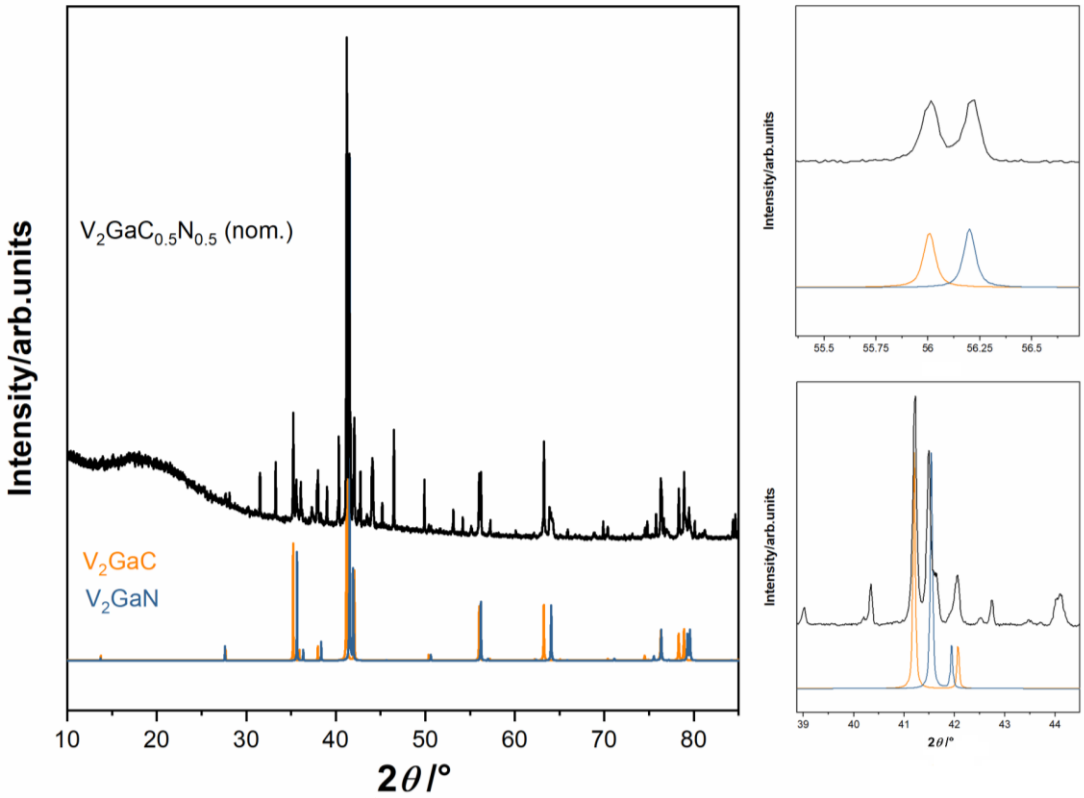

Figure 43: Powder X-Ray diffraction data of a $V_2GaC_{0.5}N_{0.5}$ sample (including enlarged 2θ regions), which was tried to conventionally synthesize by mixing elemental precursors and applying the same reaction conditions as described for the sol-gel assisted approach. Besides V-Ga side phases, the data show the simultaneous presence of both parent phases, V_2GaC and V_2GaN. The powder XRD of the parent phases were simulated based on the structural model of V_2GaC[117] and the determined lattice parameters (**Table 34-38**) using the software VESTA.[153]

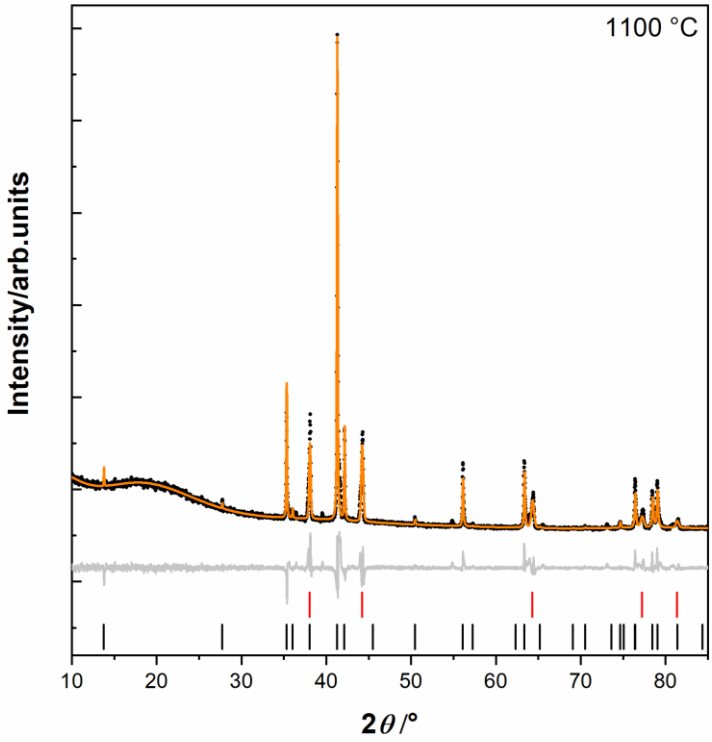

Figure 44: Results of the Rietveld refinement (orange line), and residuum curve (grey line) of the X-Ray powder diffraction data (black dots) of a conventionally prepared solid-state $V_2GaC_{0.5}N_{0.5}$ sample annealed at 1100 °C for ten hours. The refinement was conducted based on the structural models of V_2GaC[117] (black) and VN[146] (red).

Initial exploration of the samples using X-ray photoelectron spectroscopy was performed using a standard Al-K_α soft X-ray source. Whilst this provided good data for most of the core levels, the Ga LMM Auger series overlaps significantly with several essential core level spectra in this system, including N 1*s* and V 2*p*, making analysis and interpretation impossible (**Figure 45**).

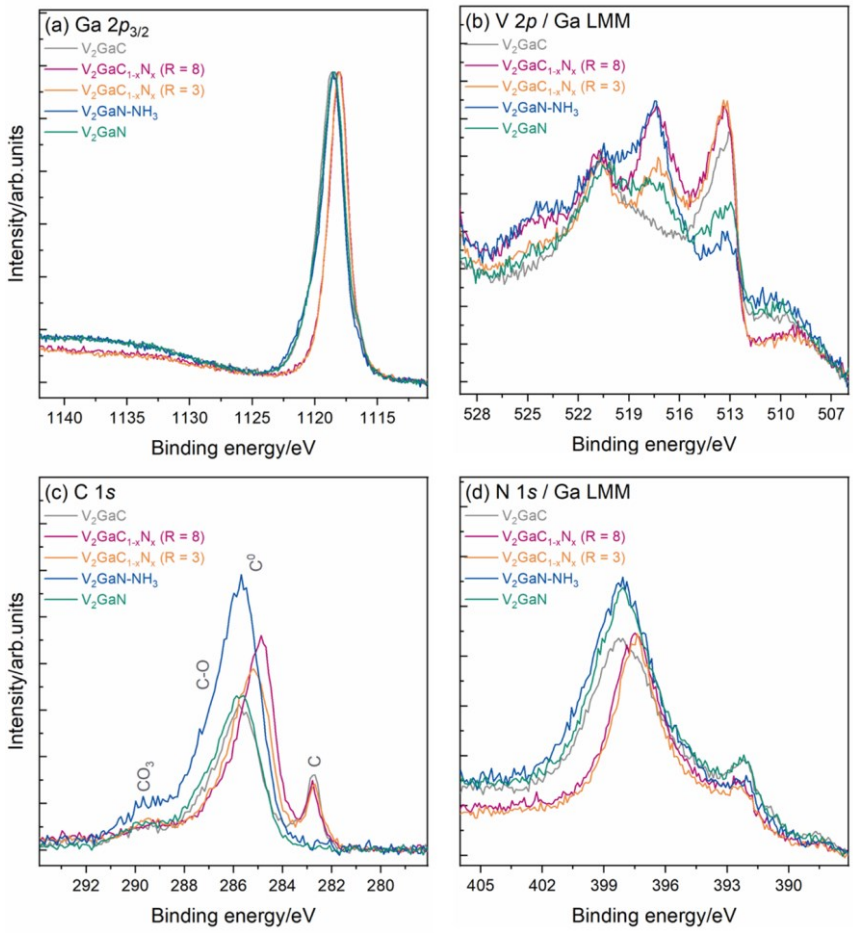

Figure 45: Soft X-ray photoelectron spectroscopy (SXPS, hv = 1.5 keV) data of the main core levels of the nitrides, carbonitrides, and carbide phases in the 211 V-Ga-C-N system, including (a) Ga 2p3/2, (b) V 2p, (c) C 1s, and (d) N 1s. The V 2p and N 1s core level spectra show severe overlap with several features of the Ga LMM series preventing data analysis and interpretation.

Whilst core lines appear at the same binding energy in photoelectron spectra, independent of the excitation energy, Auger lines appear at specific kinetic energy. Changing the excitation energy used in a photoemission experiment will consequently move Auger lines relative to photoelectron lines. Therefore, HAXPES can be used to obtain spectra, which do not show any Auger contributions within the spectral range of interest (**Figure 46**).[74] **Figure 47** shows the four main HAXPES core level spectra of all samples in the 211-V-Ga-C-N system. The Ga $2p_{3/2}$ core level (**Figure 47(a)**) shows sharp features at low binding energy (BE) from Ga in all investigated samples. Subtle differences in BE (Δ = 0.23 eV) are observed, with the pure carbide being the lowest in BE and the pure nitride being the highest in BE. In addition, all samples show contributions from oxidized environments, with clear differences between the pure carbide, nitride, and carbonitride. Whilst the SXPS spectra shown (**Figure 46**) are dominated

by the surface oxide layer, this contribution is lower in HAXPES due to the increased probing depth. As all samples were handled in air, it is expected that the surface of the samples will be partially oxidized.

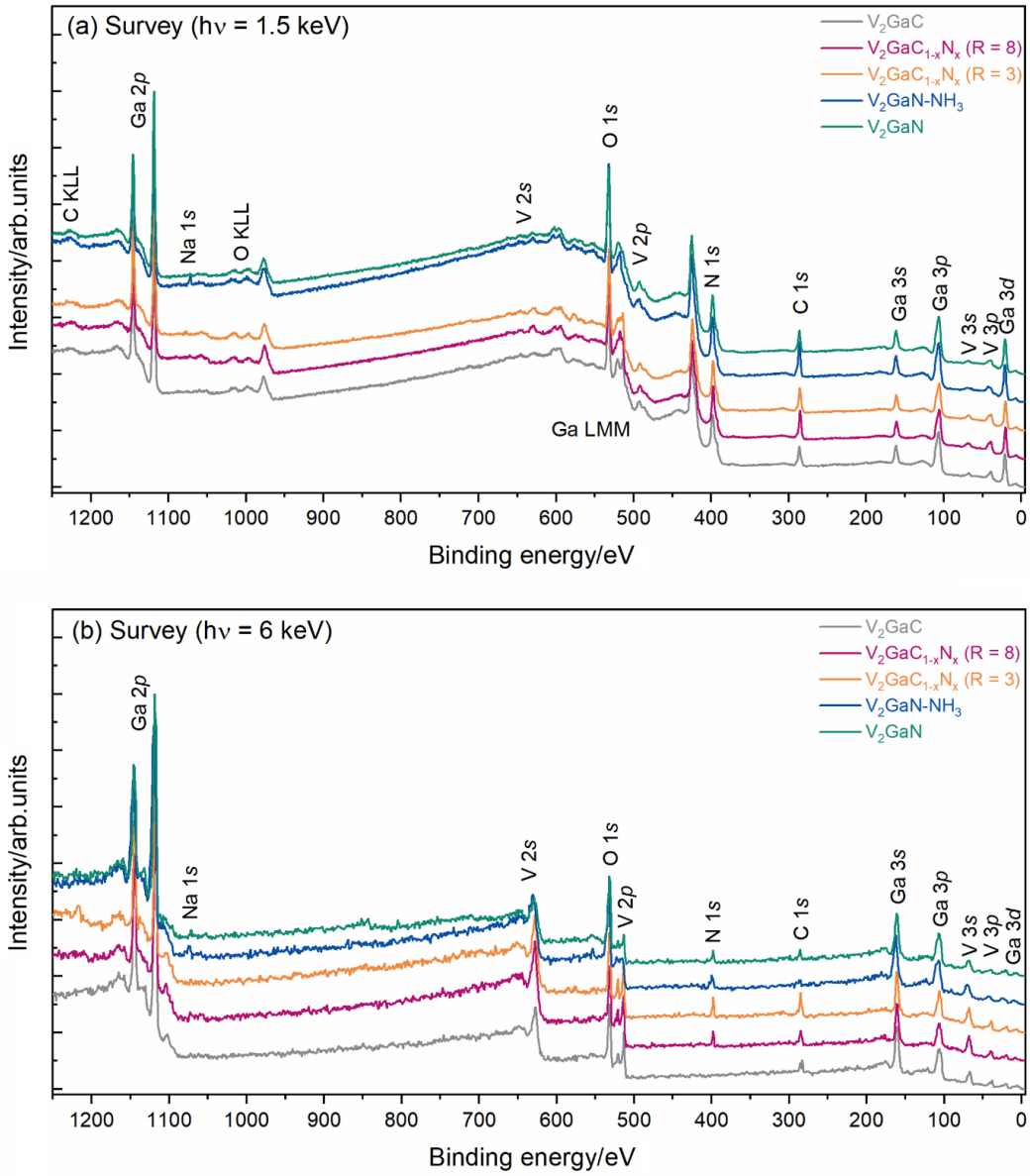

Figure 46: X-ray Photoelectron survey spectra of the nitrides, carbonitrides, and carbide phases in the 211 V-Ga-C-N system, including (a) SXPS data at *hv* = 1.5 keV and (b) HAXPES data at *hv* = 6 keV. All major core and Auger lines are labelled within the graphs.

Due to the differences in the spectral shape of the liquid ammonia-based sample, its data is separately discussed below. The V 2*p* core level for all other samples (**Figure 47(b)**) shows the typical doublet, with the $2p_{1/2}$ state considerably broadened by Coster-Kronig effects.[154] V_2GaC exhibits the sharpest, asymmetric $2p_{3/2}$ feature at 512.8 eV. The spectra for V_2GaN and the mixed phase are broader and shifted to higher BE. In addition, all N-containing samples reveal clear contributions of oxidized states at higher BE. The C-1*s* spectra (**Figure 47(c)**) clearly distinguish between the pure nitride samples, and the carbide and carbonitride phases. Only the latter phases have a clear low BE feature at 282.7 eV. All samples exhibit varying contributions from adventitious carbon (C^0) from exposure to air as well as small

amounts of C-O environments. Finally, in the N 1*s* spectra (**Figure 47(d)**) V_2GaN shows one clear feature at 398.2 eV for the NV_6 environments A lower BE feature (397.5 eV) is found for the $V_2GaC_{1-x}N_x$ sample, commensurate with mixed $N_{1-x}C_xV_6$ environments. No nitrogen is detected in the carbide sample. The liquid ammonia-based sample clearly differs across all HAXPES spectra. This is due to partial charging of the surface overlayer of this sample. In both SXPS and HAXPES, the $V_2GaN\text{-}NH_{3(l)}$ sample shows the highest degree of a surface overlayer as well as the presence of vanadium oxide consistent with the XRD analysis. The SXPS data for this sample (**Figure 45**), where charge compensation could be used, shows a Ga $2p_{3/2}$ line shape comparable to that of the V_2GaN sample. Furthermore, the lower BE features across its HAXPES spectra match those of V_2GaN environments observed for the sample prepared through the solid-state route.

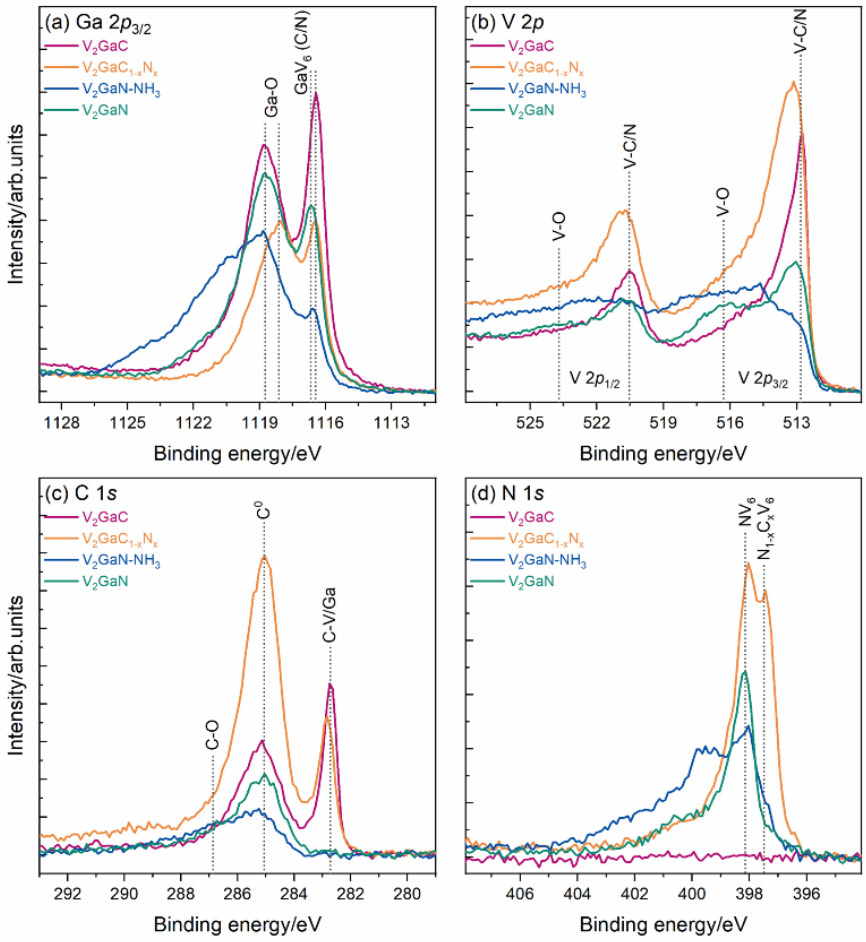

Figure 47: HAXPES data of all samples in the 211-V-Ga-C-N system, including (a) Ga $2p_{3/2}$, (b) V 2*p*, (c) C 1*s* and (d) N 1*s* core levels. All spectra were collected at $h\nu$ = 6 keV.

4.2.5. Conclusion

In this chapter, by combining non-conventional precursor synthesis methods, such as the sol-gel "urea-glass" and liquid ammonia method with conventional solid-state preparation techniques, an alternative synthesis approach for the 211-V-Ga-C-N MAX phase system was introduced. Besides the synthesis of the pure carbide and nitride phases, the sol-gel-based method represented a valuable option to synthesize a hitherto unknown carbonitride phase $V_2GaC_{1-x}N_x$. The mixed C/N nature within the M_6X octahedra of the new carbonitride phase was proven by means of X-ray powder diffraction, electron energy loss spectroscopy, and X-ray photoelectron spectroscopy, respectively. On the other hand, the liquid-ammonia based approach provides a new way to access the hardly investigated research field of nitride MAX phases, whose syntheses are challenging due to inhibiting factors occurring during nitride synthesis. Additionally, SEM micrographs revealed the potential of hybrid solid-state techniques to specifically influence the morphology of the obtained MAX phases depending on the synthesis process. Overall, these findings underline the beneficial aspect of non-conventional approaches to not only extend the phase variety but also to be a tool for targeted solid-state product design, that may be extended to further non-oxide compounds, even beyond MAX phases.

4.2.6. Supplementary Information

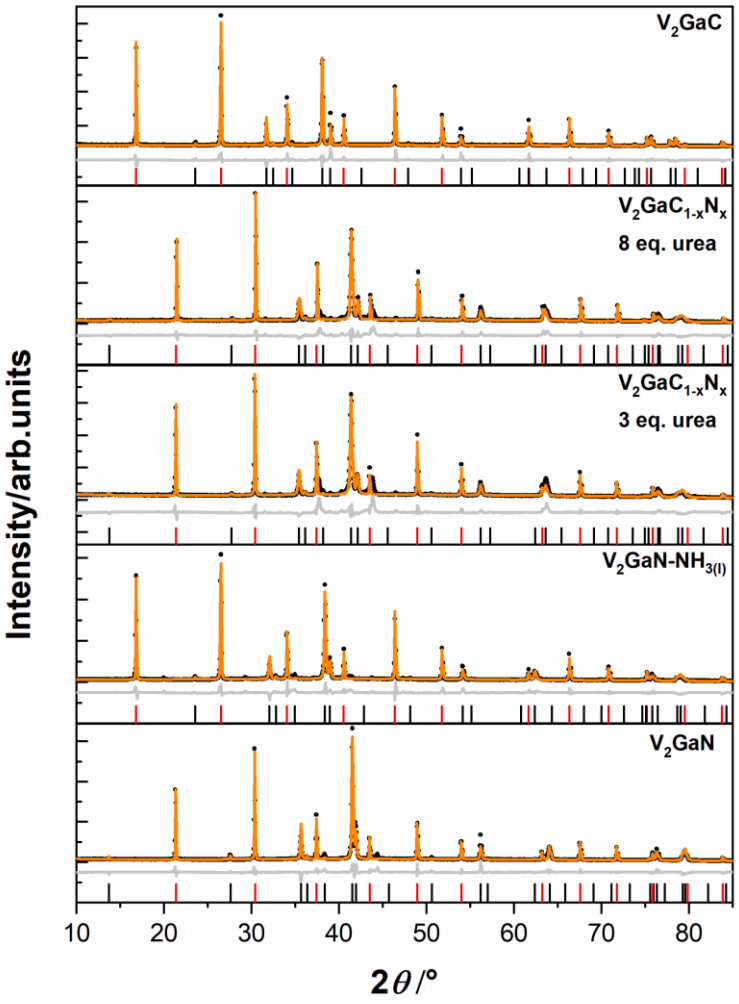

Figure 48: Powder XRD patterns (black) and Rietveld refinements (orange), residuum (grey) of the various MAX phase samples with LaB_6 to increase the accuracy for lattice parameter determination. The refinements were conducted based on the structure models of LaB_6[155] (red) and V_2GaC[117] (black).

Table 34: Results of the Rietveld refinement of V_2GaN with LaB_6 as an internal standard.

Phase name	V_2GaN	LaB_6
Percentage/weight-%	48(4)	52(4)
Spacegroup	*P*6$_3$/*mmc*	*Pm*-3*m*
Lattice parameters *a, c*/ Å	2.905(9) 12.913(8)	4.1568260(8)
Cell volume/ Å^3	94.37(8)	71.827
Background order	5	
R_p	8.97	
R_{wp}	13.36	
R_{exp}	50.21	
GOF	0.27	

Table 35: Results of the Rietveld refinement of V_2GaN-liq. NH_3 with LaB_6 as an internal standard.

Phase name	V_2GaN-$NH_{3(l)}$	LaB_6
Percentage/weight-%	33(4)	67(4)
Spacegroup	*P*6$_3$/*mmc*	*Pm*-3*m*
Lattice parameters *a, c*/ Å	2.912(2) 12.893(2)	4.1568260(8)
Cell volume/ Å^3	94.67(2)	71.827
Background order	5	
R_p	10.13	
R_{wp}	14.40	
R_{exp}	50.62	
GOF	0.28	

Table 36: Results of the Rietveld refinement of $V_2GaC_{1-x}N_x$ (3 eq.urea) with LaB_6 as an internal standard.

Phase name	$V_2GaC_{1-x}N_x$	LaB_6
Percentage/weight-%	57(5)	43(5)
Spacegroup	*P*6$_3$/*mmc*	*Pm*-3*m*
Lattice parameters *a, c*/ Å	2.924(3) 12.863(2)	4.1568260(8)
Cell volume/ Å^3	95.20(2)	71.827
Background order	5	
R_p	10.50	
R_{wp}	16.17	
R_{exp}	54.57	
GOF	0.30	

Table 37: Results of the Rietveld refinement of $V_2GaC_{1-x}N_x$ (8 eq.urea) with LaB_6 as an internal standard

Phase name	$V_2GaC_{1-x}N_x$	LaB_6
Percentage/weight-%	56(3)	44(4)
Spacegroup	*P*6$_3$/*mmc*	*Pm*-3*m*
Lattice parameters *a, c*/ Å	2.929(2) 12.869(2)	4.1568260(8)
Cell volume/ Å^3	95.59(2)	71.827
Background order	5	
R_p	9.82	
R_{wp}	14.68	
R_{exp}	55.49	
GOF	0.26	

Table 38: Results of the Rietveld refinement of V_2GaC with LaB_6 as an internal standard.

Phase name	V_2GaC	LaB_6
Percentage/weight-%	29(3)	71(4)
Spacegroup	*P6₃/mmc*	*Pm-3m*
Lattice parameters *a, c*/ Å	2.939(7) 12.875(6)	4.1568260(8)
Cell volume/ Å^3	96.33(6)	71.827
Background order	5	
R_p	9.26	
R_{wp}	14.28	
R_{exp}	52.44	
GOF	0.27	

Table 39: Summary of the phase fractions extracted from the Rietveld refinements shown in **Figure 36**.

Phase fractions/ weight-%	MAX phase	VN	V_2O_3
V_2GaN(solid-state)	95(7)	5(7)	-
$V_2GaN(NH_{3(l)})$	70(9)	11(6)	19(9)
$V_2GaC_{1-x}N_x$ (3 eq. Urea)	78(9)	22(9)	-

Table 40: Results of the Rietveld refinement of a conventionally prepared $V_2GaC_{0.5}N_{0.5}$ sample annealed at 1100 °C for ten hours.

Phase name	$V_2GaC_{0.5}N_{0.5}$	VN
Percentage/weight-%	36(3)	64(3)
Spacegroup	*P6₃/mmc*	*Fm-3m*
Lattice parameters *a, c*/ Å	2.934(8) 12.862(4)	4.095(2)
Cell volume/ Å^3	95.89(3)	68.65(2)
Background order	15	
R_p	6.77	
R_{wp}	11.02	
R_{exp}	4.69	
GOF	2.35	

Table 41: Summary of the EDX measurements for V_2GaN (solid-state).

Spot	V-At-%	Ga-At-%
1	57.48	42.52
2	59.96	40.04
3	55.05	44.95
4	62.97	37.03
5	67.15	32.85
Average:	60.522	39.478
Deviation:	± 4.23	± 4.23

Table 42: Summary of the EDX measurements for V_2GaN ($NH_{3(l)}$).

Spot	V-At-%	Ga-At-%
1	62.11	37.89
2	59.12	40.88
3	63.11	36.89
4	67.08	32.92
5	64.67	35.33
Average:	63.22	36.78
Deviation:	± 2.65	± 2.65

Table 43: Summary of the EDX measurements for $V_2GaC_{1-x}N_x$ (R = 3).

Spot	V-At-%	Ga-At-%
1	63.62	36.38
2	63.55	36.45
3	66.06	33.94
4	65.61	34.39
5	67.83	32.17
Average:	65.33	34.67
Deviation:	± 1.61	± 1.61

Table 44: Summary of the EDX measurements for $V_2GaC_{1-x}N_x$ (R = 8).

Spot	V-At-%	Ga-At-%
1	64.61	35.39
2	62.11	37.89
3	67.47	32.53
4	63.87	36.13
5	68.00	32.00
Average:	65.21	34.79
Deviation:	±2,22	±2.22

Table 45: Summary of the EDX measurements for V_2GaC.

Spot	V-At-%	Ga-At-%
1	70.90	29.10
2	68.50	31.50
3	66.55	33.45
4	63.28	36.72
5	62.06	37.94
Average:	66.26	33.74
Deviation:	±3.26	±3.26

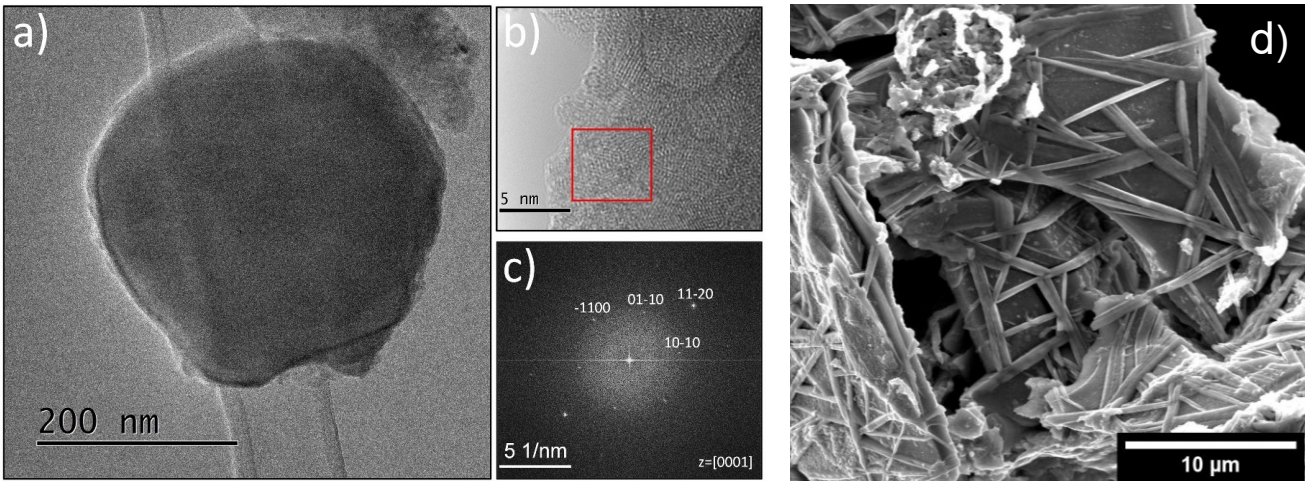

Figure 49: TEM (a) and HRTEM (b) images of V_2GaN-NH_3. Fast Fourier transform of V2GaN-NH3 (c) from the region indicated by the red rectangle in (b). SEM micrograph showing the typical morphology of $V_2GaC_{1-x}N_x$ prepared using 8 eq. urea during the $VC_{1-c}N_x$ precursor synthesis (d).

4.3. Sol-gel assisted synthesis of the carbonitride MAX phase $Cr_2GaC_{1-x}N_x$

4.3.1. Motivation

In order to substantiate and prove the findings of chapter 4.2 whether the introduced sol-gel assisted synthesis approach forms a suitable route to synthesize carbonitride MAX phases, $Cr_2GaC_{1-x}N_x$is chosen as a new hitherto unknown system. Besides the synthesis, the comprehensive investigation of the functional properties in comparison to the parent phases is desirable since the pure nitride exhibits a magnetic transition in form of a spin density wave.

4.3.2. Experimental section

Step 1: $CrC_{1-x}N_x$ synthesis

Following the "urea-glass" method,[156] 6.0 g (22.5 mmol, 1 eq.) of $CrCl_3 \cdot 6H_2O$ (Alfa Aesar, 99 %) were dissolved in ~8 ml ethanol and heated to 50 °C, before 6.8 g (113.2 mmol, 5 eq.) urea (>99 %, Sigma Aldrich) were added. After 30 minutes of stirring, a highly viscous and greenish gel was obtained, which was then transferred into an alumina crucible and annealed inside a horizontal tube furnace (*Carbolite*) at 780 °C (3 °C/min heating rate) for five hours under flowing nitrogen. The product was washed with 3×10 ml of de-ionized (DI) water and stored under atmospheric conditions.

Step 2: MAX phase synthesis

In accordance with the introduced preparation techniques in chapter 4.2, the Cr_2GaC phase was prepared by using exclusively elemental precursors, while nitride and carbonitride precursors, respectively, were used for the synthesis of Cr_2GaN and carbonitride $Cr_2GaC_{1-x}N_x$:

$$2\ Cr + Ga + C \rightarrow Cr_2GaC$$

$$Cr_2N + Ga \rightarrow Cr_2GaN$$

$$CrC_{1-x}N_x + Ga + Cr \rightarrow Cr_2GaC_{1-x}N_x$$

All precursor amounts were based on 0.5 g of the desired MAX phase (**Table 46**). First, gallium flakes (Alfa Aesar, < 99 %) were cut under atmospheric conditions and subsequently transferred into an argon-filled glovebox. Inside the glovebox, the gallium flakes were loosely mixed with the remaining reactants (chromium, 99 %, Sigma-Aldrich; chromium nitride, Alfa Aesar; graphite, <99 %, Alfa Aesar) according to the reaction equations above and pressed into a dense pellet (⌀= 10 mm, 3 t, 5 s). Afterwards, the pellets were transferred into fused silica ampoules and heat treated either in the microwave oven (*CEM Microwave Technology Ltd.*) under flowing argon or vertical tube furnace (*Carbolite*) under vacuum (**Table 47**). Prior to characterization of the samples, the pellets were finely ground using an agate mortar.

Table 46: Weighing amounts of the prepared MAX phase samples. All amounts are calculated based on the nominal compositions of 0.5 g of the target material.

Phase	m(Cr) in g	m(Cr_2N) in g	m($CrC_{1-x}N_x$) in g	m(Ga) in g	m(C) in g
Cr_2GaC	0.2800 (1.0 eq.)	-	-	0.1877 g (1.0 eq.)	0.0291 (0.9 eq.)
Cr_2GaN	-	0.3068	-	0.1857 g (1.0 eq.)	-
$Cr_2GaC_{1-x}N_x$	0.1385 (1.0 eq.)	-	0.1716 (1.0 eq.)	0.1857 (1.0 eq.)	-

Table 47: Temperature programs of the target materials, heat treated either using the microwave oven (watts and minutes) or the vertical tube furnace (temperature and hours).

Nominal composition	Temperature programs
Cr_2GaC	1300 W, 20 min, 7 g carbon
$Cr_2GaC_{1-x}N_x$	800 W, 30 min, 7 g carobn
Cr_2GaN[157]	740 °C, 5 h, 5 K/min

4.3.3. Characterization

X-ray powder diffraction data were obtained using a *Stadi P* (*Stoe & Cie GmbH*) with monochromatized Cu-$K_{\alpha,1}$ radiation (λ = 1.540596 Å) and the *Mythen 1K* (*Dectris*) detector in transmission geometry at room temperature. For measurements, small sample amounts were deposited between X-ray amorphous adhesive film (*Scotch*) on a flat sample holder and rotated orthogonally to the X-ray source. Rietveld refinements were performed using the program *TOPAS* (*Bruker*) and the *FullProf*-suite[158].

Temperature dependent X-ray diffraction was done on a purpose build setup using transmission geometry and Mo-$K\alpha_1$ (λ = 0.7107Å) radiation. The sample was mixed with *NIST SRM 640d* silicon powder and glued on a thermally conductive graphite foil. Temperature was controlled using a closed cycle He-cryofurnace.

Ab initio calculations based on density functional theory (DFT) were performed using the Vienna *ab initio* simulation package (VASP),[159,160] which the projector augmented wave implemented. The generalized gradient approximation (GGA) of Perdew−Burke−Ernzerhof was used as the exchange correlation functional.[161] The wave functions were expanded with a 24 × 24 × 6 Monkhorst-Pack k-sampling grid and cutoff energy of 500 eV. Calculations for different ratios of N and C were performed within the virtual crystal approximation (VCA) model.[162] The precision of total energy convergence for the self-consistent field (SCF) calculations was 10^{-6} eV. All structures were fully optimized until the maximal Hellmann–Feynman force was less than 10^{-3} eV/Å.

SEM images were taken at the *XL30 FEG* (*Philips*) using an acceleration voltage of 20 kV adapted with an *APOLLO X-SDD* detector (*EDAX*) for collecting EDX data. The EDX data was evaluated using the software *EDAX GENESIS*.

Bright-field (BF) high resolution TEM (HRTEM) and scanning TEM (STEM) images were acquired with a *Jeol 2200FS* transmission electron microscope at an acceleration voltage of 200 kV using a 2k × 2k *GATAN UltraScan1000XP CCD* camera. The local chemical composition was determined using EDX in STEM mode with an Oxford windowless 80 mm^2 *SDD X-MaxN 80 TLE* detector with 0.21 sr solid angle. HRTEM data were analyzed using *Gatan Micrograph Suite* and *Oxford's Aztec* software.

SXPS measurements were initially conducted using a laboratory-based *Thermo Scientific K-Alpha* XPS instrument ($h\nu$ = 1486.7 eV), however, at this photon energy the family of Ga LMM Auger peaks (located between kinetic energies of 790-1100 eV) overlaps with the key N 1s and Cr 2*p* core levels. For this reason, synchrotron-based XPS measurements were conducted, where the tunability of the soft X-ray energy enables moving the Auger lines relative to the core levels. Soft and hard X-ray photoelectron spectroscopy (SXPS and HAXPES) measurements were conducted at *beamline I09* (Surface and Interface Structural Analysis) at the *Diamond Light Source*, UK. The overdone decision was made to conduct the SXPS measurements at a photon energy of 1794.3 eV (1.8 keV). This shifts the family of Ga LMM Auger peaks towards higher binding energies, thereby revealing the N 1*s* and Cr 2*p* core levels. This photon energy was achieved by using a 400 lines/mm plane grating monochromator, which provided a total energy resolution of approximately 400 meV (determined by extracting the 16/84% width of a polycrystalline gold foil Fermi edge). HAXPES measurements were conducted at a photon energy of 5926.7 eV (5.9 keV), achieved using a Si(111) double crystal monochromator and a Si(004) post-channel-cut crystal, whilst providing a total energy resolution of approximately 300 meV. The end-station at I09 operates under a base pressure of 3×10^{-10} mbar and is equipped with a *VG Scienta Omicron EW4000* high-voltage electron analyzer with a wide ±28° acceptance angle. Samples were mounted on adhesive conductive carbon tape with the X-ray spot for both beamlines converging on the same sample position. Survey, key core level (Ga $2p_{3/2}$, Cr 2*p*, O 1*s*, N 1*s*, C 1*s*) and valence band (VB) spectra were acquired at both photon energies.

Electronic transport, vibrating sample magnetometry (VSM) and specific heat measurements were studied in *a PPMS DynaCool system* (*Quantum Design*). For VSM, dried powders (20−30 mg) were weighed and put into polymer capsules. Measurements were taken within the field range of ±9 T at variable temperatures ranging from 3 to 400 K. Resistivity measurements were carried out in four-point geometry at a constant current of 10 mA using a custom-made sample holder and the electrical transport option (ETO). Dense pellets were prepared by placing powder samples into a 12 mm diameter cylindrical mold and applying a force of 7.5-9 tons using a manual hydraulic press. Pressed samples with an average thickness of 0.3 mm (Cr_2GaN) and 0.44 mm ($Cr_2GaC_{1-x}N_x$) were carefully cut into a rectangle (5 mm

wide and 10 mm long). Specific heat was measured using the heat capacity option. The $Cr_2GaC_{1-x}N_x$ sample powder (92 mg) was pressed in cylindrical shape with 3 mm diameter by a hydraulic press.

4.3.4. Structural analysis

While the two parent phases Cr_2GaC and Cr_2GaN were synthesized using commercial reactants, the first step of the carbonitride synthesis of $Cr_2GaC_{1-x}N_x$ is based on the sol-gel synthesis of $CrC_{1-x}N_x$ following the "urea glass"-method.[19] As shown in the refined XRD data the precursor material was obtained single phase with an estimated crystallite size < 80 nm (**Figure 50**, **Table 48**).

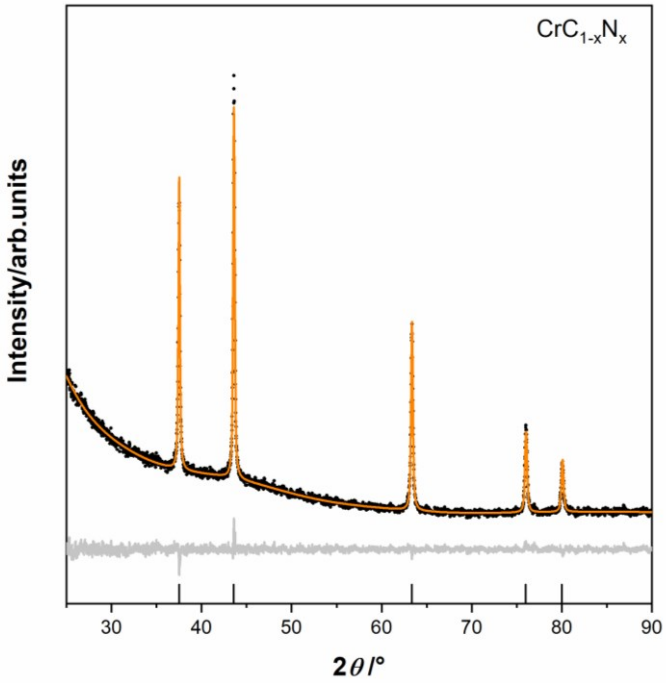

Figure 50: Rietveld refinement (orange line), residuum curve (grey) of the X-ray powder diffraction data of the precursor chromium carbonitride (black) based on the structural model of CrN.[163]

Table 48: Results of the Rietveld refinement of the $CrC_{1-x}N_x$ precursor.

Phase name	$CrC_{1-x}N_x$
Percentage/weight-%	100
Spacegroup	*Fm-3m*
Lattice parameters *a*/ Å	4.1476(9)
Cell volume/ Å^3	71.35(5)
Crystallite size (Lorentz)/nm	71(5)
Background order	15
R_p	2.93
R_{wp}	3.72
R_{exp}	2.97
GOF	1.25

Results of the Rietveld refinements of the XRD data including the extracted lattice parameters of the targeted $Cr_2GaC_{1-x}N_x$ MAX phase samples are shown in **Figure 51** and **Table 49**. The data of the nitride-based MAX phase were fitted to the structural model of Cr_2GaN,[139] while the data of the carbide and carbonitride phase were fitted to the structural model of Cr_2GaC.[123] As shown in **Figure 50**, all samples were obtained nearly single-phase with only small amounts of side phases, such as Cr_3GaN (3.3 wt-% in Cr_2GaN; 0.7 wt% in $Cr_2GaC_{1-x}N_x$), $CrGa_4$ (3.9 wt-% in Cr_2GaN; 1.8 wt-% in Cr_2GaC), and Cr_3Ga (0.3 wt-% in Cr_2GaC). The obtained lattice parameters of both, the carbide Cr_2GaC and nitride Cr_2GaN phase are in good agreement with the values reported in the literature.[123,139] Comparing the *c*-lattice parameter of the carbonitride phase $Cr_2GaC_{1-x}N_x$ with that of the parent compounds, it is closer to that of the carbide than that of the nitride. This can also be visualized in the enlarged 2θ region of the (103) and (006) peaks, where the (006) peak of the nitride phase exhibits a noticeable shift compared to the other two phases. On the other hand, the *a*-lattice parameters of all three phases are too narrowly distributed to point out significant differences.

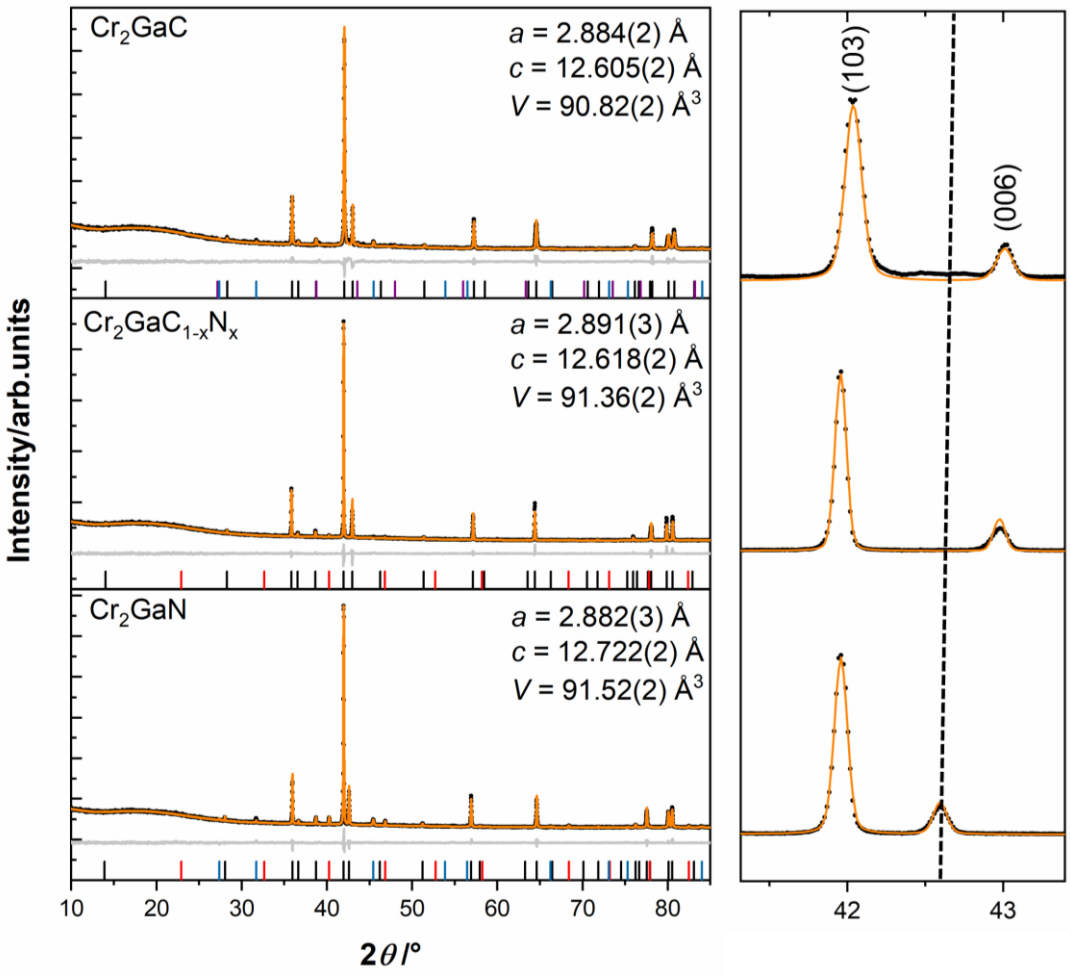

Figure 51: Results of the Rietveld refinements (orange lines) and residuum curves (grey) of the X-ray powder diffraction data (black dots) of Cr_2GaN, Cr_2GaC and $Cr_2GaC_{1-x}N_x$. The refinements were conducted based on structural models of Cr_2GaN[139]/Cr_2GaC[123] (black), Cr_3GaN (red),[164] $CrGa_4$ (blue), [165] Cr_3Ga (purple).[166]

Table 49: Results of the Rietveld refinement of the targeted $Cr_2GaC_{1-x}N_x$ MAX phase samples.

Phase name	Cr_2GaC	$Cr_2GaC_{1-x}N_x$	Cr_2GaN
Spacegroup	$P6_3/mmc$	$P6_3/mmc$	$P6_3/mmc$
Lattice parameters/Å	a = 2.884(2) c = 12.605(2)	a = 2.891(3) c =12.618(2)	a =2.882(3) c =12.722(2)
Cell volume/Å^3	90.82(2)	91.36(2)	91.52(2)
Background order	15	15	15
R_p	3.74	3.15	3.19
R_{wp}	5.73	5.09	4.55
R_{exp}	2.09	1.82	2.04
GOF	2.74	2.80	2.23

Overall, a simple estimation of the carbon/nitrogen amount based on lattice parameter comparison is not feasible and further modeling and investigations by means of XPS or EDX measurements are necessary. This is supported by theoretical calculations (**Table 50**) which reveal that no Vegard behavior is expected when varying the C/N ratio on the *X*-site.

Table 50: Results of the *ab initio* calculation including theoretical lattice constants (*a,c*), the magnetic moment per unit cell and the Fermi energy for $Cr_2GaC_{1-x}N_x$ ($0 \leq x \leq 1$).

$Cr_2GaC_{1-x}N_x$	Lattice constant *a* (Å)	Lattice constant *c* (Å)	Magnetic moment (μB/unit cell)	Fermi energy (eV)
x = 0.0	2.871	12.510	0	7.994
x = 0.1	2.873	12.497	0	7.998
x = 0.2	2.874	12.481	0	8.016
x = 0.3	2.875	12.467	0	8.027
x = 0.4	2.877	12.453	0	8.042
x = 0.5	2.878	12.440	0.001	8.058
x = 0.6	2.881	12.423	0.048	8.060
x = 0.7	2.891	12.394	1.778	8.007
x = 0.8	2.926	12.271	3.653	7.852
x = 0.9	2.928	12.238	3.759	7.851
x = 1.0	2.933	12.196	3.786	7.855

Besides room-temperature X-ray powder diffraction data, temperature-dependent (20-300 K) diffraction data were obtained in order to investigate possible structural anomalies that was initially observed for the nitride phase by TONG *et al.*[118] The latter was attributed to a spin density wave (SDW) transition, shown with an abrupt increase of the *c/a* lattice parameter ratio at 170 K. Thus, temperature-dependent diffraction data can be used as an indicator for an SDW state in the carbonitride phase. Analogous to the room temperature diffraction data, Rietveld refinements were conducted to extract the temperature-dependent lattice parameters of the samples. As shown in **Figure 52 (a)**, the *a*-lattice parameter decreases approximately monotonically for both, the Cr_2GaN and Cr_2GaC phase, whereas the *c*-lattice parameter of the nitride phase shows an anomalous behavior in form of a sharp increase at around 140 K (**Figure 52(b)**). In general, these results are in good agreement with the reported data by TONG *et al.*[118], however, the anomalous *c*-lattice parameter change appears at ~30 K lower temperatures than what was reported previously. For the carbonitride phase $Cr_2GaC_{1-x}N_x$, no anomalous structural change was observed, rather the behavior was similar to the carbide phase Cr_2GaC. Since no anomalous change in the structure is observed, this indicates that the SDW is suppressed in the carbonitride but can be reproduced for the nitride.

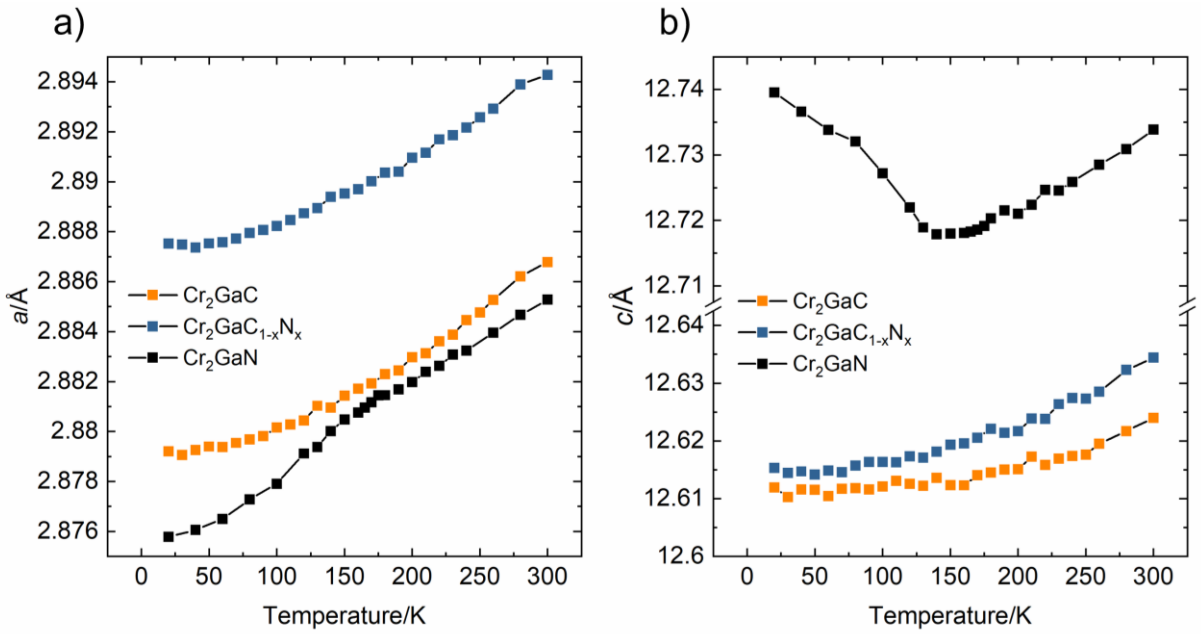

Figure 52: Temperature dependent (20-300 K) lattice parameters of Cr_2GaN, Cr_2GaC and $Cr_2GaC_{1-x}N_x$. a) shows the *T*-dependency of the *a*-lattice parameter, while b) shows the *T*-dependency of the c-lattice parameter.

To further investigate the morphology and composition of the synthesized MAX phases, electron microscopy studies were conducted. However, due to the literature known parent phases, the following data is restricted to the new carbonitride $C_2GaC_{1-x}N_x$. SEM micrographs reveal the morphology of the latter, which can be described as a mixture of typical MAX phase layered structures (**Figure 53(c)**), as well as particles, whose surfaces are covered with smaller drop-like substructures (**Figure 53(a)**), typical

for sol-gel-based syntheses. On the other hand, TEM micrographs show a mixture of elongated and circular particles (**Figure 53(b)**), whereas the corresponding HRTEM micrograph (**Figure 53(d)**) reveals the high crystallinity of the sample which is supported by the FFT shown in the inset of **Figure 53(d)**.

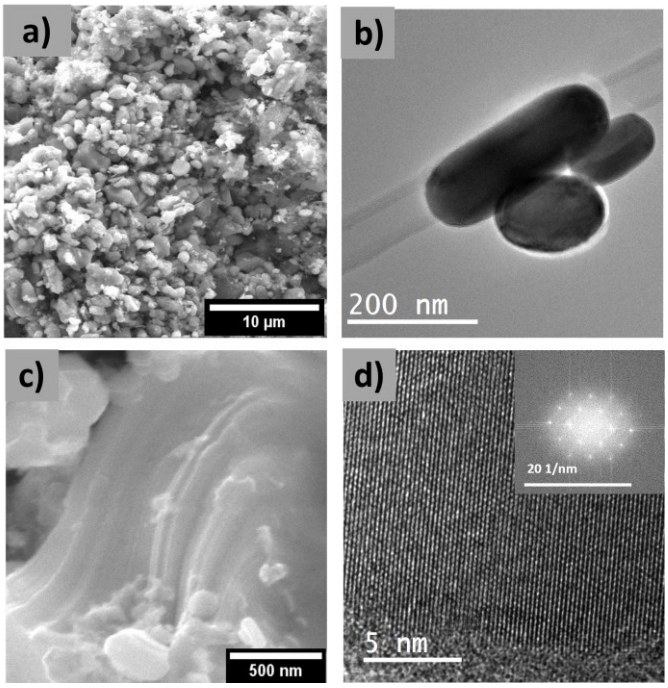

Figure 53: SEM electron micrographs (a,c) showing the morphology of the carbonitride MAX phase, while (HR)TEM micrographs show the particle shape (b) and the well-ordered MAX phase typical structure (d), supported by FFT (d, inset).

STEM-EDX mappings were conducted to estimate the C/N ratio in the MAX phase, since this technique provides a powerful tool to determine local stoichiometries. In **Figure 54**, a representative elemental map particle of the investigated phase is shown. All expected atomic signals of the MAX phase are detected, however, the carbon and nitrogen signals are slightly inhomogeneously distributed. Nonetheless, both elemental signals are present over the whole particle. Averaged over the whole area and calculated related to the nitrogen amount, the elemental ratio of the phase can be quantified as $Cr_{51}Ga_{24}C_{17}N_8$, leading to an estimated overall C/N ratio of ~2:1. The detected oxygen signal can be explained by surface oxidation of the particles originating from the sol-gel-based synthesis procedure and treatment under ambient conditions.

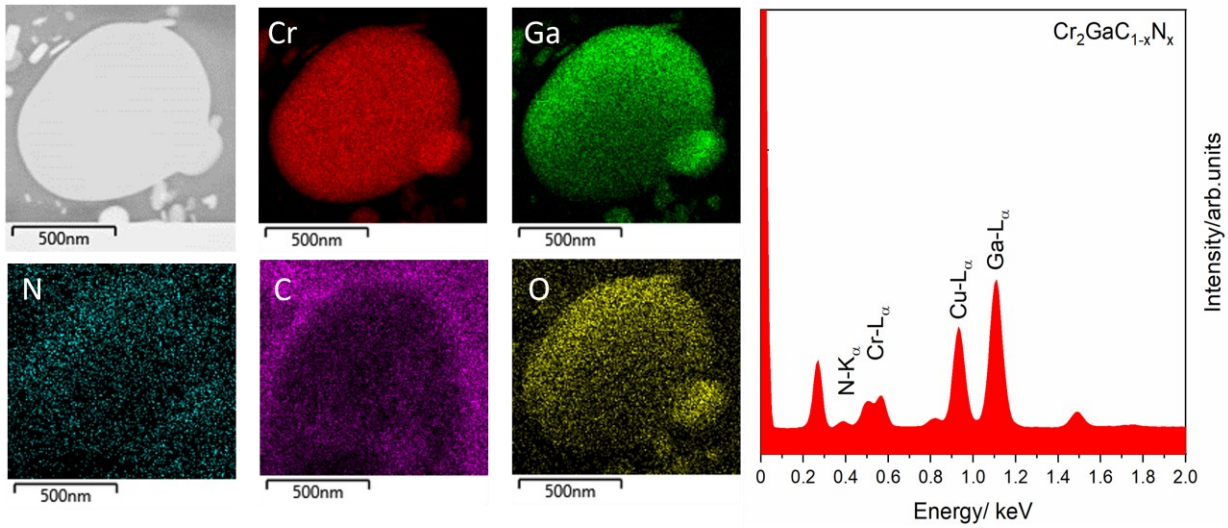

Figure 54: STEM-EDX mappings showing the distribution of the elements in the MAX phase material, including a representative EDX spectrum for determining the C/N ratio.

To complement the previously discussed structural analysis and infer the chemical state of the material, SXPS and HAXPES data on the three samples were collected at beamline I09 at photon energies of 1.8 and 5.9 keV, respectively. Changing the photon energy (*hν*) between the soft and hard X-ray regimes during the measurements allows for control over the probing depth, a strategy exploited in the previous chapter 4.2. The maximum relativistic inelastic mean free path (IMFP) of photoelectrons exiting the Cr_2GaC sample surface can be calculated using the TPP-2M predictive formula implemented in the QUASES software package.[167]

Cr_2GaC does not exist in the QUASES database. Therefore, a new material was created (assuming a bulk density of 7.09 g/cm^3,[168] atomic mass of 185.73 u, 19 valence electrons, and a 0 eV band gap). The maximum rel. IMFP of photoelectrons from Cr_2GaC at a photon energy of 1.8 and 5.9 keV is calculated to be 2.7 and 7.2 nm, respectively, equating to an estimated probing depth of 8.1 and 21.6 nm (assuming 3×IMFP is the probing depth).

The survey spectra collected at both photon energies (**Figure 55**) display strong signals from the expected elements (Ga, Cr, O, C and N). Minor signals from chlorine (≈200 and 270 eV) and sodium (≈1071 eV) are also observed in the spectra of the Cr_2GaN and Cr_2GaC samples, respectively. The SXP spectra show that using a photon energy of 1.8 keV ensured that the Ga LMM Auger peaks did not overlap with the key core levels, which is possible as the Auger transition is a function of kinetic energy, and therefore its binding energy (BE) position can be moved by changing the photon energy. **Figure 56** displays the Ga 2$p_{3/2}$, Cr 2*p*, N 1*s*, and C 1*s* core level spectra as a function of photon energy. The O 1*s* and valence band spectra collected with SXPS and HAXPES can be found in **Figure 57**.

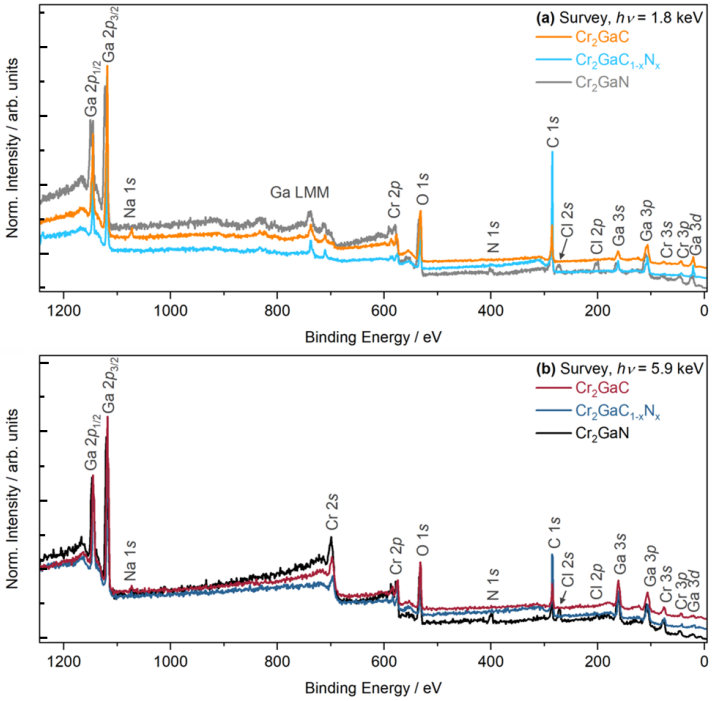

Figure 55: Survey spectra collected for the three carbonitride MAX phase samples with synchrotron-based (a) SXPS ($h\nu$ = 1.8 keV) and (b) HAXPES ($h\nu$ = 5.9 keV). The spectra are normalized to the maximum height of the Ga $2p_{3/2}$ peak and are offset vertically for clarity.

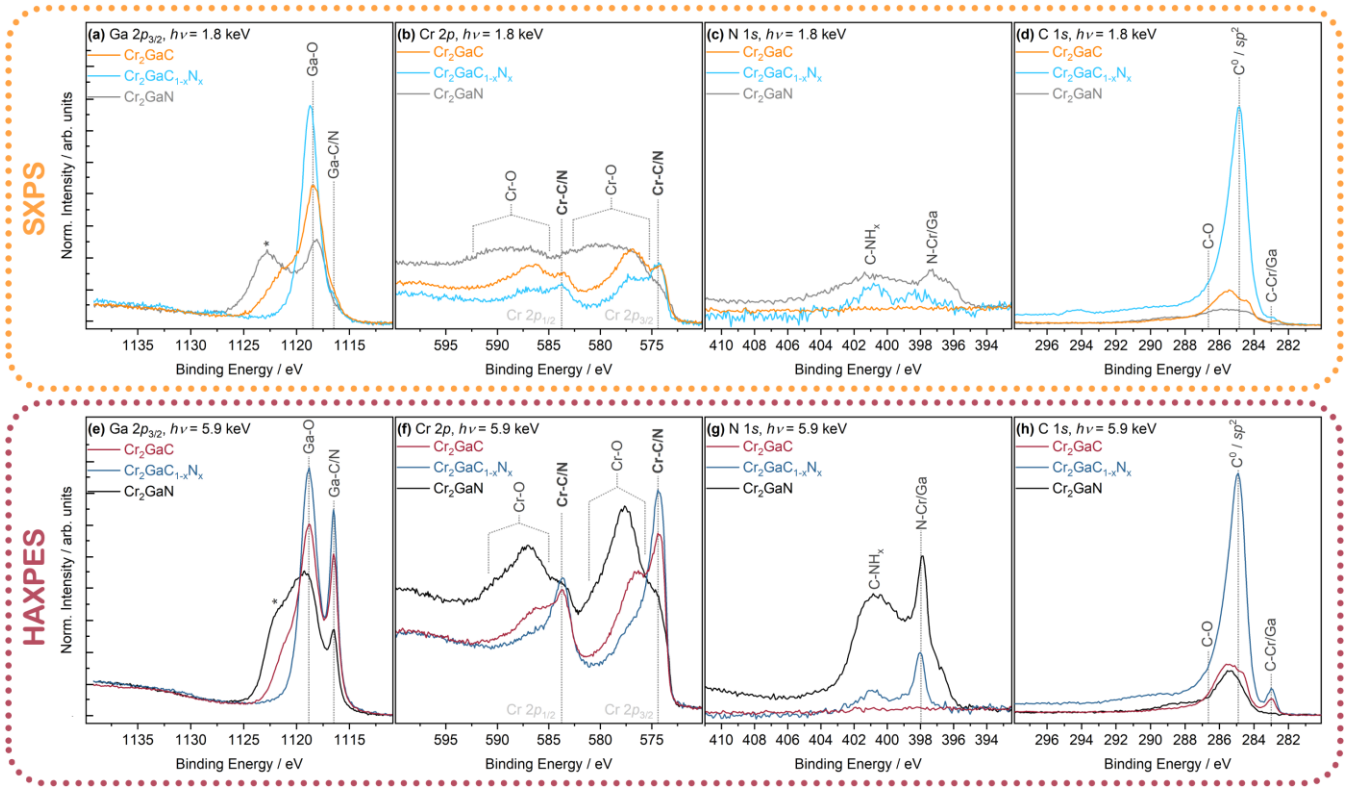

Figure 56: Labelled SXPS ($h\nu$ = 1.8 keV) and HAXPES ($h\nu$ = 5.9 keV) core level spectra of the carbonitride samples, including (a/e) Ga $2p_{3/2}$, (b/f) Cr 2*p*, (c/g) N 1*s*, and (d/h) C 1*s*. The top row (a-d) contains the spectra collected with SXPS, and the bottom row (e-h) contains the equivalent spectra collected with HAXPES. The spectra are normalized to the total spectral Ga $2p_{3/2}$ area, and the *y*-axis is set so that each spectrum has a similar signal-to-noise ratio.

The collected valence band spectra **(Figure 57**) show that for all samples a distinct Fermi edge is observed, with it being more distinct when measured with HAXPES, indicating metallic character. The presence of a Fermi edge enables the binding energy (BE) scale of all core level spectra to be referenced to the intrinsic Fermi energy (E_F) of the respective samples.

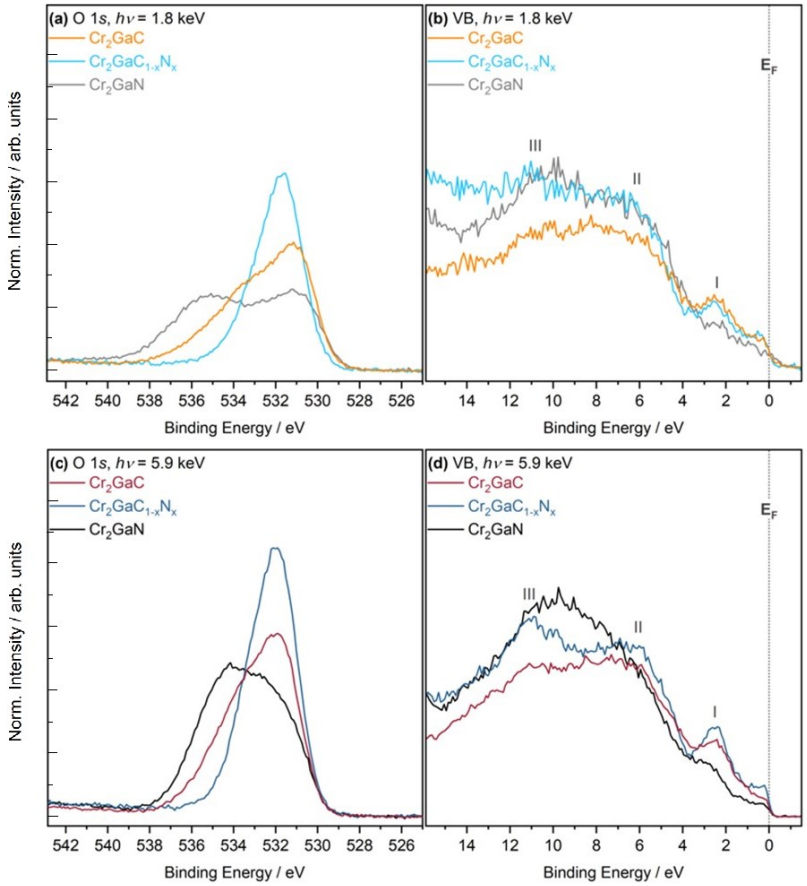

Figure 57: Additional SXPS ($h\nu$ = 1.8 keV) and HAXPES ($h\nu$ = 5.9 keV) spectra collected for the three carbonitride MAX phase samples including the (a/c) O 1*s* and (b/d) valence band (VB) spectra. The spectra are normalized to the total spectral area of the Ga $2p_{3/2}$ core level and the binding energy scale is calibrated to the intrinsic Fermi energy (E_F) of the sample.

Due to the nature of the samples and the lack of charge compensation mechanisms at the synchrotron, partial charging occurred during the measurements, leading to different levels of distortion on the higher BE side of the spectra. This was also experienced in the V-Ga-C-N system (chapter 4.2). Nevertheless, the spectra still provide valuable insight into the chemical states of the samples. The Ga $2p_{3/2}$ spectra displayed in **Figure 56** show that when measured with SXPS, a main intensity peak at 1118.6 eV is observed, commensurate with an oxygen-terminated gallium (Ga-O) chemical environment. This peak is the most intense for the mixed carbonitride phase. A subtle asymmetry is also observed on the lower BE side of this peak when measured with soft X-rays, which is attributed to the Ga-C/N environment (chapter 4.2). **Figure 56 (e)** shows that with increasing photon energy (and therefore increasing probing depth), the intensity of this Ga-C/N environment (BE = 1116.5 eV) significantly increases relative to the Ga-O peak intensity. This suggests that the surface of these samples is oxidized, whereas the bulk is

carbonitride-richer. An additional peak and/or broadening is observed on the higher BE side of the Ga-O peak with both soft and hard X-rays (labelled with an asterisk, *). The assignment of this spectral feature is difficult to confirm owing to the partial charging of the spectra and, therefore, will not be discussed further. Similar charging effects are found in the other core level spectra. Additionally, the XRD data show small amounts of side phases and the resulting chemical environments will contribute to the core level spectra. The Cr 2*p* spectra displayed in **Figure 56 (b)** and **(f)** display similar attributes to the Ga $2p_{3/2}$ core level in that a low BE peak at 574.3 eV (Cr $2p_{3/2}$) is observed, and its signal intensity is enhanced with HAXPES. This peak is attributed to the primary Cr-C/N environment,[169,170] and given the depth sensitivity of this peak, it again suggests that the carbonitride is situated toward the bulk of the sample. The higher BE features observed in the Cr 2*p* spectra are associated with an oxygen-terminated Cr environment (Cr-O)[169,170] As for the Ga $2p_{3/2}$ core level, the side phases observed in XRD will also contribute to the Cr 2*p* spectra.

The N 1*s* and C 1*s* spectra displayed in **Figure 56 (c)** and **(g)**, and **(d)** and **(h)**, respectively, provide direct confirmation that the desired carbonitride phase was obtained. The lower BE peak at 283 eV in the C 1*s* spectra is commensurate with a metal-carbide environment (C-Cr/Ga) (chapter 4.2),[171] and is only observed in the Cr_2GaC and $Cr_2GaC_{1-x}N_x$ samples. In the N 1*s* spectra, the lower BE peak at 398.0 eV is commensurate with a metal-nitride environment (N-Cr/Ga) (chapter 4.2),[172], and is only observed in the expected sample. In both the C/N 1*s* spectra, the carbonitride environments are more easily observed with HAXPES, which indicates that the bulk of these samples is carbonitride-rich, whereas the surface is oxidized. Furthermore, in both the N and C 1*s* spectra the intensity of metal carbide/nitride peaks increase with respect to the total Ga $2p_{3/2}$ in the expected trend. Higher BE features are also observed in both C/N 1*s* spectra, with the C 1*s* spectra dominated by graphitic sp^2 carbon, adventitious carbon (C^0) and carbon-oxygen species, whereas in the N 1*s* spectra a broader peak is observed at +2.8 eV from the N-Ga/Cr and is most likely attributed to organic nitrogen species (e.g., C-NH_x).[173] Lastly, it is noted that with respect to the total Ga $2p_{3/2}$ peak intensity, the mixed carbonitride sample has the most intense C 1*s* signal, in both soft and hard XP spectra. **Figure 56** (**d**,**h**) show that the total normalized C 1*s* signal intensity of the mixed carbonitride sample is roughly three times that of the signal measured on the nitride and carbide samples. The reason for the dominant C signal in the carbonitride sample can be related to the synthesis procedure. A sol-gel synthesis approach was employed, using urea as a gelling agent. During the heat treatment step, urea will be converted into amorphous carbon that is also retained in the product phase. The SEM images verifies that free amorphous carbon particles are indeed present at the surface and throughout the sample (**Figure 53**). This also explains why the dominant peak within the C 1*s* spectra for the mixed carbonitride sample displays an asymmetric profile, commensurate with a graphitic sp^2-like environment.[170]

4.3.5. Magnetic analysis

In order to further investigate the influence of the carbon amount on the materials properties of the MAX phases, magnetic measurements were conducted. **Figure 58** shows the temperature-dependent magnetization curves of all three materials in a small field of $B = 10$ mT and a temperature range of 3-400 K.

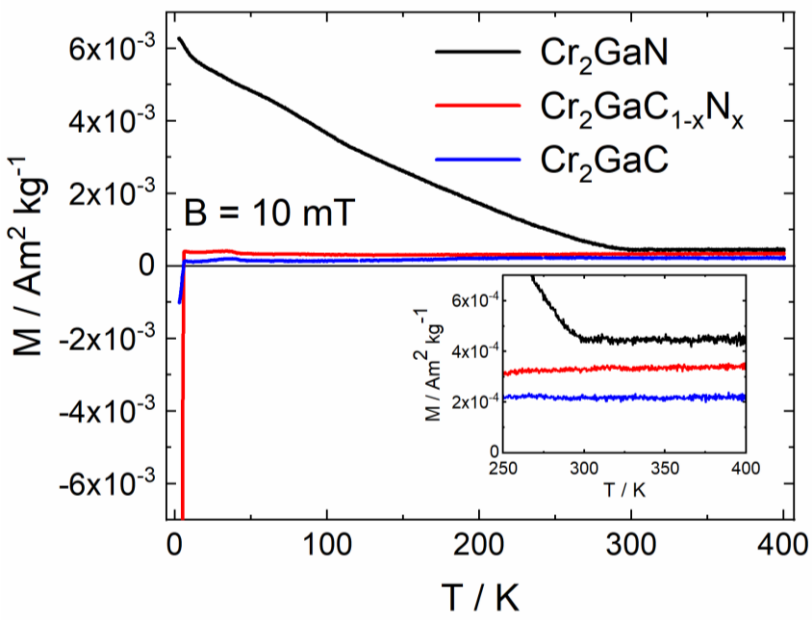

Figure 58: Temperature-dependent magnetization curves of Cr_2GaC, $Cr_2GaC_{1-x}N_x$, and Cr_2GaN in a field of B = 10 mT and a temperature range of 3-400 K.

Practically over the whole temperature range, both carbon-containing phases showing an almost temperature-independent behavior, indicating Pauli paramagnetism, as discussed in chapter 3.2. However, it must be noted that the magnetic state of the carbonitride $Cr_2GaC_{1-x}N_x$ switches to diamagnetic response at around 7 K, pointing towards superconducting characteristics. In contrast, the pure nitride phase Cr_2GaN exhibits a strong temperature dependent magnetization in the temperature range of 3-300 K, since the magnetization values varying of more than one order of magnitude, which can be attributed to the SDW state in the system.[119] At 300 K however, this changes towards Pauli paramagnetism, analogous to Cr_2GaC and $Cr_2GaC_{1-x}N_x$.

Figure 59 (a) shows the isothermal field-dependent magnetization curves of the new carbonitride phase $Cr_2GaC_{1-x}N_x$. From 20-300 K, all curves are strictly linear at high fields and the absolute magnetization at 300 K at 9 T (0.30 Am^2kg^{-1}) only differs by ~15 % from the absolute magnetization at 3 K (0.35 Am^2kg^{-1}), which confirms the Pauli paramagnetic behavior as discussed above. Also confirming the temperature-dependent measurements (**Figure 58**), the hysteresis curves exhibit at 3 K and 5 K a superconducting response as shown in the inset of **Figure 59 (a)**. Besides, both curves show a slight

non-linearity that can be explained by small amounts of paramagnetic impurities which are not visible in the XRD data.

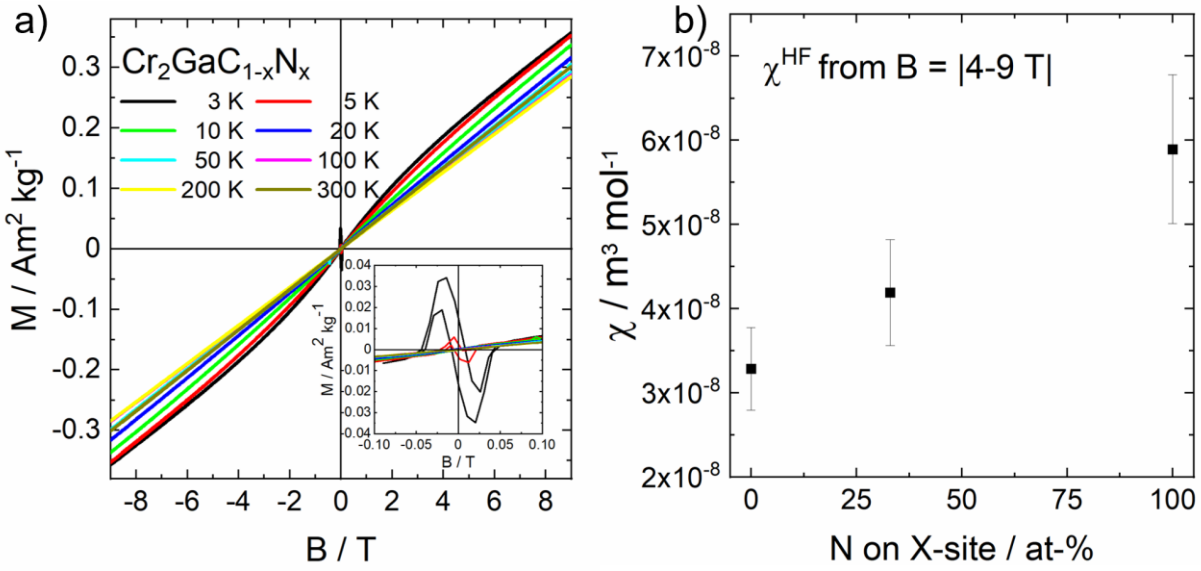

Figure 59: a) Field-dependent magnetization of $Cr_2GaC_{1-x}N_x$ at various temperatures between 3-300 K. b) Magnetic susceptibility from the field-dependent magnetization data of Cr_2GaC, $Cr_2GaC_{1-x}N_x$, and Cr_2GaN at 300 K. The susceptibility is extracted from linear fitting of the signal in the interval $|B|$ = 4-9 T. The nitrogen amount is based on the EDX measurements presented in **Figure 54**.

Figure 59 (b) showing the magnetic susceptibility values extracted from the linear fitting of the field-dependent magnetization curves at 300 K in the interval of $|B| = 4\text{-}9$ T. Supporting the temperature-dependent magnetization data in **Figure 58**, the susceptibility significantly increases by increasing the nitrogen amount on the *X*-site of the MAX phase by the factor of almost two from carbide to nitride. Based on the determined nitrogen amount of the carbonitride phase (**Figure 53**) earlier this chapter, these results suggests a linear correlation of the susceptibility and the amount of nitrogen in the MAX phase. In order to further evaluate the possible superconducting behavior of the carbonitride phase below 7 K, specific heat, as well as transport measurements were conducted. While the latter should show a zero net resistivity at the critical temperature T_c, the specific heat should show an abrupt change at T_c.[174] As shown in **Figure 60**, no anomalous behavior of the specific heat in the low temperature range can be observed, which disproves the possibility of a new carbonitride bulk superconductor. Nonetheless, the low-temperature specific heat can be used to calculate the density of states at the Fermi level ($D(E_F)$ if plottet as C_pT^{-1} against T^2 (**Figure 60** inset) leading to a linear correlation expressed by the following equation (1):[118,175]

$$\frac{C_p}{T} = \gamma + \beta \cdot T^2 \qquad (1)$$

β is the phonon specific heat coefficient (2):[176]

$$\beta = n \cdot \left(\frac{12\pi^4}{5}\right) \cdot N_A \cdot k_B \cdot \theta_D^{-3} \quad (2)$$

β = phonon specific heat coefficient
N = number of electrons
N_A = Avogadro constant
k_B = Boltzmann constant
θ_D = Debye temperature

While γ is the so-called Sommerfeld constant, which is directly connected to $D(E_F)$ in metallic MAX phase systems (3):[176,177]

$$\gamma = \frac{1}{3} \cdot \pi^2 \cdot k_B^2 \cdot D(E_F) \quad (3)$$

γ = Sommerfeld constant
k_B = Boltzmann constant
$D(E_F)$ = density of states at the Fermi level

By performing a linear regression of the specific heat data,[118] where β represents the slope of the function while γ is the y intercept, $D(E_F)$ of the carbonitride is 10.23 eV $^{-1}$, which is around 20 % higher than the calculated value for a nitrogen amount of 30 % presented in **Table 50**. The deviation can be most likely explained by the presence of the amorphous carbon in the material system, influencing the Debye temperature θ_D.

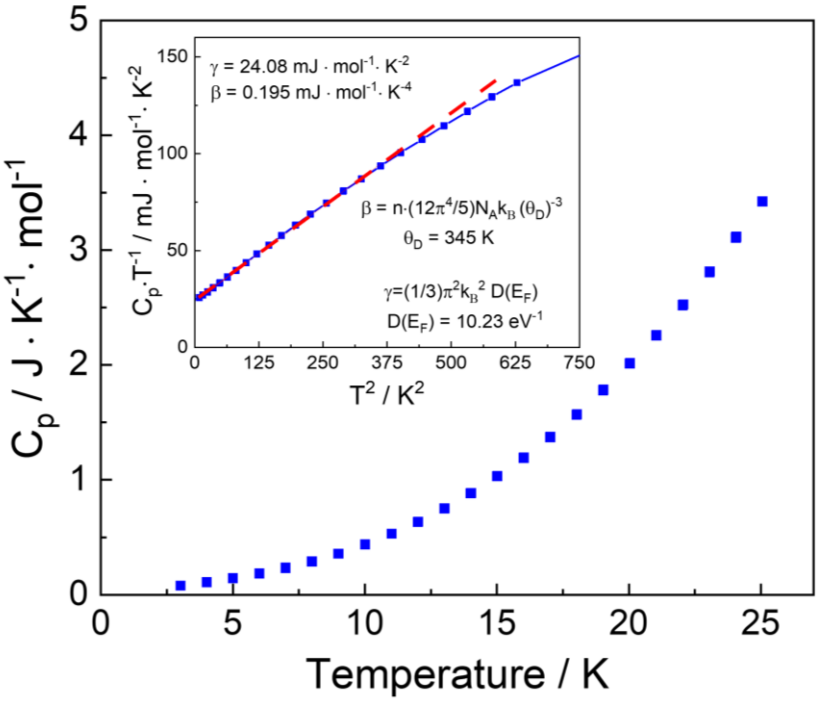

Figure 60: Low-temperature specific heat measurements including the inset of C_pT^{-1} plotted against T^2.

Analogous to the specific heat measurements, transport measurements do not show any superconducting behavior of the carbonitride phase at the proposed critical temperature T_C of 7 K derived from the magnetic measurements. Only the typical metallic behavior for MAX phases is observed since the resistivity steadily decreases upon cooling with a remaining resistivity of 29 $\mu\Omega$m at 4 K. On the other hand, the pure nitride phase exhibits the literature reported anomalous behavior which can be assigned to the spin-density wave transition, however with 117 K, again at lower temperatures.[119] By applying a magnetic field of $B = 1$ T, the transport properties of the nitride phase are slightly influenced resulting in a small difference of the residual resisitivity RRR (ρ (300 K)/ρ(4 K)) of $\sim$ 3 %. In general, the lower RRR values compared to literature values,[118] can be explained due to differences in the pellet preparation process.

Overall the absence of bulk superconducting properties in both, transport and specific heat measurements, can be assigned to small amounts of side phases (e.g., Ga-N compounds[178]) which could not be identified in the XRD data.

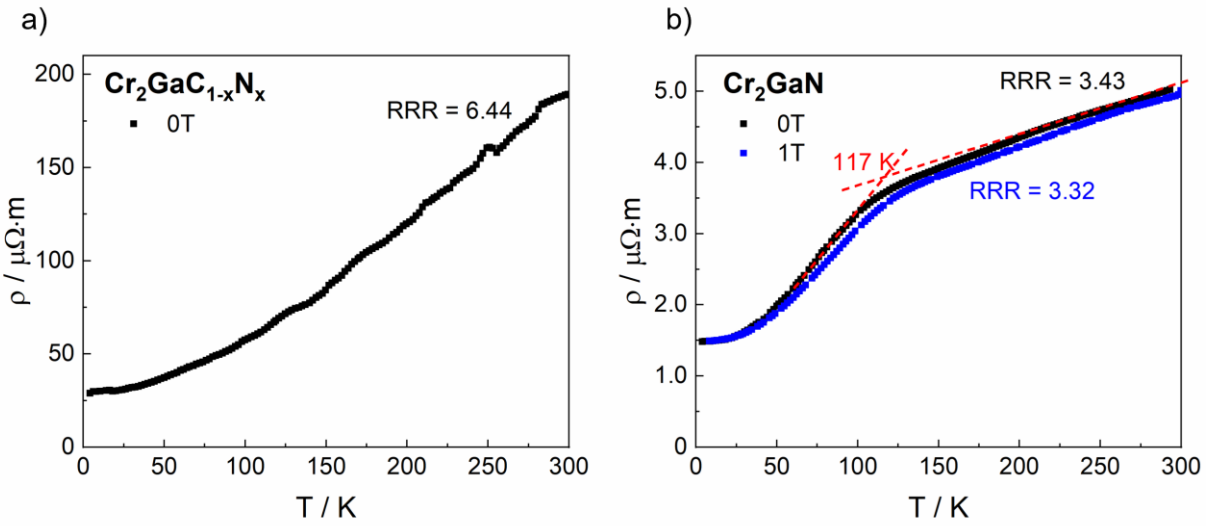

Figure 61: Temperature dependence of the electrical resistivity of the carbonitride $Cr_2GaC_{1-x}N_x$ in zero magnetic field (a) and the nitride Cr_2GaN (b) which was measured at both, zero magnetic field and a field of B = 1 T.

4.3.6. Conclusion

In this chapter, the synthesis and characterization of Cr_2GaN, Cr_2GaC, and the hitherto unknown carbonitride $Cr_2GaC_{1-x}N_x$ phase were performed. The latter was synthesized applying the sol-gel assisted urea-glass method (chapter 4.2), however, by drastically reducing the reaction time of the final MAX phase formation due to microwave heating. The carbonitride character was confirmed by means of X-ray powder diffraction data, HAXPES measurements, as well as STEM-EDX measurements, which also provide a carbon/nitrogen ratio of 2:1, resulting in a sum formula of $Cr_2GaC_{0.67}N_{0.33}$. Temperature-dependent XRD measurements confirm the literature-reported anomalies in the lattice parameter evolution of the pure nitride Cr_2GaN, that are referred to a spin density wave state (SDW) in the system. On the other hand, the carbonitride and carbide did not show any anomalies, leading to a suppression of the SDW state by the incorporation of carbon into the MAX phase lattice. In order to further analyze the functional properties of the materials, magnetic-, heat capacity-, as well as resistivity measurements were performed. Magnetic analysis revealed Pauli paramagnetic behavior of the carbide-based phases, while the pure nitride exhibits a strong temperature-dependent magnetization due to the SDW at $T < 300$ K. Furthermore, the susceptibility of the materials is dependent on the nitrogen amount on the *X*-site of the MAX phase and is increasing by increasing the latter. Field-dependent magnetization data suggested a superconducting behavior of the carbonitride below $T = 7$ K, which was disproved by heat capacity and transport measurements. Overall, this study substantiates the new sol-gel-assisted method (chapter 4.2) as a valuable option to synthesize new carbonitride MAX phases exhibiting materials properties deviating from their parent phases, which simultaneously provides a new option for targeted materials design of MAX phases and beyond.

4.4. Synthesis of the *X*-site solid-solution MAX phase $V_2GeC_{1-x}N_x$ ($0 \leq x \leq 1$)

4.4.1. Motivation

The previous two chapters 4.2 and 4.3 dealt with the development of a new a wet-chemical assisted synthesis approach where it is challenging to accurately adjust the precise carbon amount in the MAX phase. This leads to the exploration of a new hybrid solid-state approach, where a microwave-assisted nitride precursor synthesis can be applied. Vanadium again forms the *M*-element, however with a change on the *A*-site, switching to germanium which leads to the hitherto unknown carbonitride $V_2GeC_{1-x}N_x$. While several studies of the parent carbide phase exist, [55,177,179,180] no profound characterization data of V_2GeN have been reported, yet. Therefore, this study additionally aims to investigate the functional properties of the materials and to evaluate the influence of the adjusted carbon amount in the MAX phase structure.

4.4.2. Experimental section

Step 1: VN precursor synthesis

In order to prevent oxygen impurities during the weighing process, the following steps were performed inside an Ar-filled glovebox. According to VAIDHYANATHAN *et al.*[181], 1 g (15.4 mmol) vanadium powder (Alfa Aesar, ~325 mesh, 99.5 %) and 1 g (18.7 mmol) NH_4Cl (technical) were finely ground using an agate mortar. Afterwards, the reactant powder was pressed into a dense pellet (⌀= 10 mm, 5 t, 30 s) and transferred into a fused silica ampoule, equipped with a custom-made vacuum adapter. Subsequently, the sample was transferred into the microwave oven (*CEM, MARS6*) and flushed for 10 minutes with flowing nitrogen before commencing the heat treatment (800 W, 30 min, 7 g carbon as susceptor material) under continuous nitrogen flow. Prior to characterization, the pellets were finely ground and stored under atmospheric conditions.

Step 2: MAX phase synthesis

The V_2GeC phase was prepared by using exclusively elemental precursors, while VN (step 1) was used for the synthesis of V_2GeN and the carbonitride $V_2GeC_{1-x}N_x$, according to the following reaction equations:

$$2\ V + Ge + C \rightarrow V_2GeC$$

$$2\text{-}x\ V + x\ VN + 1\ Ge + 1\text{-}x\ C \rightarrow V_2GeC_{1-x}N_x$$

$$1V + 1\ VN + 1\ Ge \rightarrow V_2GeN$$

All precursor amounts were based on producing two pellets of 0.5 g each of the desired MAX phase. A detailed summary can be found in **Table 51**. Inside the glovebox, germanium (99.999 %,

Thermoscientific) was mixed with the remaining reactants vanadium (Alfa Aesar, ~325 mesh, 99.5 %), vanadium nitride (step 1), and graphite (Alfa Aesar >99.9 %, APS 2-15 μm) according to the aforementioned reactions and pressed into a dense pellet (⌀= 10 mm, 5 t, 30 s). Afterwards, the pellets were transferred into fused silica ampoules and heat treated in a chamber furnace (*Snoltherm*) following a defined temperature program (**Table 52**). Prior to characterization of the samples by means of XRD SEM, and HAXPES, the pellets were finely ground using an agate mortar.

Table 51: Weighing amounts of the prepared MAX phase samples. All amounts are calculated based on the nominal compositions of 0.5 g of the target material.

Nominal composition	*m*(V) in g	*m*(VN) in g	*m*(Ge) in g	*m*(C) in g
V_2GeC	0.2731 (2.00 eq.)	-	0.1947 (1.00 eq.)	0.0322 (1.00 eq.)
$V_2GeC_{0.75}N_{0.25}$	0.2380 (1.75 eq.)	0.0434 (0.25 eq.)	0.1941 (1.00 eq.)	0.0241 (0.75 eq.)
$V_2GeC_{0.50}N_{0.50}$	0.2040 (1.50 eq.)	0.0867 (0.50 eq.)	0.1936 (1.00 eq.)	0.0160 (0.50 eq.)
$V_2GeC_{0.25}N_{0.75}$	0.1693 (1.25 eq.)	0.1295 (0.75 eq.)	0.1931 (1.00 eq.)	0.0080 (0.25 eq.)
V_2GeN	0.1351 (1.00 eq.)	0.1723 (1.00 eq.)	0.1926 (1.00 eq.)	-

Table 52: Summary of the temperature programs for the synthesis of the target materials.

Nominal composition	Temperature programs
V_2GeC	1000 °C, 10 h, 10 K/min
$V_2GeC_{0.25}N_{0.75}$	1000 °C, 10 h, 10 K/min
$V_2GeC_{0.50}N_{0.50}$	1000 °C, 30 h, 10 K/min
$V_2GeC_{0.25}N_{0.75}$	1000 °C, 30 h, 10 K/min
V_2GeN	1000 °C, 30 h, 10 K/min

Step 3: Densification by Spark Plasma Sintering

For further characterization of V_2GeC, $V_2GeC_{0.5}N_{0.5}$, and V_2GeN, 0.85 g of the sample material were densified using spark plasma sintering (*Dr. SinterLab SPS-211Lx, Fuji*). Here, the powders were transferred into a graphite die (⌀= 10 mm), equipped with two graphite stamps and graphite foil to separate the powder from the die wall and stamps (chapter 2.2.2). During the pressing process, the initial pressure was set to 30 MPa at room temperature, before the temperature was increased to 600 °C. Subsequently, the pressure was set to 100 MPa before the temperature was further increased to 1000 °C, which was held for 15 minutes. The samples were cooled to room temperature, before the pressure was released. Remaining graphite residues were removed by polishing the pellets on a diamond plate.

4.4.3. Characterization

XRD data were obtained using a *Stadi P* (*Stoe & Cie GmbH*) with monochromatized Cu-$K_{\alpha,1}$ radiation ($\lambda = 1.540596$ Å) and the *Mythen 1K* (*Dectris*) detector in transmission geometry at room temperature. For measurements, small sample amounts were deposited between X-ray amorphous adhesive film (Scotch) on a flat sample holder and rotated orthogonally to the X-ray source.

Rietveld refinements were performed using the program *TOPAS* (*Bruker*). First, the side phase amounts in weight-% were determined based on the structural model of V_2GeC,[182] before a detailed refinement of the lattice parameters was conducted based on the Le Bail method.

SEM images were taken at the *XL30 FEG* (*Philips*) using an acceleration voltage of 25 kV adapted with an *APOLLO X-SDD* detector (EDAX) for collecting energy dispersive X-ray spectroscopy (EDX) data. The EDX data was evaluated using the software *EDAX GENESIS*.

Hard X-ray photoelectron spectroscopy (HAXPES) was used to characterize the chemical environments and oxidation states of the samples. Data were collected at beamline *P22* at *PETRAIII*, German Electron Synchrotron DESY in Hamburg, Germany.[145] A photon energy of 6 keV was used for all experiments, with the energy selected using a Si (111) double-crystal monochromator. A *Phoibos 225HV* analyzer (*SPECS*, Berlin, Germany) was used with the small area lens mode and a slit size of 3 mm. Spectra were collected at room temperature using a pass energy of 30 eV. The total energy resolution in this setup was determined to be 245 meV 16/84% Fermi edge (E_F) width of a polycrystalline gold foil. Samples were mounted using conducting carbon tape.

Magnetic measurements were performed with a magnetic property measurement system *MPMS-3* (*Quantum Design*). Isofield measurements were carried out with a continuous heating and cooling rate of 2 K·min^{-1}. Isothermal measurements were performed by stabilizing the magnetic field at each measurement point. To avoid non-linearities in the magnetization signal at low magnetic fields, the magnetic susceptibility χ was calculated from the difference of the isofield magnetization curves measured in magnetic fields of 5 and 7 T, such that $\chi(T) = (M(T)_{7T} - M(T)_{5T})/2T$. Complementary, the susceptibility was determined from the linear regression of the isothermal magnetization curves in the field range from 5 to 7 T. In addition, the temperature-dependence of the susceptibility in alternating magnetic fields χ_{AC} was measured by stabilizing the temperature at each measurement point, using an alternating field of 0.001 T with a frequency of 10 s^{-1}.

The electrical resistivity was measured with a two-electrode setup implemented in a physical property measurement system *PPMS-14T* (*Quantum Design*). A detailed description of the measurement setup can be found elsewhere.[183]

4.4.4. Structural analysis

Starting from the elemental precursors to synthesize the carbide phase V_2GeC, the amount of nitrogen was nominally increased (25 at-% each) by adding vanadium nitride according to the chemical equations shown above. The highly crystalline VN precursor material was obtained single phase (**Figure 62(a)**) and the extracted lattice parameters fit well to those reported in literature (**Table 53**).[146] Furthermore, SEM micrographs (**Figure 62(b)**) reveal a highly porous morphology due to the continuous nitrogen flow during the synthesis.

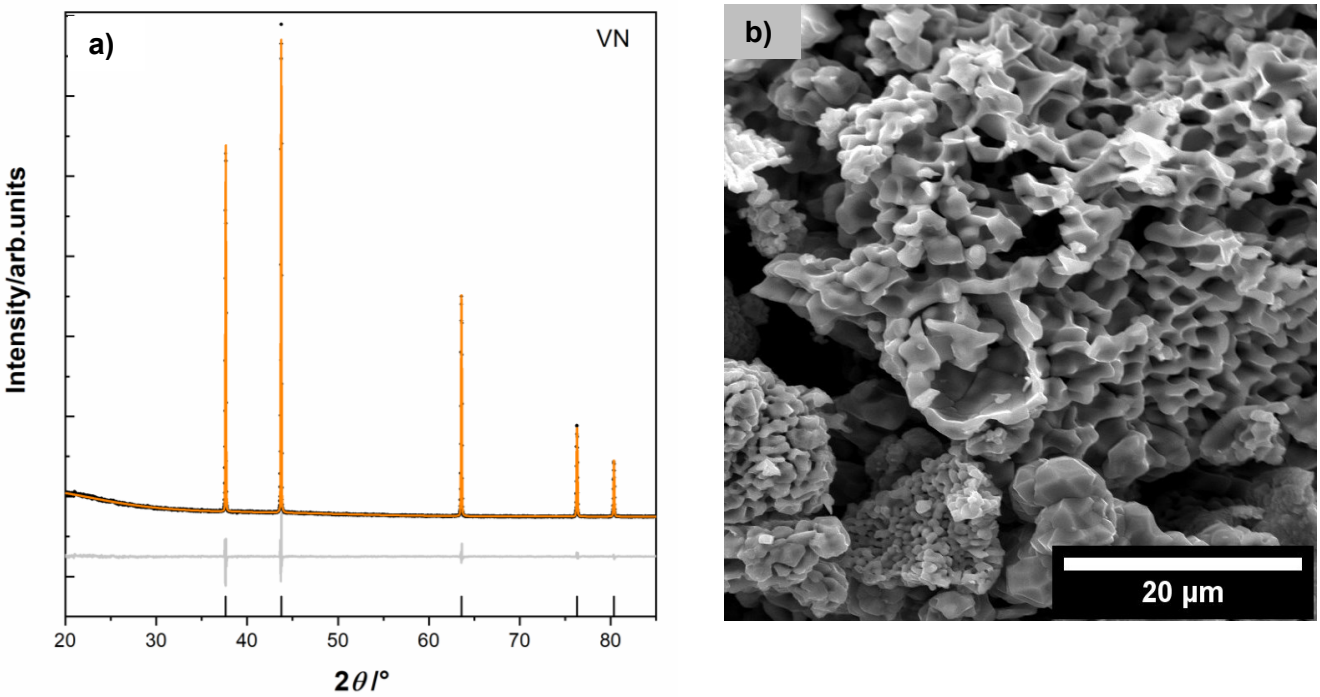

Figure 62: a) Rietveld refinement (orange line), residuum curve (grey) of the X-ray powder diffraction data of the precursor vanadium nitride (black) based on the structural model of VN.[146] b) SEM micrograph, showing the morphology of the precursor.

Table 53: Results of the Rietveld refinement of the VN precursor.

Phase name	VN
Percentage/weight-%	100
Spacegroup	*Fm-3m*
Lattice parameters *a*/ Å	4.1357(2)
Cell volume/ Å^3	70.74(1)
Background order	10
R_p	3.79
R_{wp}	5.52
R_{exp}	2.78
GOF	1.99

The XRD data of the full set of solid-solution phases in the system $V_2GeC_{1-x}N_x$ ($0 \leq x \leq 1$) are shown in **Figure 63**. All samples are obtained nearly single phase. In the following, a more detailed analysis performing Rietveld refinements (**Figure 64**) is conducted with the compositions of the two parent phases V_2GeC and V_2GeN, as well as the solid solution phase with a nominal doping amount of $x = 0.50$, $V_2GeC_{0.5}N_{0.5}$.

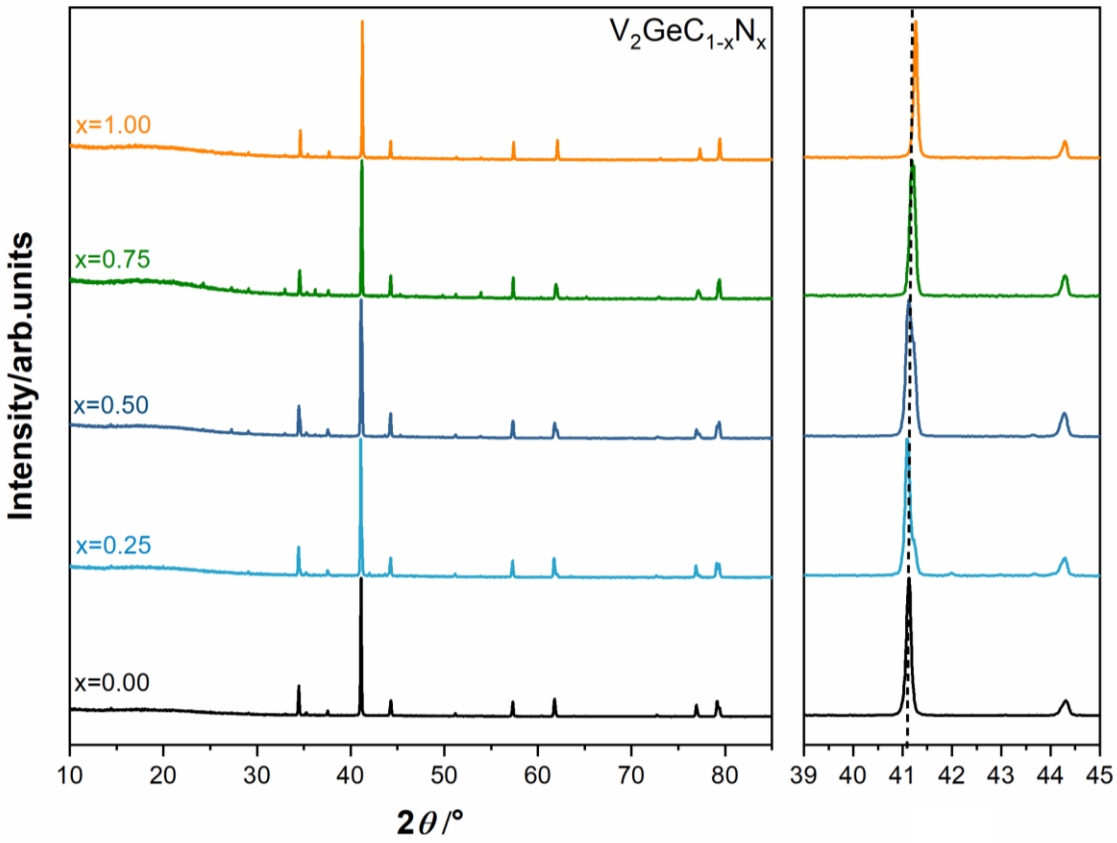

Figure 63: XRD data of the full set of solid-solution phases in the system $V_2GeC_{1-x}N_x$ ($0 \leq x \leq 1$) including the enlarged region of ~39-45° 2θ.

For the pure carbide phase, no additional side phase peaks are detected and the lattice parameters fit well to those initially reported by JEITSCHKO *et al.*,[32] as well as to experimental values of more recent work by PHATAK *et al.*[184] Both, the carbonitride and nitride samples, show small amounts of vanadium nitride and elemental germanium as assignable side phases, however in total only less than 6 wt-% each are found, substantiating a good sample quality (**Table 55**). For detailed extraction and comparison of the lattice parameters of all three target materials, Le Bail refinements were performed (**Figure 64,Table 54)** using the structural model of V_2GeC[184] providing the space group $P6_3/mmc$. By increasing the nitrogen amount towards 50 at-%, a small elongation in the *c*-direction is observed, while the *a*-lattice parameter decreases. Overall, this results in a shrinkage of the cell volume by ~0.4 Å^3. Similar behavior applies to the pure nitride phase. However, here, the *c*-lattice parameter increases slightly more significantly than for the carbonitride, while the decrease of the *a*-lattice parameter almost follows a linear trend (**Figure 64**). Despite the non-linear increase of the *c*-parameter, which can also

occur due to instrumentation inaccuracies in an investigated range of only ~0.007 Å, the cell volume again exhibits a shrinkage (~0.4 Å^3). This is consistent with the smaller atomic radius of nitrogen (1.79 Å) compared to carbon (1.90 Å).[115] Furthermore, the structural parameters of the carbonitride sit almost exactly in between the two parent phases which confirms the nominal composition of $V_2GeC_{0.5}N_{0.5}$. In comparison to the 211 V-Ga-C-N system (chapter 4.2), a similar evolution of the lattice parameters from carbide to nitride was observed which further supports the obtained structural results.[185]

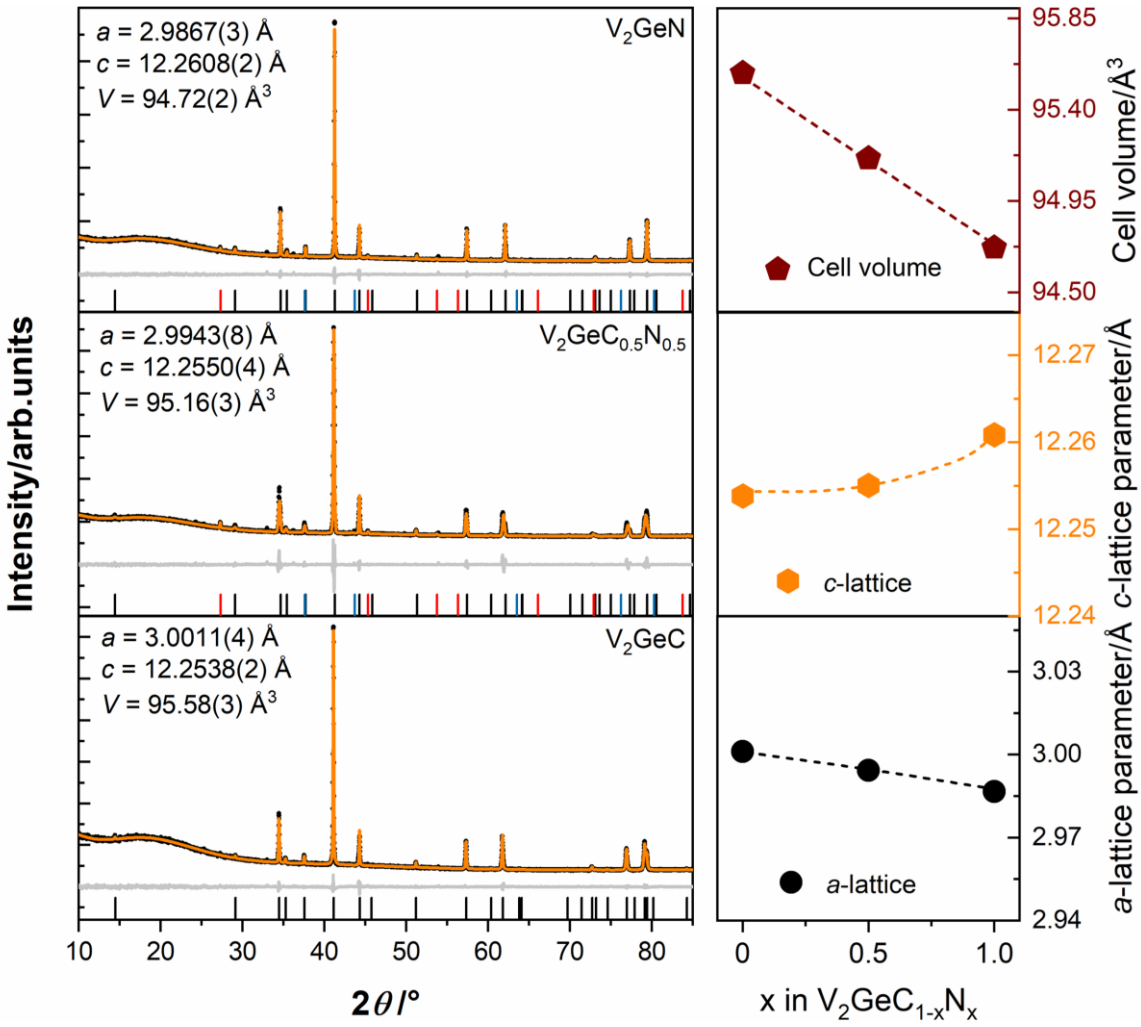

Figure 64: Le Bail refinements (orange lines) of the XRD data (black dots) of V_2GeC, $V_2GeC_{0.5}N_{0.5}$, V_2GeN, based on the structural model of V_2GeC[184] providing the space group *P*6$_3$*/mmc*. Red markers represent germanium[186] peak positions and blue markers vanadium nitride[146] peak positions. Besides, the lattice parameters (*a*,*c*), as well as the cell volumes of the respective phases are plotted against the nominal nitrogen amount. The dashed lines are drawn for guidance.

Table 54: Results of the Le Bail refinements of V_2GeC, $V_2GeC_{0.5}N_{0.5}$ and V_2GeN including literature values of V_2GeC ($P6_3/mmc$).[184]

Phase name	V_2GeC (lit)[184]	V_2GeC	$V_2GeC_{0.5}N_{0.5}$	V_2GeN
Lattice parameters/Å	a = 3.001 c = 12.2601	a = 3.0011(4) c =12.2538(2)	a =2.9943(8) c =12.2550(4)	a = 2.9867(3) c =12.2608(2)
Cell volume/Å^3	95.36	95.58(3)	95.16(3)	94.72(2)
Background order		15	15	15
R_p		2.80	5.15	2.87
R_{wp}		3.94	8.53	4.18
R_{exp}		2.55	3.25	2.45
GOF		1.55	2.62	1.71

Table 55: Summary of the phase fractions extracted from the Rietveld refinements of the target materials.

Phase fractions/ weight-%	MAX phase	VN	Ge
V_2GeC	100	-	-
$V_2GeC_{0.5}N_{0.5}$	94.9(3)	3.2(3)	1.9(2)
V_2GeN	94.8(5)	1.2(3)	4.1(5)

The morphology of the target materials is investigated using SEM. As shown in **Figure 65** (**a-c)**, all samples exhibit MAX phase typical anisotropic layered structures, partially covered with smaller substructures. EDX measurements do not show any anomalies and confirm the 2:1 ratio of V/Ge of the samples. A representative EDX spectrum of V_2GeC is shown in **Figure 65** (**d)**. Interestingly, despite significant differences in the respective time for the heat treatments of the materials (10 h, carbide; 30 h, (carbo)nitride) no obvious differences in the morphologies are present. The required increase in reaction time for the (carbo)nitride can be explained by the involvement of the stable binary nitride precursor vanadium nitride. As a reference, a 10 h heat treatment for the nitrogen-containing materials only leads to a phase mixture of the respective MAX phase, germanium, vanadium nitride, and the intermetallic phase Ge_3V_5, as could be shown by ex-situ XRD data (**Figure 66**). In addition, this analysis provides further insights into the reaction mechanism: initially an intermetallic *MA* phase is formed before the reaction of the *MA* phase with the remaining reactants completes the conversion towards the MAX phase. Similar behavior is observed for the 211 V-Ga-C-N system (chapter 4.2).

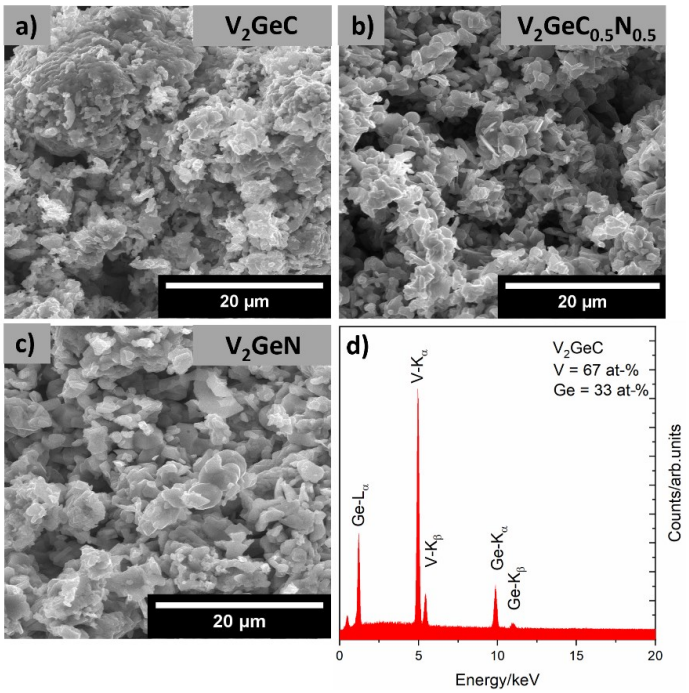

Figure 65: SEM micrographs (a-c) showing the morphology of V_2GeC (a), $V_2GeC_{0.5}N_{0.5}$ (b) and V_2GeN (c), respectively. Figure (d) shows a representative EDX spectrum by the example of V_2GeC.

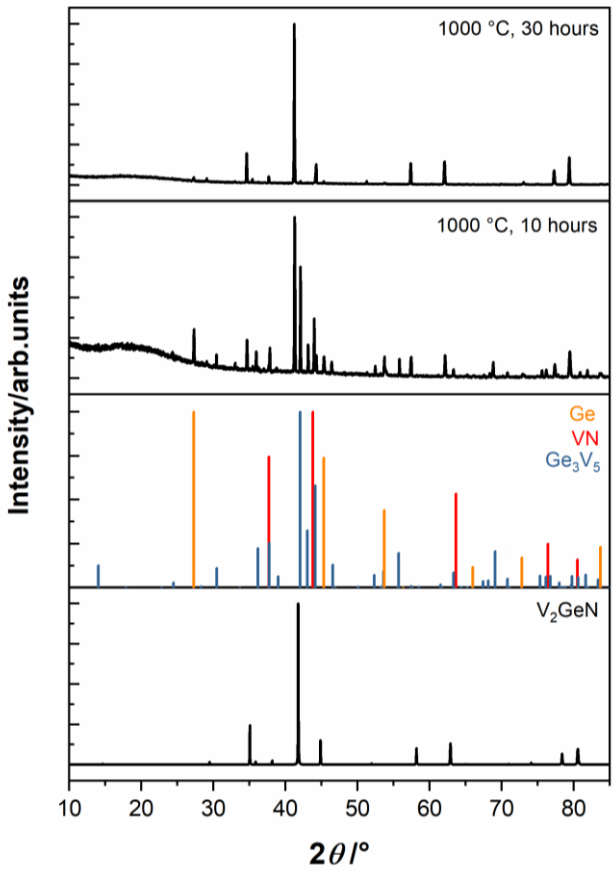

Figure 66: X-ray powder diffraction data of V_2GeN samples which were applied to different heat treatments (10 h and 30 h). As compared with the calculated literature data (peak positions and intensities) of V_2GeN (based on V_2GeC[184]), Ge,[186] VN,[146] and Ge_3V_5[187], the formation can be described as follows: First, the MA phase is formed, before the latter is reacting with the remaining reactants towards the MAX phase.

HAXPES was used to identify the elements and their chemical states present in the three samples, with survey spectra showing all expected lines (**Figure 67**).

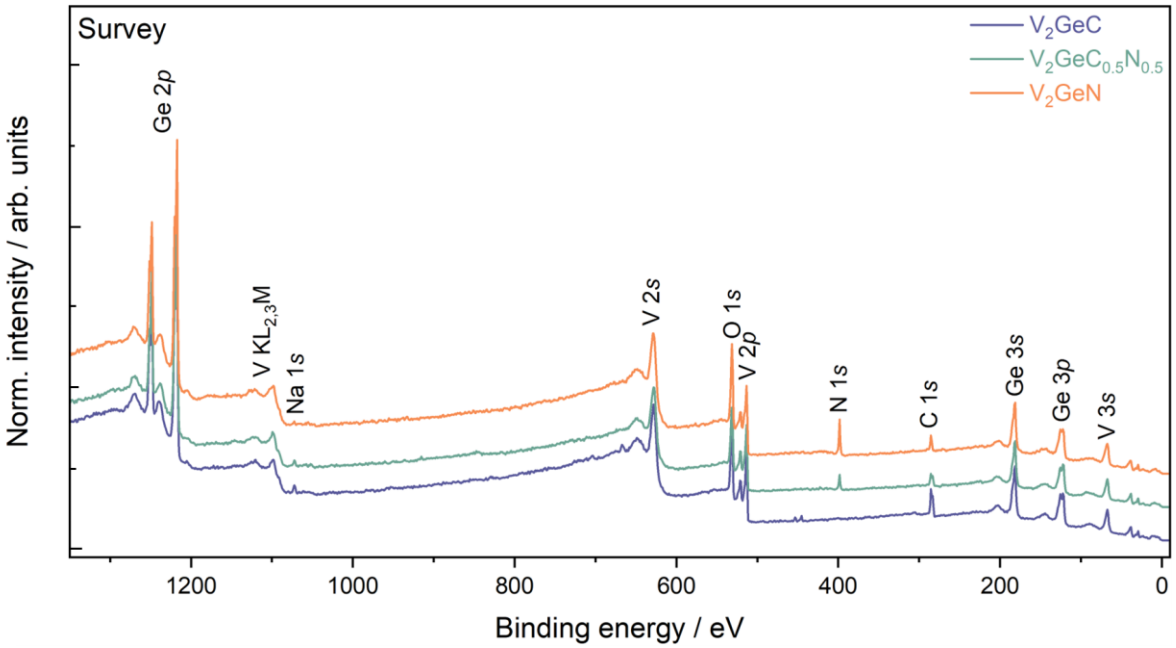

Figure 67: HAXPES survey spectra of V_2GeC, $V_2GeC_{0.5}N_{0.5}$, and V_2GeN with all major lines labeled.

The Ge $2p_{3/2}$ core level (**Figure 68(a)**) shows a main contribution at a binding energy (BE) of 1217.2 eV from GeV_6 environments. In addition, contributions from Ge^{+4} oxide (GeO_2) appear in all samples at a BE of 1220.0 eV. As all samples were handled in air, partial oxidation is expected. The V 2*p* core level spectra (**Figure 68**(**b**)) show the typical doublet, with the $2p_{1/2}$ state considerably broadened by Coster-Kronig effects.[154] All samples show clear V-C/N environments with the V $2p_{3/2}$ peak occurring at 512.9 eV. In addition, all samples show contributions from oxidized states at higher BE. Relative to the carbide phase, the carbonitride and nitride phases show a slight reduction in the amount of V present.
The C 1*s* spectra (**Figure 68**(**c**)) clearly distinguish between the pure nitride, and the carbide and carbonitride phases. Only the latter two have a sharp low BE feature at 282.8 eV. All samples exhibit varying contributions from adventitious carbon (C^0) from exposure to air. Finally, the N 1*s* spectra (**Figure 68**(**d**)) show one dominant feature at 398.0 eV for the NV_6 environments in the nitride and carbonitride phases. No nitrogen signal is detected in the carbide phase. Additional low-intensity shoulders on the higher and lower BE sides of this main peak are ill-defined but could arise from vanadium nitride as found from XRD as well as from NH_x and $N_{1-x}C_xV_6$ environments. By comparing the peak intensities of the pure nitride and carbide phases (assuming they are 1:1 Ge:C/N) to those in the carbonitride phase, the C/N ratio is estimated to be 0.56:0.44.

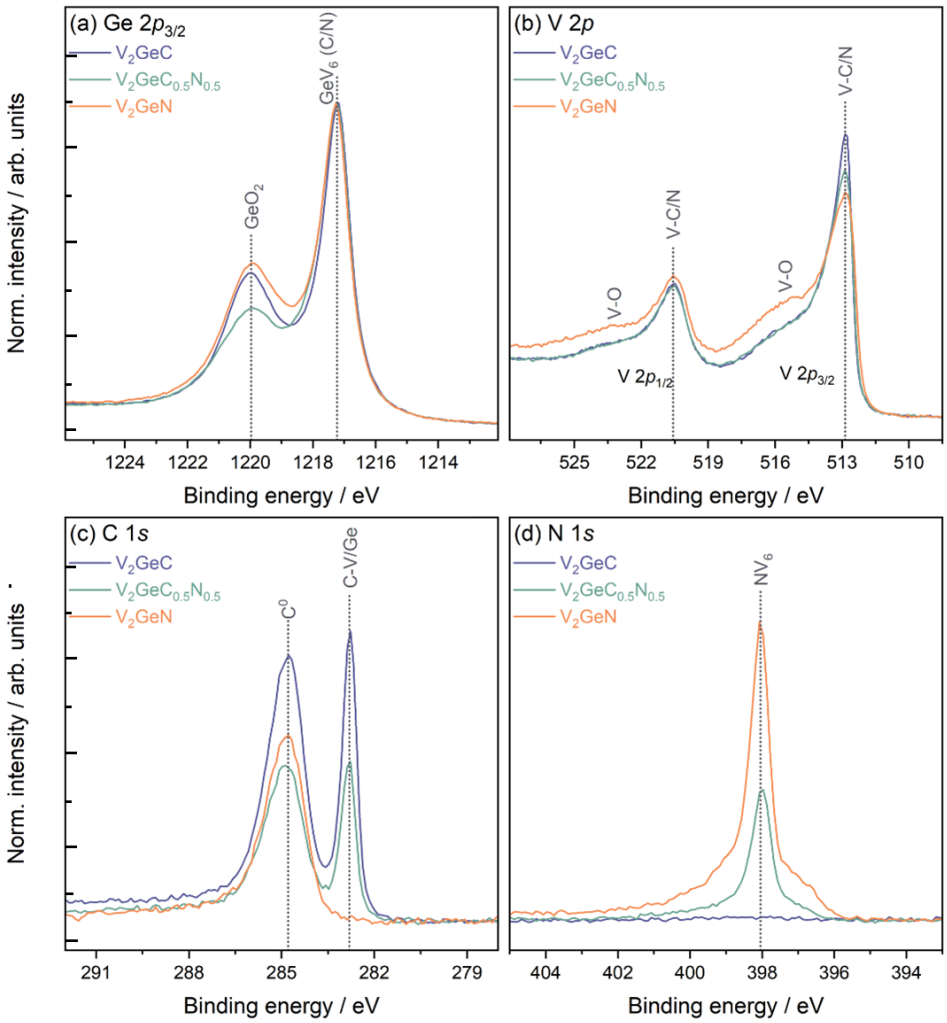

Figure 68: HAXPES core level data of V_2GeC, $V_2GeC_{0.5}N_{0.5}$, and V_2GeN, including (a) Ga $2p_{3/2}$, (b)V 2*p*, (c) C 1*s*, and (d) N 1*s*. All spectra are normalized to the maximum height of their respective Ge $2p_{3/2}$ spectra.

4.4.5. Magnetic and electronic analysis

The magnetic properties of V_2GeC, $V_2GeC_{0.5}N_{0.5}$ (nominal) and V_2GeN are shown in **Figure 69** and are summarized in **Table 56**. The isothermal magnetization curves (**Figure 69(a-c)**) show distinctively different magnetization behavior for all three MAX phases at 300 and 2 K. At 300 K, all compounds show a strictly linear field-dependent magnetization, typical for paramagnetic MAX phases.[39,188] However, at 2 K, the magnetization is non-linear with respect to the magnetic field and the hysteresis loops of $V_2GeC_{0.5}N_{0.5}$ and V_2GeN are indicating the presence of a superconducting state. As the dimensionless volume susceptibility is substantially larger than a value of χ = -1 ($V_2GeC_{0.5}N_{0.5}$: $\chi_{2K} = -0.010$, V_2GeN: $\chi_{2K} = -0.017$) the feature in the hysteresis loops does not represent MAX phase bulk superconductivity, but most likely a superconducting secondary phase such as a V-O-N species,[189] which is not assignable in the XRD data. On the other hand, the absence of the superconducting state in V_2GeC substantiates its phase purity.

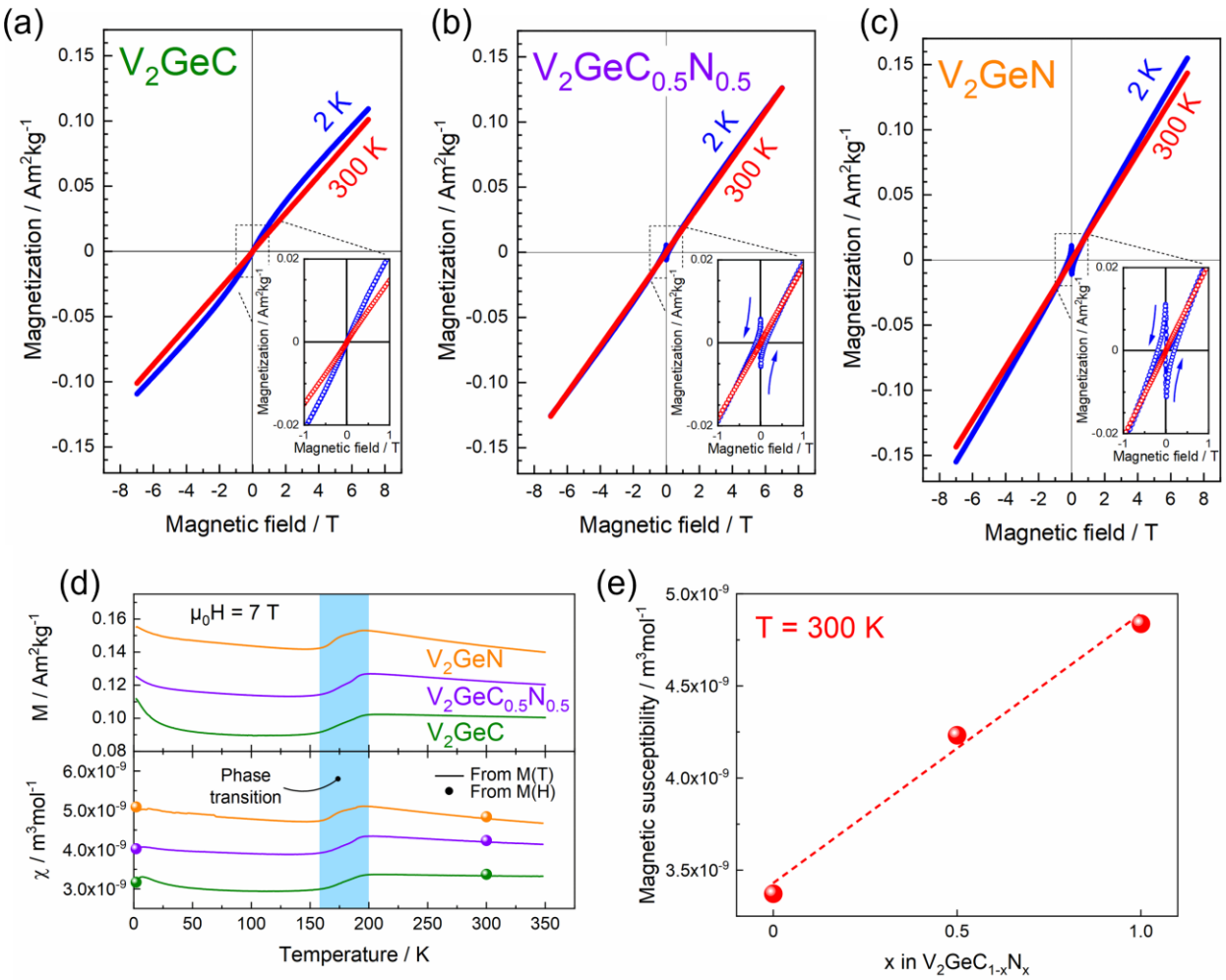

Figure 69: Isothermal magnetization curves at 300 K (red) and 2 K (blue) of (a) V_2GeC, (b) $V_2GeC_{0.5}N_{0.5}$ and (c) V_2GeN. The insets show the curves around zero magnetic field in more detail. (d) Isofield magnetization curves in a magnetic field of 7 T (top panel) and magnetic susceptibility curves (bottom panel) of V_2GeC (green), $V_2GeC_{0.5}N_{0.5}$ (violet) and V_2GeN (orange). The susceptibility has been determined from isofield (solid lines) and isothermal (circles) magnetization measurements. The temperature range showing the phase transition is highlighted. (e) Magnetic susceptibility at 300 K as a function of the nominal nitrogen content in $V_2GeC_{1-x}N_x$ MAX phases. The dashed line is drawn to guide the eye.

The isothermal and isofield magnetization curves as well as magnetic susceptibility curves (**Figure 69(d)**) show that the magnetization and susceptibility increase with a higher nitrogen content (**Figure 69(e)**, **Table 56**), indicating an enhanced exchange upon nitridation similar to the 211 Cr-Ga-C-N system.[119] In addition, the temperature dependence of the magnetization and susceptibility reveal the presence of a phase transition in the investigated $V_2GeC_{1-x}N_x$ MAX phases. For all samples, the transition occurs in the same temperature range from 200 K to 160 K and is accompanied by a similar decrease in magnetization and susceptibility upon cooling, reminiscent of the antiferromagnetic to paramagnetic phase transition in Cr_3GeN.[190,191] However, the exact nature of this transition still has to be elucidated. A magnified representation of the phase transition via the inverse magnetic susceptibility χ^{-1} can be found in **Figure 70**.

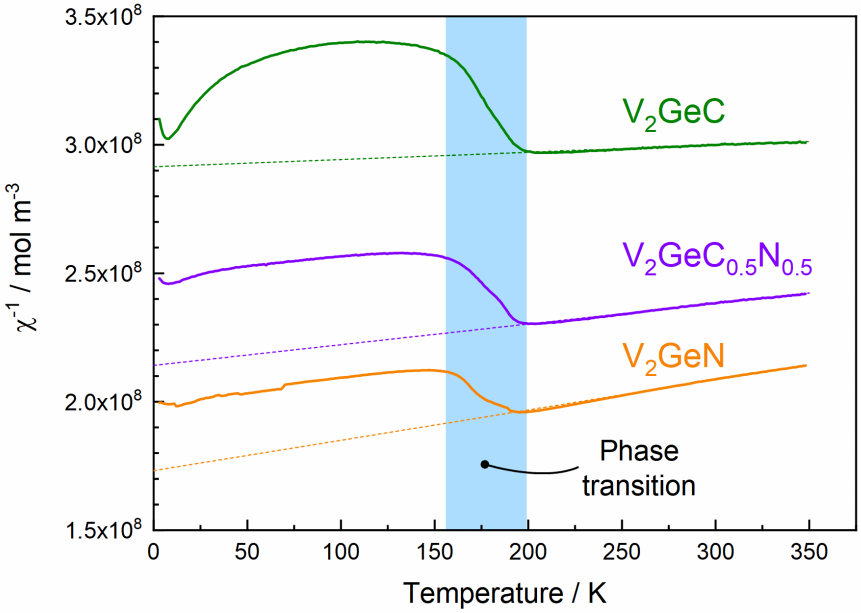

Figure 70: Inverse magnetic susceptibility χ^{-1} of V_2GeC (green), $V_2GeC_{0.5}N_{0.5}$ (violet) and V_2GeN (orange), based on the data shown in **Figure 69** (d). Dashed lines are drawn to guide the eye. The temperature range showing the phase transition is highlighted.

Furthermore, it should be noted that the temperature dependence of the magnetization appears to be tailored by increasing the nitrogen amount in the materials. While the magnetization of the parent carbide phase V_2GeC almost stays constant for temperatures above $T > 200$ K, representing the MAX phase-typical Pauli paramagnetic behavior,[119,188] the carbonitride and even stronger the pure nitride exhibits a noticeable decrease in the magnetization in the same temperature range upon heating. For temperatures below ~40 K, the small increase of the susceptibility may be attributed to small paramagnetic impurities. Comparing the most frequent magnetically studied Cr-based MAX phases in literature, such as Cr_2AC (A = Al, Ga, Ge),[108,119,192] the here reported magnetic susceptibility of V_2GeC at 300 K exhibits smaller values. This can be most likely explained due to an increased electron density on the *M*-site[188] and is also consistent for the nitride phase V_2GeN compared with Cr_2GaN.[119] Compared to V_2AlC,[39] V_2GeC exhibits higher susceptibility values.

Table 56: Summary of magnetic and electronic transport properties of V_2GeC, $V_2GeC_{0.5}N_{0.5}$ and V_2GeN MAX phases, including the magnetization at 300 K and 7 T $M_{300K,7T}$, the magnetic susceptibility at 300 K χ_{300K} and the electrical resistivity values at 300 K ρ_{300K} and 10 K ρ_{10K}.

MAX phase	$M_{300K,7T}$	χ_{300K}	χ_{300K}	ρ_{300K}	ρ_{10K}
	Am^2kg^{-1}	m^3mol^{-1}	emu $g^{-1}Oe^{-1}$	$\mu\Omega m$	$\mu\Omega m$
V_2GeC	0.101	$3.4x10^{-9}$	$1.4x10^{-6}$	1.05	0.40
$V_2GeC_{0.5}N_{0.5}$	0.126	$4.2x10^{-9}$	$1.8x10^{-6}$	0.93	0.27
V_2GeN	0.144	$4.8x10^{-9}$	$2.0x10^{-6}$	0.80	0.27

The temperature dependence of the electrical resistivity of V_2GeC, $V_2GeC_{0.5}N_{0.5}$ and V_2GeN is shown in **Figure 71** and is represented in **Table 56** with electrical resistivity values for 300 K and 10 K. A metallic behavior can be observed in all three MAX phases as the electrical resistivity decreases upon cooling. This agrees with the substantial electron populations observed at the Fermi energy (E_F) of all three samples in HAXPES valence spectra (**Figure 72**). No significant change in electrical resistivity is present at the identified transition around 200 K to 160 K (**Figure 69(d)**), indicating the absence of substantial crystal structure modifications upon the alteration of the magnetic state of the MAX phases, as reported for Cr_2GaN.[118] The *X*-site modification of the $V_2GeC_{1-x}N_x$ MAX phase, however, allows to substantially tune the electrical resistivity, resulting in an ~25 % increase at 300 K from the nitride phase V_2GeN to the carbide counterpart V_2GeC.

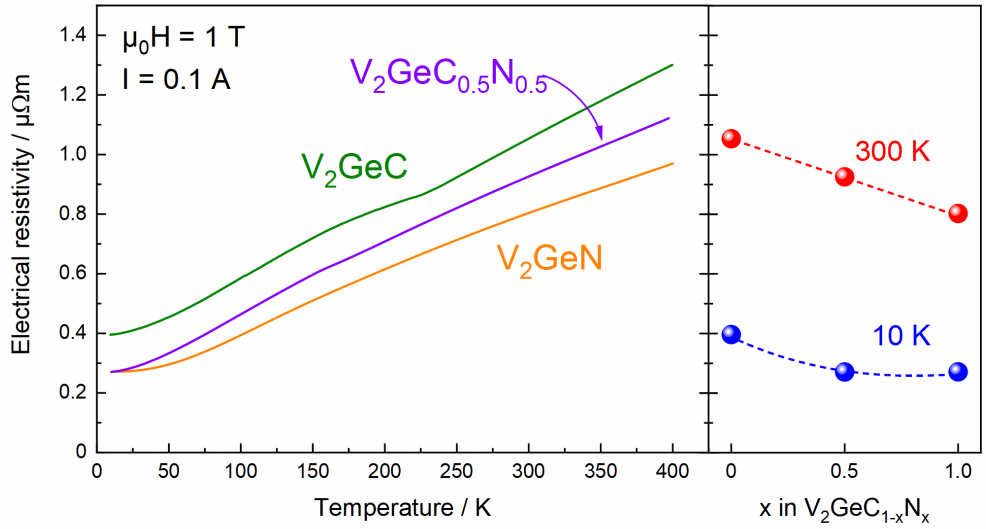

Figure 71: Temperature-dependence of the electrical resistivity (left panel) of V_2GeC (green), $V_2GeC_{0.5}N_{0.5}$ (violet) and V_2GeN (orange), measured in a magnetic field of 1 T and with a current of 0.1 A in the temperature range from 390 K to 10 K. The electrical resistivity at 300 K (red) and 10 K (blue) is also given as a function of the nominal nitrogen content in $V_2GeC_{1-x}N_x$ MAX phases (right panel). Dashed lines are drawn to guide the eye.

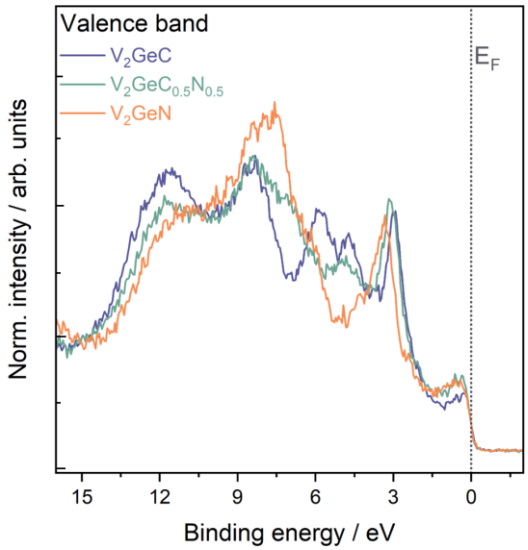

Figure 72: HAXPES valence band spectra of V_2GeC, $V_2GeC_{0.5}N_{0.5}$, and V_2GeN. The dotted line marks the position of the Fermi edge (E_F) at 0 eV.

Compared to other carbide phases, V_2GeC shows significantly higher resistivity values, such as for reactively hot-pressed Nb_2AlC[193] (threefold increase) or Ti_2AlC[128] (fivefold increase). This trend is also confirmed by V_2GeN, which shows an almost fourfold increase in comparison to reactively hot-pressed Ti_2AlN.[128] On the other hand, similar fabricated V_2AlC, using spark plasma sintering for densification, exhibits only differences in the range of 20 %,[39] while the values for reactively hot pressed V_2AlC are almost ten times smaller.[193] Particularly the latter example clearly shows that the measurement of resistivity is highly dependent on the densification technique, due to the strong influence of extrinsic contributions related to microstructural parameters such as particle size, phase purity, and degree of densification. However, for the here investigated target materials, the densification process was identical, and no phase decomposition took place during spark plasma sintering (**Figure 73**).

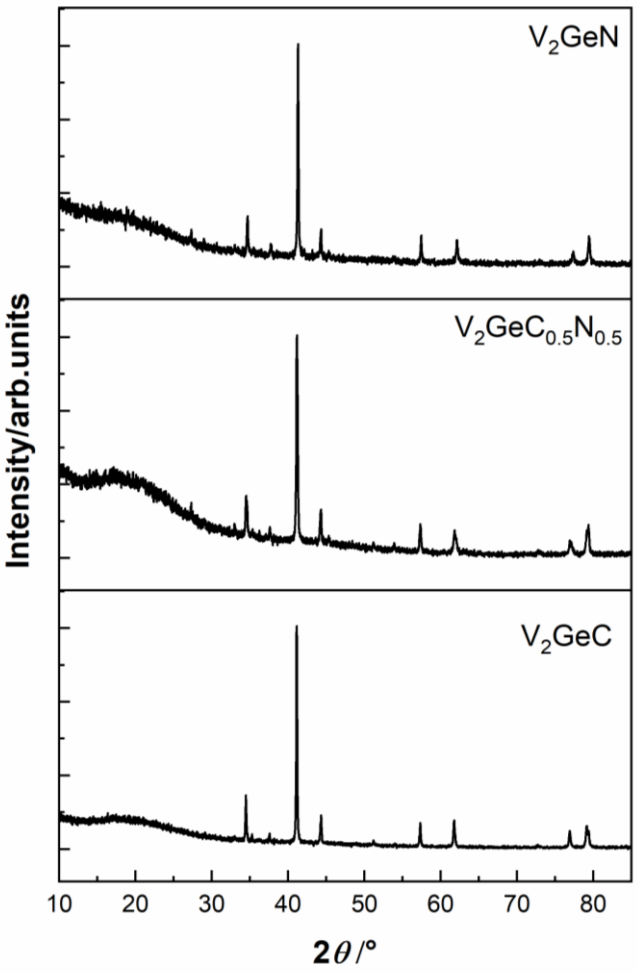

Figure 73: X-ray powder diffraction data of the target materials after the densification process via spark plasma sintering.

Therefore, differences in the observed characteristics can be related to the chemical modification on the *X*-site. By comparing the three investigated samples, it must be noted that the carbonitride phase $V_2GeC_{0.5}N_{0.5}$ displays electrical resistivity values between those of the parent phases, contrary to the comparable 211 carbonitride MAX phase system $Ti_2AlC_{0.5}N_{0.5}$.[128] This in turn allows to tailor the electronic transport over a significantly larger range compared to the Ti-Al-C-N system and enables a continuous monotonic tuning of electrical transport properties by *X*-site modifications related to the nitrogen content in $V_2GeC_{1-x}N_x$.

4.4.6. Conclusion

In this chapter, the MAX phase synthesis of V_2GeC, the hitherto unknown carbonitride phase with the nominal sum formula $V_2GeC_{0.5}N_{0.5}$ and the almost unknown nitride phase V_2GeN was demonstrated, using a hybrid solid-state preparation procedure consisting of a microwave-assisted precursor synthesis followed by a conventional heat treatment and densification by spark plasma sintering. Rietveld refinements provide the first crystallographic data for $V_2GeC_{0.5}N_{0.5}$, as well as for V_2GeN, and confirm a constant decrease in the cell volume going from carbide to nitride. SEM micrographs reveal the MAX phase-typical anisotropic morphology, which was not influenced by the composition or longer reaction times. HAXPES shows the local chemical environments, identifies secondary and surface species, and confirms the carbon to nitrogen ratio to be almost 50:50. To further elucidate their functional properties, magnetic and electrical resistivity measurements were performed. All phases exhibit paramagnetic behavior at room temperature with the potential to be specifically influenced by composition modifications on the *X*-site of the MAX phase structure. All samples exhibit a magnetic phase transition in the temperature region of 160 K - 200 K, however, its exact nature still must be elucidated. Likewise, resistivity measurements confirm the trend of specifically influencing the functional properties of the V-Ge-C-N system by varying the composition of the *X*-site, since a higher nitrogen amount leads to a lower resistivity. All in all, these findings strongly demonstrate the demand for research in (carbo)nitride MAX phases, which can serve as new starting materials for additional solid-solution experiments. This can drive improved and targeted materials synthesis to challenge property limits (e.g., magnetism, electrical conductivity) which are hitherto predominantly dictated by carbides and their *M*-site solid-solutions.

5. Manganese-based antiperovskite phases

5.1. State of the Art

As introduced in chapter 2.1.2, the substance class of antiperovskite phases (X_3AB) exhibits a manifold spectrum of various property profiles, such as magnetism. Particularly, the latter is dominated by Mn-based antiperovskite phases, with A: Al, Zn, Ga, Ge, Sn, In and B: C, N, B, which show a plethora of magnetic ordering configurations, as well as magnetostructural transitions combined with narrow hysteresis properties.[23] The latter two are crucial aspects for magnetocaloric materials that possess the ability to emit or absorb heat when exposed to a changing magnetic field.[23,194] This behavior is based on the magnetocaloric effect (MCE), which can be defined as a reversible change of the thermodynamical parameters temperature (T) and entropy (S) dependent on a changing external magnetic field.[194] If adiabatic conditions are maintained during the magnetization/demagnetization process of the material, the total entropy S stays constant and an adiabatic temperature change (ΔT_{ad}) occurs due to an increase in the lattice entropy S_{lat}.[194] With this regard, it was frequently proven that the antiperovskite phase Mn_3GaC forms a promising example as a magnetocaloric material.[17,22,195] Magnetostructurally, it shows a first-order transition from a low-temperature antiferromagnetic state to a high-temperature ferromagnetic state at around T_i = 165 K[17,196] accompanied by a small volume contraction of the unit cell (≈ -0.5 %)[197,198] (**Figure 74**) and a second-order transition to the paramagnetic state at the Curie temperature T_C = 248 K.[196] In terms of its magnetocaloric properties, the phase exhibits an inverse magnetocaloric effect with a ΔT_{ad} of -5.4 K in a field change of 2 T (sample cools upon applying a field), combined with a large entropy change (ΔS_T = 15 J kg^{-1} K^{-1}) and a narrow thermal hysteresis of 4 K.[17,22]

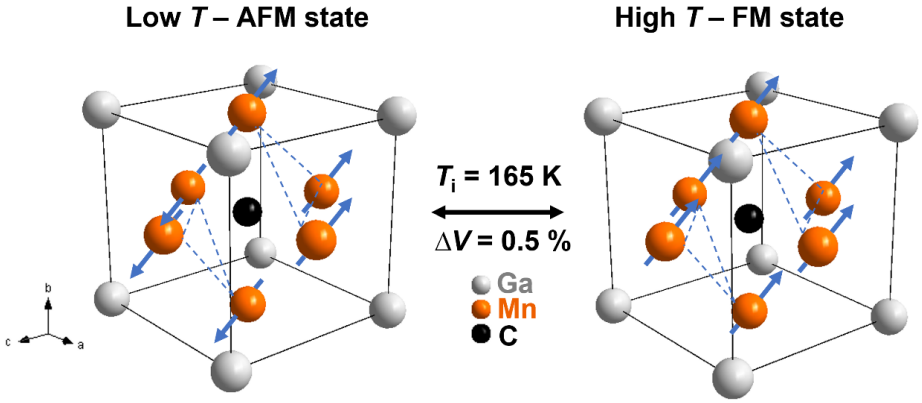

Figure 74: Crystal structure of Mn_3GaC (*Pm*-3*m*) including the spin configurations of the low-temperature AFM state and the high temperature FM state according to García *et al.*[199]

However, it has to be emphasized that the magnetic properties of the system are highly sensitive depending on the materials stoichiometry due to complex and competing coupling interactions within the phase.[11] For instance, small changes in the carbon occupancy, leading to a small decrease of the cell volume and can already significantly influence the AFM/FM transition in the system.[200–202] On the other hand, this allows to specifically tune the properties, as shown with the doping of cobalt[203] or

nickel[204] where a stabilization of the ferromagnetic state is realized, whereas chromium[205] suppresses the FM state at doping amounts of already x > 0.15. Another interesting candidate with respect to magnetocaloric properties is the phase Mn_3SnC which undergoes a first-order magnetostructural transition from a high-temperature paramagnetic state to a low-temperature magnetically very complex state, accompanied by a small thermal hysteresis. Its magnetic complexity arises from two different types of Mn atoms in the crystal lattice.[206] Nonetheless, also this system is very interesting for doping studies as shown with the synthesis of the solid-solution phase $Mn_3Ga_{1-x}Sn_xC$.[207] However, from the synthetic point of view, the material has only been synthesized via time-consuming (> 7 days) conventional high-temperature solid-state routes,[17,195,198,204,206] analogous to the majority of the antiperovskite phases in general.[11] Besides the known disadvantages regarding energy efficiency, conventional routes are also restricted in influencing materials properties, such as the morphology and microstructure.[2] Those can also be a crucial factor for the magnetic behavior of materials and thus, the development of new synthesis procedures still offers a big potential for improvement in the field of antiperovskite materials.[194]

5.2. Sol-gel synthesis of the antiperovskite Mn_3GaC

5.2.1. Motivation

As introduced in the previous chapter 5.1, Mn_3GaC forms a potential magnetocaloric material that has been only synthesized via time consuming methods (> 7 days). As proven in the discussed MAX phase projects, wet-chemical methods can dramatically reduce the reaction time with the benefit to influence materials properties such as the morphology. Since one-step sol-gel-based synthesis methods for carbide MAX phases have been reported,[24,208] this study aims to apply those approaches to the Mn_3GaC system to rapidly synthesize the promising target material and to introduce a new synthesis procedure for carbide-based antiperovskite phases.

5.2.2. Experimental section

2.14 g (6.09 mmol, 3 eq.) Manganese(III)acteylactonate (Thermo Scientific, 97 %), 0.81 g (2.03 mmol, 1.0 eq.) gallium(III)nitrate, octahydrate (ChemPur, 99 %), and 3.51 g (18.27 mmol, 9.0 eq.) / 1.76 g (9.14 mmol, 4.5 eq.) citric acid (Alfa Aesar, 99 %) were dissolved in 10 ml EtOH and stirred for 30 minutes at 70 °C until a highly viscous greenish gel was obtained.

The latter was then transferred into an alumina crucible and heated to 1050 °C (3 K/min) for five hours under flowing argon inside a horizontal tube furnace (*Carbolite*). After heat treatment, a black, sponge-like material was obtained that was ground with an agate mortar into a finely dispersed powder and stored under atmospheric conditions. No further purification steps were applied.

5.2.3. Characterization

X-ray powder diffraction data was obtained using a *Stadi P* (*Stoe & Cie GmbH*) with monochromatized Cu-$K_{\alpha,1}$ radiation (λ = 1.540596 Å) and the *Mythen 1K* (*Dectris*) detector in transmission geometry at room temperature.

For measurements, small sample amounts were deposited between X-ray amorphous adhesive film (*Scotch*) on a flat sample holder and rotated orthogonally to the X-ray source. Rietveld refinements were performed using the program *TOPAS* (*Bruker*).

SEM images were taken at the *XL30 FEG* (*Philips*) using an acceleration voltage of 20 kV, adapted with an *APOLLO X_SDD detector* (*EDAX*) for collecting EDX data. The EDX data were evaluated using the software *EDAX GENESIS*.

DSC/TGA measurements were conducted using the simultaneous thermal analyzer *STA 449 F3 Jupiter*®(*Netzsch*). 12.62 mg of a predried gel (100 °C, 10 h) were heated up to 1100 °C, with a heating rate of 5 K/min under argon atmosphere.

Magnetic properties were studied by vibrating sample magnetometry (VSM) in a PPMS *DynaCool* system (*Quantum Design*). Dried powder (5-10 mg) was weighed and put into polymer capsules. Measurements were taken within the field range of ±2 T at variable temperatures ranging from 3 to 400 K. For the CA 4.5 sample, additional high-temperature data was taken by mixing the sample powder with inert Zircar cement and pasted on the heater stick. The obtained data was fitted to the low-temperature data in the overlapping temperature interval of 310–370 K since the exact amount of sample powder is unknown.

The magnetic entropy change was determined from the field-dependent magnetization in the first quadrant starting from saturation at B = 2-4 T in the temperature interval 10-390 K and varying temperature steps based on analyses described elsewhere.[209]

5.2.4. Structural analysis

Rietveld refinements of the X-Ray powder diffraction were performed using the structural model of Mn_3GaC (space group: *Pm*-3*m*).[210] In order to investigate the potential of tuning the materials properties by influencing the reactant composition, the amount of citric acid has been varied (4.5 and 9.0 equivalents) during the preparation process. This leads to the following nomenclature of CA4.5 and CA9 in the following chapter. However, due to the structural similarity of both samples, the following structural characterization is only referred to the CA9 sample. Nonetheless, a full summary of the Rietveld refinements including the CA4.5 sample and a CA9 sample, annealed for additional 7 days at 800 °C can be found in the Supplementary Information (chapter 5.2.6). As shown in **Figure 75**, the structural model (orange line) was fitted to the diffraction data (black dots) and vertical markers represent the theoretical peak positions of the antiperovskite phase. The desired product was obtained

single phase without any noticeable crystalline side phase peaks. Only a higher background at low 2θ values indicates the presence of amorphous carbon in the product as a result of the carbothermic reduction mechanism.[24] On first sight, the refined lattice parameters (a = 3.8898(3) Å, **Table 57**) fit well to the ones, initially reported by BOUCHAUD and FRUCHART *et al.* in the mid 60's (a = 3.896 Å).[211]

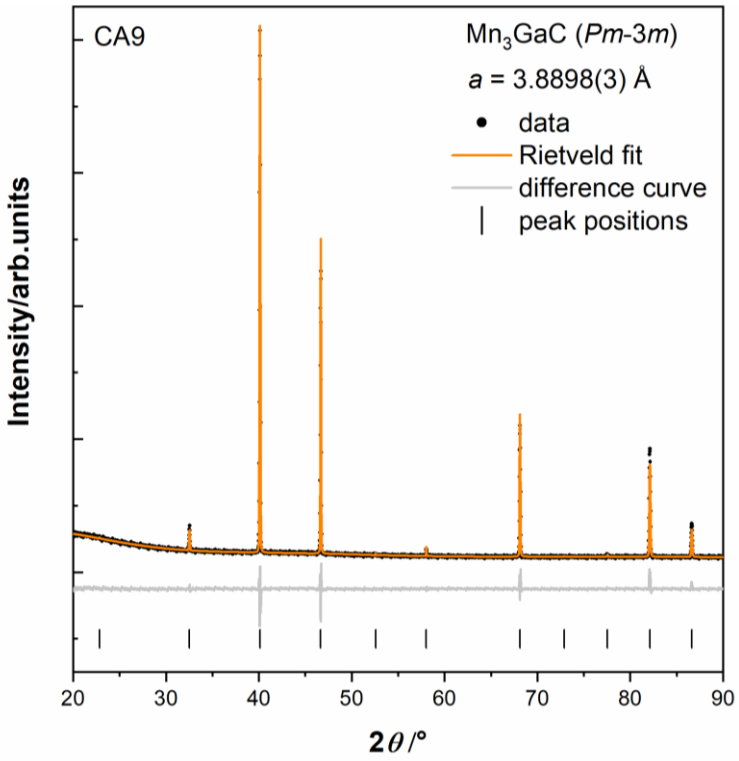

Figure 75: Results of the Rietveld refinement (orange line) and residuum curve (grey) of the X-ray powder diffraction data (black dots) of Mn_3GaC (CA9). The refinement was performed based on the structural model of Mn_3GaC[210] (space group *Pm*-3*m*). Vertical markers represent the peak positions of the Antiperovskite phase.

Table 57: Results of the Rietveld refinement of Mn_3GaC (CA9) based on the structural model of Mn_3GaC.[210]

Phase name	Mn_3GaC
Percentage/weight-%	100
Spacegroup	*Pm-3m*
Lattice parameters a/ Å	3.8898(3)
Cell volume/ Å^3	58.85(2)
Background order	10
R_p	3.05
R_{wp}	4.40
R_{exp}	1.25
GOF	3.51

However, further investigations by the same group showed that only a small deficiency of carbon exhibits a slight but detectable decrease in the lattice parameters, accompanied with a suppression of the AFM/FM transition (see magnetic properties). Also, more recent reports discussed the influence on the lattice parameters depending on the carbon amount.[200,201] Independently, it was shown that stoichiometric Mn_3GaC (1.0 eq. carbon) exhibit a cell volume $V > 59$ Å^3, whereas non-stoichiometric Mn_3GaC_{1-x} phases exhibit cell volumes below the 59 Å^3 benchmark, which also includes the early works of BOUCHAUD and FRUCHART *et al.*[202] By comparing the cell volumes of the sol-gel derived Mn_3GaC compounds reported here, all samples exhibit values close, however, below $V = 59$ Å^3, providing a first indication for a carbon deficiency in the Mn_3GaC phases. Here, it must be emphasized that these structural differences compared to the literature reports are tiny and therefore only serve as a first indication. Additionally, the minimal differences of the lattice parameters between the sol-gel derived samples, that can also occur through measurement-based inaccuracies, will not be further discussed. A much more powerful tool to comprehensively discuss the effects of the apparent carbon deficiency is to use characterize the samples magnetically (see chapter 5.2.4). The microstructure of the product is revealed by electron micrographs. It differs from conventional solid-state approaches known for big and coarse structures and shows small, partly anisotropic substructures covering the surface of the particles (**Figure 76 (a,b)**). This morphology is very similar to other citric acid sol-gel based approaches described in literature.[24,55] Additionally, elemental EDX mappings show the homogeneous distribution of both, manganese and gallium in the sample, achieved due to the atomic mixing of the reactants using the wet-chemical based approach (**Figure 76 (c,d)**).

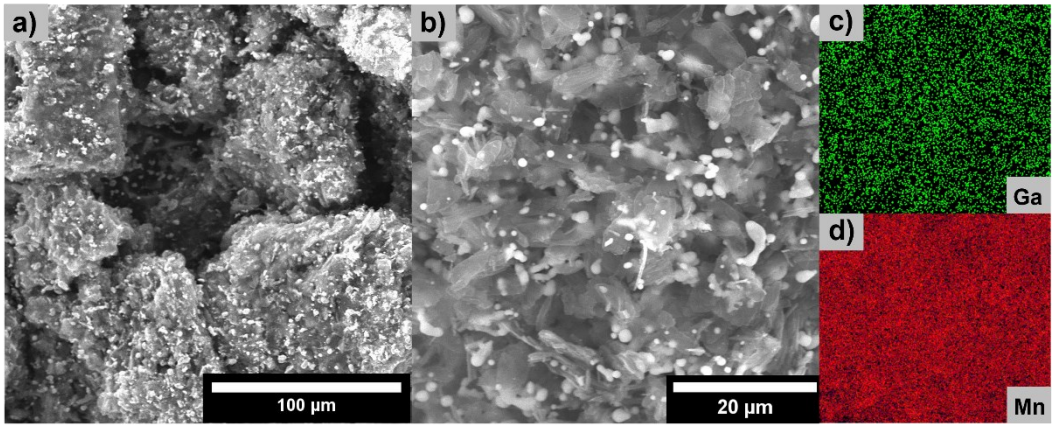

Figure 76: SEM micrographs showing the morphology of the obtained Mn_3GaC product (a,b) combined with elemental EDX mappings (c,d) showing the homogeneous distribution of gallium and manganese. The EDX mappings are based on micrograph b.

To further study the reaction mechanism of the formation of the sol-gel derived Mn_3GaC phase, *ex situ* X-ray powder diffraction data, as well as DSC-TG measurements of a dried gel were carried out. For the *ex situ* X-ray diffraction data, four individual gel samples were prepared following the procedure

described in the experimental section and heated at four different temperature levels (450 °C, 750 °C, 900 °C, and 1050 °C) for five hours under flowing argon. Up to 750 °C, the binary cubic oxide MnO forms the main phase, however, no crystalline Ga-based phase can be identified within this temperature range. At 900 °C, the oxide is partially transformed into the carbide antiperovskite phase and a phase mixture of MnO and Mn_3GaC is present, whereas at 1050 °C only diffraction peaks of the desired product can be observed. On the other hand, the DSC/TG measurements exhibit the most noticeable peak at around 240 °C. This strong exothermic peak can be attributed to the combustion of the nitrate as an oxidizer and citrate as an "organic fuel".[51] This process is also accompanied with the strongest mass loss of nearly 75 %. Further organic decomposition takes place at around 400 °C combined with the formation of the MnO and most probably an amorphous gallium oxide species. Until around 900 °C, the DSC curve increases almost constantly which is ended by an exothermic peak at 1025 °C. The latter can be attributed to the final carbothermic reduction towards the Mn_3GaC phase and confirms the reaction temperature of 1050 °C within the tube furnace. Considering the obtained data, all observations follow recent extensive studies of SIEBERT *et al.* to propose a general reaction mechanism to obtain ternary carbides via sol-gel chemistry over an oxide intermediate phase via a carbothermic reduction reaction.[212]

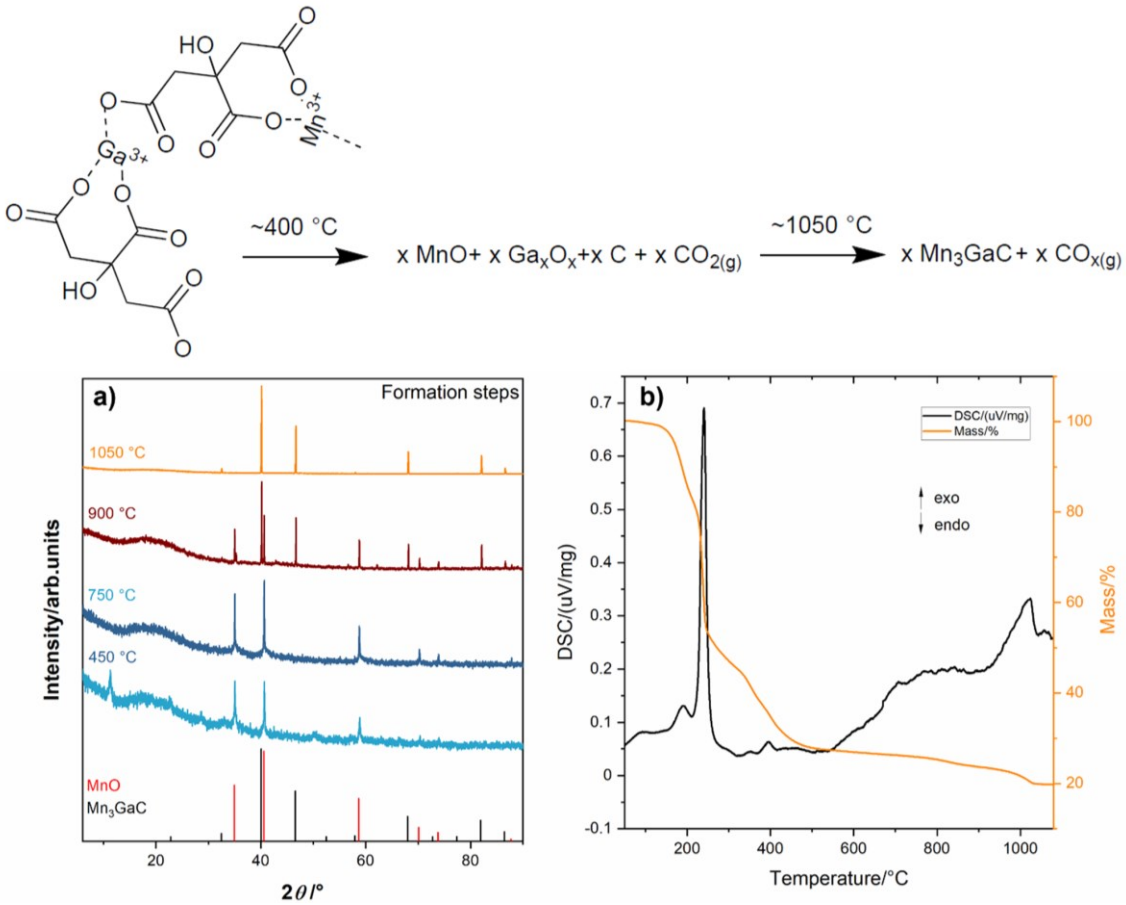

Figure 77: *Ex situ* powder X-ray diffraction data of samples heated at different temperature levels including the literature data of Mn_3GaC[210] and MnO[213] (a). (b) shows a simultaneous thermal analysis (DSC/TGA) of a dried gel heated from room temperature up to 1100 °C. The data is summarized in the form of a proposed reaction scheme above.

5.2.5. Magnetic analysis

While all samples are essentially phase pure as revealed by X-ray diffraction and Rietveld refinement the magnetic response gives further information on the crystal quality and especially on deviations from the stoichiometric occupancy of the respective lattice sites. The magnetic phase transition temperatures T_i = 165 K and T_C = 248 K as obtained in the stoichiometric volume material are highly sensitive to the local symmetry of Mn and C and the Mn-Mn distance in the antiperovskite structure. For example, BOUCHAUD and FRUCHART *et al.* reported that T_i is depressed with carbon deficiency, and the antiferromagnetic response is suppressed at $\delta = 0.05$ in $Mn_3GaC_{1-\delta}$.[202] Further, Lewis et al. did not find any AFM-FM transition in C-deficient $Mn_3GaC_{0.78}$ while T_C rose to 295 K.[200] This has been attributed to the promotion of weak near-neighbour 90° Mn–Mn interaction in the carbon-deficient compound (8 Mn atoms in the octahedra) being in sum stronger than the 180° Mn–C–Mn interaction, leading to the dominant ferromagnetism at low temperature.[200]

Figure 78 (a-c) presents the temperature-dependent magnetization after zero field cooling (ZFC), field-cooling (FC) and field warming (FW) in B = 10 mT of the samples prepared with citric acid ratios of CA4.5, CA9 and after additional annealing of CA9 at 800°C for 7 days, respectively. In general, the expected phase transitions in all samples are obtained, however, at different temperatures and with significant or even dominating contributions of ferromagnetic response at low temperatures. The CA4.5 and CA9 samples show T_i = 100 K and 130 K, respectively, while the width of the transition is broader than in stoichiometric Mn_3GaC with sharp 1st order MCE. This already points towards a local distribution of the C-deficiency. Further, the decrease of the magnetization at the Curie temperature is significantly broadened as well (370-410 K for CA4.5 and 300-360 K for CA9) and shoulders indicate the presence of local distributions of stoichiometry. Annealing of the CA9 sample at 800°C for 7 days maintains T_i and sharpens the high-temperature transition to T_C = 316 K while the ferromagnetic contribution to the signal rises. Note that a fully antiferromagnetic sample should give magnetization values close to zero at low temperatures. **Figure 78 (d)** presents the magnetic hysteresis loops of the CA9 and the annealed sample at 3 K, 200 K, and 350 K representing temperatures in which stoichiometric Mn_3GaC is in the antiferromagnetic, ferromagnetic, and paramagnetic state, respectively. However, a ferromagnetic response with a narrow hysteresis and a saturation magnetization of about 45 $Am^2\ kg^{-1}$ is obtained, pointing towards C-deficient $Mn_3GaC_{1-\delta}$ as well. At 200 K, these values slightly decrease to 40 $Am^2\ kg^{-1}$ for CA9 and 37 $Am^2\ kg^{-1}$ for the annealed sample while at 350 K paramagnetic response is obtained for the annealed sample, and a small magnetization maintained for CA9.

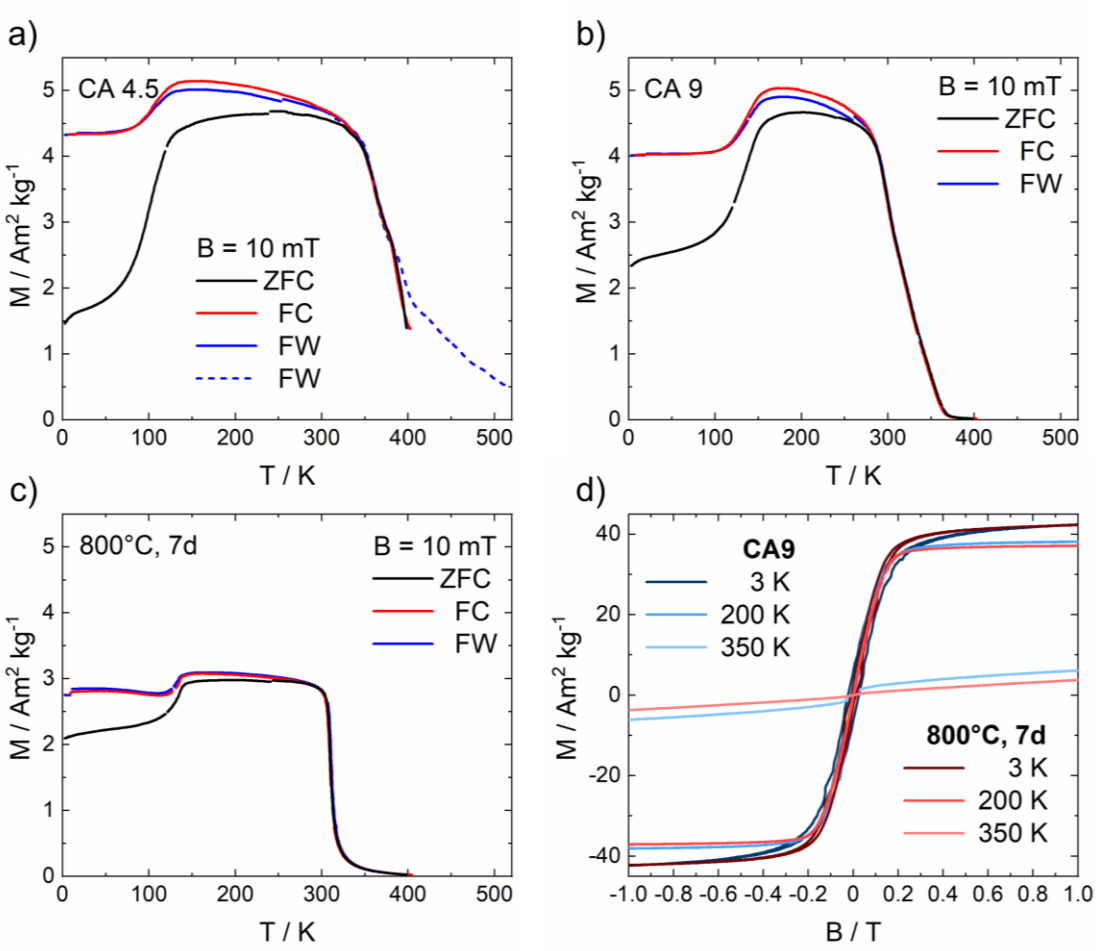

Figure 78: Magnetometry. Zero field-cooled (ZFC), field-cooled (FC) and field-warmed (FW) curves in B = 10 mT of the samples with citric acid ratios of (a) CA4.5, (b) CA9 and (c) after additional annealing of CA9 at 800°C for 7 days. Panel (d) presents magnetic hysteresis loops at 3K, 200 K, and 350 K of CA9 and after annealing representing the temperatures at which antiferromagnetic, ferromagnetic, and paramagnetic order is obtained in volumetric Mn_3GaC.

The magnetic entropy change of the CA9 sample is presented in **Figure 79**. The measurements were conducted twice as indicated by Run1 and Run2 in B_{max} = 4 (2) T, respectively. In large fields, the entropy change is highly dominated by the broad minimum centered at 300 K. This is the FM/PM transition. Like the temperature-dependent magnetization in small fields in **Figure 78 (b)** the entropy change appears highly broadened as compared to stoichiometric Mn_3GaC. Such slight stoichiometry variations, however, have a strong influence on both, T_i and T_C, and consequently a distribution of transition temperatures is obtained. It must be noted that, in principle, the best magnetocaloric performance is obtained at 300 K for CA9 and cooling is possible over a wide temperature range between 150 K and 350 K using the normal magnetocaloric effect of the FM/PM transition. However, the absolute entropy change of $|\Delta S_M| = 1$ J kg^{-1} K^{-1} is too small for applications.

Scientifically more interesting is the small maximum at lower temperatures originating from AFM/FM transition of parts of the CA9 sample as indicated in **Figure 79** small fields. This maximum shifts with the external field from about 140 K in $B = 0.1$ T to 117 K in $B = 1$ T and above.

Thus, a (nearly) stoichiometric grain suspects to undergo the AFM/FM phase transition at T_i can be influenced by its FM environment. Overall, the magnetic entropy change of the sol-gel prepared sample CA9 is highly governed by off-stoichiometric Mn_3GaC FM response rather than the inverse magnetocaloric effect at T_i.

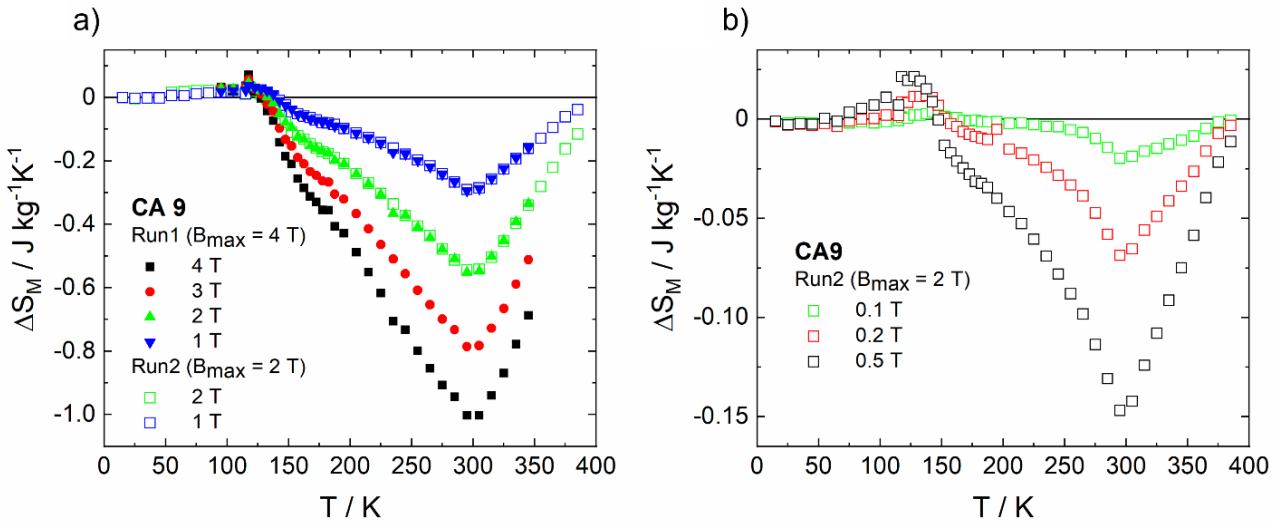

Figure 79: Magnetic entropy change ΔS_M of the CA9 sample in various fields. (a) high fields, (b) low fields.

The magnetic data clearly show the sensitivity of Mn_3GaC to slight C-deficiencies and forms a powerful tool to discuss such features that are very hard to quantify by XRD and Rietveld refinement, which, however, already provide first insights of the materials composition. Nonetheless, the presented sol-gel route is time- and thus cost-efficient for synthesizing materials with antiperovskite structure, with the great potential to tune the magnetic behavior by only varying the experimental parameters. The optimization of the synthesis route may provide the recipe for close to stoichiometric Mn_3GaC which in turn can be further tuned to larger intervals for magnetocaloric cooling.

5.2.6. Conclusion

In this chapter, a rapid citric acid-based sol-gel approach for the synthesis of the antiperovskite phase Mn_3GaC was introduced. X-ray powder diffraction data confirm the preparation of a highly phase pure product, indicating a slight carbon deficiency in comparison to literature reports. SEM images and EDX mappings exhibit a typical sol-gel like morphology with small, partly anisotropic substructures covering the surface of the particles and a homogeneous distribution of the elements. In addition, the reaction mechanism of the Mn_3GaC phase was elucidated combining *ex situ* XRD data with DSC/TGA measurements and can be described as a carbothermic reduction reaction with MnO as an intermediate phase. Furthermore, the magnetic behavior of the material was studied by vibrating sample magnetometry. It shows the literature-known AFM-FM-PM transitions, however with different transition temperatures and a total entropy change of $|\Delta S_M| = 1$ J kg^{-1} K^{-1} which is dominated by the FM/PM transition. Overall, these data support the findings of carbon deficiency as already indicated by XRD data. Despite the resulting deviations in the magnetic properties, it must be stressed, that by only varying the citric acid amount in the reaction mixture, the magnetic state can be specifically influenced in terms of stabilizing/destabilizing the ferromagnetic state of the antiperovskite phase. Consequently, this shows that the sol-gel approach possesses a great potential to be further developed and tuned in future studies by only varying the reaction parameters, leading to a new powerful and efficient alternative to the preparation of carbide antiperovskite phases.

5.2.7. Supplementary Information

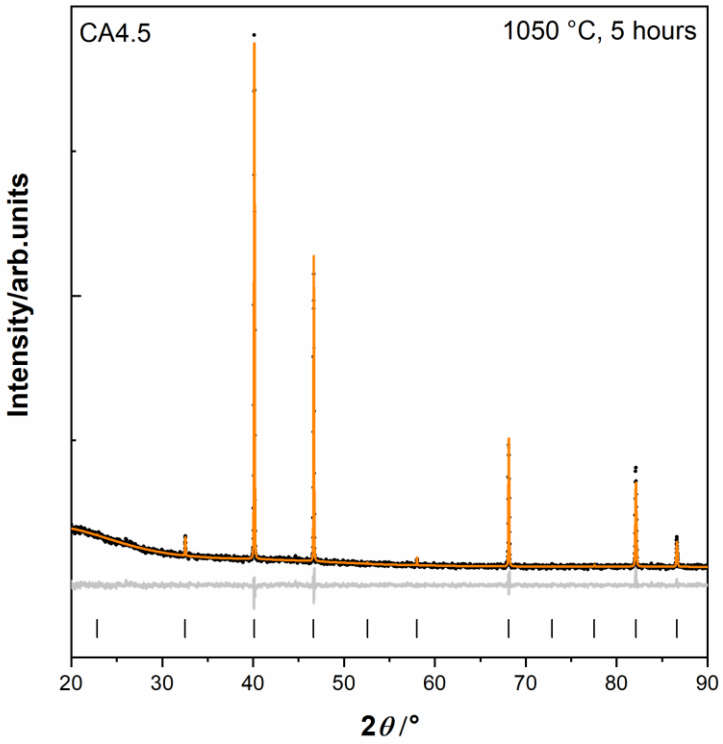

Figure 80: Results of the Rietveld refinement (orange line) and residuum curve (grey) of the X-ray powder diffraction data (black dots) of Mn_3GaC (CA4.5), 5 hours. The refinement was performed based on the structural model of Mn_3GaC[210] (space group *Pm*-3*m*). Vertical markers represent the peak position of the antiperovskite phase.

Table 58: Results of the Rietveld refinement of Mn_3GaC (CA4.5) based on the structural model of Mn_3GaC.[210]

Phase name	Mn_3GaC
Percentage/weight-%	100
Spacegroup	*Pm-3m*
Lattice parameters *a*/ Å	3.8906(4)
Cell volume/ Å^3	58.89(2)
Background order	15
R_p	3.27
R_{wp}	4.30
R_{exp}	2.28
GOF	1.88

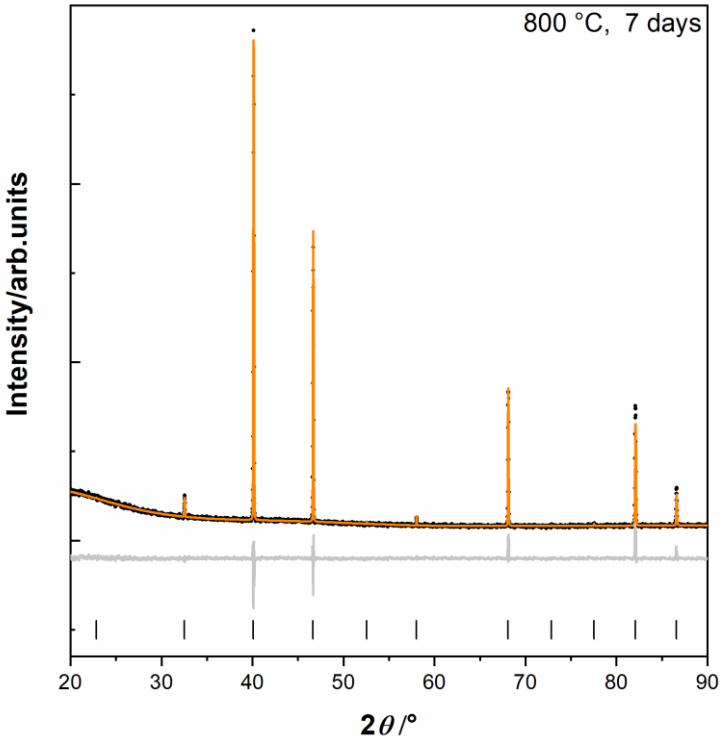

Figure 81: Results of the Rietveld refinement (orange line) and residuum curve (grey) of the X-ray powder diffraction data (black dots) of Mn_3GaC (CA9), 7 days. The refinement was performed based on the structural model of Mn_3GaC[1] (space group *Pm*-3*m*). Vertical markers represent the peak position of the antiperovskite phase.

Table 59: Results of the Rietveld refinement of Mn_3GaC (CA9, 7 days annealing time) based on the structural model of Mn_3GaC.[210]

Phase name	Mn_3GaC
Percentage/weight-%	100
Spacegroup	*Pm-3m*
Lattice parameters *a*/ Å	3.8916(3)
Cell volume/ Å^3	58.94(2)
Background order	15
R_p	3.05
R_{wp}	4.40
R_{exp}	1.25
GOF	3.51

5.3. Sol-gel synthesis of the antiperovskites $Mn_{2.8}Cr_{0.2}GaC$ and Mn_3SnC

5.3.1. Motivation

In order to prove the suitability and versatility of the introduced sol-gel method in chapter 5.2, this study aims to investigate the doping behavior of Mn_3GaC and to synthesize an additional magnetocaloric interesting antiperovskite phase Mn_3SnC by following the same general synthesis procedure.

5.3.2. Experimental section

Synthesis of $Mn_{2.8}Cr_{0.2}GaC$:

2.00 g (6.09 mmol, 2.80 eq.) Manganese(III)acteylactonate (Thermo Scientific, 97 %), 0162 g (0.41 mmol, 0.20 eq.) chromium(III)nitrate, nonahydrate (Acros Organics, 99 %), 0.81 g (2.03 mmol, 1.00 eq.) gallium(III)nitrate, octahydrate (ChemPur, 99 %), and 3.51 g (18.27 mmol, 9.00 eq.) citric acid (Alfa Aesar, 99 %) were dissolved in 10 ml EtOH and stirred for 30 minutes at 70 °C until a highly viscous greenish gel was obtained.
The latter was then transferred into an alumina crucible and heated to 1050 °C (3 K/min) for five hours under flowing argon inside a horizontal tube furnace (*Carbolite*). After heat treatment, a black, sponge-like material was obtained that was ground with an agate mortar into a finely dispersed powder and stored under atmospheric conditions. No further purification steps were applied.

Synthesis of Mn_3SnC:

1.78 g (5.10 mmol, 3 eq.) Manganese(III)acteylactonate (Thermo Scientific, 97 %), 0.38 g (1.70 mmol, 1 eq.) tin (II) chloride, dihydrate (ChemPur, 98+ %), and 2.93 g (15.3 mmol, 9 eq.) citric acid (Alfa Aesar, 99 %) were dissolved in 10 ml EtOH and stirred for 30 minutes at 70 °C until a highly viscous gel was obtained. The latter was then transferred into an alumina crucible and heated to 1050 °C (3 K/min) for five hours under flowing argon inside a horizontal tube furnace (*Carbolite*). After heat treatment, a black, sponge-like material was obtained that was ground with an agate mortar into a finely dispersed powder. In order to remove side phases, the powder was transferred into a solution of 4N HCl and stirred for 4 hours at room temperature, filtered, and dried at 100 °C for 1 hour. The final product was stored under atmospheric conditions.

5.3.3. Characterization

X-ray powder diffraction data was obtained using a *Stadi P* (*Stoe & Cie GmbH*) with monochromatized Cu-$K_{\alpha,1}$ radiation (λ = 1.540596 Å) and the *Mythen 1K* (*Dectris*) detector in transmission geometry at room temperature. For measurements, small sample amounts were deposited between X-ray amorphous

adhesive film (*Scotch*) on a flat sample holder and rotated orthogonally to the X-ray source. Rietveld refinements were performed using the program *TOPAS* (*Bruker*).

SEM images were taken at the *XL30 FEG* (*Philips*) using an acceleration voltage of 20 kV, adapted with an *APOLLO X_SDD detector* (*EDAX*) for collecting EDX data. The EDX data were evaluated using the software *EDAX GENESIS*.

5.3.4. Structural analysis

In order to investigate the suitability of the introduced sol-gel process for Mn_3GaC (chapter 5.2) for elemental variations and doping experiments, the literature known target materials $Mn_{2.8}Cr_{0.2}GaC$[205] and Mn_3SnC[206] were synthesized. In **Figure 82**, the XRD data of the solid-solution phase $Mn_{2.8}Cr_{0.2}GaC$ is compared to the parent phase Mn_3GaC. Analogous to the latter, the solid-solution phase was obtained phase pure and no additional side phase peaks are present in the XRD data. By zooming into the region of the (111) main peak, a small shift towards lower 2θ values can be observed, indicating a slight increase of the cell volume.

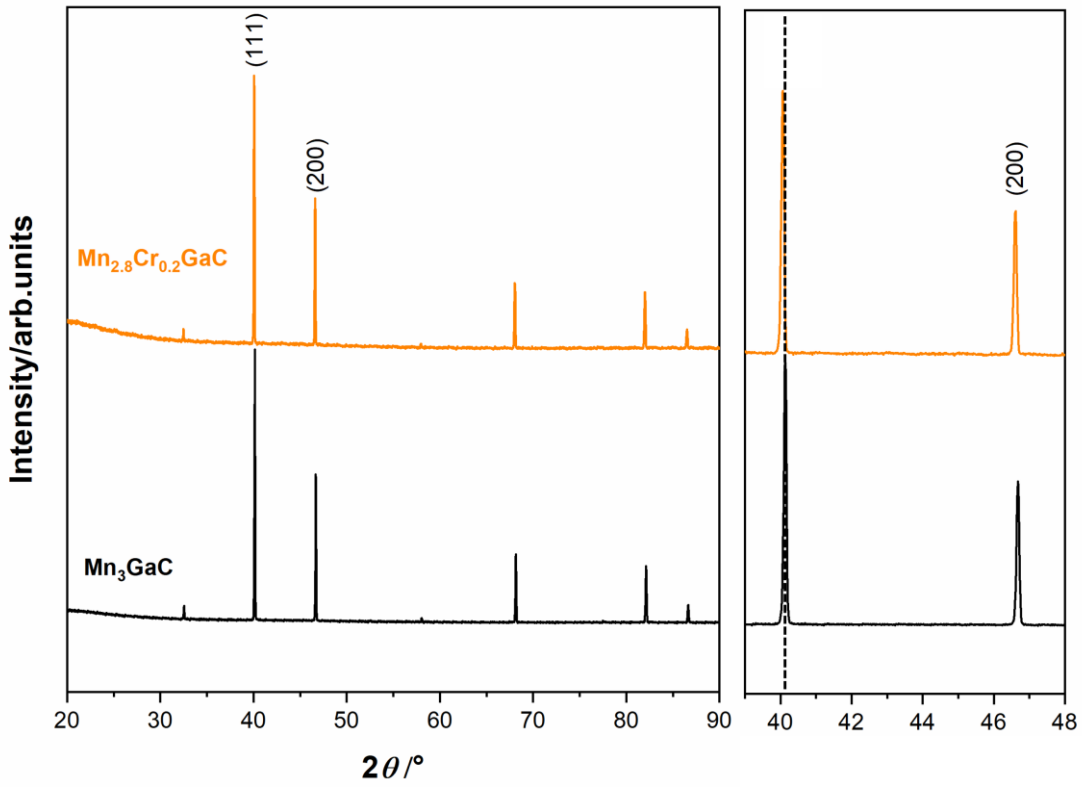

Figure 82: XRD data of sol-gel derived Mn_3GaC and $Mn_{2.8}Cr_{0.2}GaC$ including the enlarged region of the (111) main peak.

The apparent increase of the cell volume is confirmed by performing Rietveld refinements based on the structural model of Mn_3GaC (**Figure 83** and **Table 60**).[210] This is in accordance with literature results by HARADA *et al.*[205] who also reported a slight expansion of the Mn_3GaC cell volume by doping chromium into the structure. The microstructure of the product was investigated using electron

microscopy (**Figure 83** inset). Again, partly anisotropic substructures are covering the surface of the particles which is analogous to the results reported in chapter 5.2. Additionally, elemental mappings show a homogeneous distribution of the elements throughout the particles, confirming the successful incorporation of chromium into the antiperovskite structure.

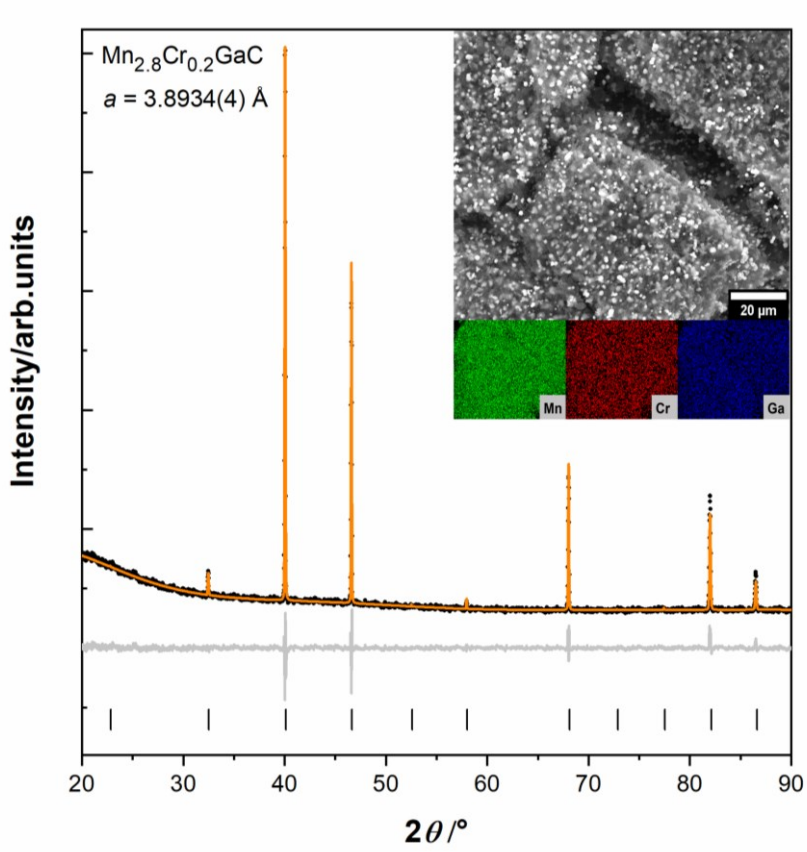

Figure 83: Results of the Rietveld refinement (orange line) and residuum curve (grey) of the X-ray powder diffraction data (black dots) of $Mn_{2.8}Cr_{0.2}GaC$. The refinement was performed based on the structural model of Mn_3GaC[210] (space group *Pm*-3*m*). Vertical markers represent the peak positions of the antiperovskite phase. The inset shows an SEM micrograph combined with elemental EDX mappings, revealing the morphology and the homogeneous distribution of the respective elements Mn, Cr, and Ga.

Table 60: Results of the Rietveld refinement of $Mn_{2.8}Cr_{0.2}GaC$ based on the structural model of Mn_3GaC.[210]

Phase name	$Mn_{2.8}Cr_{0.2}GaC$
Percentage/weight-%	100
Spacegroup	*Pm-3m*
Lattice parameters *a*/ Å	3.8934(4)
Cell volume/ Å^3	59.02(2)
Background order	10
R_p	3.80
R_{wp}	5.27
R_{exp}	2.75
GOF	1.91

Besides the successful doping experiment on the *M*-site, the gallium-based *A*-site was fully replaced by a tin halide salt in the sol-gel process without any further experimental variations. As shown in the XRD data in **Figure 84**, after the heat treatment a phase mixture of the target material Mn_3SnC as well as the side phases MnO, and $MnSn_2$ was obtained.

This behavior could be explained due to a reduced reduction potential by using halide salts instead of typical nitrate-based metal salts, which normally act as the oxidants, while the citric acid forms as the "organic fuel".[51] However, further studies would be necessary to substantiate these assumptions.

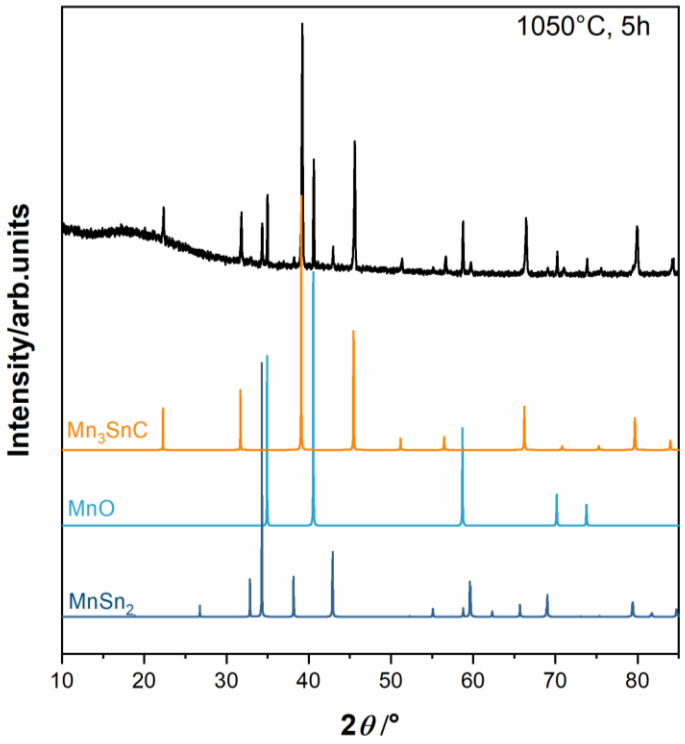

Figure 84: XRD data of sol-gel derived unwashed Mn_3SnC, including the theoretical peak positions of Mn_3SnC,[214] MnO,[215] and $MnSn_2$.[216]

Nonetheless, by washing the phase mixture with 4N HCl, the side phases can be removed, resulting in a single-phase Mn_3SnC material. The significantly higher background at lower 2θ angles can be explained by remaining amorphous carbon in the product due to the citric acid-based sol-gel approach (**Figure 85**). For extraction of the lattice parameters, Rietveld refinements were performed based on the structural model of Mn_3SnC. Here the experimental values are consistent with the values reported in the literature and thus support the suitability to expand the citric acid-based sol-gel method to other antiperovskite phases.

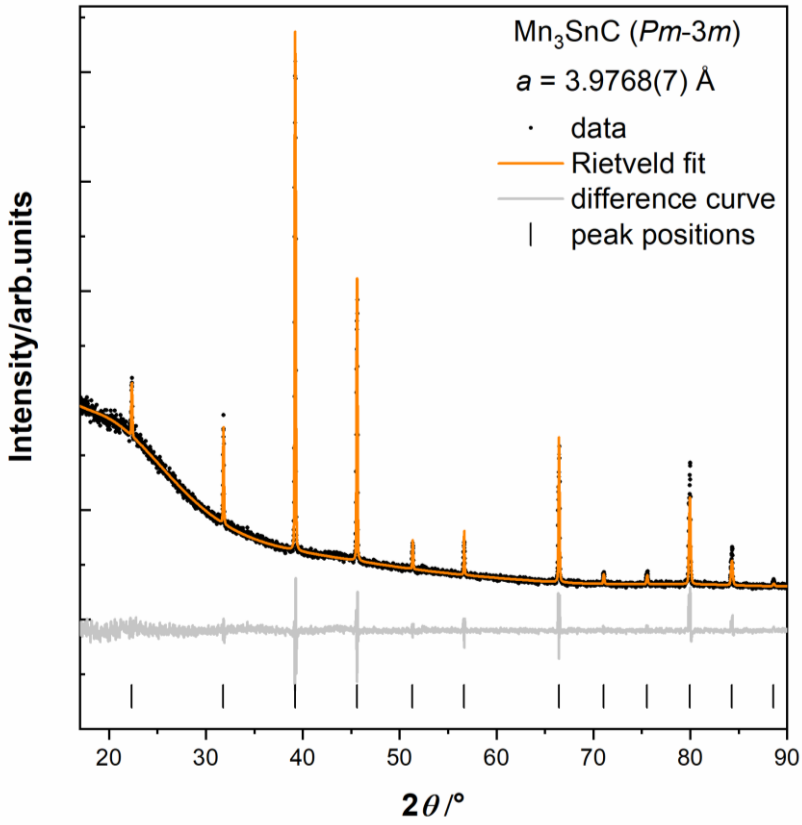

Figure 85: Results of the Rietveld refinement (orange line) and residuum curve (grey) of the X-ray powder diffraction data (black dots) of Mn_3SnC. The refinement was performed based on the structural model of Mn_3SnC[214] (space group *Pm*-3*m*). Vertical markers represent the peak positions of the antiperovskite phase.

Table 61: Results of the Rietveld refinement of Mn_3SnC based on the structural model of Mn_3SnC.[214]

Phase name	Mn_3SnC
Percentage/weight-%	100
Spacegroup	*Pm-3m*
Lattice parameters *a*/ Å	3.9768(7)
Cell volume/ $Å^3$	62.89(4)
Background order	15
R_p	2.40
R_{wp}	3.95
R_{exp}	1.74
GOF	2.27

5.3.5. Conclusion

In this chapter, the citric acid-based sol-gel process (introduced in chapter 5.2) was expanded towards first doping experiments on the *M*-site, resulting in the antiperovskite phase $Mn_{2.8}Cr_{0.2}GaC$ (nominal). Furthermore, gallium was replaced by tin in the process leading to Mn_3SnC. The Cr-doped Mn_3GaC was obtained single phase without any further purification steps needed. Rietveld refinements and SEM/EDX mappings confirm the successful formation of the product phase exhibiting a homogeneous distribution of the respective elements. On the other hand, in the synthesis of Mn_3SnC a further purification step was required by washing the phase mixture with diluted HCl solution. However, this leads to a phase pure product without any detectable crystalline side phase amounts. The synthesis of both systems confirms the versatility of the sol-gel process with a big potential to be applied to other carbide-based antiperovskite materials.

6. Summary

In this work, efficient, non-conventional solid-state methods were applied for the synthesis of selected MAX phases and antiperovskite materials. In the context of MAX phases, three hitherto unknown *M*-site solid-solution phases, as well as three new *X*-site solid-solution phases were prepared and comprehensively characterized.

The first project dealt with the synthesis of the solid-solution phase $(V_{1-x}Cr_x)_2GaC$ $(0 \leq x \leq 1)$ by using the rapid microwave heating technique (reaction times $\leq$ 1 hour), as for all following *M*-site solid-solution phases. The system showed no miscibility gap and the refined lattice parameters follow Vegard's law. Magnetic characterization revealed that all samples exhibit Pauli paramagnetic behavior, however, with a variation in the susceptibilities up to 400 % and a maximum at a nominal composition of $(V_{0.20}Cr_{0.80})_2GaC$. *Ab initio* calculations confirmed these observations and characterized the system as a prototypical itinerant Pauli paramagnet, which is nearly magnetically ordered by considering the Stoner theory ($I \cdot n(E_F) = 0.82$).

The second *M*-site solid-solution was solely based on the doping of V_2GaC with manganese, resulting in $(V_{1-x}Mn_x)_2GaC$. Up to a nominal doping level of 11 at-% no side phases were detected in the XRD data, however, the evolution of the lattice parameters did not follow a clear trend, only an overall decrease in the cell volume was observed. Despite the single-phase diffraction patterns up to 11 at-%, EDX mappings revealed slight inhomogeneities in the manganese distribution, indicating the presence of a small amount of side phases that complicate further magnetic analyses. Nonetheless, the majority was homogeneously distributed, confirming a mostly successful doping behavior for small amounts of manganese (<11 at-%).

The starting point of the third *M*-site solid-solution system was the parent phase Cr_2GaC which was successfully doped with molybdenum up to a nominal level of 50 at-% resulting in $(Cr_{1-x}Mo_x)_2GaC$ $(0 \leq x \leq 0.50)$. These results were confirmed by a linear trend of the lattice parameters, satisfying Vegard's law, and predominantly homogeneous elemental mappings. However, above 50 at-% the sample quality decreased heavily and Mo_2C switched to the thermodynamic more stable main phase in the system. The exact reasons for the suppression/decomposition still must be elaborated with further experiments.

The second focus regarding MAX phases was laid on the *X*-site. In the first project, a new two-step process to synthesize nitride and carbonitride MAX phases was introduced. First, nitrogen-rich precursors were synthesized by using the "urea-glass" sol-gel approach and the liquid ammonia method. While the latter leads to pure binary nitride phases, the sol-gel approach produces ternary carbonitride precursors. In a second step, the precursors were mixed with elemental reactants and heat treatment finalized the product formation of the MAX phase. Proof of concept of this method was demonstrated on the 211-V-Ga-C/N system, resulting in the synthesis of a hitherto unknown carbonitride $V_2GaC_{1-x}N_x$. The

mixed C/N nature was proven by means of X-ray powder diffraction, electron energy loss spectroscopy, and X-ray photoelectron spectroscopy, respectively. Additionally, SEM micrographs revealed that the morphology can be specifically influenced depending on the synthesis process, substantiating the beneficial aspect of non-conventional synthesis approaches.

The introduced sol-gel-assisted approach was then applied to the 211 Cr-Ga-C/N system leading to the synthesis of $Cr_2GaC_{1-x}N_x$. Here, the final heat treatment was substituted by microwave heating, increasing the time and energy efficiency tremendously. Again, the carbonitride character was proven by means of XRD, XPS, as well as STEM/EDX analysis. Furthermore, temperature-dependent X-ray powder diffraction analysis, magnetic characterization, as well as resistivity measurements were performed to investigate potential similarities to the spin density wave system of the nitride parent phase Cr_2GaN. However, all analyses showed that the incorporation of carbon leads to a suppression of the spin density wave state.

In the third project, a different hybrid solid-state approach was applied. First, a binary nitride was synthesized using a microwave-assisted synthesis approach, which was then further processed analogous to the first *X*-site solid-solution project, leading to the synthesis of $V_2GeC_{1-x}N_x$ ($0 \leq x \leq 1$). For further analysis, the parent phases and the carbonitride phase with $x = 0.50$ were densified using spark plasma sintering. Magnetic analysis revealed the paramagnetic state of the phases, however, with the potential to be tuned by varying the composition of the *X*-site, as the magnetization and susceptibility increase with increasing nitrogen amount. A similar trend was shown with resistivity measurements, where an increasing nitrogen amount led to a decrease in the resistivity.

In the field of antiperovskites, it was concentrated on the synthesis of the magnetocaloric interesting phase Mn_3GaC. While for the MAX phases, a new hybrid two-step process was introduced, for the Mn_3GaC a one-step citric acid-based sol-gel approach was applied for the first time, resulting in a highly phase pure product with only 5 hours of reaction time. The reaction mechanism that was elucidated by DSC/TGA measurements can be described as a carbothermic reduction. Magnetic analysis of the phase revealed the literature-known AFM-FM-PM transitions, however with different transition temperatures and a total entropy change of $|\Delta S_M| = 1$ J kg^{-1} K^{-1} which is dominated by the FM/PM transition. This is an indication of a carbon deficiency in the lattice and supports findings additionally obtained by XRD analysis. Nonetheless, by only varying the citric acid amount in the synthesis procedure, it was shown that the magnetic state can be specifically influenced in terms of stabilizing/destabilizing the ferromagnetic state of the antiperovskite phase.

In order to prove the suitability of this method for other antiperovskite systems, the solid-solution phase $Mn_{2.8}Cr_{0.2}GaC$ and the Sn-based phase Mn_3SnC were synthesized following the same procedure. Both materials were obtained single-phase, even though the Mn_3SnC needed a further purification step. Furthermore, EDX mappings confirmed a uniform distribution of chromium in the solid-solution phase.

7. Conclusion

The center of this work revolved around the synthesis and characterization of MAX phases and antiperovskite materials, two fascinating materials classes, which both possess a plethora of intriguing functional properties. The classical property profile of the former, dictated by the combination of metallic and ceramic properties, has broadened over recent years by exploring further functionalities such as magnetism by incorporating suitable elements (e.g., Mn or Fe). However, particularly the magnetic properties of MAX phases are still puzzling and highly complex due to challenges in the preparation of the target materials and the formation of disturbing side phases. Since the main synthesis routes in the literature are still based on conventional methods that strongly support the formation of thermodynamically stable side phases, one central aim of this work was to explore different strategies and non-conventional synthesis procedures to face this problem and to synthesize the target materials time and energy efficient.

Therefore, the first part of this work dealt with the rapid method of microwave heating, with its potential to enable the formation of metastable products due to fast reaction times, as well as high heating and cooling rates.[1,45] However, in contrary to only focusing on doping with manganese or iron, the first synthesis project $(V_{1-x}Cr_x)_2GaC$ aimed to understand the influence on magnetic properties of stepwise increasing the electron density over a complete solid-solution row before investigating other solid solution systems such as $(V_{1-x}Mn_x)_2GaC$ or $(Cr_{1-x}Mo_x)_2GaC$. In particular, the identification of $(V_{1-x}Cr_x)_2GaC$ as an itinerant Pauli paramagnet that is nearly magnetically ordered ($I \cdot n(E_F) = 0.82$), can now serve as a new guidance for future doping studies. It holds the potential to induce long-range magnetic ordering in MAX phases, potentially, without the mandatory doping of significant amounts of magnetic elements on the *M*-site. This in turn could strongly reduce the amount of possible side phases that are negatively influencing further characterization and application studies.

Apart from magnetically interesting *M*-site solid-solution phases, the consideration of changing the *X*-site composition of MAX phases to influence the functional or magnetic properties is not a frequently discussed option in the literature. Up to now, Cr_2GaN[119] forms the hitherto only parent nitride phase that has been magnetically characterized, while carbonitrides, in general, represent an almost unexplored field concerning MAX phases. Similar to the *M*-site doping, preparative challenges aggravate the synthesis of nitrogen-containing MAX phases. This led to the second project of this work, to develop new synthesis strategies for carbonitride and nitride MAX phases, as well as to gain new insights into the functional and magnetic properties of these materials based on varying the nitrogen amount. By combining literature-known wet-chemical/microwave-assisted methods with conventional preparation techniques, two new strategies to synthesize carbonitrides and nitrides have been developed. These approaches have the great potential to be expanded beyond the investigated V/Cr-Ga/Ge-C-N systems and to significantly increase the phase variety in the field of nitrides and carbonitrides. Besides the new

synthesis approaches, the characterization studies revealed that the nitrogen-containing materials exhibit improved magnetic properties in comparison to the carbide counterparts with the opportunity to be tailored based on the nitrogen amount. This provides a further variation and supporting opportunity next to *M*-site doping approaches, which simultaneously opens a new broad field of research in magnetic studies of MAX phases.

On the other hand, selected antiperovskite materials such as Mn_3GaC already possess the previously discussed and desired magnetic ordering, however, exhibiting the similarity that their synthesis is also mainly restricted to conventional methods. This led to the third main project of this work to establish a new time-saving synthesis route only based on a wet-chemical approach for an already magnetically ordered material. Due to the simplicity of the established synthesis strategy, it holds great potential to be expanded to further carbide-based antiperovskites or to approach hitherto unknown systems that have been already proposed.[217] This in turn could lead to the synthesis of new magnetocaloric interesting materials combined with an enhanced processability and the potential to be applied in future cooling systems.

Overall, this work demonstrated the great capability of alternative synthesis approaches, so far known as “unconventional” solid-state methods, to not only improve the processability and time efficiency of the respective syntheses but also to enable the preparation of new functional materials with targeted materials design and tailored properties. With this regard, it must be emphasized that the introduced and discussed methods are not only restricted to the presented material classes of MAX phases and antiperovskites. Instead, they shall provide new strategies in all different fields of nitride and carbide-based materials where a substitution of energy- and time-consuming conventional solid-state methods is conceivable.

8. References

[1] J. P. Siebert, C. M. Hamm, C. S. Birkel, *Appl. Phys. Rev* **2019**, *6*, 41314.

[2] M. F. Groh, M. Heise, M. Kaiser, M. Ruck, *Nachrichten aus der Chemie* **2013**, *61*, 26–29.

[3] M. W. Barsoum, *MAX Phases: Properties of Machinable Ternary Carbides and Nitrides*, Wiley, **2013**.

[4] L. Chen, Y. Li, K. Chen, X. Bai, M. Li, S. Du, Z. Chai, Q. Huang, *Small Struct.* **2023**, *4*, 2200161.

[5] Z. Du, C. Wu, Y. Chen, Q. Zhu, Y. Cui, H. Wang, Y. Zhang, X. Chen, J. Shang, B. Li, W. Chen, C. Liu, S. Yang, *Adv. Energy Mater.* **2022**, *12*, 2103228.

[6] A. S. Ingason, A. Petruhins, M. Dahlqvist, F. Magnus, A. Mockute, B. Alling, L. Hultman, I. A. Abrikosov, P. O. Å. Persson, J. Rosen, *Mater. Res. Innov.* **2014**, *2.2*, 89–93.

[7] A. S. I. and M. D. and J. Rosen, A. S. Ingason, M. Dahlqvist, J. Rosén, A. S. Ingason, M. Dahlqvist, J. Rosén, M. Max, *J. Phys. Condens. Matter* **2016**, *28*, 433003.

[8] M. Naguib, O. Mashtalir, J. Carle, V. Presser, J. Lu, L. Hultman, Y. Gogotsi, M. W. Barsoum, *ACS Nano* **2012**, *6*, 1322–1331.

[9] M. Naguib, M. W. Barsoum, Y. Gogotsi, *Adv. Mater.* **2021**, *33*, 2103393.

[10] G. Rose, *J. für Prakt. Chemie* **1840**, *19*, 459–468.

[11] Y. Wang, H. Zhang, J. Zhu, X. Lü, S. Li, R. Zou, Y. Zhao, *Adv. Mater.* **2020**, *32*, 1905007.

[12] W. Xia, Y. Zhao, F. Zhao, K. Adair, R. Zhao, S. Li, R. Zou, Y. Zhao, X. Sun, *Chem. Rev.* **2022**, *122*, 3763–3819.

[13] Z. Deng, M. Ou, J. Wan, S. Li, Y. Li, Y. Zhang, Z. Deng, J. Xu, Y. Qiu, Y. Liu, C. Fang, Q. Li, L. Huang, J. Zhu, S. Han, J. Han, Y. Zhao, *Chem. Mater.* **2020**, *32*, 8827–8835.

[14] M. Oudah, A. Ikeda, J. N. Hausmann, S. Yonezawa, T. Fukumoto, S. Kobayashi, M. Sato, Y. Maeno, *Nat. Commun.* **2016**, *7*, 13617.

[15] B. He, C. Dong, L. Yang, X. Chen, L. Ge, L. Mu, Y. Shi, *Supercond. Sci. Technol.* **2013**, *26*, 125015.

[16] K. Asano, K. Koyama, K. Takenaka, *Appl. Phys. Lett.* **2008**, *92*, 161909.

[17] T. Tohei, H. Wada, T. Kanomata, *J. Appl. Phys.* **2003**, *94*, 1800–1802.

[18] M. Sokol, V. Natu, S. Kota, M. W. Barsoum, *Trends Chem.* **2019**, *1*, 210–223.

[19] C. Giordano, C. Erpen, W. Yao, B. Milke, M. Antonietti, *Chem. Mater.* **2009**, *21*, 5136–5144.

[20] A.-M. Zieschang, R. Seshadri, B. Albert, *Chem. Mater.* **2017**, *29*, 621–628.

[21] A.-M. Zieschang, Nanopartikuläre 3d-Übergangsmetallnitride Aus Flüssigem Ammoniak, Technische Universität Darmstadt, **2019**.

[22] Ö. Çakır, M. Acet, *Appl. Phys. Lett.* **2012**, *100*, 202404.

[23] F. Scheibel, T. Gottschall, A. Taubel, M. Fries, K. P. Skokov, A. Terwey, W. Keune, K. Ollefs, H. Wende, M. Farle, M. Acet, O. Gutfleisch, M. E. Gruner, *Energy Technol.* **2018**, *6*, 1397–1428.

[24] J. P. Siebert, L. Bischoff, M. Lepple, A. Zintler, L. Molina-Luna, U. Wiedwald, C. S. Birkel, *J. Mater. Chem. C* **2019**, *7*, 6034–6040.

[25] G. Deysher, C. E. Shuck, K. Hantanasirisakul, N. C. Frey, A. C. Foucher, K. Maleski, A. Sarycheva, V. B. Shenoy, E. A. Stach, B. Anasori, Y. Gogotsi, *ACS Nano* **2020**, *14*, 204–217.

[26] H. Kudielka, H. Rohde, *Zeitschrift für Krist.* **1960**, *114*, 447–456.

[27] W. Jeitschko, H. Nowotny, F. Benesovsky, *Monatshefte für Chemie* **1964**, *95*, 178–179.

[28] W. Jeitschko, H. Nowotny, F. Benesovsky, *Monatshefte für Chemie* **1964**, *95*, 156–157.

[29] W. Jeitschko, H. Nowotny, F. Benesovsky, *Monatshefte für Chemie* **1963**, *94*, 672–676.

[30] W. Jeitschko, H. Nowotny, F. Benesovsky, *Monatshefte für Chemie* **1963**, *94*, 1201–1205.

[31] W. Jeitschko, H. Nowotny, F. Benesovsky, *Monatshefte für Chemie* **1964**, *95*, 431–435.

[32] W. Jeitschko, H. Nowotny, F. Benesovsky, *Monatshefte für Chemie* **1963**, *94*, 844–850.

[33] M. W. Barsoum, T. El-Raghy, *J. Am. Ceram. Soc.* **1996**, *79*, 1953–1956.

[34] M. W. Barsoum, *Prog. Solid State Chem.* **2000**, *28*, 201–281.

[35] J. Wang, T.-N. Ye, Y. Gong, J. Wu, N. Miao, T. Tada, H. Hosono, *Nat. Commun.* **2019**, *10*, 2284.

[36] N. Kubitza, C. Büchner, J. Sinclair, R. Snyder, C. S. Birkel, *Chempluschem* **2023**, *88*, e202300214.

[37] K. Sobolev, H. Pazniak, M. Farle, V. Rodionova, U. Wiedwald, *J. Mater. Chem. C* **2021**, *9*, 16516–16522.

[38] J. P. Siebert, S. Mallett, M. Juelsholt, H. Pazniak, U. Wiedwald, K. Page De, C. S. Birkel, K. Page, C. S. Birkel, *Mater. Chem. Front.* **2021**, *5*, 6082–6091.

[39] C. M. Hamm, M. Dürrschnabel, L. Molina-Luna, R. Salikhov, D. Spoddig, M. Farle, U. Wiedwald, C. S. Birkel, *Mater. Chem. Front.* **2018**, *2*, 483–490.

[40] C. M. Hamm, J. D. Bocarsly, G. Seward, U. I. Kramm, C. S. Birkel, *J. Mater. Chem. C* **2017**, *5*, 5700–5708.

[41] A. Petruhins, J. Lu, L. Hultman, J. Rosen, *Mater. Res. Lett.* **2019**, *7*, 446–452.

[42] Q. Tao, J. Lu, M. Dahlqvist, A. Mockute, S. Calder, A. Petruhins, R. Meshkian, O. Rivin, D. Potashnikov, E. N. Caspi, *Chem. Mater.* **2019**, *31*, 2476–2485.

[43] M. A. Peña, J. L. G. Fierro, *Chem. Rev.* **2001**, *101*, 1981–2018.

[44] H. J. Kitchen, S. R. Vallance, J. L. Kennedy, N. Tapia-Ruiz, L. Carassiti, A. Harrison, A. G. Whittaker, T. D. Drysdale, S. W. Kingman, D. H. Gregory, *Chem. Rev.* **2014**, *114*, 1170–1206.

[45] K. J. Rao, B. Vaidhyanathan, M. Ganguli, P. A. Ramakrishnan, *Chem. Mater.* **1999**, *11.4*, 882–895.

[46] O. Guillon, J. Gonzalez-Julian, B. Dargatz, T. Kessel, G. Schierning, J. Räthel, M. Herrmann, *Adv. Eng. Mater.* **2014**, *16*, 830–849.

[47] Z. A. Munir, U. Anselmi-Tamburini, M. Ohyanagi, *J. Mater. Sci.* **2006**, *41*, 763–777.

[48] E. D. Rodeghiero, B. C. Moore, B. S. Wolkenberg, M. Wuthenow, O. K. Tse, E. P. Giannelis, *Mater. Sci. Eng. A* **1998**, *244*, 11–21.

[49] L. L. Hench, J. K. West, *Chem. Rev.* **1990**, *90*, 33–72.

[50] M. Kallala, C. Sanchez, B. Cabane, *Phys. Rev. E* **1993**, *48*, 3692–3704.

[51] A. E. Danks, S. R. Hall, Z. Schnepp, *Mater. Horiz.* **2016**, *3*, 91–112.
[52] Ľ. Bača, N. Stelzer, *J. Eur. Ceram. Soc.* **2008**, *28*, 907–911.
[53] C. Giordano, C. Erpen, W. Yao, M. Antonietti, *Nano Lett.* **2008**, *8*, 4659–4663.
[54] L. Zhao, K. Fang, D. Jiang, D. Li, Y. Sun, *Catal. Today* **2010**, *158*, 490–495.
[55] J. P. Siebert, K. Patarakun, C. S. Birkel, *Inorg. Chem.* **2022**, *61*, 1603–1610.
[56] J. J. Lagowski, *Synth. React. Inorganic, Met. Nano-Metal Chem.* **2007**, *37*, 115–153.
[57] G. W. A. Fowles, D. Nicholls, *Q. Rev. Chem. Soc.* **1962**, *16*, 19.
[58] D. S. Thompson, M. J. Stone, J. S. Waugh, *J. Phys. Chem.* **1966**, *70*, 934–935.
[59] J. F. Chittum, H. Hunt, *J. Phys. Chem.* **1936**, *40*, 581–589.
[60] S. Hartweg, A. H. C. West, B. L. Yoder, R. Signorell, *Angew. Chemie* **2016**, *128*, 12535–12538.
[61] A. M. Zieschang, J. D. Bocarsly, M. Dürrschnabel, H. J. Kleebe, R. Seshadri, B. Albert, *Chem. Mater.* **2018**, *30*, 1610–1616.
[62] W. Massa, *Kristallstrukturbestimmung*, GWV Fachverlage GmbH, Wiesbaden, **2009**.
[63] A. R. West, *Solid State Chemistry and Its Applications*, John Wiley & Sons, Ltd, Chichester, **2014**.
[64] R. E. Dinnebier, S. J. . Billinge, *Powder Diffraction: Theory and Practice*, RSC Publishing, **2008**.
[65] H. M. Rietveld, *J. Appl. Crystallogr.* **1969**, *2*, 65–71.
[66] *ICSD Inorganic Structure Database*, Karlsruhe, **2020**.
[67] B. H. Toby, *Powder Diffr.* **2006**, *21*, 67–70.
[68] B. H. Toby, *Int. Tables Crystallogr.* **2019**, *H*, 465–472.
[69] B. AXS, *TOPAS V.6*, Karlsruhe, **2016**.
[70] P. Scherrer, *Nachrichten von der Gesellschaft der Wissenschaften zu Göttingen* **1918**, *2*, 98–100.
[71] F. T. L. Muniz, M. A. R. Miranda, C. Morilla dos Santos, J. M. Sasaki, *Acta Crystallogr. Sect. A Found. Adv.* **2016**, *72*, 385–390.
[72] A. Le Bail, H. Duroy, J. L. Fourquet, *Mater. Res. Bull.* **1988**, *23*, 447–452.
[73] F. A. Stevie, C. L. Donley, *J. Vac. Sci. Technol. A* **2020**, *38*, 063204.
[74] C. Kalha, N. K. Fernando, P. Bhatt, F. O. L. L. Johansson, A. Lindblad, H. H. Rensmo, L. Z. L. Z. Medina, R. Lindblad, S. Siol, L. P. H. H. Jeurgens, C. Cancellieri, K. Rossnagel, K. Medjanik, G. Schönhense, M. Simon, A. X. Gray, S. Nemšák, P. Lömker, C. Schlueter, A. Regoutz, G. Schonhense, M. Simon, A. X. Gray, S. Nemsak, P. Lomker, C. Schlueter, A. Regoutz, *J. Phys. Condens. Matter* **2021**, *33*, 233001.
[75] B. J. Inkson, in *Mater. Charact. Using Nondestruct. Eval. Methods* (Eds.: G. Hübschen, I. Altpeter, R. Tschuncky, H.-G. Herrmann), Woodhead Publishing, **2016**, pp. 17–43.
[76] B. J. Griffin, *Scanning* **2011**, *33*, 162–173.
[77] G. Schwedt, T. C. Schmidt, O. J. Schmitz, *Analytische Chemie Grundlagen, Methoden Und Praxis*, WILEY-VCH Verlag GmbH & Co. KG, Weinheim, **2016**.

[78] V. J. Keast, *Mater. Charact.* **2012**, *73*, 1–7.

[79] S. Foner, *Rev. Sci. Instrum.* **1959**, *30*, 548–557.

[80] I. Galili, D. Kaplan, Y. Lehavi, *Am. J. Phys.* **2006**, *74*, 337–343.

[81] M. Faraday, *Philos. Trans. R. Soc. London* **1832**, *122*, 125–162.

[82] A. O. Adeyeye, G. Shimon, in *Magn. Surfaces, Interfaces, Nanoscale Mater.* (Eds.: R.E. Camley, Z. Celinski, R.L.B.T.-H. of S.S. Stamps), North-Holland, **2015**, pp. 1–41.

[83] Y. Singh, *Int. J. Mod. Phys. Conf. Ser.* **2013**, *22*, 745–756.

[84] D. Q. M. Craig, M. Reading, *Thermal Analysis of Pharmaceuticals*, CRC Press, **2006**.

[85] S. R. Byrn, G. Zografi, X. (Sean) Chen, in *Solid State Prop. Pharm. Mater.*, **2017**, pp. 124–141.

[86] J. C. Schuster, H. Nowotny, *Dedic. to Prof. Dr. Konrad Schubert his 65th Birthd.* **1980**, *71*, 341–346.

[87] J. C. Schuster, H. Nowotny, C. Vaccaro, *J. Solid State Chem.* **1980**, *32*, 213–219.

[88] S. Sridharan, H. Nowotny, **1983**, *74*, 468–472.

[89] I. Salama, T. El-Raghy, M. W. Barsoum, *J. Alloys Compd.* **2002**, *347*, 271–278.

[90] M. W. Barsoum, J. Golczewski, H. J. Seifert, F. Aldinger, *J. Alloys Compd.* **2002**, *340*, 173–179.

[91] T. Lapauw, B. Tunca, D. Potashnikov, A. Pesach, O. Ozeri, J. Vleugels, K. Lambrinou, *Sci. Rep.* **2018**, *8*, 12801.

[92] Z. Liu, L. Zheng, L. Sun, Y. Qian, J. Wang, M. Li, *J. Am. Ceram. Soc.* **2014**, *97*, 67–69.

[93] V. J. Keast, S. Harris, D. K. Smith, *Phys. Rev. B* **2009**, *80*, 214113.

[94] Y. Tan, Y. Xia, Z. Teng, C. Chen, X. Zhou, H. Zhang, *J. Eur. Ceram. Soc.* **2021**, *41*, 4658–4665.

[95] D. Yu, Y. Tan, *Ceram. Int.* **2021**, *47*, 30188–30193.

[96] L. Wang, Q. Chen, T. Yang, B. Guo, Y. Cheng, W. Xu, *J. Mater. Sci. Mater. Electron.* **2022**, *33*, 17446–17452.

[97] L. Qu, G. Bei, B. Stelzer, H. Rueß, J. M. Schneider, D. Cao, S. van der Zwaag, W. G. Sloof, *Ceram. Int.* **2019**, *45*, 1400–1408.

[98] M. W. Barsoum, I. Salama, T. El-Raghy, J. Golczewski, W. D. Porter, H. Wang, H. J. Seifert, F. Aldinger, *Metall. Mater. Trans. A Phys. Metall. Mater. Sci.* **2002**, *33*, 2775–2779.

[99] A. S. Ingason, A. Mockute, M. Dahlqvist, F. Magnus, S. Olafsson, U. B. Arnalds, B. Alling, I. A. Abrikosov, B. Hjörvarsson, P. O. Å. Persson, J. Rosen, *Phys. Rev. Lett.* **2013**, *110*, 195502.

[100] J. M. Schneider, Z. Sun, R. Mertens, F. Uestel, R. Ahuja, *Solid State Commun.* **2004**, *130*, 445–449.

[101] M. Dahlqvist, B. Alling, J. Rosen, *J. Phys. Condens. Matter* **2015**, *27*, 95601.

[102] M. Jaouen, M. Bugnet, N. Jaouen, P. Ohresser, V. Mauchamp, T. Cabioc'h, A. Rogalev, *J. Phys. Condens. Matter* **2014**, *26*, 176002.

[103] A. Petruhins, A. S. Ingason, J. Lu, F. Magnus, S. Olafsson, J. Rosen, *J. Mater. Sci.* **2015**, *50*, 4495–4502.

[104] R. Salikhov, A. S. Semisalova, A. Petruhins, A. S. Ingason, J. Rosen, U. Wiedwald, M. Farle, *Mater. Res. Lett.* **2015**, *3*, 156–160.

[105] M. Magnuson, M. Mattesini, *J. Magn. Magn. Mater.* **2020**, *501*, 166470.

[106] A. Mockute, P. O. Å. Persson, F. Magnus, A. S. Ingason, S. Olafsson, L. Hultman, J. Rosen, *Phys. status solidi – Rapid Res. Lett.* **2014**, *8*, 420–423.

[107] A. Mockute, J. Lu, E. J. Moon, M. Yan, B. Anasori, S. J. May, M. W. Barsoum, J. Rosen, *Mater. Res. Lett.* **2015**, *3*, 16–22.

[108] Z. Liu, T. Waki, Y. Tabata, H. Nakamura, *Phys. Rev. B* **2014**, *89*, 54435.

[109] Q. Tao, R. Salikhov, A. Mockute, J. Lu, M. Farle, U. Wiedwald, J. Rosen, *APL Mater.* **2016**, *4*, 86109.

[110] D. Ohmer, I. Opahle, H. K. Singh, H. Zhang, *J. Phys. Condens. Matter* **2019**, *31*, 405902.

[111] A. M. Malik, J. Rohrer, K. Albe, *Phys. Rev. Mater.* **2023**, *7*, 44408.

[112] H Ebert, S Mankovskyy, H Freyer, M Deng, *J. Phys. Condens. Matter* **2003**, *15*, S617.

[113] M Deng, H Freyer, J Voitländer, H Ebert, *J. Phys. Condens. Matter* **2001**, *13*, 8551.

[114] B. L. Gyorffy, *Phys. Rev. B* **1972**, *5*, 2382–2384.

[115] M. Rahm, R. Hoffmann, N. W. Ashcroft, *Chem. - A Eur. J.* **2016**, *22*, 14625–14632.

[116] L. Vegard, *Zeitschrift für Phys.* **1921**, *5*, 17–26.

[117] I. R. Shein, A. L. Ivanovskii, *Phys. C Supercond.* **2010**, *470*, 533–537.

[118] H. Tong, S. Lin, Y. Huang, P. Tong, W. Song, Y. Sun, *Intermetallics* **2019**, *105*, 39–43.

[119] Z. Liu, T. Waki, Y. Tabata, K. Yuge, H. Nakamura, I. Watanabe, *Phys. Rev. B - Condens. Matter Mater. Phys.* **2013**, *88*, 1–7.

[120] P. Mohn, *Magnetism in the Solid State: An Introduction*, Springer Science & Business Media, **2002**.

[121] C. Hu, C. Li, J. Halim, S. Kota, D. J. Tallman, M. W. Barsoum, *J. Am. Ceram. Soc.* **2015**, *98*, 2713–2715.

[122] T. Ungár, *Scr. Mater.* **2004**, *51*, 777–781.

[123] J. Etzkorn, M. Ade, D. Kotzott, M. Kleczek, H. Hillebrecht, *J. Solid State Chem.* **2009**, *182*, 995–1002.

[124] R. J. Fries, C. P. Kempter, *Anal. Chem.* **1960**, *32*, 1898.

[125] A. L. Greenaway, C. L. Melamed, M. B. Tellekamp, R. Woods-Robinson, E. S. Toberer, J. R. Neilson, A. C. Tamboli, *Annu. Rev. Mater. Res.* **2020**, *51*, 1–28.

[126] J. M. D. Coey, P. A. I. Smith, *J. Magn. Magn. Mater.* **1999**, *200*, 405–424.

[127] T. Joelsson, A. Hörling, J. Birch, L. Hultman, *Appl. Phys. Lett.* **2005**, *86*, 111913.

[128] T. Scabarozi, A. Ganguly, J. D. Hettinger, S. E. Lofland, S. Amini, P. Finkel, T. El-Raghy, M. W. Barsoum, *J. Appl. Phys.* **2008**, *104*, 73713.

[129] Z. J. Lin, M. J. Zhuo, M. S. Li, J. Y. Wang, Y. C. Zhou, *Scr. Mater.* **2007**, *56*, 1115–1118.

[130] M. W. Barsoum, M. Ali, T. El-Raghy, *Metall. Mater. Trans. A Phys. Metall. Mater. Sci.* **2000**, *31*, 1857–1865.

[131] Y. Liu, L. Zhang, W. Xiao, L. Zhang, Y. Pu, S. Guo, *Mater. Lett.* **2015**, *149*, 5–7.

[132] W. Jeitschko, H. Nowotny, F. Benesovsky, *Monatshefte für Chemie* **1963**, *94*, 1198–1200.

[133] L. Gröner, L. Mengis, M. Galetz, L. Kirste, P. Daum, M. Wirth, F. Meyer, A. Fromm, B. Blug, F. Burmeister, *Materials (Basel)*. **2020**, *13*, DOI 10.3390/ma13092085.

[134] B. Keskin, S. A. Naziri Mehrabani, S. Arefi-Oskoui, V. Vatanpour, O. Orhun Teber, A. Khataee, Y. Orooji, I. Koyuncu, *Carbohydr. Polym.* **2022**, *296*, 119913.

[135] P. Urbankowski, B. Anasori, T. Makaryan, D. Er, S. Kota, P. L. Walsh, M. Zhao, V. B. Shenoy, M. W. Barsoum, Y. Gogotsi, *Nanoscale* **2016**, *8*, 11385–11391.

[136] Y. Li, J. Liu, W. Liu, X. Zhu, H. H. Wen, *Philos. Mag.* **2015**, *95*, 2831–2837.

[137] A. D. Bortolozo, G. Serrano, A. Serquis, D. Rodrigues, C. A. M. Dos Santos, Z. Fisk, A. J. S. MacHado, *Solid State Commun.* **2010**, *150*, 1364–1366.

[138] W. Jeitschko, I. L. Nowotny, F. Benesovsky, H. Nowotny, F. Benesovsky, *Monatshefte für Chemie* **1964**, *95*, 178–179.

[139] O. Beckmann, H. Boller, H. Nowotny, F. Benesovsky, *Monatshefte für Chemie* **1969**, *100*, 1465–1470.

[140] Y. Li, J. Liang, H. Ding, J. Lu, X. Mu, P. Yan, X. Zhang, K. Chen, M. Li, P. O. Å. Persson, L. Hultman, P. Eklund, S. Du, H. Yang, Z. Chai, Q. Huang, *Appl. Phys. Rev.* **2021**, *8*(3).

[141] H. Ding, Y. Li, J. Lu, K. Luo, K. Chen, M. Li, P. O. Å. Persson, L. Hultman, P. Eklund, S. Du, Z. Huang, Z. Chai, H. Wang, P. Huang, Q. Huang, *Mater. Res. Lett.* **2019**, *7*, 510–516.

[142] M. Li, J. Lu, K. Luo, Y. Li, K. Chang, K. Chen, J. Zhou, J. Rosen, L. Hultman, P. Eklund, P. O. Å. Persson, S. Du, Z. Chai, Z. Huang, Q. Huang, *J. Am. Chem. Soc.* **2019**, *141*, 4730–4737.

[143] M. A. Pietzka, J. C. Schuster, *J. Am. Ceram. Soc.* **1996**, *79*, 2321–2330.

[144] T. Cabioc'h, P. Eklund, V. Mauchamp, M. Jaouen, *J. Eur. Ceram. Soc.* **2012**, *32*, 1803–1811.

[145] C. Schlueter, A. Gloskovskii, K. Ederer, I. Schostak, S. Piec, I. Sarkar, Y. Matveyev, P. Lömker, M. Sing, R. Claessen, C. Wiemann, C. M. Schneider, K. Medjanik, G. Schönhense, P. Amann, A. Nilsson, W. Drube, *AIP Conf. Proc.* **2019**, *2054*.

[146] S. Hosoya, T. Yamagishi, M. Tokonami, *J. Phys. Soc. Japan* **1968**, *24*, 363–367.

[147] C. E. Rice, W. R. Robinson, *J. Solid State Chem.* **1977**, *21*, 145–154.

[148] J. P. Siebert, S. Mallett, M. Juelsholt, H. Pazniak, U. Wiedwald, K. Page De, C. S. Birkel, *Mater. Chem. Front* **2021**, *5*, 6082.

[149] A. Bouhemadou, *Solid State Sci.* **2009**, *11*, 1875–1881.
[150] J. H. VANVUCHT, H. A. C. Bruning, D. HC, D. AH, *Philips Res. Reports* **1964**, *19*, 407.
[151] G. Hug, M. Jaouen, M. W. Barsoum, *Phys. Rev. B* **2005**, *71*, 24105.
[152] W. Yu, V. Mauchamp, T. Cabioc'H, D. Magne, L. Gence, L. Piraux, V. Gauthier-Brunet, S. Dubois, *Acta Mater.* **2014**, *80*, 421–434.
[153] K. Momma, F. Izumi, *J. Appl. Crystallogr.* **2011**, *44*, 1272–1276.
[154] R. Nyholm, N. Martensson, A. Lebugle, U. Axelsson, *J. Phys. F Met. Phys.* **1981**, *11*, 1727.
[155] A. A. Eliseev, V. A. Efremov, G. M. Kuz'mischeva, K. S. Konovalova, *So.Phys.-Crystallogr.* **1986**, *31*, 478–479.
[156] C. Giordano, M. Antonietti, *Nano Today* **2011**, *6*, 366–380.
[157] L. Farber, M. W. Barsoum, *J. Mater. Res.* **1999**, *14*, 2560–2566.
[158] J. Rodríguez-Carvajal, *Phys. B Condens. Matter* **1993**, *192*, 55–69.
[159] G. Kresse, D. Joubert, *Phys. Rev. B* **1999**, *59*, 1758–1775.
[160] G. Kresse, J. Furthmüller, *Phys. Rev. B* **1996**, *54*, 11169–11186.
[161] J. P. Perdew, K. Burke, M. Ernzerhof, *Phys. Rev. Lett.* **1996**, *77*, 3865–3868.
[162] L. Bellaiche, D. Vanderbilt, *Phys. Rev. B* **2000**, *61*, 7877–7882.
[163] R. Blix, *Zeitschrift für Phys. Chemie* **1929**, *3B*, 229–239.
[164] M. Nardin, G. Lorthioir, M. Barberon, R. Madar, M. E. Fruchart, R. Fruchart, *Comptes Rendus Hebd. des Seances des Sci. Ser. C, Sci. Chim.* **1972**, *274*, 2168–2171.
[165] H.-G. Meissner, K. Schubert, *Zeitschrift für Met.* **1965**, *56*, 523–530.
[166] "Materials Data on Cr_3Ga by Materials Project (Dataset) | DOE Data Explorer," can be found under https://www.osti.gov/dataexplorer/biblio/dataset/1188696, **2021.**
[167] H. Shinotsuka, S. Tanuma, C. J. Powell, D. R. Penn, *Surf. Interface Anal.* **2015**, *47*, 871–888.
[168] M. Project, "Materials Data on Cr_2GaC," DOI doi:10.17188/1195337, **2020**.
[169] M. Detroye, F. Reniers, C. Buess-Herman, J. Vereecken, *Appl. Surf. Sci.* **1999**, *144–145*, 78–82.
[170] M. H. Tran, A. M. Malik, M. Dürrschnabel, A. Regoutz, P. Thakur, T.-L. Lee, D. Perera, L. Molina-Luna, K. Albe, J. Rohrer, *Dalt. Trans.* **2020**, *49*, 12215–12221.
[171] A. Picone, A. Lodesani, M. Capra, A. Brambilla, F. Bottegoni, M. Jugovac, A. K. Kundu, P. M. Sheverdyaeva, P. Moras, *Appl. Surf. Sci.* **2022**, *599*, 153926.
[172] I. Bertóti, *Surf. Coatings Technol.* **2002**, *151–152*, 194–203.
[173] K. Artyushkova, *J. Vac. Sci. Technol. A* **2020**, *38*, 31002.
[174] W. Nolting, in (Ed.: W. Nolting), Springer Berlin Heidelberg, Berlin, Heidelberg, **2014**, pp. 279–415.
[175] P. Tong, Y. P. Sun, X. B. Zhu, W. H. Song, *Phys. Rev. B* **2006**, *73*, 245106.
[176] L. Schoop, M. Hirschberger, J. Tao, C. Felser, N. P. Ong, R. J. Cava, *Phys. Rev. B* **2014**, *89*, 224417.

[177] S. Lin, Y. Huang, L. Zu, X. Kan, J. Lin, W. Song, P. Tong, X. Zhu, Y. Sun, *J. Alloys Compd.* **2016**, *680*, 452–461.

[178] N. E. Alekseevskii, G. V Samsonov, O. I. Shulishova, *Zh. Eksperim. i Teor. Fiz.* **1963**, *44*.

[179] B. Manoun, S. Amini, S. Gupta, S. K. Saxena, M. W. Barsoum, *J. Phys. Condens. Matter* **2007**, *19*, 456218.

[180] M. Magnuson, O. Wilhelmsson, M. Mattesini, S. Li, R. Ahuja, O. Eriksson, H. Högberg, L. Hultman, U. Jansson, *Phys. Rev. B* **2008**, *78*, 35117.

[181] B. Vaidhyanathan, D. K. Agrawal, R. Roy, *J. Mater. Res.* **2000**, *15*, 974–981.

[182] J.-X. Yi, P. Chen, D.-L. Li, X.-B. Xiao, W.-B. Zhang, B.-Y. Tang, *Solid State Commun.* **2010**, *150*, 49–53.

[183] D. Y. Karpenkov, A. Y. Karpenkov, K. P. Skokov, I. A. Radulov, M. Zheleznyi, T. Faske, O. Gutfleisch, *Phys. Rev. Appl.* **2020**, *13*, 34014.

[184] N. A. Phatak, S. K. Saxena, Y. Fei, J. Hu, *J. Alloys Compd.* **2009**, *475*, 629–634.

[185] N. Kubitza, A. Reitz, A.-M. Zieschang, H. Pazniak, B. Albert, C. Kalha, C. Schlueter, A. Regoutz, U. Wiedwald, C. S. Birkel, *Inorg. Chem.* **2022**, *61*, 10634–10641.

[186] A. S. Cooper, *Acta Crystallogr.* **1962**, *15*, 578–582.

[187] H. Holleck, H. Nowotny, F. Benesovsky, *Monatshefte für Chemie und verwandte Teile anderer Wissenschaften* **1963**, *94*, 497–501.

[188] N. Kubitza, R. Xie, I. Tarasov, C. Shen, H. Zhang, U. Wiedwald, C. S. Birkel, *Chem. Mater.* **2023**, *35*, 4427–4434.

[189] A. Wexler, W. S. Corak, *Phys. Rev.* **1952**, *85*, 85–90.

[190] S. Lin, P. Tong, B. S. Wang, Y. N. Huang, W. H. Song, Y. P. Sun, *J. Alloys Compd.* **2014**, *584*, 308–314.

[191] A. Reitz, H. Pazniak, C. Shen, H. K. Singh, K. Jayanthi, N. Kubitza, A. Navrotsky, H. Zhang, U. Wiedwald, C. S. Birkel, *Chem. Mater.* **2022**, *34*, 10304–10310.

[192] Z. Liu, K. Takao, T. Waki, Y. Tabata, H. Nakamura, *J. Phys. Conf. Ser.* **2017**, *868*, 12016.

[193] J. D. Hettinger, S. E. Lofland, P. Finkel, T. Meehan, J. Palma, K. Harrell, S. Gupta, A. Ganguly, T. El-Raghy, M. W. Barsoum, *Phys. Rev. B* **2005**, *72*, 115120.

[194] O. Gutfleisch, T. Gottschall, M. Fries, D. Benke, I. Radulov, K. P. Skokov, H. Wende, M. Gruner, M. Acet, P. Entel, M. Farle, *Philos. Trans. R. Soc. A Math. Phys. Eng. Sci.* **2016**, *374*, 20150308.

[195] F. Scheibel, T. Gottschall, K. Skokov, O. Gutfleisch, M. Ghorbani-Zavareh, Y. Skourski, J. Wosnitza, Ö. Çakır, M. Farle, M. Acet, *J. Appl. Phys.* **2015**, *117*, 233902.

[196] D. Fruchart, E. F. Bertaut, *J. Phys. Soc. Japan* **1978**, *44*, 781–791.

[197] T. Kanomata, M. Kikuchi, T. Kaneko, K. Kamishima, M. I. Bartashevich, H. A. Katori, T. Goto, *Solid State Commun.* **1997**, *101*, 811–814.

[198] M.-H. Yu, L. H. Lewis, A. R. Moodenbaugh, *J. Appl. Phys.* **2003**, *93*, 10128–10130.

[199] J. García, J. Bartolomé, D. Goṅzález, R. Navarro, D. Fruchart, *J. Chem. Thermodyn.* **1983**, *15*, 1059–1069.

[200] L. H. Lewis, D. Yoder, A. R. Moodenbaugh, D. A. Fischer, M. H. Yu, *J. Phys. Condens. Matter* **2006**, *18*, 1677.

[201] E. T. Dias, K. R. Priolkar, A. K. Nigam, *J. Magn. Magn. Mater.* **2014**, *363*, 140–144.

[202] J.-P. Sénateur, J.-P. Bouchaud, R. Fruchart, *Bull. Minéralogie* **1967**, *90*, 537–543.

[203] T. Tohei, H. Wada, T. Kanomata, *J. Magn. Magn. Mater.* **2004**, *272–276*, E585–E586.

[204] B. S. Wang, P. Tong, Y. P. Sun, W. Tang, L. J. Li, X. B. Zhu, Z. R. Yang, W. H. Song, *Phys. B Condens. Matter* **2010**, *405*, 2427–2430.

[205] T. Harada, K. Tsuda, R. Chiba, T. Kanomata, T. Kaneko, *J. Magn. Magn. Mater.* **1995**, *140–144*, 135–136.

[206] Çaklr, F. Cugini, M. Solzi, K. Priolkar, M. Acet, M. Farle, *Phys. Rev. B* **2017**, *96*, 014436.

[207] E. T. Dias, K. R. Priolkar, Ö. Çakir, M. Acet, A. K. Nigam, *J. Appl. Phys.* **2015**, *117*, 123901.

[208] J. P. Siebert, M. Juelsholt, D. Günzing, H. Wende, K. Ollefs, C. S. Birkel, *Inorg. Chem. Front.* **2022**, *9*, 1565–1574.

[209] V. Franco, J. S. Blázquez, B. Ingale, A. Conde, *Annu. Rev. Mater. Res.* **2012**, *42*, 305–342.

[210] D. Fruchart, E. F. Bertaut, F. Sayetat, M. Nasr Eddine, R. Fruchart, J. P. Sénateur, *Solid State Commun.* **1970**, *8*, 91–99.

[211] J. Bouchaud, R. Fruchart, R. Pauthenet, M. Guillot, H. Bartholin, F. Chaissé, *J. Appl. Phys.* **1966**, *37*, 971–972.

[212] J. P. Siebert, M. Juelsholt, D. Günzing, H. Wende, K. Ollefs, C. S. Birkel, *Inorg. Chem. Front.* **2022**, *9*, 1565–1574.

[213] S. C. Duan, X. L. Guo, H. J. Guo, J. Guo, *Ironmak. Steelmak.* **2017**, *44*, 168–184.

[214] J. Yan, Y. Sun, Y. Wen, L. Chu, M. Wu, Q. Huang, C. Wang, J. W. Lynn, Y. Chen, *Inorg. Chem.* **2014**, *53*, 2317–2324.

[215] S. Sasaki, K. Fujino, Y. Takéuchi, *Proc. Japan Acad. Ser. B* **1979**, *55*, 43–48.

[216] E. E. Havinga, H. Damsma, J. M. Kanis, *J. Less Common Met.* **1972**, *27*, 281–291.

[217] H. K. Singh, I. Samathrakis, N. M. Fortunato, J. Zemen, C. Shen, O. Gutfleisch, H. Zhang, *npj Comput. Mater. 2021 71* **2021**, *7*, 1–9.

Erklärungen

§8 Abs. 1 lit. c der Promotionsordnung der TU Darmstadt

Ich versichere hiermit, dass die elektronische Version meiner Dissertation mit der schriftlichen Version übereinstimmt und für die Durchführung des Promotionsverfahrens vorliegt.

§8 Abs. 1 lit. d der Promotionsordnung der TU Darmstadt

Ich versichere hiermit, dass zu einem vorherrigen Zeitpunkt noch keine Promotion versucht wurde und zu keinem früheren Zeitpunkt an einer in- oder ausländischen Hochschule eingereicht wurde. In diesem Fall sind nähere Angaben über Zeitpunkt, Hochschule, Dissertationsthema und Ergebnis des Versuchs mitzuteilen.

§9 Abs. 1 der Promotionsordnung der TU Darmstadt

Ich versichere hiermit, dass die vorliegende Dissertation selbstständig und nur unter Verwendung der angegebenen Quellen verfasst wurde.

§9 Abs. 2 der Promotionsordnung der TU Darmstadt

Die Arbeit hat bisher noch nicht zu Prüfungszwecken gedient.

Darmstadt, den_____

_____

Niels Kubitza